Materials for Halide-Based Thin Film Solar Cells

A dissertation accepted by
The Faculty of Engineering, Institute of Materials Science
University of Duisburg-Essen

for award of the academic degree of
Doctor of Natural Sciences
Doctor rerum naturalium (Dr. rer. nat.)

Thesis submitted by
Maryam Khazaee
M.Sc. Nanobiophysics, TU Dresden
Essen, August 2018

1st Examiner: Prof. Dr. rer. nat. Doru C. Lupascu
2nd Examiner: Prof. Dr. rer. nat. Roland Schmechel
Date of Oral Examination: 06.11.2018

Dedication

This work is dedicated to my dearest husband, Siavash, who has been a constant source of support and encouragement. I am truly thankful for having you in my life. This work is also dedicated to my parents, who have always loved me unconditionally. Especially my mother who has taught me to work hard for the things that I aspire to achieve.

Declaration

I declare that I have prepared the submitted work myself, unassisted and without using any other resources than those indicated. All the direct or indirect cited information from other sources (including the electronic sources) is duly acknowledged without exceptions. The material, in this or similar form, has not been previously submitted, either in full or in part, for other exams at this or any other academic institution. This dissertation is the outcome of my original work and the work done in collaboration has been duly acknowledged.

Maryam Khazaee

Essen, August 2018

Acknowledgment

First and foremost, I would like to express my appreciation to Prof. Dr. Doru C. Lupascu and Prof. Dr. David. B. Mitzi, my supervisors, for giving me the chance to be part of their research teams and for their constant support and encouragement during my doctoral studies.

I specially thank Prof. Dr. Roland Schmechel and Prof. Dr. Niels Benson from the Institute of Technology for Nanostructures at Duisburg-Essen University for providing me the access to their laboratories and for their kind support and helpful discussion, which were essential for this thesis. I especially thank Karsten Rojek from Benson's team for his assistance and helpful discussions in the lab.

Then comes my UDE-MAT family. I would like to express my gratitude to all of you. Particular thanks go to Dr. Vladimir Shvartsman for his constant support and encouragement and his assistance for KPFM measurements. Harsh Trivedi and Christian Hübner, I am very thankful for your generous support. I will cherish the happy moments with our Kicker team Christian Fettkenhauer, Naveed, Christian Hübner, Kevin, Domenic, and Tommy. I also thank the technical support from Patrick Dubray. Irina Anusca, I am grateful for your support and encouragement.

I gratefully acknowledge the generous assistance of Dr. Wei Xia and Prof. Dr. Martin Muhler at Ruhr-University Bochum to do the functionalization of carbon nanotubes and helpful discussion. I am very grateful to Prof. Jacob L. Jones at NC State University, USA for providing me with the lab facilities. Also, I would like to acknowledge the support from the Jones's team, especially Hanhan Zhou who helped me to perform SEM/EDX measurements. I would like to thank Prof. Dr. Ian G. Hill and his research group for the collaboration at Dalhousie University, Canada. Their support for PES measurements and analysis of data is truly acknowledged. I would like to express my gratitude for Prof. Mark Rümmeli and Dr. Rafael G. Mendes at Leibniz Institute for Solid State and Materials Research (IFW) Dresden for assisting me in the TEM measurements. I also acknowledge their endless help with preparing manuscripts for papers. I gratefully acknowledge the generous assistance of Dr. Steffen Oswald, Ralph Dachauer, Dr. Thomas Mayer, Catherine G. Mckenas, and Dr. Carrie L. Donley to perform XPS measurements and analysis.

My sincere thanks to Dr. Kasra Sardashti for his help in experiments, measurement, and interpretation of data and his fruitful discussions. Especial thanks go to Dr. Jon-Paul Sun for his kind support for PES measurements and useful discussion. I would like to thank all of my colleagues at Duke University. Thanks to Betul Teymur, Wiley Dunlap-Shohl, Garrett Wessler, Tianyang Li, Qiwei Han. It was an unforgettable opportunity working with you.

Finally, I would like to express my gratitude towards my beloved parents for their kind support. I highly admire my husband Siavash for his endless support and kindness to make this thesis complete. Thanks for always being there for me. My praiseworthy friends, Sedigheh Alizadeh Lemjiri, Moharram Eslami, Stefan Mebs, Virginia Darnell, and Zahibollah Djudaki, thank you for your generous support.

Abstract

Organic–inorganic perovskite solar cells (PSCs) have recently emerged as high-performance and low-cost thin film solar cells and moved to the forefront of photovoltaics research. Fabrication of high-quality solution-processed perovskite thin films is one of the critical factors affecting performance of PSCs. In this study, the effect of several parameters consisting of antisolvent treatment, solvent evaporation rate, casting solvent, and chlorine incorporation was examined on the surface morphology and crystallinity of solution processed methylammonium lead iodide ($CH_3NH_3PbI_3$) perovskite films. Solvent engineering has been performed in order to optimize morphology of the perovskite thin films. For this purpose, a mixture of gamma butyrolactone (GBL) and dimethylsulphoxide (DMSO) has been used to dissolve individual perovskite components followed by a toluene drop-casting step during thin film deposition. The structural, chemical and optical properties of $CH_3NH_3PbI_3$ perovskite have been investigated using several microscopy and spectroscopy techniques. Thermal stability of the solution processed $CH_3NH_3PbI_3$ film has been examined using X-ray photoelectron spectroscopy (XPS). Photovoltaic performance of pristine and chlorine-incorporated perovskite materials has been studied using an inverted-structure solar cell configuration.

Despite the recent progress in fabricating hybrid organic–inorganic lead halide perovskite solar cells, their toxicity and low stability remain as major drawbacks, thereby hindering large-scale commercialization. Given the isoelectronic nature of lead(II) and bismuth(III) ions, potentially stable and nontoxic alternatives for efficient light absorption in thin-film photovoltaic (PV) devices may be found among bismuth-based halide semiconductors. However, high-quality polycrystalline films of many of these systems have not been demonstrated so far.

In this work a versatile and facile two-step coevaporation approach has been utilized to fabricate $A_3Bi_2I_9$ (A = Cs, Rb) and $Ag_xBi_yI_{x+3y}$ ($AgBi_2I_7$, $AgBiI_4$, and Ag_2BiI_5) polycrystalline films with smooth, pinhole-free morphology and average grain size of > 200 nm. The process involves an initial two-source evaporation step (involving CsI, RbI or AgI, and BiI_3 sources), followed by an annealing step under BiI_3 vapor or N_2. This fabrication method offers a reproducible approach to grow films with high purity and enhanced morphology. Among these compounds, non-toxic and air-stable silver bismuth iodide semiconductors are promising light absorber candidates for photovoltaic applications owing to a suitable band gap for multi- or single-junction solar cells. Recently, solution-based film fabrication approaches have been investigated for several silver bismuth iodide stoichiometries. However, to date, no report of the vacuum-deposited silver bismuth iodide films has appeared. X-ray diffraction (XRD) in combination with scanning electron microscopy (SEM)/energy-dispersive X-

ray spectroscopy (EDX) analysis reveal formation of the pure cubic phase ($Fd\bar{3}m$) $AgBi_2I_7$ or $AgBiI_4$, with > 3 µm average grain size, or the rhombohedral phase ($R\bar{3}m$) Ag_2BiI_5, with > 200 nm average grain size. A phase transition from the rhombohedral to the cubic structure is investigated via temperature-dependent X-ray diffraction (TD-XRD). Planar-junction PV devices are prepared based on the coevaporated $AgBiI_4$ films, with titanium dioxide (TiO_2) and poly(3-hexylthiophene) (P3HT) as electron and hole-transport layers, respectively. The best-performing device exhibited power conversion efficiency (PCE) of as high as 0.9 % with open-circuit voltage (V_{OC}) > 0.8 V in the reverse scan direction.

Recently, carbon nanotubes (CNTs) have demonstrated the capability to enhance efficiency and stability of organic and perovskite solar cells due to their high electrical conductivity and hydrophobic nature of the tubes. Determination of work function of the tubes is an essential task before utilizing them in the device structure, to avoid introducing an unfavorable energy barrier in the solar cell device. In this work, the synthesis and characterization of gas phase oxygen- and nitrogen-functionalized multi-walled carbon nanotubes (OMWCNTs and NMWCNTs) and the dispersibility of these tubes in organic solvents have been investigated. A combination of structural investigation techniques have been employed to monitor CNTs surface functional groups. Elemental analysis demonstrated that the oxygen and nitrogen content increased with increasing treatment time of MWCNT in HNO_3 vapor. Moreover, the degree of nitrogen modification to the tubes is correlated with the oxygen amount on the surface of tubes. A direct observation using Kelvin probe force microscopy (KPFM) has depicted the effects of gas-phase functionalization of the tubes on their work functions.

Zusammenfassung

Organisch-anorganische Perowskit-Solarzellen (englisch: PSCs) haben sich in letzter Zeit zu leistungsstarken und kostengünstigen Dünnschichtsolarzellen entwickelt und sind an die Spitze der Photovoltaikforschung gerückt. Die Herstellung von leistungsfähigen Perowskit-Dünnschichten, die durch Abscheidung direkt aus der Lösung erhalten werden, ist einer der kritischen Faktoren, die die Leistung von PSCs beeinflussen. In dieser Studie wurde die Wirkung verschiedener Parameter, bestehend aus einer Antilösungsmittelbehandlung, Lösungsmittelverdampfungsrate, Gießlösungsmittel und Chloreinlagerung, auf die Oberflächenmorphologie und Kristallinität von in Lösung verarbeiteten Methylolonium-Bleiiodid ($CH_3NH_3PbI_3$) Perowskitfilmen untersucht. Die Optimierung der eingesetzten Lösemittel während der einzelnen Herstellungsschritte ist nötig, um die Morphologie der Perwoskit-Dünnschichten zu verbessern. Dabei wurde zunächst eine Mischung aus Gamma-Butyrolacton (GBL) und Dimethylsulfoxid (DMSO) verwendet, um einzelne Perowskit-Komponenten zu lösen, gefolgt von einem Toluol-Tropfen-Gießschritt während der Dünnfilm-Abscheidung. Die strukturellen, chemischen und optischen Eigenschaften von Methylammonium-Bleiiodid ($CH_3NH_3PbI_3$) Perowskit wurden mit verschiedenen mikroskopischen und spektroskopischen Methoden untersucht. Die thermische Stabilität der Lösung prozessierten $CH_3NH_3PbI_3$-Filme wurde mittels Röntgenphotoelektronenspektroskopie (englisch: XPS) untersucht. Die photovoltaische Leistung von reinen und Chlor-inkorporierten Perowskit-Materialien wurde unter Verwendung einer Solarzellenkonfiguration mit invertierter Struktur untersucht.

Trotz der jüngsten Fortschritte bei der Herstellung von hybriden organisch-anorganischen Bleihalogenid-Perowskit-Solarzellen bleiben ihre Toxizität und geringe Stabilität als Hauptnachteile erhalten, wodurch eine großtechnische Kommerzialisierung erschwert wird. Angesichts der isoelektronischen Natur von Blei (II) - und Bismut (III) -Ionen könnten Halbleiter auf Bismutbasis potentiell stabile und nichttoxische Alternativen für eine effiziente Lichtabsorption in Dünnschichtphotovoltaikvorrichtungen darstellen. Jedoch konnten bisher kaum hochqualitative polykristalline Filme aus solchen Systemen hergestellt werden. In dieser Arbeit wurde ein vielseitiger und einfacher zweistufiger Co-Verdampfungsansatz zur Herstellung von polykristallinen Filmen aus $A_3Bi_2I_9$ (A = Cs, Rb) und $Ag_xBi_yI_{x+3y}$ ($AgBi_2I_7$, $AgBiI_4$, und Ag_2BiI_5) mit glatter, porenfreier Morphologie und mittlerer Korngröße von > 200 nm eingesetzt. Das Verfahren beinhaltet einen anfänglichen Zwei-Quellen-Verdampfungsschritt (mit CsI-, RbI- oder AgI- und BiI_3-Quellen), gefolgt von einem Temperungsschritt unter BiI_3-Dampf oder N_2. Diese Herstellungsmethode bietet einen reproduzierbaren Ansatz, um Filme mit hoher Reinheit und verbesserter Morphologie zu züchten. Unter diesen Verbindungen sind nicht-toxische und luftstabile Silber-Bismutiodid-

Halbleiter vielversprechende Lichtabsorber-Kandidaten für photovoltaische Anwendungen aufgrund einer geeigneten Bandlücke für Mehrfach- oder Einzelübergangs-Solarzellen. Vor kurzem wurden lösungsbasierte Filmherstellungsansätze für mehrere Silberbismutiodid-Stöchiometrien untersucht. Es ist jedoch noch keine Veröffentlichung über den im Vakuum abgeschiedenen Silber-Bismutiodid-Film erschienen. Röntgenbeugung (englisch: XRD) in Kombination mit Rasterelektronenmikroskopie (englisch: SEM) / energiedispersiver Röntgenspektroskopie (englisch: EDX) zeigt die Bildung der reinen kubischen Phase ($Fd\bar{3}m$) $AgBi_2I_7$ oder $AgBiI_4$ mit > 3 µm mittlerer Korngröße, oder die rhomboedrische Phase ($R\bar{3}m$) Ag_2BiI_5 mit einer durchschnittlichen Korngröße von > 200 nm. Ein Phasenübergang von rhomboedrischer zu kubischer Struktur wird über temperaturabhängige Röntgenbeugung (englisch: TD-XRD) untersucht. Planarer Übergang PV-Geräte werden auf der Grundlage der co-verdampften $AgBiI_4$-Filme mit Titandioxid (TiO_2) und Poly(3-hexylthiophen) (P3HT) als Elektronen- bzw. Lochtransportschichten hergestellt. Das Gerät mit der besten Leistung zeigte eine Leistungsumwandlungseffizienz (PCE) von bis zu 0,9 % bei einer Leerlaufspannung (V_{OC}) von > 0,8 V in der Rückwärtsabtastrichtung. In jüngster Zeit haben Kohlenstoffnanoröhren (englisch: CNTs) die Fähigkeit gezeigt, die Effizienz und Stabilität von organischen und Perowskit-Solarzellen aufgrund ihrer hohen elektrischen Leitfähigkeit und hydrophoben Natur der Röhren zu verbessern. Die Bestimmung der Austrittsarbeit der Röhren ist eine wesentliche Aufgabe, bevor sie in der Bauelementstruktur verwendet werden, um das Einbringen einer unerwünschten Energiebarriere in die Solarzellenvorrichtung zu vermeiden. In dieser Arbeit wurde die Synthese und Charakterisierung von sauerstoff- und stickstofffunktionalisierten mehrwandigen Kohlenstoffnanoröhren (englisch: OMWCNTs und NMWCNTs) in Gasphase und die Dispergierbarkeit dieser Röhren in organischen Lösungsmitteln untersucht. Eine Kombination von Strukturuntersuchungstechniken wurde verwendet, um funktionelle CNT-Oberflächengruppen zu überwachen. Die Elementaranalyse zeigte, dass der Sauerstoff- und Stickstoffgehalt mit zunehmender Behandlungszeit von MWCNT in HNO_3-Dampf anstieg. Darüber hinaus korreliert der Grad der Stickstoffmodifikation in den Röhren mit der Sauerstoffmenge auf der Oberfläche der Röhren. Eine direkte Beobachtung mittels Kelvin-Sonden-Kraftmikroskopie (englisch: KPFM) hat die Auswirkungen der Gasphasenfunktionalisierung der Röhren auf ihre Arbeitsfunktionen gezeigt.

Table of Contents

List of Symbols

A	Absorbance
α	Absorption coefficient
C_i	Concentration
c	Speed of light
C	Capacitance
d	Lattice spacing
e	Elementary charge
e^-	Electron
e^+	hole
ε	Extinction coefficient
E_B	Binding energy
E_g	Band gap energy
E_γ	Photon energy
E_k	Kinetic energy
Φ	Photon flux density
φ_{tip}	Tip work function
ϕ	Work function
h	Planck’s constant
J_{SC}	Short circuit current density
$\mathrm{J}_{\mathrm{mpp}}$	Current density at maximum power point
k	Crystal momentum
l	Optical pathway
λ	Wavelength
P_{in}	Incident Power
$\mathrm{P}_{\mathrm{mpp}}$	Power at maximum power point
ν	Frequency
R	Reflected light
T	Temperature
θ	Diffraction angle
t	Tolerance Factor
μ	Octahedral factor
V_{ac}	AC voltage
V_{CPD}	Contact potential difference
V_{dc}	DC voltage
V_{mpp}	Voltage at maximum power point
V_{OC}	Open circuit voltage
ω_{e}	Frequency of ac voltage

List of Abbreviations

Ag	Silver
Al	Aluminium
Au	Gold
AM	Air mass
α-Si	Amorphous silicon
ARXRD	Angle resolved X-ray diffractometry
AES	Auger electron spectroscopy
AFM	Atomic force microscopy
Bi	Bismuth
CBM	Conduction band maxima
CdTe	Cadmium telluride
CIGS	Copper indium gallium selenide
CPD	Contact potential difference
Cs	Cesium
CZTS	Copper zinc tin sulfide
C60	Fullerene
DMF	N,N-dimethylformamide
DMSO	Dimethylsulphoxide
DSSCs	Dye-sensitized solar cells
EDX	Energy-dispersive X-ray spectroscopy
ETM	Electron transport material
ETL	Electron transport layar
FF	Fill factor
FTIR	Fourier transform infrared spectroscopy
FTO	Fluorine doped tin oxide
GBL	Gamma butyrolactone
HRTEM	High resolution transmission electron microscopy
HTL	Hole transport layer
HTM	Hole transport material
IE	Ionization energy
IPES	Inverse photoemission spectroscopy
ITO	Indium tin oxide
IQE	Internal Quantum Efficiency
KPFM	Kelvin probe force microscopy
LED	light-emitting diodes
LiTFSI	Bis(trifluoromethane)sulfonimide lithium salt
LUMO	Lowest unoccupied molecular orbital
MAI	Methylammonium iodide: CH_3NH_3I
MACl	Methylammonium chloride
$MAPbI_3$	Methylammonium lead iodide: $CH_3NH_3PbI_3$
MPP	Maximum power point

Mp-TiO_2	Mesoporous-titanium dioxide
MWCNT	Multiwalled carbon nanotube
NREL	National renewable energy laboratory
OSC	Organic solar cell
PCBM	Phenyl-C61-butyric acid methyl ester (PCBM)
PCE	Power conversion efficiency
PEDOT:PSS	Poly(3,4-ethylene-dioxy-thiophene):polystyrene
PES	Photoelectron Spectroscopy
PMWCNT	Purified multiwalled carbon nanotube
PSC	Perovskite solar cell
P3HT	Poly(3-hexylthiophene
PTAA	Poly(triaryl amine), Poly[bis(4-phenyl)(2,4,6-trimethylphenyl)amine]
PV	Photovoltaic
Rb	Rubidium
SEM	Scanning electron miscopy
t-BP	4-*tert*-Butylpyridine
TCO	Transparent conductive oxide
TD-XRD	Temperature dependent XRD
TGA	Thermogravimetric analysis
TPD	Temperature-programmed desorption
XPS	X-ray photoelectron spectroscopy
UHV	Ultra-high vacuum
UPS	Ultraviolet photoelectron spectroscopy
UV-Vis	Ultraviolet-visible
VBM	Valence band maxima

Chapter 1. Introduction

1.1 Brief History of PV

The electricity production is mostly based on carbon based fossil fuels which are finite resources in form of coal, natural gas and petroleum. As the energy conversion to electricity in these fuels is by means of conventional combustion, they produce vast amount of pollution which has severe environmental impact. Nowadays it has become general knowledge that the emissions produced from combustion of these fuels has got to a point that leads to global warming and climate change.[1]

The only solution is to use renewable energies like sun, wind, ocean and many other resources that are sustainable. These resources exist over wide geographical areas, in contrast to carbon based fossil fuels, which are concentrated in a limited number of countries. Furthermore, deployment of renewable energy facilities has resulted in significant energy security and economic benefits such as creation of green jobs and reduction of the fossil fuel prices. And more importantly, renewable energies have little or no waste products such as carbon dioxide or other chemical pollutants, which leads to minimal environmental impact and mitigation of climate change.[2]

Harnessing solar energy by means of photovoltaic technology (PV) is an effective method to produce electricity from solar energies. Moreover, with the ever growing energy consumption worldwide, it can make an important contribution to the economy of each country.

PV installation has considerably increased in recent years, especially 2017 was a historic year for the solar power sector, whereby the number of globally installed solar PV capacities exceeded the other power generation technologies. In fact, solar not only saw more new capacity deployed than fossil fuels and nuclear combined, but also it added nearly twice as much capacity as wind power (Figure 1).[3] From 2016 to 2017, the cumulative installed solar PV power capacity grew by 32% to 404.5 GW up from 306.4 GW and it is expected to be between 813.3–1270.5 GW by the end of 2022 (Figure 2).[3] Despite remarkable growth rates in recent years, the total share of renewables has reached only 12.1% of total global power output in 2017, indicating a long way to go for renewables.

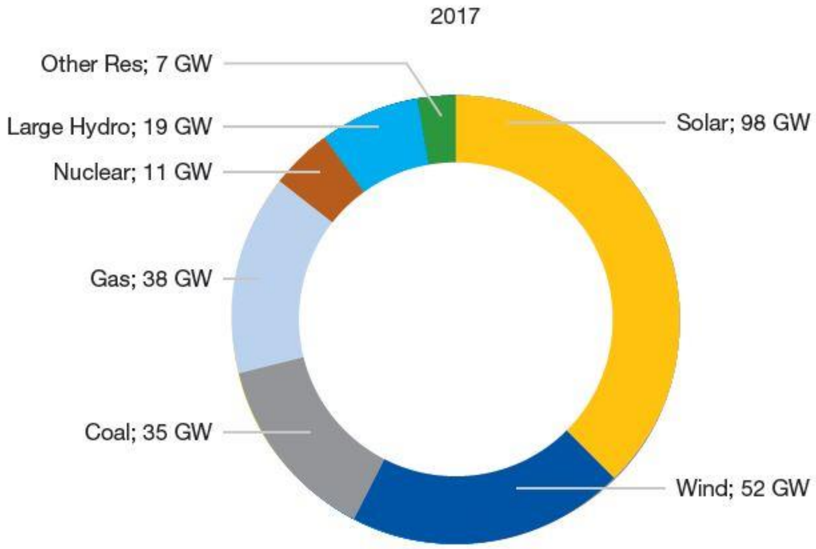

Figure 1. *Net power generating capacity which was globally added in 2017 by main technology.*[3]

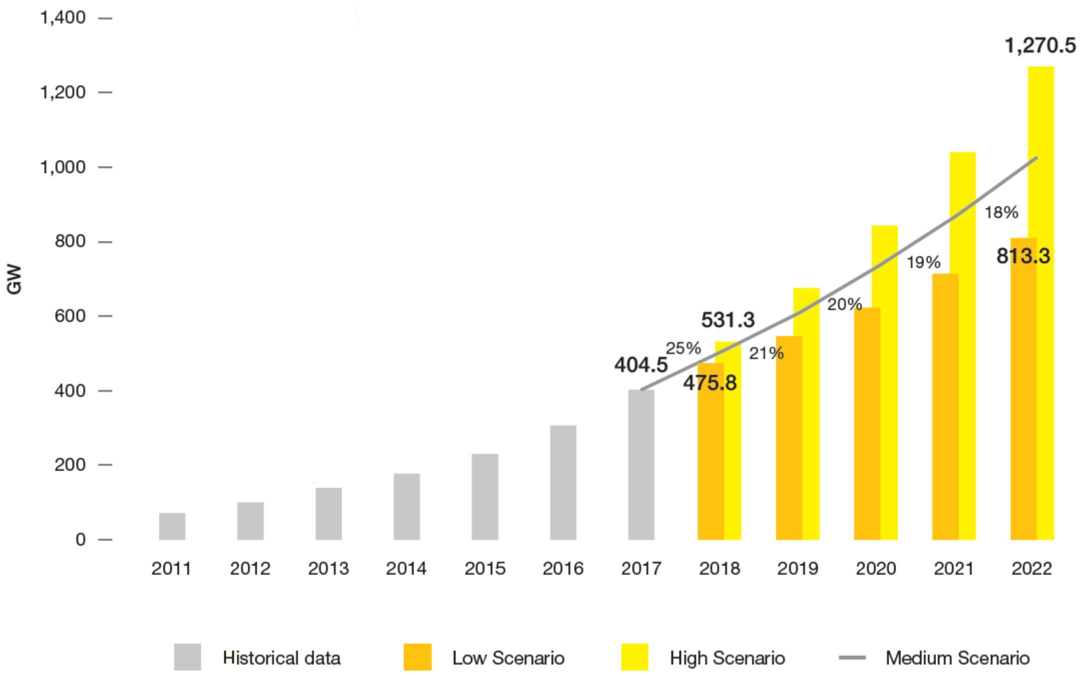

Figure 2. *World annual solar PV market scenarios until 2022.*[3]

Among different PV technologies, thin film solar cells have significantly attracted attention due to the reduction of material usage and subsequent decrease in the production cost along with facile production procedures (Figure 3).[4] Thin film solar cells have shown the susceptibility to offer lightweight and mechanically flexible devices. In this technology, the thickness of the light absorber layer is a few tens or hundreds of nanometers (nm), as opposed to hundreds of microns for crystalline silicon, allowing for a substantial reduction in material usage. In addition the raw materials for this technology are readily available at low cost. Due to the recent high demand for photovoltaic modules, a silicon supply shortage has been created, providing a great chance for thin-film photovoltaic modules to enter the market. However, only 10 % of the global solar market belongs to thin film technology revealing the necessity of further improvement in this field.[3] Amorphous silicon (α-Si), copper indium gallium selenide (CIGS), and cadmium telluride (CdTe) are the three major thin film technologies, which are widely commercialized. Despite the numerous benefits of using these materials in solar technology, materials toxicity and shortage are the two major issues associated with these technologies, which has inspired scientist to search for other potential materials for thin film technology. These efforts have resulted in the exploration of the next generation solar technologies consisting of perovskite, quantum dot, and copper zinc tin sulfide (CZTS).

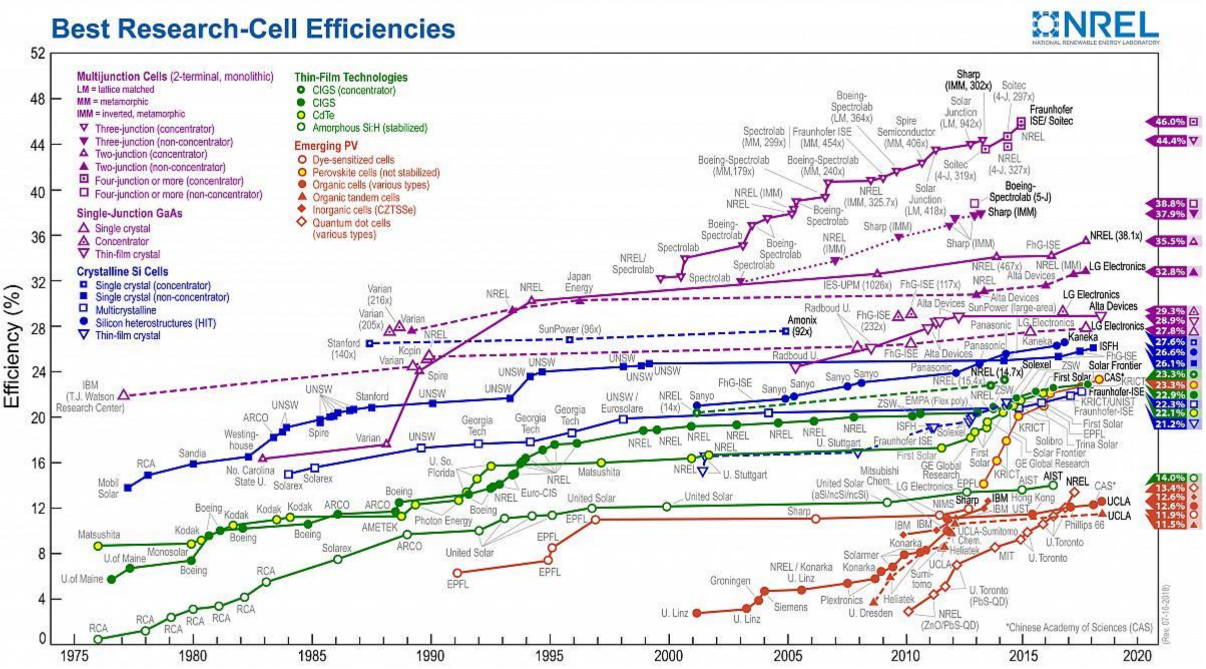

***Figure 3**. Best research-cell efficiencies chart for different PV technologies taken from NREL online source.*[4]

Perovskite solar cells have recently attracted great interest as next generation solar cells primarily due to their remarkable progress in this field. From their emergence, a substantial number of studies have been performed in the last five years resulting in an unprecedented rise in PCE to over 23% (Figure 3)[4] and significant improvement in the lifetime of the devices.

Within this Chapter, background information and underlying physical principles of photovoltaic technology will be described followed by a short introduction of the properties of perovskite materials and their PV performance. Furthermore, two main methodologies for fabrication of PSCs will be presented and different device configurations of PSCs will be discussed. Finally, the current challenges facing PSCs and potential solutions for overcoming these obstacles will be described in details.

1.2 Physical Principles of Solar Cell

1.2.1 Physics of Semiconductors

In a semiconductor material, the highest occupied band containing the valence band electrons is called the valence band (VB) and the lowest unoccupied band is called conduction band (CB). These bands are separated by an energy gap called band gap. When the band gap of materials is in the range 0.5 to 3 eV, these materials are distinguished as semiconductors.[5] Only semiconductors are appropriate for photovoltaics, because the large band gap of insulating materials does not permit them to absorb visible light. The band gap is significantly crucial for photovoltaic materials, since it enables electrons to remain in higher energy levels long enough to be exploited.

Mechanism of Carrier Generation: Since the electrons in the VB are involved in bonding, certain amount of energy (equivalent to the band gap energy (E_g)) is required to excite these electrons to the nearest unoccupied level in the conduction band. Thus an incident photon with energy E_γ will promote an electron from the VB to the CB if it provides $E_\gamma \geq E_g$. When the electron is removed from the VB by absorbing a photon, a positively charged vacancy, normally called hole, remains in the VB (Figure 4a). The created free electron and hole in this way are available to conduct electricity. Low energy photons ($E_\gamma < E_g$) cannot promote electrons across the band gap (Figure 4b), thereby the energy of these photons is wasted in solar cells.

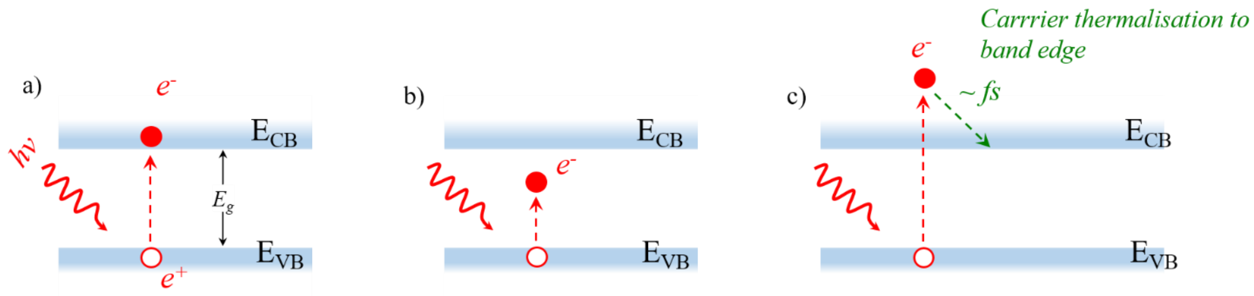

Figure 4. *The mechanism of electron excitation in a semiconductor material. a) The incident photon has energy $E_\gamma = E_g$, which can promot electron to CB; b) the incident photn has energy $E_\gamma < E_g$, thus the energy is not enough to excite the electron to the CB; c) the photon energy $E_\gamma > E_g$ is higher than band gap, thus it promotes the electron to the CB and the electron will be relaxed to the CB edge via thermalisation process.*

For photons with high energy ($E_\gamma > E_g$), an electron can be easily promoted across the band gap. In this case, thermalisation of electron occurs, which is a quick relaxation (femtoseconds (fs)) of the promoted electron with an excess energy to the lowest available energy state in the CB (the CB edge)

(Figure 4c). The required energy for charge generation can be provided by the vibrational energy of the lattice (phonons), light (photons) or the kinetic energy of another carrier.

Carrier Recombination: This is an electronic relaxation process which decreases the number of free carries and releases energy. It occurs via losing an electron or hole through the decay of an electron to a lower energy state. As shown in Figure 5, there are three different ways of releasing energy via recombination consisting of radiative, non-radiative and Auger recombination.[5] Among these, radiative recombination is the most important one for photovoltaics. Radiative and Auger recombinations are categorized as unavoidable recombination, while non-radiative recombination is distinguished as avoidable recombination. A short description of each mechanism is given below:

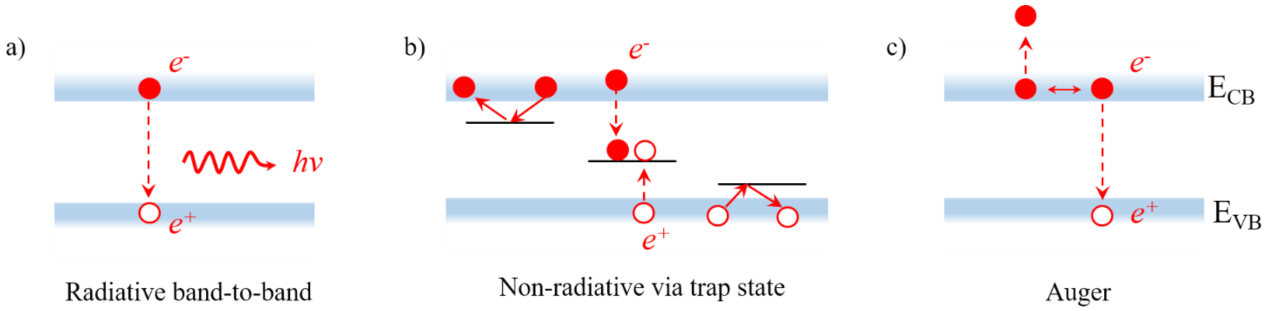

***Figure 5**. Mechanism of a) radiative, b) non-radiative and c) Auger recombinations.*

- **Radiative Recombination**: this is a spontaneous decay of an electron from CB to VB together with the emission of a photon with energy equal to E_g (Figure 5a).
- **Non-radiative Recombination**: trap states are sub-band gap levels acting as recombination centers when the energy of the state lies deep in the band gap. In such case electron recombines into the trap state and the energy releases as heat through phonon emission (Figure 5b, middle trap). Electron trap and hole trap states are those if the states are close in energy to CB or VB (Figure 5b, right and left traps), respectively. These localized states serve to slow down the transport of carries but they do not remove them. Moreover, surfaces and interfaces between different crystal regions in a heterostructure material are the area, in which the defect density is high shortening the electron and hole capture times.

- **Auger Recombination**: This is a non-radiative process where two similar carriers (e.g. electron) interact resulting in the decay of one electron across the band gap. The energy release through recombination yields an increase in the kinetic energy of the other carrier by an amount equal to the band gap. As the excited carrier relaxes to the CB edge, it releases that extra energy as heat (Figure 5c).

Direct and Indirect Band Gap Semiconductors: As mentioned, the band gap (E_g) is the minimum amount of energy difference between the top of the VB and the bottom of the CB. However, the top of the VB and the bottom of the CB are not generally at the same value of the electron momentum (*k*). This results in categorizing semiconductor materials in to two types: direct and indirect band gaps.

In a **direct band gap semiconductor**, the top of the VB and the bottom of the CB occur at the same value of k, as depicted in Figure 6a. Therefore, an incident photon with sufficient energy of E_g can promote an electron from VB to CB and create electron-hole pair. Also, an electron can directly emit a photon decaying from the CB to VB energy level.[5]

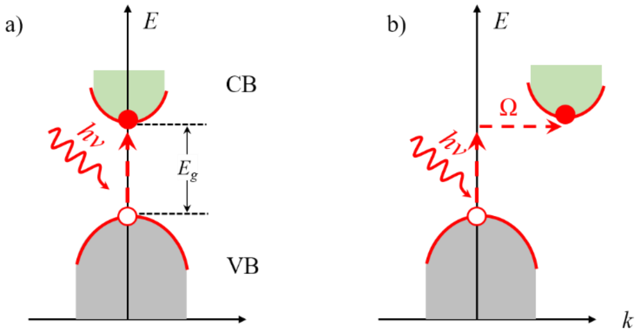

Figure 6*. Energy (E) versus crystal momentum (k) for a) direct and b) indirect band gap semiconductor.*

In an **indirect band gap semiconductor**, the maximum energy of the VB occurs at a different value of k in respect to the minimum in the CB energy level, as illustrated in Figure 6b. In such a semiconductor, an incident photon with energy of E_g is not on its own sufficient to create an electron-hole pair, and also a photon cannot be emitted by decaying an electron from CB to VB. This is due to the fact that the electron must pass through an intermediate state (Ω) and transfer momentum to or from a phonon – the crystal lattice vibration – of the correct momentum.

The radiative recombination is far slower in indirect band gap materials than direct band gap ones. This is due to the involvement of the absorption or emission of phonons, where the phonon momentum equals to the difference between the electron and hole momentum and cannot carry crystal momentum (It can also involve a crystallographic defect, which performs essentially the same role).[5] Thin-film solar cells are made of direct band gap semiconductors (such as CdTe, CIGS or CZTS), which absorb the light in a very thin region, and consequently can be made with a very thin active layer in the range of some nanometers.

Due to the fact that at low temperatures there are fewer phonons, it is less likely that a photon and phonon can be simultaneously absorbed to create an indirect transition as indirect band gap semiconductors need. That's why, the absorption spectrum of an indirect band gap semiconductor usually depends more on temperature than that of a direct one.

1.2.2 Solar Cell Principles

Accordingly, the two major parameters determining efficiency of a PV material are E_g and the incident photon spectrum. With a fixed incident spectrum, the efficiency depends on the band gap only. Very small or very large band gaps result in small voltage and current, respectively. Thereby, there is an optimum band gap of the materials at which efficiency of a PV is maximum. According to the Shockley–Queisser limit, a single band gap solar cell in AM1.5 has a maximum theoretical efficiency of 33% at an $E_g \sim 1.4$ eV.[5-6]

After light absorption and electron-hole generation, the solar cell must be able to collect these free charges before they recombine. An internal electric field in a solar cell, usually defined as the built-in field, transports electrons and holes in the opposite direction and feeds them to an external circuit. Figure 7 shows the equivalent circuit of a solar cell, which consists of a load and a diode. When the solar cell is illuminated, the generated photocurrent in the cell is divided between the variable resistance of the load and the diode. In this circuit, the diode provides the photovoltage to drive the photocurrent through the load. When the two terminals of the cell are isolated, the photovoltage developed by the illuminated cell has its maximum value, the open circuit voltage V_{OC}. In contrast, when the two terminals are connected, the generated photocurrent from the illuminated cell is the short circuit current J_{SC}. This is the current that flows when no voltage is applied to the cell and arise from the built-in field originating from the difference in work functions between the electrodes.

A standard solar cell behaves like a diode, with a much larger current under forward bias ($V > 0$) than under reverse bias ($V < 0$). The J-V characteristics of a solar cell under dark and illuminated conditions are shown in Figure 8.

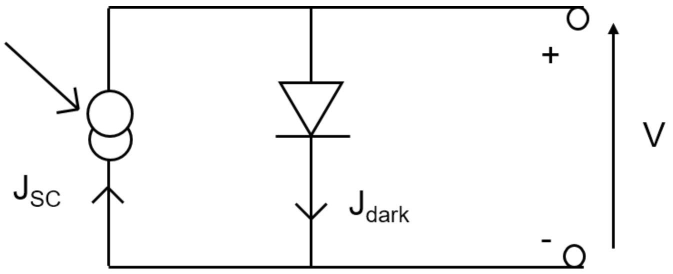

Figure 7. *Equivalent circuit of an ideal solar cell.*[5]

The maximum power point at which the highest operational voltage and current density are achieved is specified on Figure 8. The maximum current density and voltage of a solar cell are J_{SC}

and V_{OC}, respectively which at each of these operating points, there is no power output from the solar cell. The ratio between the power at the maximum power point (mpp) and the power achieved from product of V_{OC} and J_{SC} is called fill factor (FF) as:

$$FF = \frac{V_{mpp} \times J_{mpp}}{V_{oc} \times J_{sc}} \tag{1}$$

The red area shown in Figure 8 represents the operational power output at the maximum power point. The larger the area, the higher the output power will be. Higher FF also translates to a more square area and higher power output of the solar cell.

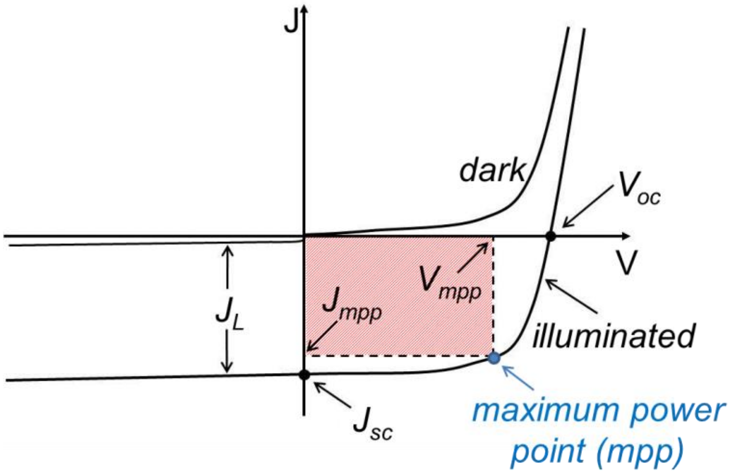

Figure 8*. Solar cell's J-V characteristic curve under dark and illuminated conditions.*

Power conversion efficiency (PCE) reveals the amount of the converted incident energy in the form of electromagnetic radiation into the electrical energy output. The efficiency of the solar cell is then calculated as the ratio of the maximum power output (P_{mpp}) of a solar cell per incident power (P_{in}) on it as:

$$PCE = \frac{P_{out}}{P_{in}} = \frac{V_{MPP} \times J_{MPP}}{P_{in}} = \frac{V_{OC} \times J_{SC} \times FF}{P_{in}} \tag{2}$$

The largest proportion of energy in the solar spectrum is in the visible region, however, due to atmospheric absorption by water vapor, ozone, oxygen, and carbon dioxide, or scattering by dust particles, the raw solar spectrum is not used for testing photovoltaic devices. Instead, air mass (AM) spectra is used which refer to the mass of air that solar radiation has passed to reach the earth. The convention for photovoltaic characterization is to use AM1.5 corresponding to light incident angle of 48.2° relative to the normal to the Earth’s surface (mid-latitudes, for example much of Europe and North America) and $P_{in} = 1000$ W m^{-2}. To characterize and evaluate the spectrally resolved properties of the solar cells, the spectral response in form of quantum efficiency is used. The ratio of the number of charge carriers collected by a solar cell to the total number of photons incident on it with a particular wavelength is called quantum efficiency (*QE*) of the solar cell and is expressed as the photon flux density of the incident light.

The definition above implies that if all photons of a certain wavelength are absorbed and the resulting minority charge carriers are collected– assuming every absorbed photon creates one electron-hole pair– then at that particular wavelength unity quantum efficiency is achieved. Since it is measured with the help of externally measured optical short circuit current density (J_{SC}), this quantity is denoted as external quantum efficiency (*EQE*), in which the optical losses as the reflection of light from the solar cell are already included and is defined with respect to the wavelength of the light as:

$$EQE(\lambda) = \frac{J_{SC}(\lambda)}{e \cdot \Phi(\lambda)} \qquad (3)$$

where e and Φ are the elementary charge and the photon flux density of the incident light, respectively. Unlike the *EQE*, the Internal Quantum Efficiency (*IQE*) excludes the reflection loss; therefore it is used to observe the losses within the solar cell independently from the cell reflection which is defined as:

$$IQE(\lambda) = \frac{EQE(\lambda)}{1 - R(\lambda)} \qquad (4)$$

where $R(\lambda)$ is the reflected light from the solar cell (reflectance) and $1–R(\lambda)$ gives the total absorbance of the solar cell ($A_{cell}(\lambda) = 1–R(\lambda)$) with respect to the wavelength of the light.

The losses within the solar cell consist of parasitic absorption not leading to generation of electron-hole pairs (free carrier absorption and defect absorption), and recombination of photo-generated charge carriers (recombination loss).

1.3 Perovskite Solar Cells (PSCs)

1.3.1 Fundamental Properties

Organic-inorganic lead halide perovskites have attracted huge attention since they were introduced as sensitizers in dye-sensitized solar cells (DSSCs).[7-9] Miyasaka and coworkers were apparently the first to report photovoltaic performance of halide perovskites; they were attracted by the self-organization potential of perovskite in the nanoporous TiO_2 layer of dye-sensitized cells. They reported $CH_3NH_3PbBr_3$ cells with an efficiency of 2.2% in 2006 and with an increase in efficiency to 3.8% by replacing bromine with iodine in 2009.[8-9] Ease of fabrication, strong solar absorption, relatively suitable band gap for single junction solar cells and low non-radiative carrier recombination rates have resulted in a rapid increase in the number of researchers working in this field and an extraordinary development of PSCs in a short period compared to organic and dye synthesized solar cells. A lot of research efforts have resulted in a jump to an efficiency up to 23% in 2018 revealing a relatively fast growing field of science.[4]

The general chemical formula of organic-inorganic perovskite absorber materials is ABX_3, where the organic cations or large inorganic cations locate at the A site ($CH_3NH_3^+$, $HC(NH_2)_2^+$, Cs^+, Rb^+). The smaller divalent metal ions reside on the B site (B = Pb^{2+}, Sn^{2+}). X is a halide ion (X = Cl^-, Br^-, I^-). Among the perovskite systems, methylammonium lead iodide ($CH_3NH_3PbI_3$) and its mixed-halide ($CH_3NH_3PbI_{3-x}Cl_x$) have attracted attention for photovoltaic application, owing to their stoichiometry-tunable band gap, high absorption coefficient, long carrier diffusion lengths, low cost, and facile fabrication techniques.[10-14] A schematic illustration of methylammonium lead iodide is shown in Figure 9. The three dimensional (3D) cubic crystal of $CH_3NH_3PbI_3$ consists of the corner-sharing lead iodide octahedra (PbI_6), in which the methylammonium cations ($CH_3NH_3^+$) occupies the space in between these octahedra in a 12-fold cuboctahedral coordination (sits in the vacancy of eight $[PbI_6]^{4-}$ octahedra). The corner-shared PbI_6 contains of lead cation (Pb^{2+}), which is surrounded by iodide anions in an octahedral structure.

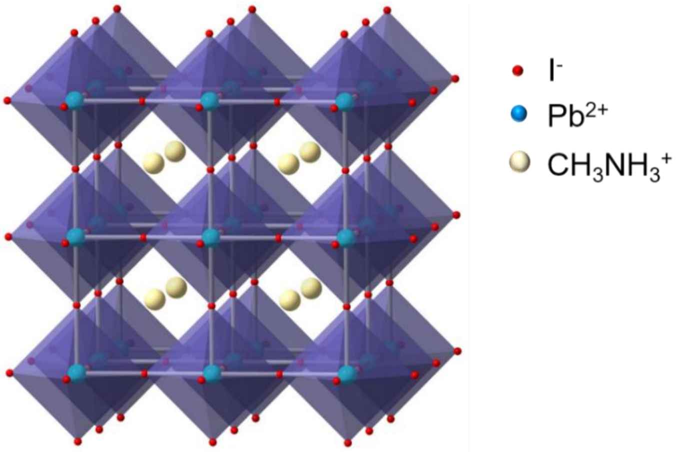

Figure 9. *Crystal structure of methylammonium lead iodide ($CH_3NH_3PbI_3$). The shaded octahedra contain lead (blue) and iodine (red) atoms surrounded by methylammonium cations (yellow).*

Tolerance factor (t) and octahedral factor (μ) are the two parameters determining whether combination of the three elements (A, B, X in ABX_3) can form a stable perovskite crystal structure.[15] As proposed by Goldschmidt,[16] tolerance factor is a magnitude, which is defined as the ratio of the separation of A and X to the separation of B and X and it can be given as:

$$t = \frac{R_A + R_X}{\sqrt{2}\,(R_B + R_X)} \tag{5}$$

where R_A, R_B and R_X are the ionic radii of the corresponding ions. Furthermore, the octahedral factor is defined as the ratio of ionic radii of B and X ($\mu = R_B/R_X$). The organohalide perovskites are stable to structural variance with a tolerance factor $0.81 < t < 1.11$ and octahedral factor $0.44 < \mu < 0.90$.[15] When $t \sim 1$ formation of a 3D cubic perovskite structure is likely (Figure 9), while low-dimensional derivatives (2D: layered, 1D: chain-like, 0D: isolated) with tetragonal or orthorhombic structures would be formed with t beyond this range. For organic-inorganic halide perovskites (ABX_3), the organic molecule (A) has bigger ionic radius than the inorganic (B) cation. Two organic molecules yielding the perovskite structure are methylammonium ($CH_3NH_3^+$) with R_A = 0.18 nm and formamidinium ($NH_2CH{=}NH_2^+$) (R_A is estimated to lie in the range 0.19–0.22 nm).[15, 17-18] When the A site is occupied by groups that are too large (e.g. long-chain alkyl amine anions), the lead halide perovskite becomes a two-dimensional (2D) layer structure.[19-20] Structural and electronic dimensionalities play important roles determining performance of photovoltaic materials, since they significantly affect the transportation of carriers in the materials.[21]

Furthermore, lead (Pb^{2+}; R_B = 0.119 nm) and tin (Sn^{2+}; R_B = 0.110 nm) have generally been tested as promising candidates for making cubic organic-inorganic halide perovskites. However, perovskite crystals containing Sn^{2+} cation tends to be unstable due to oxidation of Sn^{2+} to Sn^{4+}.[22-24] The X anion is a halogen (X = I, Cl, Br) with ionic radius of R_X = 0.181 nm for Cl^-, 0.196 nm for Br^- and R_X = 0.220 nm for I^-.

Organohalide perovskites are direct band gap semiconductors with high absorption coefficients. The optical property of these materials can be easily tuned via modification of their chemical composition, including the organic cation, the metallic cation and the ratio of the mixed halide.[25-27] The band gap tunability of perovskite materials offers a convenient approach for adjusting their optical properties for several optoelectronic applications.[28]

Dielectric properties of the materials are critical determining the mechanism of charge generation physics. Organic semiconductors possess dielectric constants < 5 yielding excitonic photoexcitation (binding energy (E_B) > 200 eV). As a consequence, a heterojunction structure is required to provide a driving force for generation of free carriers. In contrast, the calculated binding energy of organohalide perovskites is in the order of 10 meV at room temperature indicating a nonexcitonic characteristic of these materials.[27] The ambipolar charge-transport offers a relatively balanced electron and hole transport in this medium. Relatively modest charge carrier mobilities ($\mu \approx 1-100$ $cm^2\ V^{-1}\ s^{-1}$) along with long carrier diffusion lengths (100 nm – 1μm) significantly reduce carrier recombination rates in these materials allowing high internal quantum efficiency of PV devices utilizing single component organohalide photojunctions.[29-30]

Such a collection of properties makes the organic-inorganic halide perovskites very appealing for thin film PV applications.[10, 31-34]

1.3.2 Fabrication Methodologies

Film quality of the absorber layer in thin film solar cells is of substantial importance in determining the device performance. To develop high-performance PV devices, it is essential to control the morphology, crystallinity, phase purity, and uniformity of the absorber layer. The fabrication process will thus greatly affect the film quality. The two major methodologies used for deposition of perovskite films are vacuum deposition and solution-based deposition. For both methodologies, several procedures have been examined yielding different film qualities as well as different PCEs. A brief list of most commonly used fabrication procedures for deposition of perovskite films is presented below.

1.3.2.1 Solution Processing Fabrication

Single-step Solution Deposition: As shown in Figure 10a, this solution-based method involves dissolving organic halides (methylammonium iodide (MAI) or methylammonium chloride (MACl)) and PbI_2 in polar aprotic solvents such as N,N-dimethylformamide (DMF), dimethylsulfoxide (DMSO) or gamma-butyrolactone (GBL) to prepare the precursor solution. The perovskite film can be fabricated by spin-coating of the precursor solution on the substrate followed by a postdeposition annealing to produce perovskite crystals.[35] In this technique, there are several parameters controlling the uniformity and crystallinity of the final films consisting of precursor composition, processing temperatures and times, environment (oxygen and humidity levels), substrate material, and deposition parameters.[25, 36-37]

Two-step Solution Deposition: The two-step deposition approach can be performed in two different ways. In the first approach shown in Figure 10b I, a metal halide (PbI_2) seed layer is spin coated onto the substrate followed by spin coating of organic halide (MAI = CH_3NH_3I) from a solution on the dried PbI_2 film. In this process the color of the film turns from yellowish to dark brown. Then the film is annealed.[38-39]

In the second approach, first a metal halide (PbI_2) layer is spin coated onto the substrate and then dipped into a MAI precursor solution to form $MAPbI_3$ film (Figure 10b II). This step will be followed by annealing to improve the film morphology.

The two-step deposition process was developed in order to obtain more control over the film morphology of perovskite. However, since the diffusion of $CH_3NH_3I^+$ cations into the lead halide matrix occurs rapidly as the PbI_2 film is dipped into the solution, a compact $MAPbI_3$ film forms on the top layer preventing further diffusion of $CH_3NH_3^+$ cations and formation of a $CH_3NH_3PbI_3$ film. Therefore, sufficient time is required to fully convert PbI_2 to a perovskite film.[40-41]

Two-step Hybrid Deposition: This method is a modification of the two-step solution deposition method, in which the PbI_2 seed layer is spin coated from a solution onto the substrate and MAI is introduced through a vacuum-based deposition method rather than through a solution processing procedure (Figure 10b III).[42] It has been demonstrated that deposited perovskite films by this method possess improved morphology and grain size in addition to enhanced reproducibility of high-quality films in comparison with solution processed films.[42-43]

1.3.2.2 Vacuum Processing Fabrication

Dual-source Vapor Deposition: Thermal deposition is a versatile technique used for fabrication of uniform and high-quality semiconductor films. In this technique, the deposition of precursors occurs in vacuum providing a substantially clean environment for growth of films with high degree of purity. The low fabrication temperature required for the growth of perovskite films allows the compatibility of this technique with a wide range of substrates, including flexible substrates and textiles. Furthermore, the film thickness can be controlled and monitored in real-time allowing growth of films with arbitrary thicknesses.

Perovskite films can be deposited via either sequential or coevaporation methods. Figure 10c displays the thermal deposition of a perovskite film using coevaporation technique. In this case, one source will be filled with an organic precursor (MAI) and the other one with an inorganic precursor (PbI_2). Although solution processed perovskite films might have incomplete surface coverage, thermally evaporated films are extremely uniform and compact.[44-46]

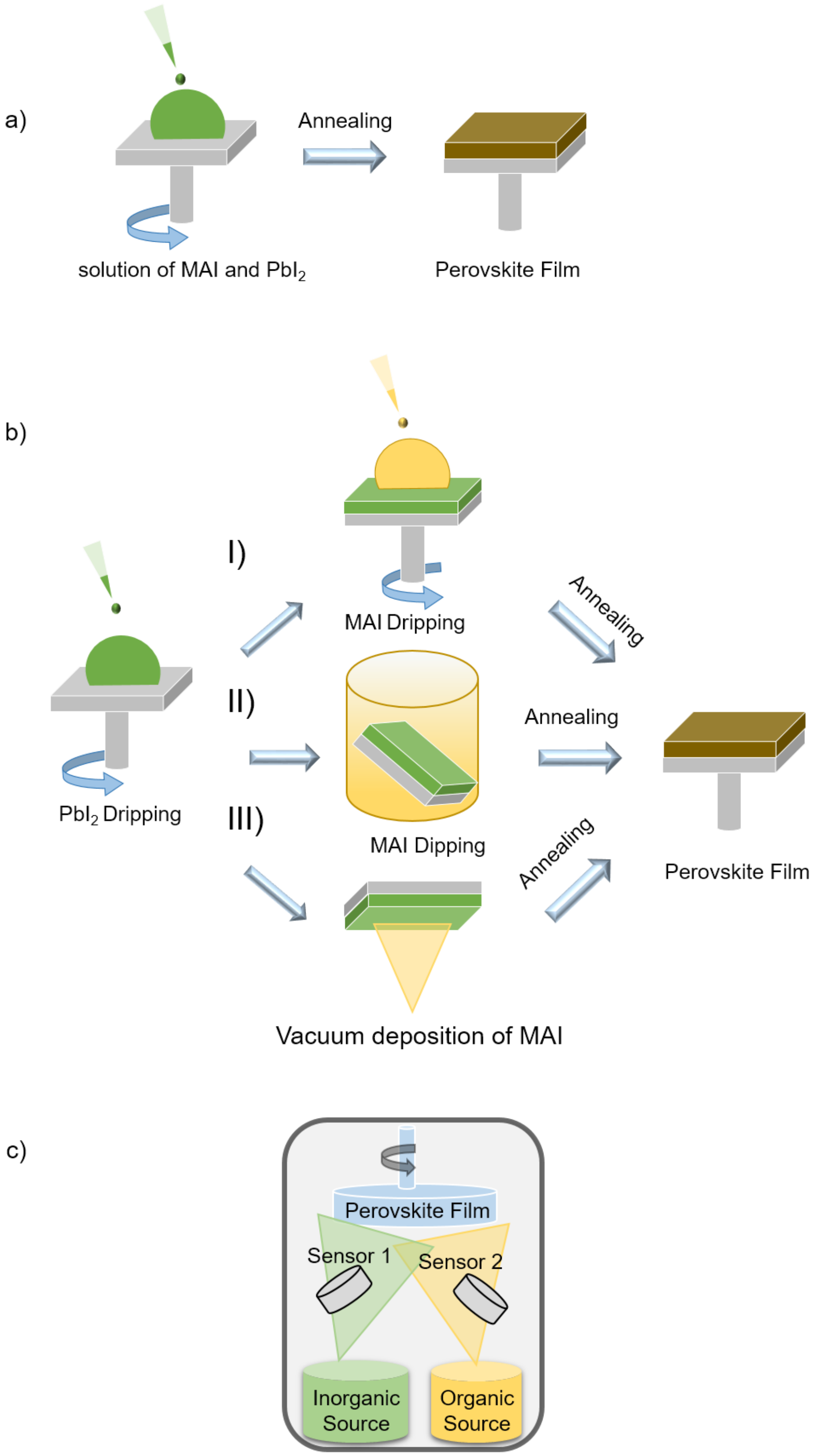

Figure 10. *Various methods for deposition of perovskite films. a) one-step solution deposition, b) two-step solution deposition, and c) dual-source vapor deposition.*

1.3.3 Device Architecture

In a PSC, perovskite material as the light absorber is placed between hole (p-type semiconductor) and electron (n-type semiconductor) transport layers covered with two electrodes. The front contact electrode is made of a transparent conductive oxide (TCO) (e.g. indium tin oxide (ITO), fluorine-doped tin-oxide), which is a wide band gap conductive material allowing light to reach the absorber layer. The back contact electrode is made of a metal (e.g. Al, Ag, Au) to act as a mirror in reflecting the unabsorbed photons back towards the absorber layer. PSCs can be developed based on three main configurations as shown in Figure 11. In an inverted configuration (Figure 11a), a hole transport layer (HTL) is directly deposited on TCO anode at low processing temperature (< 150 °C), while in both planar (Figure 11b) and mesoporous (Figure 11c) configurations, the deposition of electron transport materials on the TCO cathode occurs at T > 400 °C. A compact-titanium dioxide (TiO_2) layer is widely used in a planar structure PSCs (n-i-p) conducting electrons to the TCO cathode.

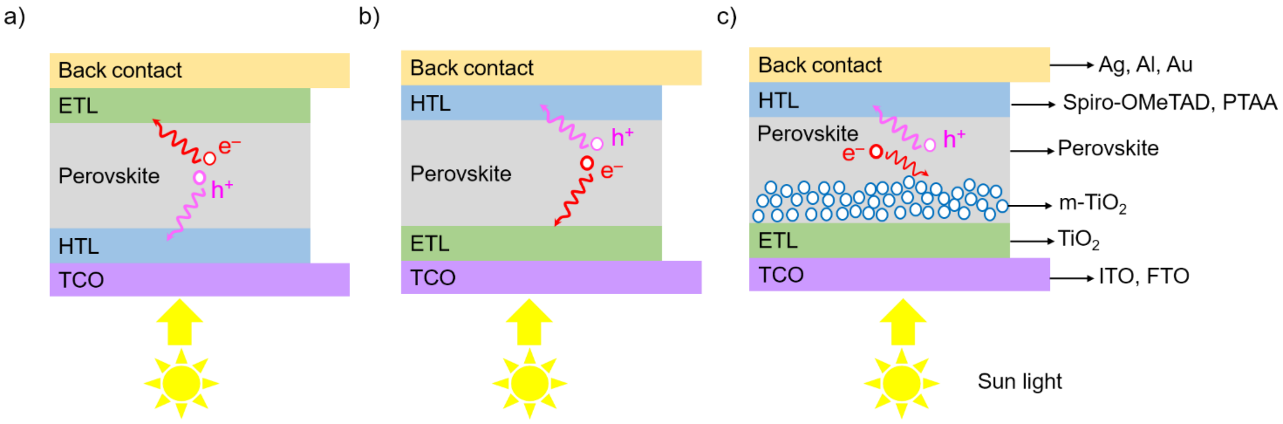

Figure 11. *Schematic representation of the three main configurations of PSCs. a) Inverted strucrure (p-i-n); b) planar strucrure (n-i-p); c) mesoporous structure.*

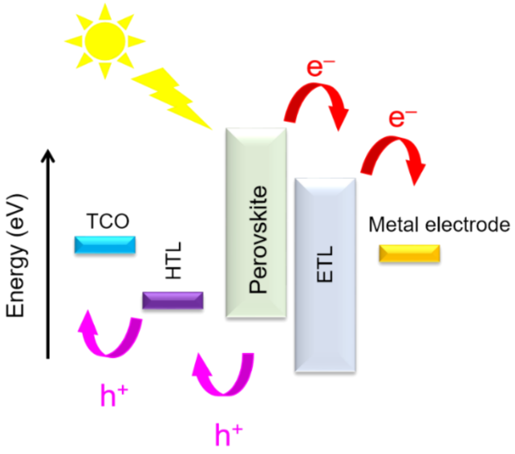

Figure 12. *Schematic illustration of charge carrier injection in an inverted structure PSCs.*

Furthermore, the mesoscopic n-i-p structure consist of a compact-TiO_2 on TCO, a 150- to 300-nm thick mesoporous metal oxide (e.g. TiO_2) that is filled with perovskite and covered with a 300-nm thick perovskite capping layer, a HTL and a metal anode (Al, Ag, Au). Charge collection of PSCs enhances by using the mesoporous structure due to decreasing charge transport distance and increasing photon absorption.[47]

In addition to the configuration employed for fabrication of PSCs, the properties of hole and electron transport materials, HTM and ETM, and their interfaces are also crucial parameters affecting performance of perovskite PV devices. Figure 12 illustrates mechanisms of charge injection in PSCs. After photoexcitation of the perovskite, the created electron and hole will be separated at the interface of perovskite-ETL/HTL followed by charge transportation to electrodes.

Several potential losses may occur in PSCs and ETL/HTL interfaces originating from either surface charge recombination or a mismatch between the perovskite valence band and the highest occupied molecular orbital (HOMO) of the hole transport material for hole injection on one side, and perovskite conduction band and n-type semiconductor conduction band (lowest unoccupied molecular orbital, LUMO when n-type semiconductor is organic) for electron injection on the other. Therefore, the appropriate choice of HTM and ETM is very important to achieve high performance devices.

1.3.4 Issues and Challenges

Lead-based halide perovskites have recently attracted substantial attention due to their remarkable semiconducting properties. Among the perovskite systems, methylammonium lead iodide ($CH_3NH_3PbI_3$) has been at the center of attention due to its notable performance in thin-film solar cells, reaching power conversion efficiencies (PCEs) beyond 22%.[4] Ease of solution-based processing coupled with inexpensive and earth-abundant constituents is expected to reduce production costs relative to commercial solar cells – e.g., silicon, CdTe, $Cu(In,Ga)(S,Se)_2$ (CIGS) and GaAs.[15] Despite the intense advancement in PCE of lead-halide perovskite solar cells (> 23%),[4] environmental toxicity of Pb and low stability under ambient conditions (light exposure, elevated temperature and humidity) remain two key issues hindering large-scale commercialization of this technology.[48-51]

With the goal of boosting stability and reducing toxicity, multiple studies have pursued partial or full substitution of the monovalent methylammonium and divalent Pb^{2+} with alternative organic and inorganic cations. Although substitution of methylammonium with formamidinium,[52] or incorporation of inorganic A^+ cations (Cs,[53] Cs alloys,[54] and Rb [55]) in place of the organic analogues has enhanced the stability of the resulting devices,[54-55] the demanded level of stability for large-scale commercialization still remains to be achieved. The less-toxic elements, tin and germanium (Sn^{2+}, Ge^{2+}) have been considered and demonstrated for the "B" site, but are environmentally unstable owing to the propensity of these elements to oxidize to the 4+ valence state (Sn^{4+} and Ge^{+4}).[23-24, 56-58] Non-toxic and stable Bi^{3+} represents another candidate to replace Pb^{2+}, offering similar ionic radius and identical electronic structure to Pb^{2+}. However, direct incorporation of Bi is complicated by its trivalent oxidation state (vs. divalent for Pb), as charge balance requirements induce structural changes to the perovskite lattice that substantially alter material properties when substituted for Pb (unless balanced by an equal amount of a monovalent cation, such as Ag^+). Recently, several semiconductor Bi-based halides, including "defect perovskites" $A_3Bi_2I_9$ (A = CH_3NH_3, NH_4, K, Rb, Cs),[59-66] "double perovskites" Cs_2AgBiX_6 (X = Br, Cl)[67-68] and several stoichiometries of silver bismuth iodide (e.g. $AgBiI_4$, $AgBi_2I_7$, Ag_3BiI_6),[69-71] have been investigated as potential absorber materials for thin film solar cells. However, so far, these systems have shown PCEs far below the Pb-based systems (maximum efficiency of 4.3%),[72] necessitating more in-depth investigations into the factors limiting their performance.[66]

Moreover, stability of solar cells under standard working conditions is the most important criteria for their large-scale commercialization. Despite lots of research efforts on enhancing stability of PSCs, this is still a crucial issue associated with this technology. PSCs can be preserved from ambient conditions by using a proper protective coating layer. It has recently been shown that the stability of PSCs has been improved employing a moisture resistant layer (e.g., carbon nanotube or graphite).[73-75]

A recent study by Snaith et al. has proven that the presence of CNTs in the conductive layer of the PSCs provides a protective layer that preserves the cell from heat and moisture degradation.[76] In another study by Boschloo et al., single walled CNTs were deposited directly onto the perovskite layer and processed further with a small amount of drop-cast Spiro-OMeTAD (hole transport material) yielding high solar cell efficiencies of around 15%.[77] Their further investigation revealed that the devices with SWCNTs-Spiro-OMeTAD as the hole transport layer and gold (Au) as the back contact yieled higher thermal stability than the devices with only Spiro-OMeTAD. These observations verify the enhancement of efficiency and stability of PSCs via utilizing CNTs in the structure of the cells.[78-79]

1.4 Motivation and Scope of This Work

From the emergence of perovskite materials in solar technology, a lot of research efforts have been invested to fully understand several characteristics of these materials. Most research, however, has been undertaken using organic-inorganic hybrid perovskites containing lead in the crystalline system. According to recent studies, toxicity of lead and instability of PSCs are still the two major challenges faced by perovskite materials.[80] Considering these facts, this study aims to play a role in moving from solution processed unstable perovskite materials towards development of more stable vacuum-based lead-free semiconductor materials for optoelectronic applications.

Initial studies focused on fabrication of compact and uniform organic-inorganic perovskite films followed by studying structural, optical, and chemical properties of these materials. In addition, PV performance of perovskite solar cells based on $CH_3NH_3PbI_3$ and $CH_3NH_3PbI_3Cl_{3-x}$ absorber materials has been investigated. Stability of fabricated $CH_3NH_3PbI_3$ film on PEDOT:PSS/ITO in addition to metal electrode in an inverted-strcuture $CH_3NH_3PbI_3$-device is presented in **Chapter 2**.

Chapter 3 details the materials and experimental methods used in the current study. A short description of frequently used characterization techniques in this research is also given.

The search for appropriate lead-free semiconductors is considered as a requisite to solve the toxicity issue associated with lead in perovskite materials. In **Chapter 4** a vacuum-based fabrication of bismuth-based semiconducting materials consisting of $A_3Bi_2I_9$ (A = Cs, Rb) and $Ag_xBi_yI_{x+3y}$ ($AgBi_2I_7$, $AgBiI_4$, and Ag_2BiI_5) is presented. This chapter focuses on structural, chemical, optical, and electrical characterization of these materials along with examination of the PV perfomance of $AgBiI_4$ and $Rb_3Bi_2I_9$.

Finally, **Chapter 5** focuses on CNTs as a promising candidate enhancing the efficiency and stability of PSCs.[51, 76-78] Gas-phase oxygen and nitrogen functionalization of MWCNTs are performed to achieve n-doped and p-doped tubes, respectively, to make them suitable to be used in the ETL and HTL of thin film solar cells. This research aims to examine the nature of the functional groups on the surface of MWCNTs and the subsequent alteration in their chemical and electrical properties. Thoroughly understanding these features is indispensable for further utilization of the tubes in electronic applications.

Chapter 2.
Materials and Methods

This Chapter is dedicated to mention the materials used in this work and to describe the methods and investigation techniques used in the development of the experiments of this thesis. In particular, in the first part both solution-based and vacuum-based synthesis and fabrication of the materials are described followed by the preparation of photovoltaic devices. In the second part, the methodology used for gas-phase functionalization of carbon nanotubes are described. Finally, the third part describes some of the characterization techniques employed.[1]

2.1 Thin Film Deposition

In this research, two main methodologies were employed for synthesis and fabrication of absorber materials used in thin film solar cells. Both of these techniques will be described in detail as follows:

2.1.1 Solution-based Deposition of Perovskite Films

The synthesis of perovskite solution is the first step for the deposition technique. Compared with other preparation methods used for synthesis of semiconductors, the synthesis and fabrication of perovskite samples are relatively easy, since no complicated equipment is required, nor strict environmental conditions. The perovskite precursors consisting of CH_3NH_3I, $PbCl_2$ and PbI_2 were purchased from Alfa Aesar and used as supplied. Perovskite solutions were synthesized as described below.

In detail, a 40 wt. % $CH_3NH_3PbI_3$ precursor solution was prepared by dissolving CH_3NH_3I and PbI_2 in a solvent at molar ratio of 1:1 and stirring at 60 °C for 12 h followed by filtering using a PTFF

---

[1] The reported work in this chapter is partly adapted with permissions from the published articles in Chemistry of Materials 2018 (Copyright (2018) American Chemical Society),[66] Journal of Materials Chemistry A 2019 (Royal Society of Chemistry),[81] and Scientific Reports 2016 (licensed under Creative Commons Attribution 4.0 International license).[82]

syringe filter (Whatman, 0.7 mm).[83-84] After preparing the perovskite solution, the perovskite film can be deposited by simple spin-coating. A small amount (150 μl) of solution was dropped onto the substrate which is fixed on the spin-coater, and then the substrate was rotated at high speed in order to spread the solution by centrifugal force to form a thin film. After spin-coating, an annealing step was performed to form a crystalline perovskite films.

The $CH_3NH_3PbI_{3-x}Cl_x$ perovskite solution was prepared by dissolving CH_3NH_3I and $PbCl_2$ at a 3:1 molar ratio in a solvent at 60 °C for 12 h followed by a filtration process (as described above). The concentration of $CH_3NH_3PbI_{3-x}Cl_x$ was 40 wt. %.[85] The perovskite solution was then coated onto the substrate by spin-coating and dried on a hot plate. Before the spin-coating procedure, the substrates and the perovskite precursors were warmed up to 60 °C. After spin-coating, the fresh perovskite films were annealed on a hot plate at 100 °C for ∼30 min to evaporate the remaining solvents in the film forming the final perovskite crystalline phase. All of the perovskite preparation and deposition procedures were performed in a N_2-filled glovebox. Several kinds of solvents were examined for dissolving perovskite and depositing thin films, which will be explained in the results and discussion chapter.

2.1.2 Vacuum Deposition of Bismuth-based Semiconductor Films

Thermal evaporation is a widely used deposition technique for growing thin films of materials. In this technique the source material is placed within an appropriate crucible and positioned within a wire heater. Sublimation or evaporation of the source material occurs, when a current passes through the wire increasing the temperature of the material to the desired level. Evaporation of materials occurs under vacuum to deposit thin films with the desired purities. The deposition rate and thickness can be monitored *in-situ* by a quartz crystal oscillating at a special frequency. As material is deposited onto the crystal the frequency of the oscillation decreases, and this can be used to calculate the mass of material deposited. Since the crystal sensor and the substrates in the evaporator are not in the same position, there is a difference between the thickness monitored on the crystal and the real thickness on the substrate. A tooling factor allows the correction of the thickness data. Calibration of the tooling factor was performed by comparing the thickness of the deposited test films (a few hundred nanometers) with their measured thickness using a surface profilometer.

In this study, semiconducting bismuth halide materials were grown using the thermal evaporation technique. BiI_3 (99.999%), CsI (99.999%), RbI (99.8%), and AgI (99.9%) were purchased in powder form from Alfa Aesar and used as supplied. Two methodologies were performed to grow thin films of $Cs_3Bi_2I_9$, $Rb_3Bi_2I_9$, and $Ag_xBi_yI_{x+3y}$.

In the first approach, a thin film (300 nm) of metal halide (MI, with M = Cs, Rb, Ag) was vacuum-deposited using a Radak source in an Angstrom Engineering (EvoVac) thermal evaporator followed by a post-deposition annealing with BiI_3 in a nitrogen-filled glovebox (Figure 13a). In order to facilitate the reaction of metal halide with BiI_3 vapor, stabilization of BiI_3 vapor was done by keeping the BiI_3 powder under a quartz cover at a desired temperature for at least 10 min. After thermal stabilization of BiI_3 vapor and quartz cover, the metal halide film was quickly brought under the quartz cover and annealed for 10 min at the desired temperature followed by quenching the annealed film to room temperature.

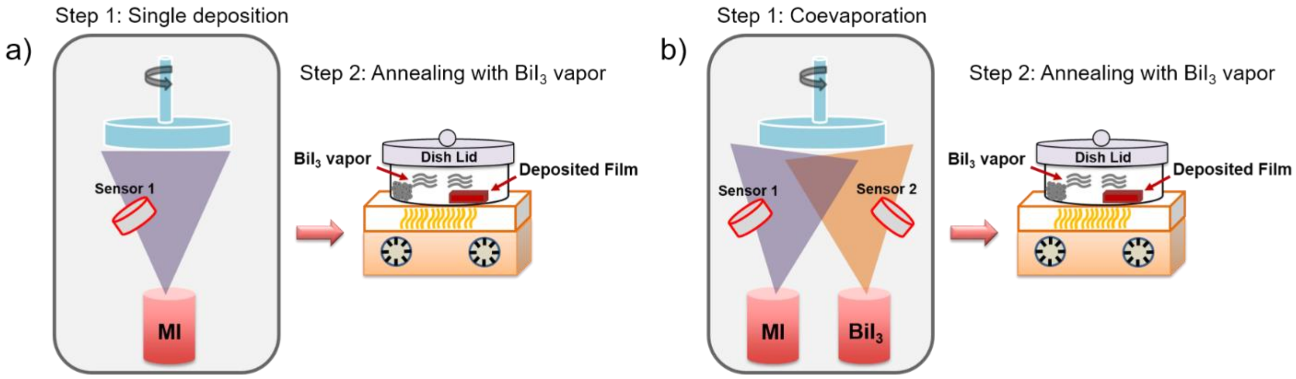

***Figure 13**. Schematic illustrations of two-step deposition method. a) step1: vacuum-based single deposition of metal halide (CsI, RbI, or AgI) and step2: post-deposition annealing under BiI_3 vapor. b) step1: coevaporation of metal halide and BiI_3 and step2: post-deposition annealing under BiI_3 vapor.*

In the second approach, the metal halide and BiI_3 were coevaporated in the thermal evaporator. For this purpose, one of the Radak sources was filled with BiI_3 and the other one with the metal halide of interest (i.e. CsI, RbI, or AgI) (Figure 13b). The deposition rate for each source was monitored *in-situ* by quartz crystal microbalances, with the base pressure during the evaporation held below 4×10^{-6} Torr.[66] To grow smooth and pinhole free single-phase crystals of each compound, several deposition rate ratios (r) between MI and BiI_3 were examined. All films were deposited with no intentional substrate heating. The deposited films were subjected to post-deposition annealing under BiI_3 vapor (under a quartz cover inside a nitrogen-filled glovebox) or N_2 followed by quenching the films to room temperature.

For each of these compounds, annealing temperatures ranging from 150-320 °C and annealing times ranging from 10-20 min were optimized for achieving polycrystalline thin films with large grain size and high crystallinity. Film thicknesses were varied in the range of 350-450 nm.[66]

2.2 Photovoltaic Devices and Characterization

2.2.1 Inverted Structure Perovskite Solar Cells

Device preparation procedures are shown in Figure 14. Precleaned indium−tin oxide (ITO) substrates were treated with ultraviolet-ozone (novascan, PSD Pro Series) for 20 min. Then, a poly(3,4-ethylene-dioxy-thiophene):polystyrene (PEDOT: PSS) (Evonik) hole transport layer was spin-coated onto the ITO substrates at 4000 rpm for 40 s and baked at 120 °C for 30 min in ambient conditions. Deposition of the other layers including perovskite layer, fullerene (C60) (Sigma Aldrich), calcium (Ca) (Sigma Aldrich), and the cathode electrode were finished in a N_2 glovebox. After optimization of the perovskite fabrication process, a thin film of perovskite was deposited on PEDOT:PSS/ITO substrate.

After the perovskite film was cooled to room temperature, C60 (50 nm) as the electron transport layer and Ca (20 nm) with high work function (2.9 eV) as the hole blocking layer were evaporated onto the perovskite film using a thermal evaporator (mBraun) with a base pressure below 3×10^{-6} Torr. Finally, the 70 nm-thick metal cathode (Ag) was formed by thermal vacuum evaporation through a shadow mask at ~ 10^{-6} Torr base pressure. Figure 15 depicts the cross-sectional scheme of the device structure and the optimized thickness of each layer. The top-view scheme of the device structure is shown in Figure 16a, which demonstrates the patterned Ag electrodes (evaporated through a shadow mask) on top of Ca/C60/perovskite/PEDOT:PSS/ITO (U-shape).

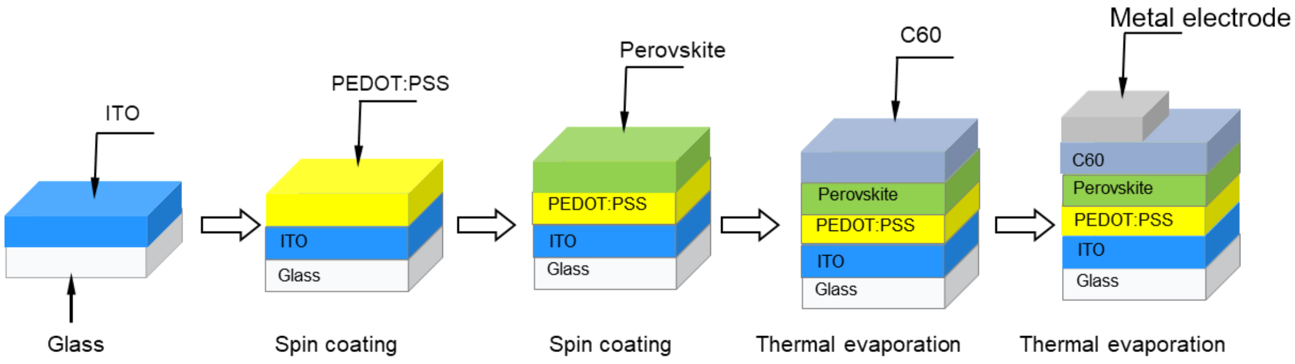

Figure 14. *Schematic representation for the deposition process of the inverted structure perovskite PV device.*

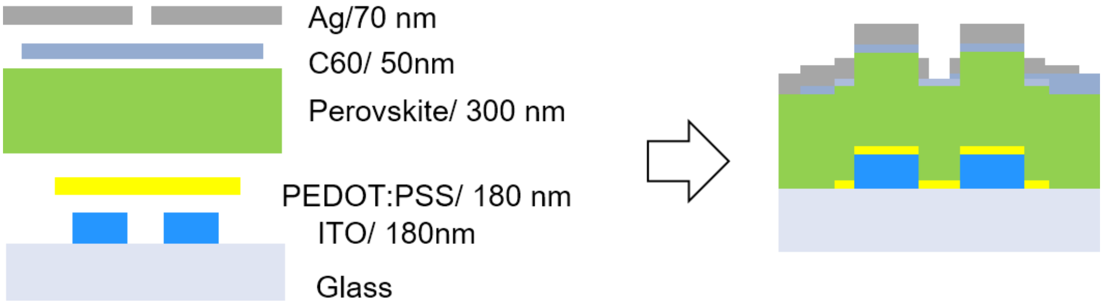

Figure 15. *Cross-sectional scheme of the developed inverted structure device showing the optimized thickness of each layer.*

Efficiency of solar cell devices can be determined via examining the current/voltage characteristic of the devices. This measurement consists of applying several potentials to the cell and measuring the corresponding output currents. Based on the obtained results from this measurement, three major parameters consisting of J_{SC}, V_{OC}, and FF can be identified for determination of the ultimate efficiency of the cell. For a working device, stability of these parameters over the life-time of the solar cell is a crucial factor determining electrical stability of the cell.

After fabrication of perovskite solar cells, current density-voltage (J-V) characterization was carried out. Since the J-V characterization device was located at ambient condition, each fabricated device was mounted on a sample holder (Figure 16b) in a N_2-filled glovebox to avoid the air-exposure of the fabricated devices (Figure 16c). J-V characterization of the inverted-structure solar cells was performed using a Wacom solar simulator and a Keithley source meter unit under 1 sun AM1.5G illumination, calibrated by a Si reference cell from Fraunhofer institute.

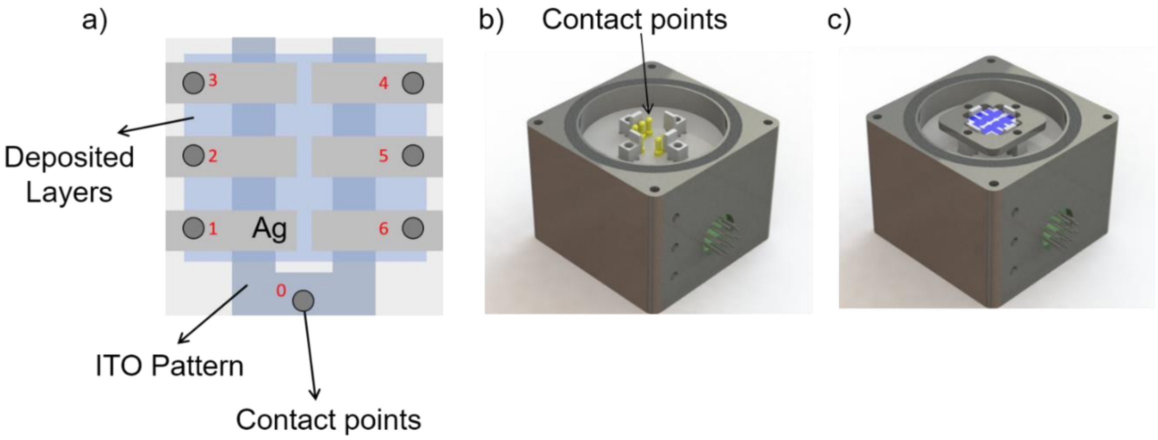

***Figure 16**. Schematic illustration of a) the architecture of perovskite PV devices with ITO as transparent anode and Ag as the metal cathode; b) sample holder with 7 contact points; c) mounted device on the sample holder, which was performed in N_2.*

2.2.2 Planar-structure Devices Based on Bismuth Halide Semiconductors

Titanium dioxide (TiO_2) solution was prepared by dissolving 2:1 (v/v) of titanium diisopropoxide bis(acetylacetonate) (75 wt. % in isopropanol, Sigma Aldrich) in ethyl alcohol (anhydrous, ≥ 99.5%, Sigma Aldrich). Spray pyrolysis was used to fabricate a thin (30–50 nm) layer of compact TiO_2 on fluorine-doped tin-oxide (FTO)-coated glass substrates (Kintec, sheet resistance = 10 Ω/sq, glass thickness = 2.2 mm). During the spray coating, the temperature of the substrates was maintained at 450 °C using a hot plate. Deposition was followed by annealing the substrates at 500 °C for 1 h. The TiO_2-coated substrates were then transferred to the thermal evaporator (as described above), wherein a thin layer of either silver bismuth iodide or rubidium bismuth iodide was deposited via coevaporation ($r = RbI/BiI_3 = 0.7$; $r = AgI/BiI_3 = 0.6$). Subsequently, post-deposition annealing was carried out. The coevaporated silver bismuth iodide was post-annealed at 180 °C for 20 min under N_2, while rubidium bismuth iodide was post-annealed at 225 °C for 10 min under BiI_3 vapor. The hole transport material, poly(3-hexylthiophene) (P3HT) (Solaris), was dissolved to a concentration of 20 mg/ml in chlorobenzene (anhydrous, Sigma Aldrich) and the solution was deposited by spin-coating at 3000 rpm for 30 s on top of the silver bismuth iodide or rubidium bismuth iodide film. Finally, 80 nm thick Au electrodes were deposited on top of the devices through a shadow mask by thermal evaporation at ~ 10^{-6} Torr base pressure.[81]

J-V characterization of the planar-structure solar cells was performed using an Oriel solar simulator and a Keithley source meter unit under 1 sun AM1.5G illumination, calibrated by a Si reference cell from Newport Corp. A mask with 0.1 cm^2 aperture area was utilized to define the active area of each cell. External quantum efficiency (EQE) spectrum of silver bismuth iodide device was recorded using an Enlitech QE–R instrument in an AC mode with chopping frequency of 165 Hz in the absence of bias voltage or illumination. Calibration of the setup was carried out using a certified silicon solar cell from Enlitech Company.[81]

2.3 Gas-Phase Oxygen and Nitrogen Functionalization of MWCNTs

MWCNTs (Baytubes® C 150 P) in powder form with outer diameters 13-16 nm were obtained from Bayer AG, Leverkusen, Germany. CNT purification was performed by washing them in 1.5 M HNO_3 under stirring for 48 h at room temperature in order to eliminate residual growth catalysts. The obtained purified tubes were entitled as PMWCNTs. Figure 17 displays the set up for oxygen modification of the tubes, in which HNO_3 vaporizes in the flask and passes through the PMWCNTs in the reaction chamber and condenses in the condenser. A connected temperature sensor to the chamber displays the chamber temperature for control. Utilizing this set up, PMWCNTs were modified by oxygen (OMWCNTs) via HNO_3 vapor at 200 °C for 48 h (OMWCNT-48) and 72 h (OMWCNT-72).

Nitrogen-containing functional groups on MWCNTs (NMWCNTs) including NMWCNTs-48 and NMWCNTs-72 were synthesized by post-treatment of OMWCNTs-48 and OMWCNTs-72, respectively. For this purpose, 50 mg OMWCNTs are loaded into a tubular reactor and treated at 400 °C for 6 h under flowing NH_3 (10% NH_3 in He, 50 ml min^{-1}) at a flow rate of 50 sccm (Figure 18). In order to investigate the nature of the oxygen functional groups on OMWCNT surfaces, temperature-programmed desorption (TPD) measurements were carried out in a horizontal quartz reactor with an inner diameter of 4 mm. An online infrared detector (Bühler Technologies, Germany) was employed to quantitatively analyze the released CO and CO_2 during the decomposition of oxygen groups from OMWCNT surfaces. OMWCNT was heated under flowing helium (99.9999%, 30 ml min^{-1}) from room temperature to 1000 °C at a heating rate of 2 °C min^{-1}. The temperature was kept constant for 2 hours at 1000 °C before cooling down to room temperature.[82]

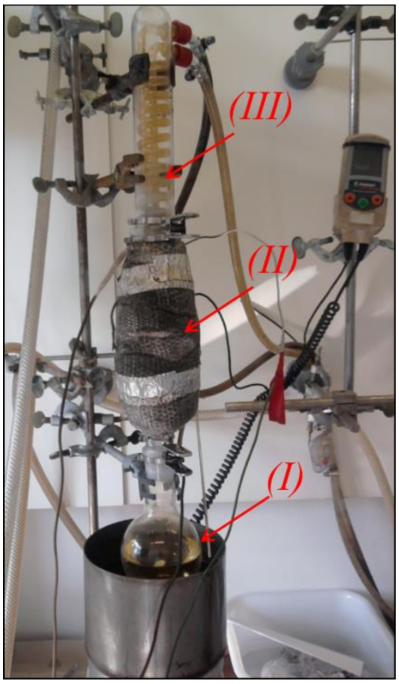

(III) Condenser

(II) Reaction chamber of MWCNT

(I) HNO_3 (150 mL , 65 vol %)

Figure 17. *The experimental set up used for gas-phase oxygen modification of MWCNTs. HNO_3 evaporates in the round-bottom flask and passes through MWCNTs in the reaction chamber and condenses in the condenser.*

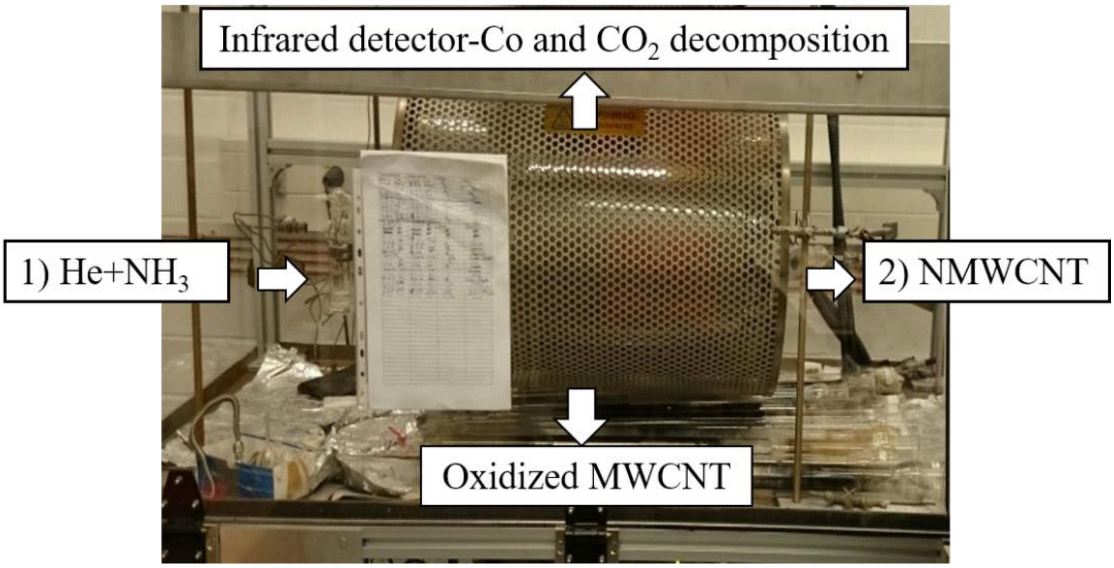

Figure 18. *Tubular reactor used for nitrogen modification of OMWCNTs. The infrared detector records the desorbed CO and CO_2 groups from the surface of OMWCNTs.*

2.4 Dispersion of Nanotubes in Organic Solvents

Organic solvents consisting of benzyl alcohol (BA), 1,2-dichlorobenzene (1,2-DB), chlorobenzene (CB), chloroform (CF), and dimethylformamide (DMF) were purchased from Sigma Aldrich and utilized as-received. Dispersion capability of all aforementioned organic solvents for CNTs dispersion including as-received MWCNTs, PMWCNTs, OMWCNTs-48 and NMWCNTs-48 was investigated by preparing 1 mg ml^{-1} of these MWCNTs in the organic solvents and tip sonicated (Bandelin, Sonopuls HD 70, Max. power: 60 W) for 15 min at 20% amplitude in an ice bath. The sonicated solutions were ultracentrifuged (Mikro 220 R, Hettich, Germany) at 10 k rpm for 1 hour to elicit larger aggregates from the dispersion. The supernatants were attentively decanted for further characterization.[82]

2.5 Characterization Techniques

2.5.1 Ultraviolet-visible (UV-vis) Spectroscopy

UV-vis spectroscopy (Shimadzu UV-2600 spectrophotometer, wavelength range: 300–900 nm) was carried out to characterize the extinction coefficient of the carbon nanotubes. Characterization of MWCNT concentration after centrifugation can be achieved by applying the Beer-Lambert law:

$$A_{\lambda} = \varepsilon l C \qquad (6)$$

where A_λ is the absorbance at a specific wavelength λ , ε is the extinction coefficient, l is the optical pathway and C is concentration (mg ml^{-1}). For this reason, the extinction coefficient of the MWCNTs was measured after sonication by dispersing 1 mg ml^{-1} CNTs in 1,2-dichlorobenzene and collecting the absorption values of diluted samples at 500 nm.[82]

In addition, optical properties of solution-processed and vacuum-processed films were investigated via collecting the absorption spectra of the deposited films using UV-vis spectrometers. Absorption spectra of perovskite films were collected using a Shimadzu UV-2600. While, a Shimadzu UV3600 spectrometer was used to study the optical properties of vacuum-based deposited films of bismuth halide semiconductors. Subsequently, direct and indirect band gaps of bismuth-based semiconductors were derived from the linear fit of the Tauc plots of the absorption data.

2.5.2 Scanning Electron Microscopy (SEM)

SEM is used for inspecting morphology and composition of specimens at very high magnifications. In this technique, focused high-energy electrons scan the surface of the sample to generate a variety of signals (e.g. secondary electron, characteristic X-ray, backscatter electrons). Among several signals produced via interaction of electrons with atoms, secondary electron and X-ray signals reveal information about morphology and chemical composition of the specimen. In this study, SEM images of perovskite films were taken using a Jeol JSM 7500F microscope.

Moreover, surface morphology of the bismuth-based semiconductor films was studied using a FEI XL30 scanning electron microscope. Compositional analysis of these grown films was carried out using SEM/ energy-dispersive X-ray spectroscopy (EDX) (FEI™ Verios 460L).

Furthermore, SEM images of the dispersed CNTs in several organic solvents were taken with an Environmental Scanning Electron Microscope (ESEM Quanta 400 FEG, FEI, Eindhoven, the Netherlands). SEM samples were prepared by dropping 10 µl CNT suspensions on clean silicon (Si) substrates.

2.5.3 Kelvin Probe Force Microscopy (KPFM)

Since KPFM is an appropriate technique that can simultaneously monitor the topography and the changes in the local work function of solid surfaces with high resolution, this technique was carried out to gain insight into the role of surface modification of the tubes on their electronic properties. Figure 19 depicts a schematic illustration of the KPFM setup for measuring the surface potential of the tubes. The surface topography of the samples was measured in the atomic force microscopy (AFM) tapping mode during the first pass for every scan line. In the second pass, the tip is kept at a fixed distance above the surface and scans the same line, while following the height profile recorded in the first pass. An electrostatic force is generated between the tip and sample via applying an AC voltage (V_{ac}) to the tip. The force along the z-axis can be expressed as

$$F(\omega_e) = \left(\frac{\partial C}{\partial Z}\right)\left(V_{dc} - V_{cpd}\right)V_{ac} sin\,(\omega_e t) \ldots \qquad (7)$$

where C is the capacitance between the AFM tip and the sample, z is the tip-sample distance, V_{cpd} is the contact potential difference, V_{dc} is an external DC voltage, and ω_e is the frequency of the ac voltage. One can nullify the electrostatic force when the applied voltage V_{dc} is equal to V_{cpd}, *i.e.* to the work function difference between the sample and the tip. Therefore, it can be concluded that the contrast in the contact potential difference (CPD) image is equivalent to the local variation in the work function or the surface potential of the sample.[86] When the conductive tip is brought to close proximity of the sample, an electrical force is produced because of the difference in the Fermi levels of the tip and the sample. Upon electron tunneling between the tip and the sample, the Fermi level of the tip will align with that of the sample. As a consequence, both the tip and the sample are charged and the produced contact potential difference (V_{CPD}) between the two is given as

$$V_{CPD} = \frac{\varphi_{tip} - \varphi_{sample}}{e} \qquad (8)$$

where φ_{tip} is the work function of the AFM tip and the φ_{sample} is the work function of the sample. In order to determine the surface potential of the nanotubes, KPFM was performed in air using an AFM device (NTEGRA, NT-MDT). For this purpose, each sample containing pristine and modified nanotubes was tip-sonicated in 1,2-dichlorobenzene for 10 min and 10 µl CNT suspension was dropped onto a clean silicon substrate followed by heat treatment to evaporate the residual solvent from the nanotubes. Platinum (Pt) coated tips were used for measuring the surface potential (SP) of the nanotubes. KPFM was performed using a two-pass technique.

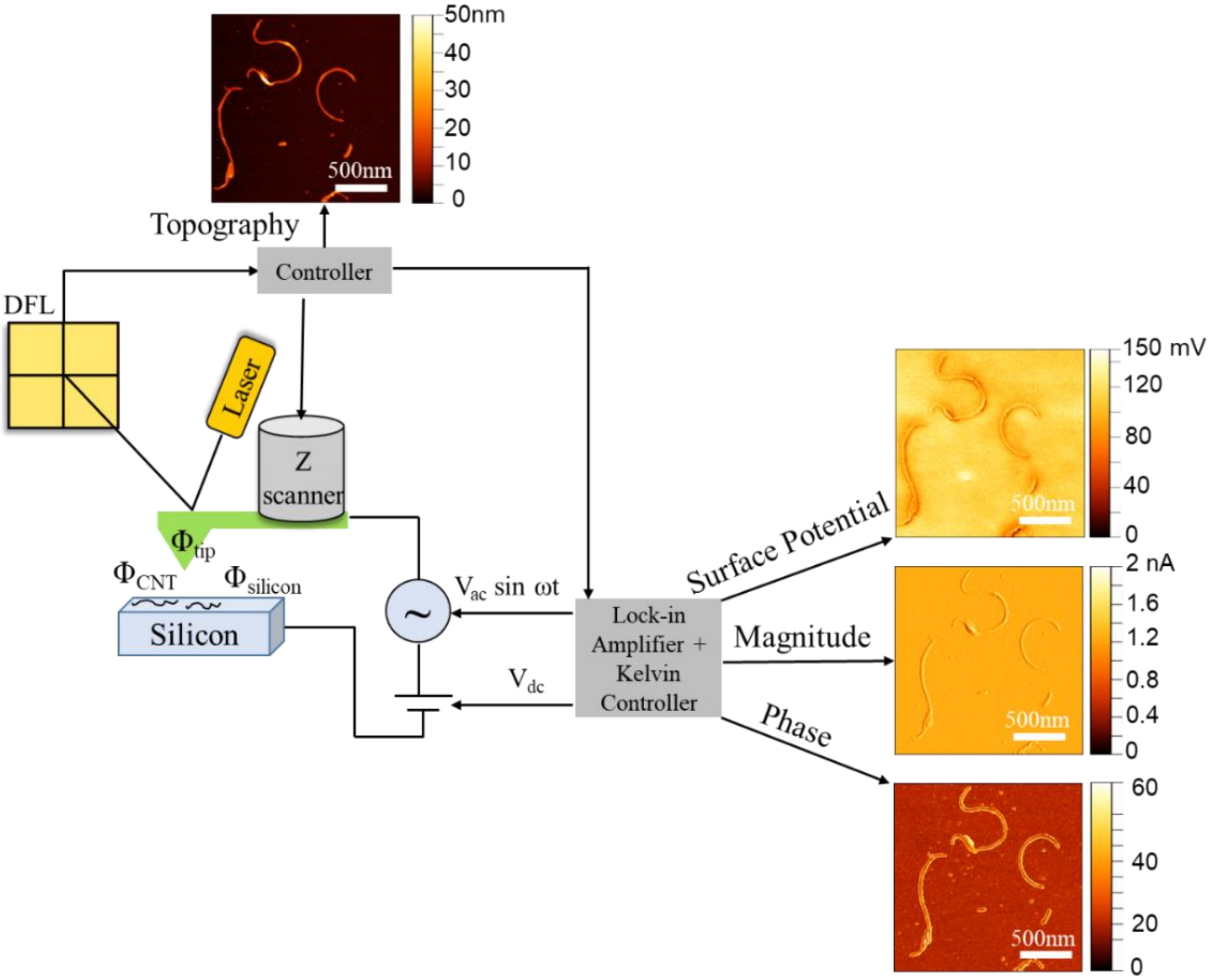

Figure 19. *Schematic illustration of KPFM characterization technique.*

2.5.4 X-ray Diffractometry (XRD)

XRD is the most effective technique to characterize the crystal structure of materials. Originally, it was designed for examining powder samples. However, this technique can be used for polycrystalline solid samples and even liquid materials. Figure 20 displays a scheme of geometric arrangement of an X-ray diffractometer. The X-ray diffractometer produces an X-ray of a single wavelength directed onto the sample surface. The inphase incident X-ray beams will be diffracted by the crystallographic planes of the crystalline material. This technique is based on the constructive interference of the monochromatic X-rays and a crystalline specimen. The deflected waves from the specimen can give information about the spacing between atomic planes of a crystal, when constructive interference occurs by satisfying Bragg’s Law:

$$n\lambda = 2d\sin\theta \tag{9}$$

where λ is the X-ray wavelength, θ is the diffraction angle, and d is the lattice spacing. An XRD instrument consists of three main parts:

1. X-ray tube: where the X-rays are produced in all directions via impacting of electrons on a metal surface (e.g. copper (Cu)) in a vacuum tube. The incident electron excites an electron in the inner shell of the metal to a higher-energy state and leaves a hole behind, which will be filled by an electron in an outer shell. An X-ray with a specific energy (e.g. Kα, Kβ) will be released through the filling process of the hole by the electron. The produced X-rays will be guided out of the tube and filtered out by passing through several slits to provide a single-wavelength (monochromatic) X-ray radiation.
2. Specimen holder: the sample in the form of a flat plate is placed on a specimen holder and the diffracted beams from the sample form a convergent beam, which is received by receiving slits (RSs).
3. Detector: the diffracted beams from the specimen will be detected by a detector. A monochromator placed in the diffracted beam path filters the wavelengths other than Kα radiation and also decreases the background radiation originating within the specimen before reaching the detector.

A spectrum of diffraction intensity versus the diffraction angle (2θ) between incident and diffracted beam is recorded by continuously changing the incident angle of the X-ray beam. Knowing the spacing of crystallographic planes by diffraction, we can determine the crystal structure (e.g. the shape, size, and volume of the unit cell) of materials, whereas the relative intensities of these peaks provide information about the arrangement of atoms within the unit cell. This technique enables us to identify the crystal structure and quality by analyzing the collected spectrum from the specimen with a database of known crystalline substances. If the collected pattern agrees well with the reference pattern, the assumed structure is considered for the specimen. In this research, the process of calculation and comparison of crystal structures were achieved by Pawley refinement. XRD measurements on the deposited films were performed under ambient conditions over the 2θ angle range of 10–50° using Cu Kα radiation (PANalytical Empyrean X-ray diffractometer).

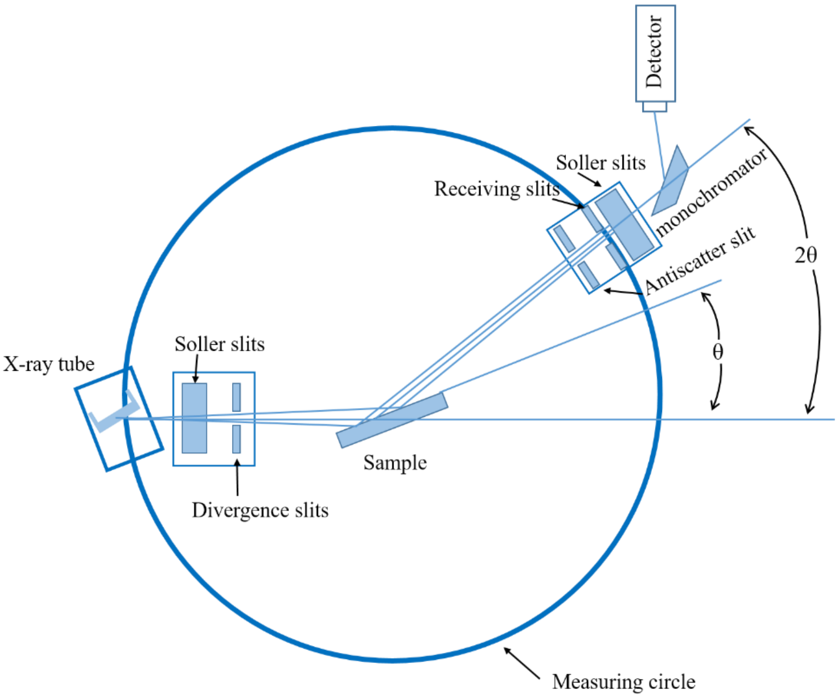

Figure 20. *Schematic diagram showing geometric arrangement of an X-ray diffractometer.*

2.5.5 Photoelectron Spectroscopy (PES)

2.5.5.1 X-ray Photoelectron Spectroscopy (XPS)

Electron spectroscopy is a powerful technique for surface chemical analysis. Elemental analysis can be performed via characterizing the emitted characteristic electrons (either Auger electrons or photoelectrons) from a characteristic energy level in a solid, revealing the nature of the chemical elements in the examined specimen. The resolution depth of this technique is ~ 5 nm, since the escaped electrons from the solid have relatively low energies (generally 20–2000 eV), originating from the uppermost atomic layers of solid. There are two types of electron spectroscopies: Auger electron spectroscopy (AES) and X-ray photoelectron spectroscopy (XPS). Regardless of the differences in their physical origins, both types of electrons provide similar information about chemical elements in the surface of materials. The focus of this research is on the utilization of XPS for surface compositional characterizations of thin films and carbon nanotubes.

Basic Principles of XPS: The X-ray photoelectron is an ejected electron from an electron shell of an atom due to the absorption of an X-ray photon by the atom (Figure 21i). Knowing the kinetic energy (E_K) of the photoelectron, the binding energy (E_B) of this electron can be calculated based on the following equation:

$$E_K = h\nu - E_B - \phi \qquad (10)$$

where h is Planck's constant, ν is the frequency of the emitted/absorbed light, and ϕ is the work function of the material (Figure 22). Elemental analysis of materials can be carried out using XPS, since the binding energies of atomic electrons have characteristic values. A typical XPS spectrum is a plot of intensity versus binding energy. Each binding energy peak in an XPS spectrum corresponds to an element and its subshell from where the photoelectron was emitted. The peaks in an XPS spectrum can be identified by comparing the experimental peaks with standard peaks in the database. The instrument for PES requires an ultrahigh vacuum environment with a vacuum pressure in the range 10^{-8}–10^{-10} mbar to avoid scattering of the photoelectrons by gas molecules on their way to reach the detector. Low energy photoelectrons can be easily scattered by gas molecules causing a reduction in the signal-to-noise ratio in the XPS spectrum.

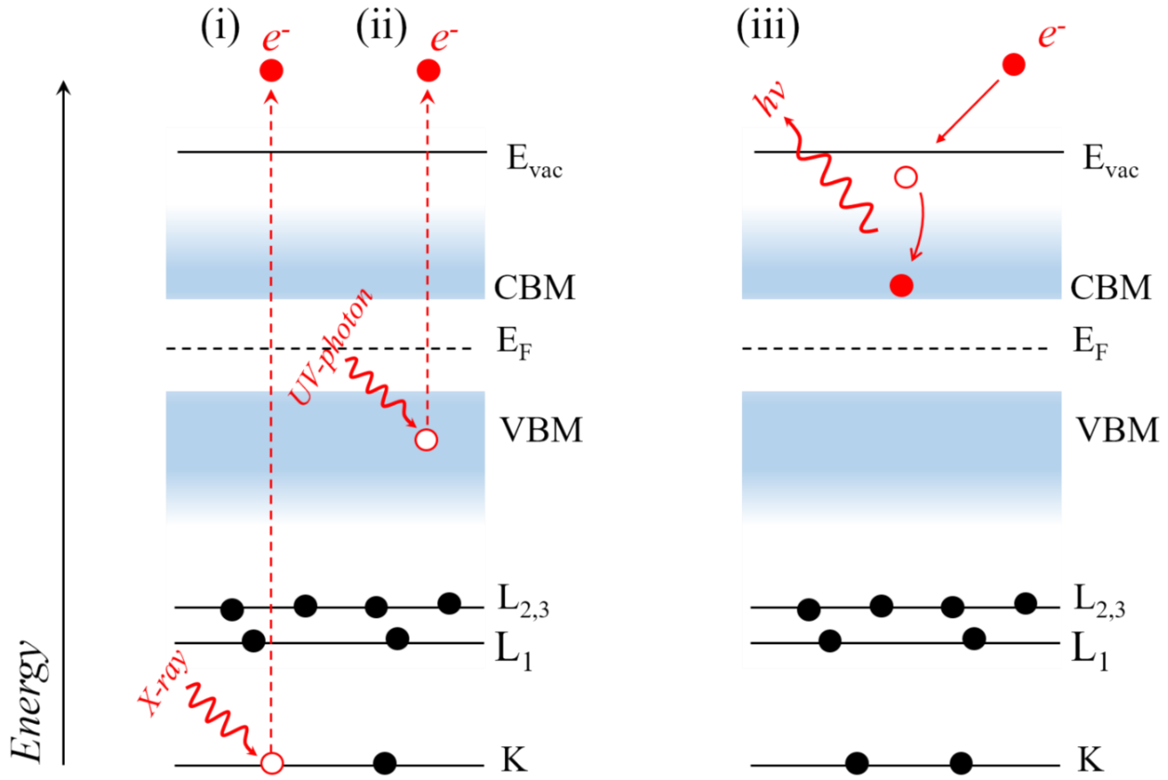

***Figure 21**. Emission processes of photoelectrons from an atom in i) XPS and ii) UPS. (iii) Schematic representation of photon emission in IPES.*

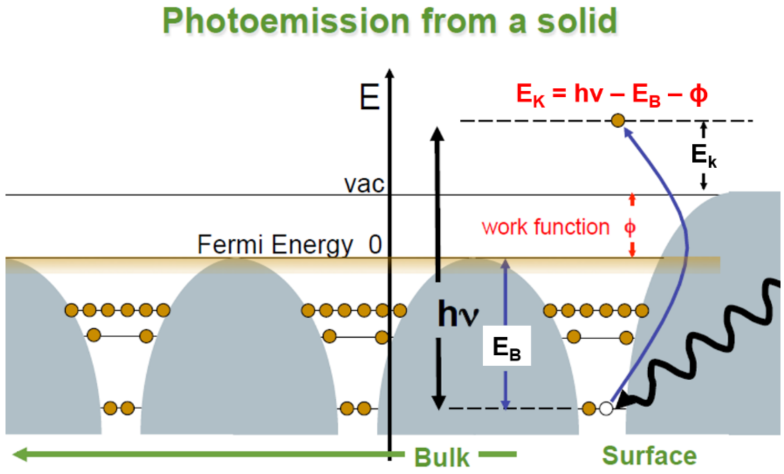

Figure 22. *Excitation process of an inner shell electron of an atom.*

2.5.5.2 Angle-resolved XPS (ARXPS)

ARXPS is a non-destructive depth profiling technique, which characterizes the composition of a film in different depths depending on the grazing angle. In this technique, the emission angle of electron collection (θ) can be varied via tilting the specimen from near normal emission (90°) to near grazing emission (θ < 90°) by assuming an elastic collision of electrons to the materials of interest, thereby enabling electron detection from different depths. Figure 23 depicts the scheme of ARXPS, where β is the angle between the X-ray source and the photoelectron detector, x is the distance from sample surface (information depth), and d is the distance that electron travels inside the sample (escape depth).

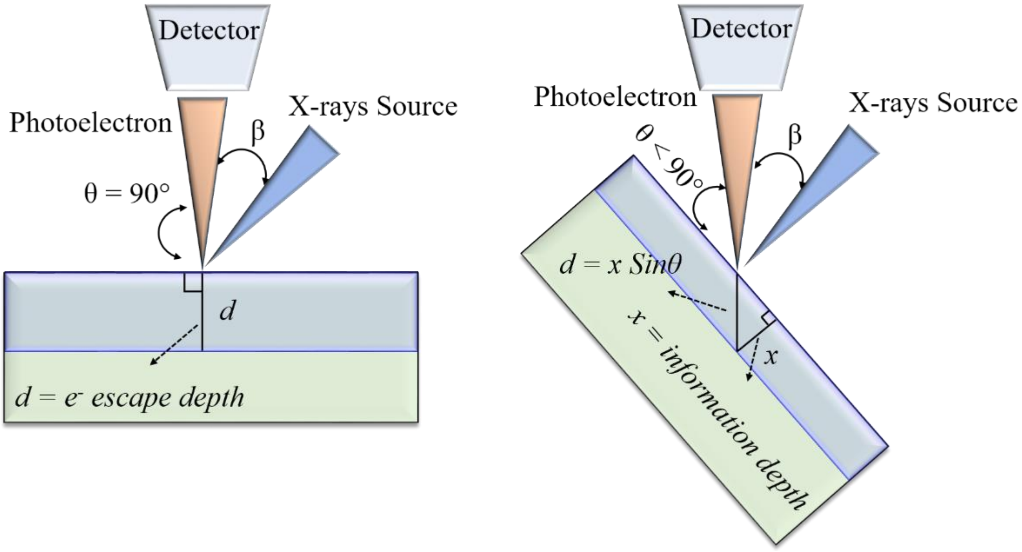

Figure 23. *Principle of angle-resolved XPS. The information depth decreases by tilting the sample with respect to the detector.*

2.5.5.3 Ultraviolet Photoelectron Spectroscopy (UPS)

Photoelectron spectroscopy is the most versatile technique to study the electronic structure of the valence bands in atoms, solids, and molecules. In the UPS technique, photoelectrons will be ejected from molecular orbitals by absorbing an ultraviolet photon instead of X-ray photon in the XPS technique (Figure 21ii). The molecular orbital energies in the valence region can be determined via measuring the kinetic energy of the emitted photoelectrons. Given the lower incident photon energies used in UPS relative to XPS, the emitted photoelectrons in UPS have lower kinetic energies than those measured in XPS, therefore the information depth of UPS reduces to 2-3 nm. As a photon source, a helium (He) discharge lamp is generally used in UPS, which emits an ultraviolet photon with an energy of 21.22 eV (He I).

2.5.5.4 Inverse Photoemission Spectroscopy (IPES)

IPES is a surface sensitive technique to probe unoccupied electronic structures of materials. In this technique, the photoemission experiment is performed in a reversed mode via bombarding a specimen with electrons of varying energy and detecting the emitted photons that are thereby produced by the decay of electrons to low-lying unoccupied states (Figure 21iii). PES and IPES are complementary techniques probing energy levels below the Fermi level and above the Fermi level, respectively. UPS and IPES can be used for the determination of the valence band maximum (VBM) and the conduction band minimum (CBM), respectively.

XPS compositional analysis of perovskite thin films ($CH_3NH_3PbI_3$) was performed using a Specs Phoibos 150 hemispherical analyzer and a Specs XR50M Al Ka (1486.6 eV) X-ray source providing a resolution of ±150 meV, as determined from the Gaussian broadening of the Fermi edge of a sputter cleaned Ag foil. XPS analysis was performed on the as-loaded and sputtered (Ar sputtered) films.

XPS, UPS, and IPES measurements were carried out under ultra-high vacuum (10^{-10} mbar) for thermally evaporated thin films of bismuth halide semiconductors deposited on ITO-coated glass substrates. For UPS and XPS studies, the analysis chamber was equipped with a hemispherical energy analyzer (Specs Phoibos 150). For XPS, Al Kα (1486.6 eV) and Mg Kα (1253.6 eV) were used. ARXPS was performed on deposited $Rb_3Bi_2I_9$ films to investigate the compositional depth profile of the corresponding films. UPS measurements were carried out using a He I (hν = 21.22 eV) source. IPES was performed in the isochromat mode, with a spectrometer utilizing a band-pass photon detector consisting of an electron multiplier/KCl photocathode coupled with a SrF_2 window. The films were analyzed as-loaded and sputtered (i.e., Ar ion source with an extractor voltage of 3 kV and a beam current of 5 μA, rastered over a 10 mm × 10 mm area). Surface sputtering was employed to test the effect of removing surface contaminants.

The surface chemistry of the nanotubes was investigated by XPS. The measurements were performed in an ultra-high vacuum setup via using PHI 5600 monochromatic Al K-alpha 350 W.

Chapter 3.
Solution Processed Organic–inorganic Lead Halide Perovskite Solar Cells

3.1 Introduction and Theory

During the last five years, significant progress has been made in perovskite solar cells employing the conventional structure. Although they exhibit high performance, the deposition of most electron transport layers such as the mesoporous (mp)-TiO_2 layer requires high-temperature (> 450 °C) processing. Several approaches have been examined for making PSCs to avoid manufacturing of high-temperature TiO_2.[51, 87]

The concepts of organic solar cells has been recently adapted to the PSCs providing a flexible fabrication of low-temperature solution-processed PSCs.[88-90] Seok et al. showed that PSCs with PEDOT:PSS as a hole transporting layer, phenyl-C61-butyric acid methyl ester (PCBM) as an electron transporting layer, spin coated $CH_3NH_3PbI_3$ as a light absorber, and a LiF/Al cathode exhibited a high efficiency of 14.1%.[91] In another study, Im et al. demonstrated inverted-structure PSCs (ITO/PEDOT:PSS/$CH_3NH_3PbI_3$/PCBM/Au) with 18.1% average PCEs. They compared the inverted-structure PSCs with the planar hybrid solar cells (FTO/TiO_2/$CH_3NH_3PbI_3$/Poly(triaryl amine), Poly[bis(4-phenyl)(2,4,6-trimethylphenyl)amine] (PTAA): 4-*tert*-Butylpyridine (*t*-BP) + Bis(trifluoromethane)sulfonimide lithium salt (Li–TFSI)/Au) and realized due to the higher electron conductivity of PCBM relative to TiO_2, the electron extraction and injection from $CH_3NH_3PbI_3$ to the electron conductor was improved resulting in the better PCE of the inverted-structure cells compared to the planar one.[83] On the basis of these observations, the low-temperature solution-processed inverted configuration PSCs are promising due to their low production cost and high PCE.

There are several critical parameters determining the morphology of perovskite thin films such as initial precursor concentrations, the kinds of solvents,[92] the time and temperature of annealing,[93] and spin-coating parameters. It is worth mentioning that wide morphological variation yields substantial differences in the photovoltaic performance of PSCs, regardless of differences in device structures and fabrication methods.[94] Therefore, it is essential to perform a comprehensive study on synthesis and characterization of solution-processed perovskite materials for photovoltaic application.

In this chapter several kinds of solvents have been investigated for fabrication of pinhole-free and compact films of perovskite ($CH_3NH_3PbI_3$ and $CH_3NH_3PbI_{3-x}Cl_x$) followed by optical and morphological characterizations of the deposited films. Furthermore, the effect of solvent engineering, spin-coating rate, and annealing conditions on the crystallization, morphology, and stability of the perovskite films has been studied. Inverted structure PSCs were prepared and photovoltaic performance of the cells were characterized. In addition, long-term nitrogen stability of the PSCs was examined. Moreover, stability of aluminum as back contact electrode in the PSCs was investigated using the XPS technique. This chapter aims to determine the role of different factors consisting of type of solvents, anti-solvent treatment, and processing conditions on the crystallization of perovskite and further photovoltaic performance of this material.

3.2 Single-step Solution Deposition of Perovskite Films

One of the key factors affecting the performance of solar cells is the fabrication of a dense and compact absorber film between electron and hole transporting layers. A poor coverage of the perovskite film has detrimental effects on the cell performance consisting of a reduction in J_{SC} due to an inhomogeneous absorbance coefficient over the film along with formation of leakage paths through the film due to the existence of pinholes, in which electron and hole transport materials come into contact with each other resulting in a reduction in the shunt resistance and subsequently decreasing V_{OC} and FF of the device.[95] Therefore, it is indispensable to develop a methodology for fabrication of dense perovskite films with the goal of achieving high performance devices.

Planar-structure perovskite solar cells (n-i-p) with planar TiO_2 and mesoporous titanium dioxide (mp-TiO_2) as ETL yield high performance devices (> 22 %) originating from an improved perovskite coverage on the scaffold-structured (mp-TiO_2). Inverted planar perovskite solar cells (p-i-n) demonstrate lower efficiency than the planar ones. Facile and low temperature fabrication steps along with high stability and small hysteresis are the advantages of the inverted-structure PSCs relative to the planar-structure devices. Recently, the PCE of inverted PSCs has approached ~ 21%, implying that the inverted PSCs can be a promising and alternative technology to realize high efficiency PSCs with lower production costs compared to the conventional PSCs.[4, 96-99]

Deposition of a uniform perovskite material on a substrate coated with hole transport materials (HTMs) is challenging due to the wetting property of some HTMs, which causes a reduction in grain boundary mobility providing a difference between nucleation and the grain growth rates.[100-101] In the one-step solution processing method for perovskite deposition on HTL, heterogeneous nucleation appears due to the early crystallization of perovskite material, forming differently sized crystals on the substrate. Appropriate choice of precursor solvents besides solvent engineering may retard the crystallization rate resulting in compact and smooth perovskite films.[84, 101-103]

Here we have investigated single-step solution-based deposition (Figure 8a) of $CH_3NH_3PbI_3$ perovskite films in an inverted device configuration to address the role of several parameters affecting the morphology of the perovskite layer as described earlier in this chapter.

3.2.1 Antisolvent Treatment of Perovskite

After PEDOT:PSS deposition (see Section 2.2.1), the substrates were transferred to a N_2-glovebox for perovskite deposition. The $CH_3NH_3PbI_3$ precursor was prepared as described in Section 2.1.1. The perovskite precursors were dissolved in the DMSO/GBL (3:7 v/v) mixed solvent. After preparation of the perovskite solution, spin-coating of $CH_3NH_3PbI_3$ on PEDOT:PSS/ITO was carried out at 3000 rpm for 30 s followed by an annealing treatment (100 °C, 30 min). The deposited perovskite film by this method was entitled as pristine perovskite. The spin-coated perovskite film showed a light yellow color immediately after spin-coating, while it turned to light gray after the annealing step.

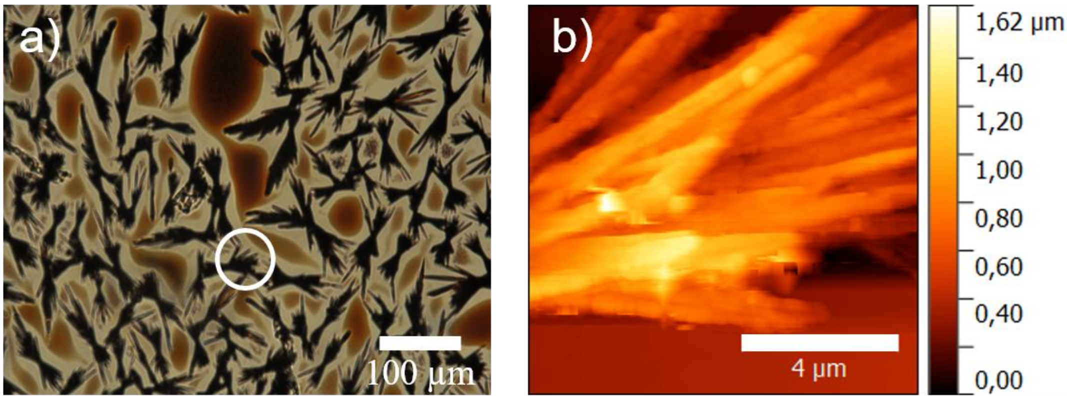

Figure 24. *a) Optical microscopy and b) AFM images of deposited pristine $CH_3NH_3PbI_3$ dissolved in DMSO/GBL (3:7 v/v) mixed solvent and annealed at 100 °C for 30 min. The perovskite was deposited without dripping any antisolvent.*

Figure 24a displays the optical microscope image of the deposited $CH_3NH_3PbI_3$ film on the HTL demonstrating a porous morphology consisting of nucleation centers and needle shaped crystals growing in the form of a dendritic structure with low coverage of the surface. AFM (NTEGRA, NT-MDT) image of the marked area in Figure 24a is shown in Figure 24b depicting the height image of the needle shape perovskite crystal with extremely high surface roughness and lengths up to ~ 16 µm. It is obvious that morphology and uniformity of the $CH_3NH_3PbI_3$ film are difficult to be controlled by the single-step deposition methodology.

To improve the morphology of the $CH_3NH_3PbI_3$ film, the effect of an antisolvent treatment was checked by applying toluene to the spin-coated perovskite film shown in Figure 25. For this purpose, 70 µl of toluene are drop-casted onto the deposited $CH_3NH_3PbI_3$ film and spin-coated at 5000 rpm for 30 s followed by thermal annealing at 100 °C for 30 min. In comparison to the needle shape perovskite film deposited without antisolvent drop-casting, the fabricated $CH_3NH_3PbI_3$ film on PEDOT:PSS/ITO possesses a dense and smooth morphology as shown in the height and magnitude AFM images (Figure 26a and b). A visual comparison of the fabricated pristine and treated perovskite films reveals a difference between the colors of the annealed films. The spin-coated yellow $CH_3NH_3PbI_3$ film turns to a light gray color via annealing without antisolvent treatment attributed to the porous perovskite morphology, while the antisolvent treated $CH_3NH_3PbI_3$ film turns to dark brown via annealing confirming the formation of a uniform crystalline film of perovskite.

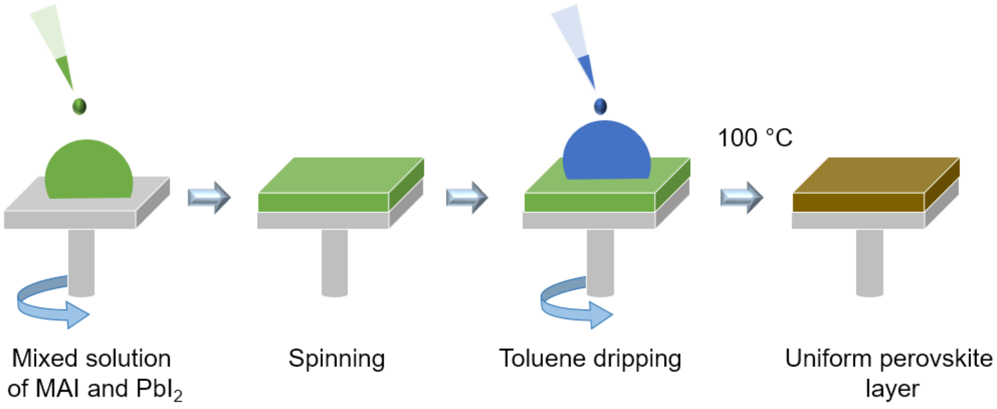

Figure 25. *Applied solvent engineering procedure for preparing uniform and dense perovskite films. Toluene was used as the anti-solven. The spin-coated film was annealed at 100 °C.*

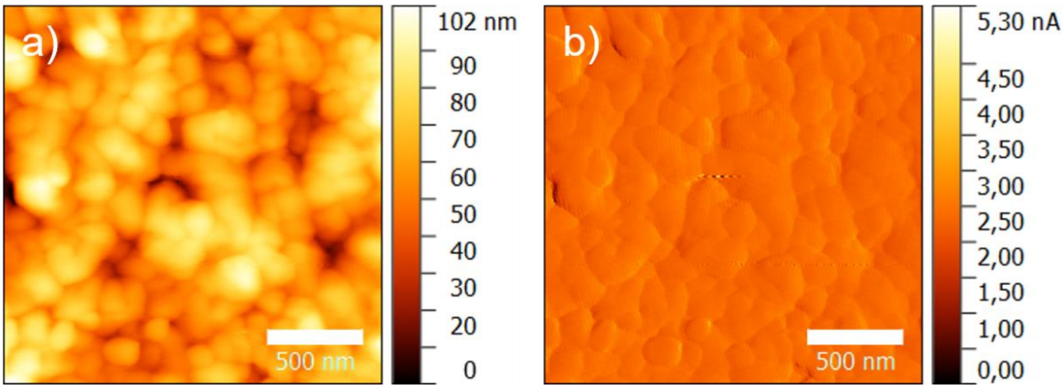

Figure 26. *Collected a) height and b) magnitude AFM images of the deposited $CH_3NH_3PbI_3$ film via applying the antisolvent (toluene) treatment.*

XRD patterns of pristine and treated $CH_3NH_3PbI_3$ films were collected and shown in Figure 27, where the pattern for PEDOT:PSS on ITO is also included for comparison. It can be seen that none of the ITO diffraction peaks marked with the dashed lines exist in the collected patterns for the perovskite films verifying a full coverage of the substrate by perovskite/PEDOT:PSS films. Evidently, the collected XRD patterns for the pristine and toluene-treated perovskite films are similar except for the appearance of a small peak at ~ 12.5° in the toluene-treated film originating from the decomposed perovskite film and formation of PbI_2.[104-105] XRD structural analysis of the grown films in combination with AFM morphological characterization verify that polycrystalline $CH_3NH_3PbI_3$ forms in both the pristine (needle-shape structure) and treated (uniform film) perovskite samples. However, depending on the treatment process (e.g. antisolvent treatment) the morphology of the perovskite film changes.

The observed crystallization of the pristine and antisolvent-treated $CH_3NH_3PbI_3$ films is related to the used solvents. In this case, DMSO forms a MAI-PbI_2-DMSO complex impeding the rapid reaction between perovskite precursors, while GBL with higher boiling point behaves as a solvent. Given the miscibility of toluene in DMSO and GBL along with not dissolving the perovskite materials, toluene drip removes excess DMSO solvent encouraging supersaturation in the cast film and hence conversion of the perovskite precursors into crystalline perovskite film.[84] The obtained results suggest that the antisolvent plays a critical role on the crystallization kinetics of the perovskite consistent with previous reports. [103]

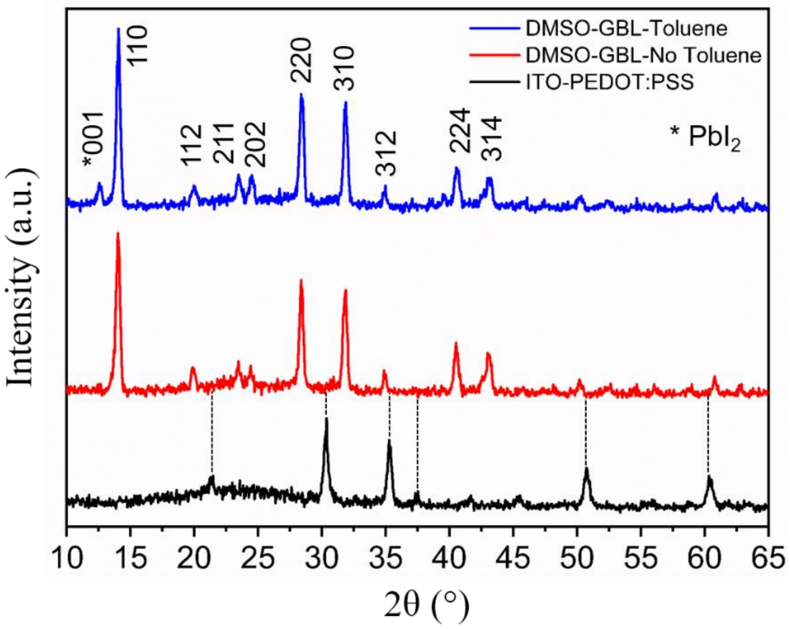

Figure 27. *Collected XRD patterns for the deposited films of a) PEDOT:PSS on ITO (black), b)* $CH_3NH_3PbI_3$ *on PEDOT:PSS/ITO (no toluene dripping) (red), and c)* $CH_3NH_3PbI_3$ *on PEDOT:PSS/ITO (with toluene dripping) (blue).* $CH_3NH_3PbI_3$ *was dissolved in DMSO:GBL (3:7 v/v).*

The absorption spectrum of the $CH_3NH_3PbI_3$ film on a glass substrate was measured (Shimadzu UV-2600 spectrophotometer, wavelength range: 300–900 nm) and is shown in Figure 28, indicating the strong capability of photon harvesting of the perovskite for the spectral range from 400 to 800 nm. The absorbance onset at 795 nm in the spectrum corresponds to an intrinsic bandgap of 1.56 eV consistent with reported values.[47, 80]

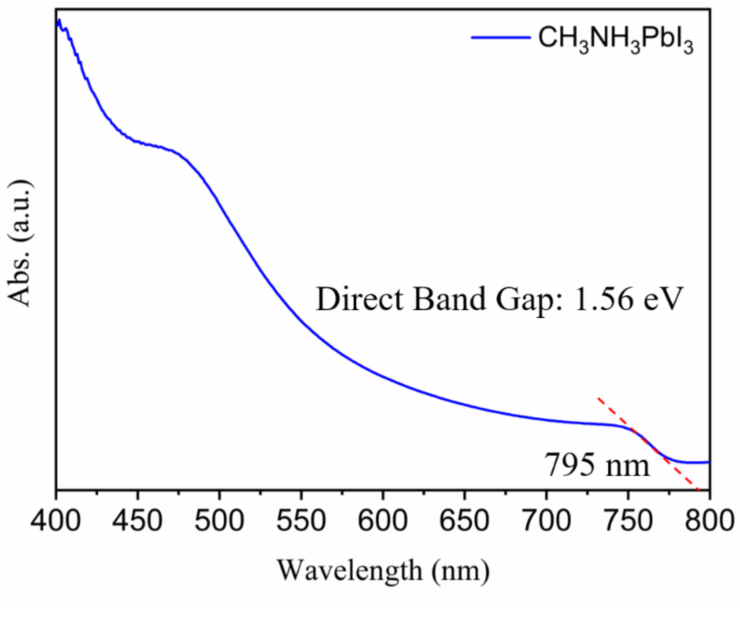

Figure 28*. Absorption spectrum of the* $CH_3NH_3PbI_3$ *film. Intersection of the tangent line and x axis is about 795 nm.*

3.2.2 Spin-coating and Annealing Conditions

The solvent evaporation rate during perovskite spin coating and annealing is a critical factor affecting the crystallization and morphology of the perovskite film and subsequently results in significant differences in the photovoltaic performance of PSCs.[94, 106] Optimization of the perovskite fabrication process was accomplished by testing various parameters including spin-coating rate and annealing conditions (e.g. temperature, heating rate). For this purpose, 40 wt.% $CH_3NH_3PbI_3$ was spin coated (two different spin coating processes) from a DMSO/GBL solution, followed by toluene dripping and a second spin coating step. Table 1 demonstrates two spin coating processes entitled as spin-coating-1 and spin-coating-2, which were applied for deposition of $CH_3NH_3PbI_3$ films.

The spin-coated films were annealed in the glovebox using two different stepwise ramp types, denoted as Ramp-1 and Ramp-2 (Figure 29). The initial annealing temperature was fixed at 25 °C (room temperature) for Ramp-1, while it was 60 °C for Ramp-2. The final annealing temperature was fixed at 100 °C for 30 min. After the annealing process, $CH_3NH_3PbI_3$ films were quenched to room temperature.

Table 1. *Applied spin coating parameters for fabrication of $CH_3NH_3PbI_3$ films on PEDOT:PSS/ITO substrate.*

Sample	Spin coating parameters
Spin-coating-1	1. Spinning at 3000 rpm for 30 s 2. Spinning at 5000 rpm for 30 s (after toluene dripping)
Spin-coating-2	3. Spinning at 500 rpm for 10 s followed by spinning at 3000 rpm for 30 s 4. Spinning at 300 rpm for 10 s followed by spinning at 5000 rpm for 30 s (after toluene dripping)

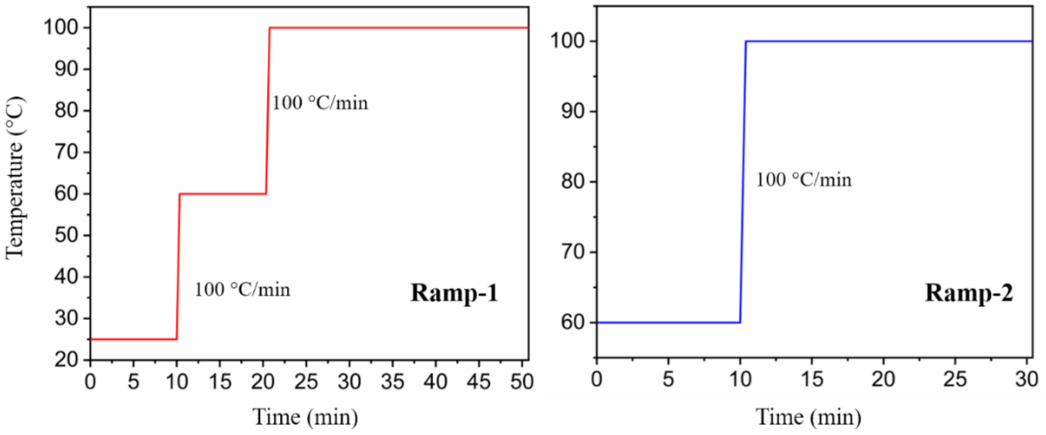

***Figure 29**. Two different annealing ramps used for drying the spin-coated $CH_3NH_3PbI_3$ films.*

Figure 30 and Figure 31 depict the surface morphologies of the deposited films via applying spin-coating-1 and spin-coatin-2 processes, respectively. A high surface coverage was obtained for all of these films. The applied treatments, which are related to the control of solvent evaporation rate, affect the crystal domain size and surface roughness of the deposited films. Among these films, the highest root mean square (RMS) value was measured for the film shown in Figure 31a, which is deposited by spin-coating 2 and Ramp-1. Comparing the deposited films via applying spin-coating 1 and 2 and annealing with Ramp-2 (Figure 30b and Figure 31b) demonstrates that the average grain size changes from ~ 600 nm to ~ 450 nm, respectively, verifying a decrease in the grain size of the film deposited by spin-coating-2/ Ramp-2 method. This film also has smaller grains than the deposited film with the same spin-coating but different ramp. These results suggest that the solvent evaporation rate can contribute to the crystallization process of the perovskite films.

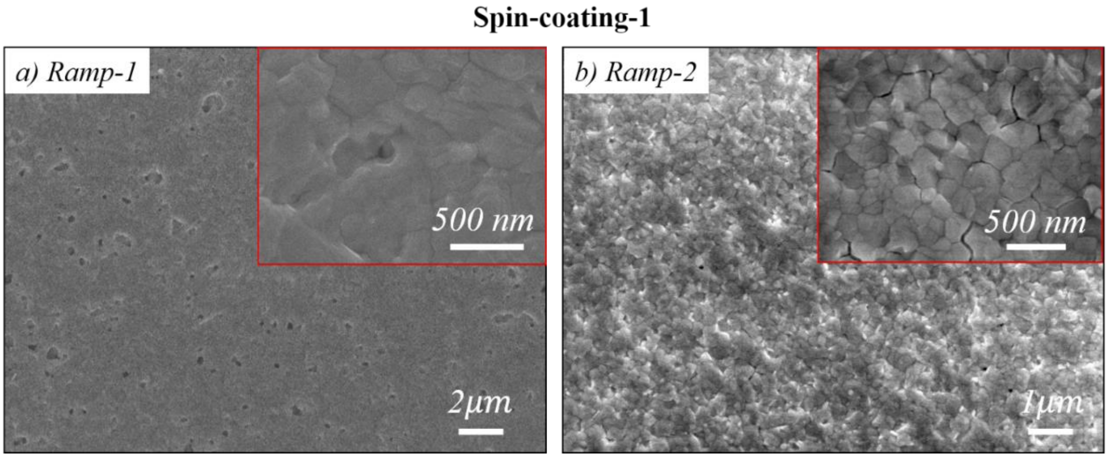

Figure 30. *Top-view SEM images of $CH_3NH_3PbI_3$ films deposited on PEDOT:PSS/ITO substrates via spin-coating-1 method. The deposited films were annealed using a) Ramp-1 and b) Ramp-2 processes. Higher magnification view of each image is shown in the inset.*

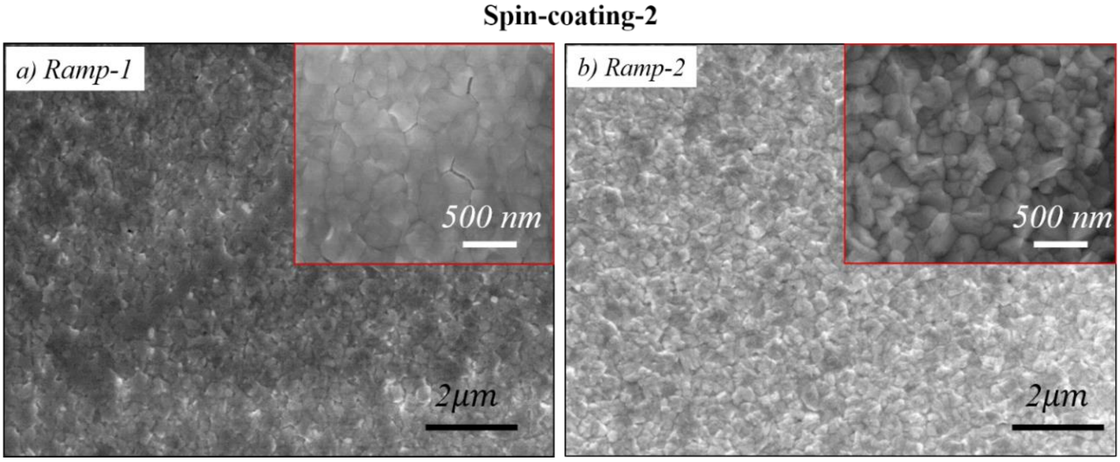

Figure 31. *SEM images of $CH_3NH_3PbI_3$ films spin-coated on PEDOT:PSS via spin-coating-2 method. The deposited films were annealed using a) Ramp-1 and b) Ramp-2 processes. The higher magnification images are shown in the inset.*

3.2.3 Casting Solvent

In order to examine the effect of casting solvent on the morphology of perovskite films, the precursor solutions (40 wt.% CH_3NH_3I:PbI_2 at a 1:1 molar ratio) were spin-coated from dimethylformamide (DMF) and a mixed DMF/GBL (97:3 v/v) in replacement for DMSO/GBL. Figure 32a and c show the deposited pristine perovskite which had been dissolved in DMF and DMF/GBL, respectively, illustrating incomplete coverage of the substrate by the crystalline $CH_3NH_3PbI_3$. Solvent engineering was examined with the goal of fabricating uniform and compact films of the perovskite. With this goal, a two step spin-coating procedure was applied consisting of 1) spin-coating $CH_3NH_3PbI_3$ precursor at 3000 rpm for 30 s, and 2) toluene dripping and spin-coating at 5000 rpm for 30 s followed by thermal annealing of the films (100 °C for 30 min) in order to convert the precursor films to a perovskite. Although solvent engineering results in a compact film of $CH_3NH_3PbI_3$ dissolved in DMSO/GBL, it does not lead to the formation of a uniform perovskite film with DMF and DMF/GBL as casting solvents. The formed perovskite films with and without toluene-dripping (Figure 32b and d) step contain large perovskite crystals separated by significant voids.

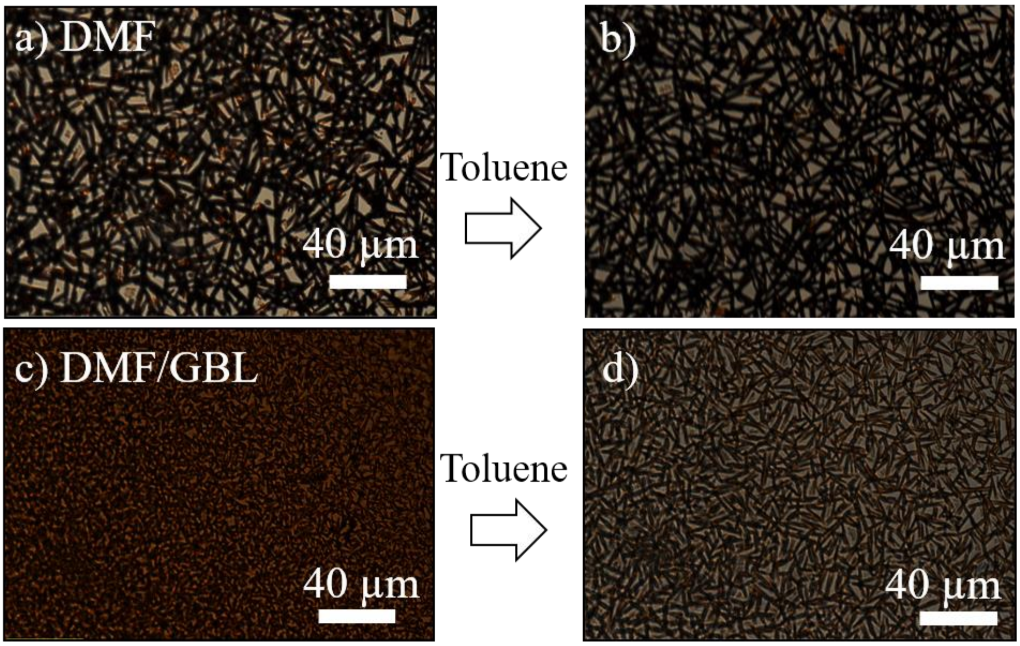

Figure 32. *Optical images of the deposited pristine* $MAPbI_3$ *solution dissolved in a) DMF and c) DMF/GBL, which were spin-coated on top of ITO/PEDOT:PSS. b) and d) show the morphology of the fabricated* $MAPbI_3$ *after toluene dripping and annealing (at 100 °C for 30 min) procedures.*

Figure 33 displays the XRD pattern of the deposited $CH_3NH_3PbI_3$ film shown in Figure 32a confirming the formation of crystalline $CH_3NH_3PbI_3$ film on PEDOT:PSS/ITO substrate. Further study is necessary to investigate the effect of several factors consisting of precursor concentration, spin-coating rate, and toluene treatment procedure (time of dripping and amount of dripped toluene) on the morphology of $CH_3NH_3PbI_3$ film dissolved in DMF and DMF/GBL.

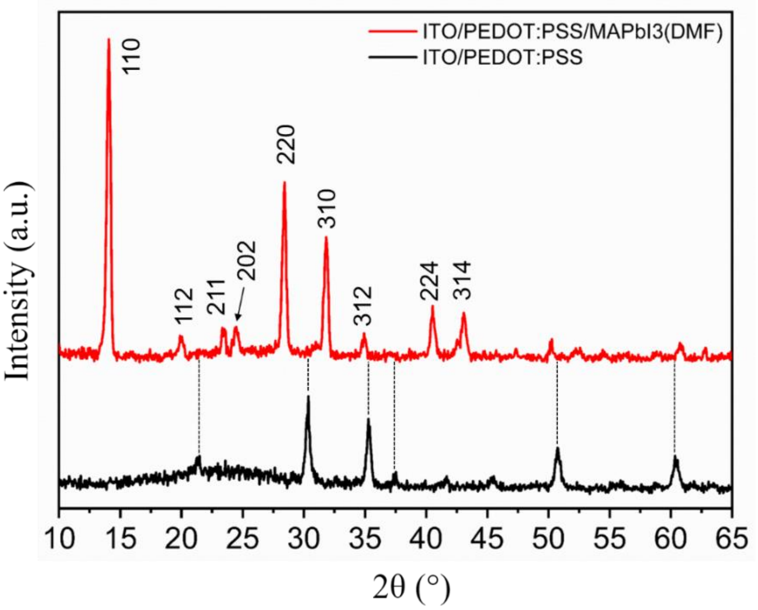

***Figure 33**. Experimental XRD patterns of the deposited films of a) PEDOT:PSS on ITO (black) and b) $CH_3NH_3PbI_3$ (dissolved in DMF) on PEDOT:PSS/ITO. $CH_3NH_3PbI_3$ film was fabricated without toluene dripping step.*

3.2.4 Chlorine Incorporation

Beside varying the processing conditions and applying solvent engineering to optimize the morphology of the $CH_3NH_3PbI_3$ perovskite film, the role of chlorine incorporation was checked by replacing PbI_2 precursor in $CH_3NH_3PbI_3$ with lead chloride ($PbCl_2$) to obtain a mixed chloride–iodide analogue ($MAPbI_{3-x}Cl_x$), where x represents a small amount of chlorine that will remain in the film. Perovskite solutions were prepared as described in Section 2.1.1. Perovskite precursors were dissolved in DMS/GBL mixed solvent or DMF. The perovskite solution was then coated onto the PEDOT:PSS/ITO substrate by spin-coating at 3000 rpm for 30 s and dried on a hot plate at 100 °C for 30 min. In order to analyze the surface morphology of the deposited films, SEM measurements were performed. Figure 34 displays the SEM images of the fabricated $CH_3NH_3PbI_{3-x}Cl_x$ films spin-cast from DMSO/GBL (Figure 34a and b) and DMF (Figure 34c and d) without toluene treatment, which were taken at different magnifications.

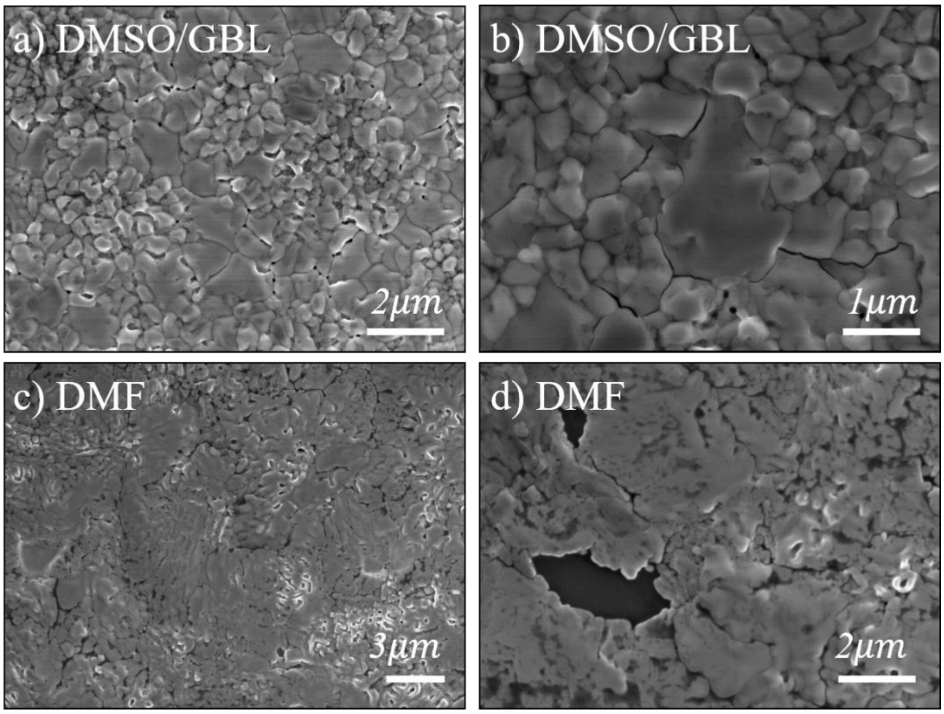

Figure 34. *SEM images of fabricated $CH_3NH_3PbI_{3-x}Cl_x$ films from a,b) DMSO/GBL and c,d) DMF on PEDOT:PSS/ITO substrate. These films were deposited without antisolvent treatment.*

As shown in Figure 34b, the perovskite film spin-coated from DMSO/GBL (without toluene treatment) forms uniform and compact films with grains as wide as 2 μm. However, the deposited perovskite from DMF contains tiny grains along with large pinholes on the surface depicting formation of a non-compact perovskite film on the substrate. XRD patterns of the deposited films were collected and shown in Figure 35, which indicate the growth of single-phase crystalline perovskite deposited from DMSO/GBL and DMF on PEDOT:PSS/ITO substrates. Clearly, no phase segregation of PbI_2 or $PbCl_2$ was detected in the XRD patterns, indicating the successful incorporation of chlorine into the crystalline structure of perovskite.

Although the $CH_3NH_3PbI_3$ film without toluene treatment contains needle-like crystals along with large voids in between, chlorine incorporation in the crystal structure of $CH_3NH_3PbI_3$ results in the formation of a dense and uniform perovskite film with large grains. Recent studies have revealed that using chloride containing precursors can facilitate perovskite crystal growth due to the size of Cl and $PbCl_2$ solubility providing chloride ions or $PbCl_2$ nanocrystals as nucleation centers.[107-109] Toluene treatment was also tested for the deposition of doped perovskite with chlorine. The SEM images of the deposited film (Figure 36) indicate the existence of pinholes on the film surface, which are marked with the arrows in Figure 36, left. Given the formation of a non-uniform perovskite film applying toluene treatment, no further anti-solvent treatment was used for fabrication of chlorine-doped $CH_3NH_3PbI_3$ film.

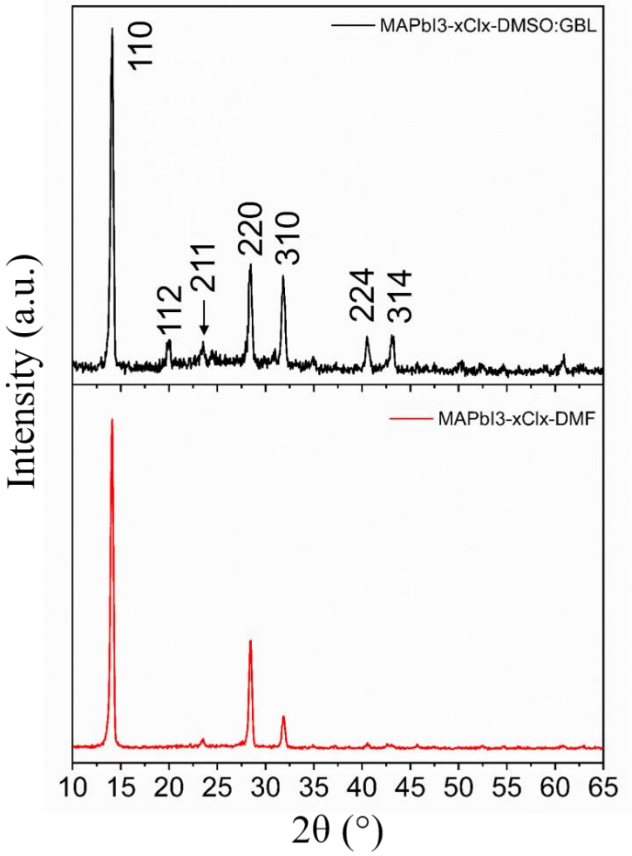

Figure 35. *Collected XRD patterns for fabricated $CH_3NH_3PbI_{3-x}Cl_x$ films on PEDOT:PSS/ITO. Perovskite solutions were spin-coated from DMSO:GBL (3:7 v/v) (black) and DMF (red) followed by annealing at 100 °C for 30 min.*

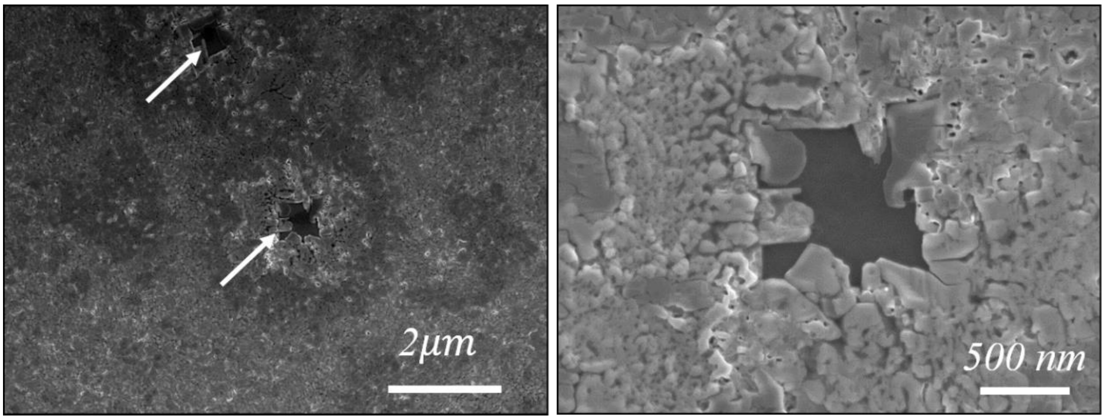

Figure 36*. SEM images of the antisolvent treated $CH_3NH_3PbI_{3-x}Cl_x$ film under low (left) and high (right) magnifications.*

3.3 Degradation of Inverted Structure Perovskite Solar Cells

3.3.1 Annealing Conditions

Thermal stability of the $CH_3NH_3PbI_3$ film was investigated via applying two different annealing conditions for the fabrication of $CH_3NH_3PbI_3$ on PEDOT:PSS/ITO (Table 2) followed by XPS analysis (Figure 37). The toluene treated $CH_3NH_3PbI_3$ films were deposited as described earlier in this chapter (see Section 3.2.1). After spin-coating, the films were left to dry at room temperature in the glovebox for 30 min to allow slow solvent evaporation. They were then annealed to crystallize the perovskite in the glovebox. The annealing condition consists of 1) annealing at 60 °C for 5 min; 2) heating from 60 °C to 80 °C with a 100 °C/min ramp rate and holding at 80 °C for 5 min;3) heating from 80 °C to 100 °C with a 100 °C/min ramp rate and holding at 100 °C for 60 min; 4) heating from 100 °C to 130 °C with a 100 °C/min ramp rate and holding at 130 °C for 20 min. For this study, one of the spin-coated $CH_3NH_3PbI_3$ film was annealed to the maximum temperature of 100 °C (step 3) entitled $MAPbI_3$-100, while the other film was annealed up to 130 °C (step 4) entitled $MAPbI_3$-130 followed by quenching of the films to room temperature. The thicknesses of the deposited films were measured using a profilometer (Ambios technology, XP-200) and recorded to be ~ 300 nm.

Table 2. *Annealing conditions applied to the spin-coated toluene-treated* $MAPbI_3$ *(dissolved in DMSO:GBL (3:7 v/v)) on PEDOT:PSS/ ITO.*

Step	Annealing Temperature	Ramping rate (°C/min)	Annealing time (min)
1	60	-	5
2	80	100	5
3	100	100	60
4	130	100	20

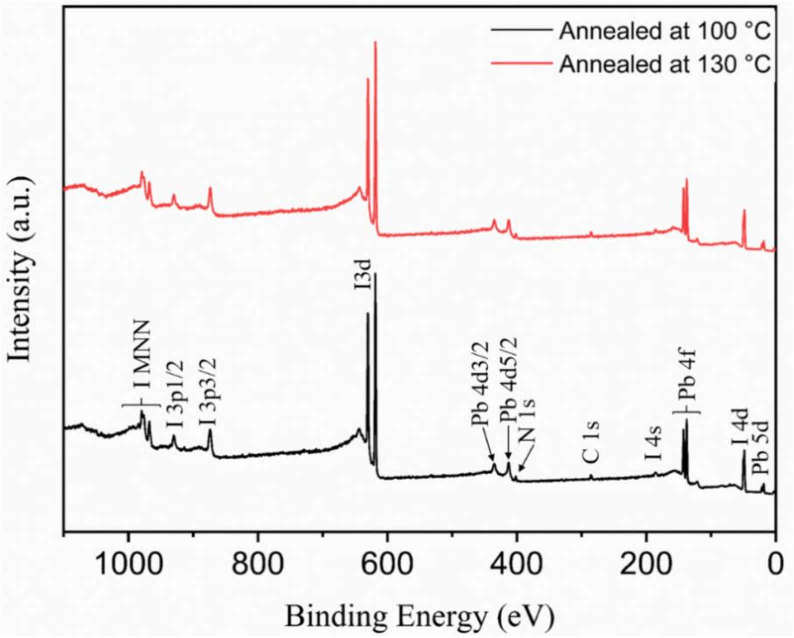

Figure 37. *Survey XPS spectra of* $MAPbI_3$*-100 (black) and* $MAPbI_3$*-130 (red). Apart from C, N, Pb, and I, no other elements were detected in the spectra.*

Between preparation and XPS measurements, the sample exposure to ambient conditions was minimized. To prevent excess exposure of the perovskite films to moisture, they were packed and transported in a dry environment and stored in the glovebox. These samples were shortly air-exposed during the loading procedure in the XPS sample holder. Figure 37 displays the XPS spectra of these two films, which contain C, N, I, and Pb peaks. There is no trace of any impurity in the spectra indicating formation of pure perovskite films. XPS C1s spectra of PEDOT:PSS and $MAPbI_3$ films deposited on ITO substrate were collected (Figure 38). As can be seen, all of these spectra contain characteristic C 1s peaks and there is no signal coming from PEDOT:PSS in the $MAPbI_3$ spectra confirming formation of pinhole-free perovskite films on top of the PEDOT:PSS layer.

XPS N 1s and I 3d spectra of $MAPbI_3$-100 and $MAPbI_3$-130 films are shown in Figure 39a and b demonstrating that the amount of N and I reduces in the $MAPbI_3$-130 film (Table 3) indicating the degradation of the perovskite layer. The observed reduction of N and I contents may originate from either the long annealing process and high annealing temperature (130 °C) or keeping the sample in the ultra-high vacuum (UHV) for some days before performing the XPS measurements.

Figure 40 shows the Pb 4f detail spectra of $MAPbI_3$-100 and $MAPbI_3$-130 films. The Pb 4f spectrum consists of two separate contributions: $4f_{7/2}$ and $4f_{5/2}$ peaks with a spin−orbit splitting of 4.9 eV. The Pb $4f_{7/2}$ peak in all spectra is found at 138.7 eV, consistent with the Pb $4f_{7/2}$ binding energies of lead halides (PbI_2, $PbCl_2$, and $PbBr_2$) and is attributed to Pb in the perovskite structure.[110-111] The Pb $4f_{5/2}$ peak is found at 143.5 eV. Two small Pb 4f peaks are observed in both spectra of $MAPbI_3$ at binding energies (~ 136.8 and 141.7 eV) labeled with "⁎" in Figure 40 consistent with metallic lead (Pb^0). These two binding energy contributions are bigger for the $MAPbI_3$-130 film indicating that the relative concentration of Pb^0 increases via increasing the annealing temperature and time. Formation of Pb^0 can be attributed to the minor removal of I_2 from the film via the annealing process verified by the XPS compositional analysis shown in Table 3. Clearly, there is a small understoichiometry in iodine for both $MAPbI_3$-100 and $MAPbI_3$-130 films.

These metallic Pb sites can serve as recombination centers in perovskite solar cells degrading the device performance. Given the Pb $4f_{7/2}$ binding energy of Pb in PbO_2 (136.8 eV), the possible presence of Pb oxide in these films cannot be excluded entirely.

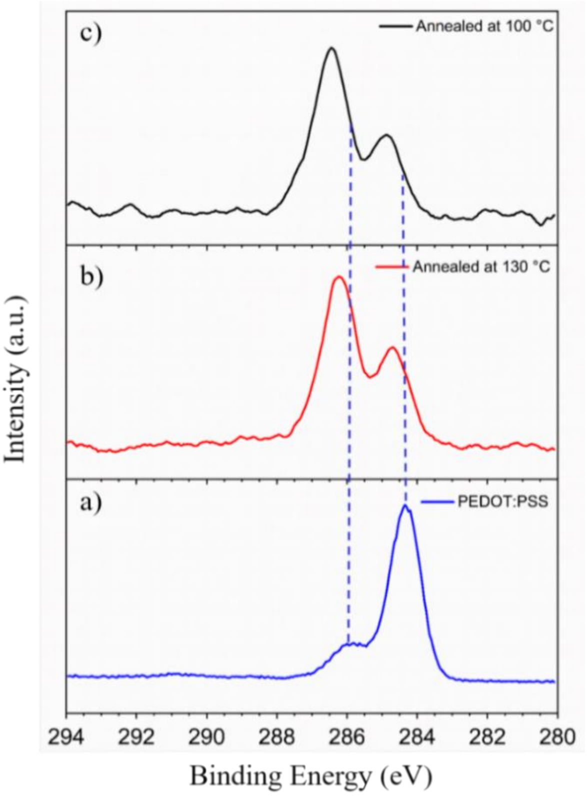

Figure 38. *Close-up Al Kα scans of C1s peaks for the deposited films of a) PEDOT:PSS (blue) (120 °C, 30 min), b) MAPbI$_3$-130, and c) MAPbI$_3$-100.*

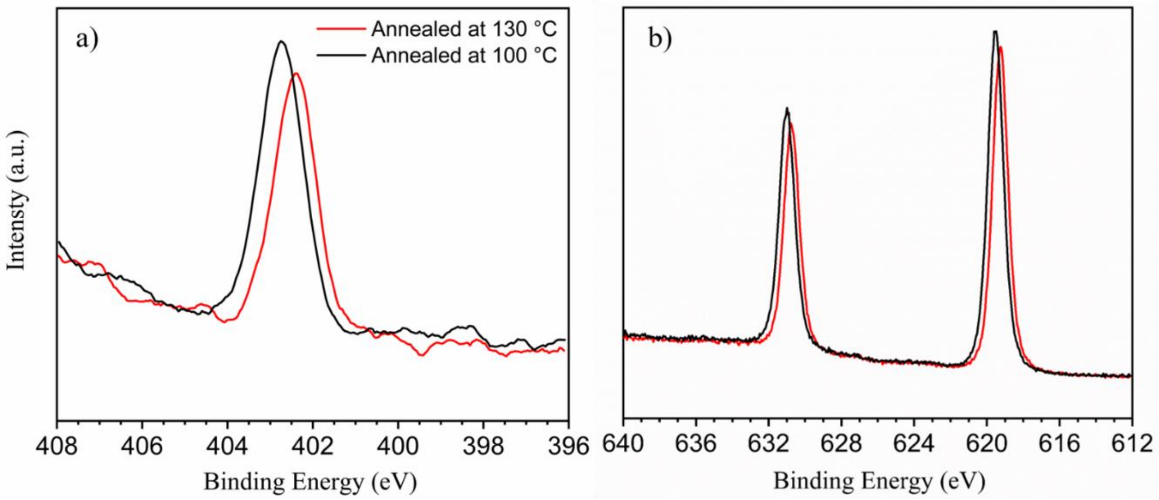

Figure 39. *Core level XPS spectra of a) N 1s and b) I 3d measured from the fabricated MAPbI$_3$-100 (black) and MAPbI$_3$-130 (red) films on PEDOT:PSS/ITO.*

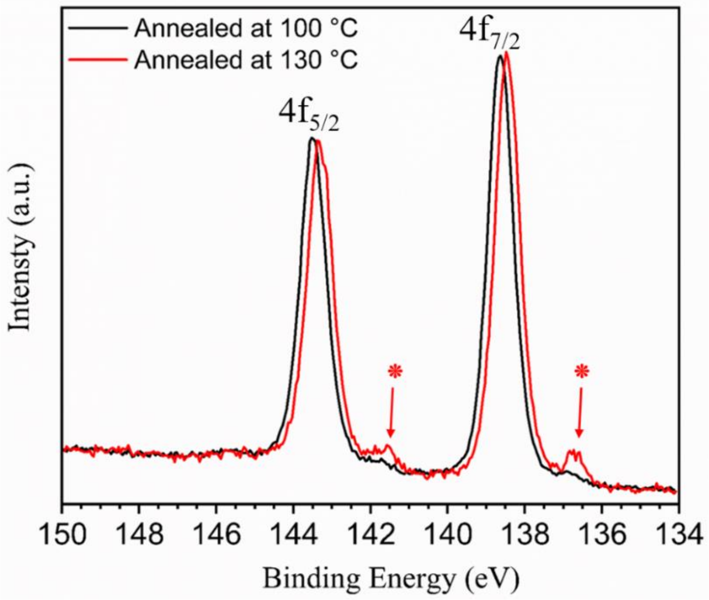

Figure 40. *Pb 4f$_{5/2}$ and 4f$_{7/2}$ detail spectra of MAPbI$_3$-100 and MAPbI$_3$-130 perovskite films deposited on PEDOT:PSS/ITO. Small peaks due to metallic lead (Pb^0) impurity are marked with "*".*

Table 3. *Atomic ratios (atom. %) derived from XPS data for the deposited MAPbI$_3$-100 and MAPbI$_3$-130 films. Normalizaion was done relative to Pb.*

Perovskite Film	Pb/Pb	I/Pb	N/Pb
MAPbI$_3$-100	1	2.46	0.81
MAPbI$_3$-130	1	2.34	0.69

3.3.2 Ion Migration in Perovskite Solar Cells

Device fabrication was performed as described in Section 2.2.1. In this case, toluene-treated $CH_3NH_3PbI_3$ film was prepared based on the description in Section 3.2.1. After the Al electrode was evaporated through a shadow mask on Ca/C60/$CH_3NH_3PbI_3$/PEDOT:PSS/ITO, its N_2 stability was tested (Figure 41a) using SEM and XPS. The high magnification cross-sectional SEM image shown in Figure 41b,c indicates that the thickness of the deposited $CH_3NH_3PbI_3$ film is ~ 300 nm, which is covered with a thin film (70 nm) of C60/ Ca on top. It was noticed that the Al cathode peeled off from the substrate, when the devices were kept in the glovebox for 2-5 h without any exposure to moisture, illumination, or oxygen. Figure 41 and Figure 42 display the SEM images of the sample demonstrating the corrosion in the Al electrode. The higher magnification SEM image of the region marked with a red circle in Figure 42 evidently displays flakes of Al deposited on top of the device (Figure 42b). An XPS surface study was performed to decipher the origin of the observed degradation in the Al cathode.

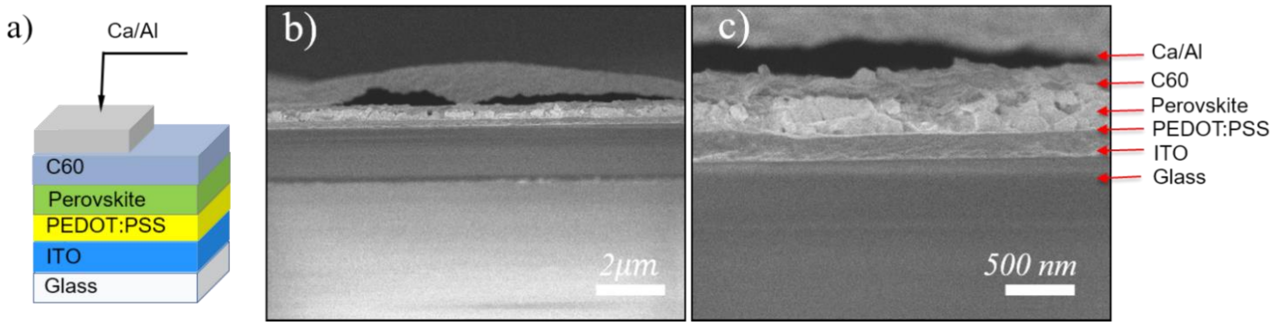

Figure 41. *a) Schematic illustration of the present PSC; b) and c) cross-sectional SEM images of ITO/PEDOT:PSS/$CH_3NH_3PbI_3$/C60/Ca/Al device showing the flakes of Al on top of the device.*

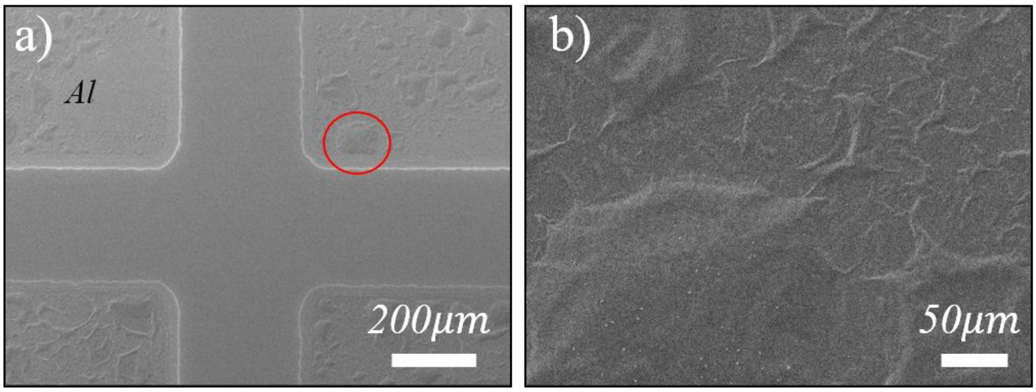

Figure 42. *a) Top-view SEM image of the device from the back-contact (Al) side and b) magnified SEM image of the marked region with the red circle.*

Figure 43 displays the Al 2p spectra of the deposited Al cathode on top of Ca/C60/ $CH_3NH_3PbI_3$/PEDOT:PSS/ITO. The film was analyzed as-loaded and sputtered (Ar ion source) to investigate not only the topmost surface composition of the film but also to attain the depth profile of the film via removing some nanometer-thick layers of the surface ensuring removal of surface contaminations. Apart from Al 2p1/2 and 2p3/2 peaks in the spectra, the peak at ~ 75.7 eV is assigned to the aluminum iodide (AlI_3) confirming the reaction of Al with iodine, which stems from the underlying perovskite film. Interestingly, the AlI_3 peak is reduced via sputtering of the surface (Figure 43) indicating the agglomeration of iodide ions at the topmost surface of the Al electrode. In the XPS spectra shown in Figure 44a, the presence of I 3d core levels is obvious on the surface of the as-loaded and sputtered films of the Al electrode, in which the intensity of these peaks decreases upon sputtering verifying the existence of less iodine atoms in the underlying layers of Al. Based on these results, it can be concluded that iodide ions in $CH_3NH_3PbI_3$ are prone to migrate to upper layers and react with the Al cathode as shown in Figure 44b. This reaction between the metal and I^- causes an irreversible degradation of the interfaces in the device. Another feasible hypothesis might be the diffusion of the evaporated metal through the thin layer of C60/Ca producing metal electrode corrosion due to metal-I^- reaction. The observed degradation of the metal electrode in this study is consistent with previously published reports.[112-114] To address the electrode corrosion, Al was replaced with Ag, which has lower reactivity compared to Al.

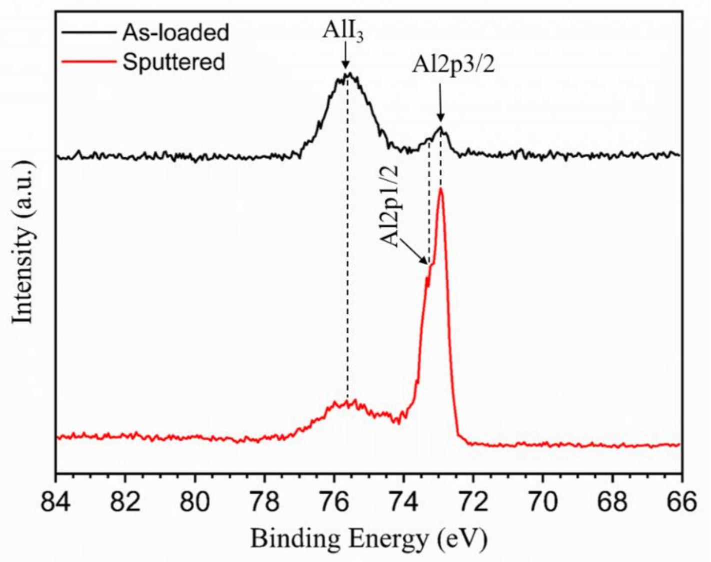

Figure 43. *XPS Al 2p$_{1/2}$ and 2p$_{3/2}$ spectra of as-loaded (black) and sputtered (red) 70 nm thick aluminium (Al) back-contact deposited on Ca/C60/CH$_3$NH$_3$PbI$_3$/PEDOT:PSS/ITO.*

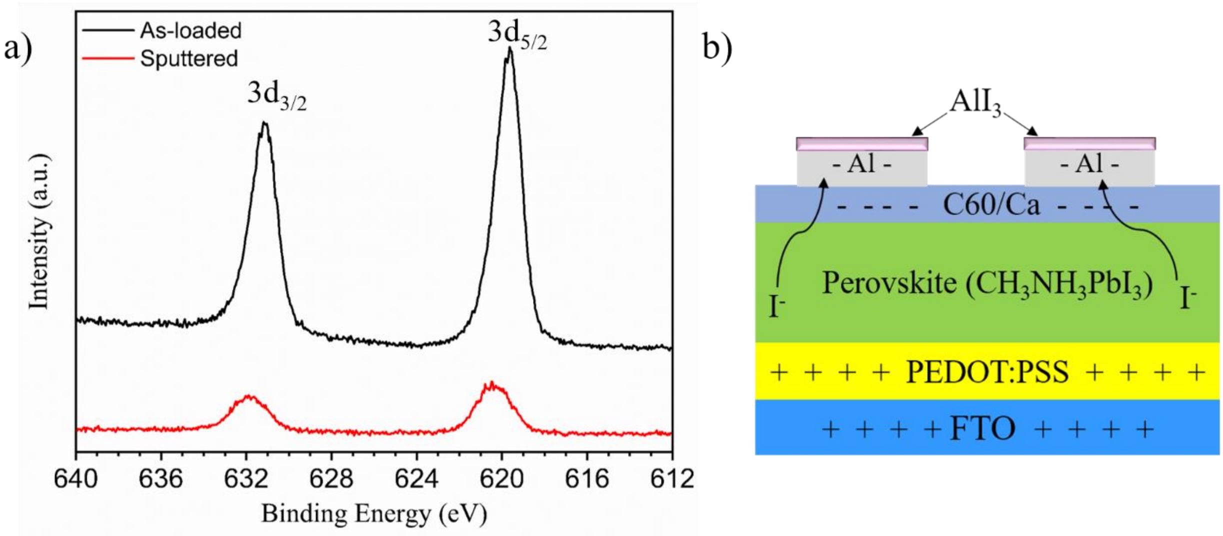

Figure 44. *a) Close-up Al Kα scans of I 3d$_{3/2}$ and 3d$_{5/2}$ spectra of as-loaded (black) and sputtered (red) 70 nm thick aluminium (Al) back-contact deposited on Ca/C60/CH$_3$NH$_3$PbI$_3$/PEDOT:PSS/ITO. b) Hypothesis of ion transport that could potentially result in cathode degradation in the CH$_3$NH$_3$PbI$_3$ solar cell made with Al cathode.*

3.4 Device Performance and Characterization

After successfully depositing pinhole-free perovskite films, PV devices were prepared using a glass/ITO/PEDOT:PSS/perovskite/C60/Ca/Ag structure (Figure 15). The inverted architecture (p-i-n) has been employed for developing PSCs owing to the negligible hysteresis observed for this architecture compared to the planar structure (n-i-p).[83, 109, 115] As described in this chapter, the perovskite absorber layer was fabricated via solution-processing of $CH_3NH_3PbI_3$ (toluene treated, see Section 3.2.1) or $CH_3NH_3PbI_{3-x}Cl_x$ (see Section 3.2.4). Furthermore, the perovskite layer was sandwiched between thin layers of PEDOT:PSS and C60 as HTL and ETL, respectively. Finally, Ca and Ag were thermally evaporated on top of the C60 layer.

Due to the crucial role of the energy level alignment between perovskite and ETL/HTL materials, proper matching between these layers causes an improvement in device performance.[116-118] Figure 45 depicts the scheme of the energy level diagram of the materials used in the present study. In this architecture, electrons are extracted from the perovskite into the lowest unoccupied molecular orbital (LUMO) of C60, while holes are transferred to the highest occupied molecular orbital (HOMO) of PEDOT:PSS. The deep HOMO level of C60 prevents the holes generated in the perovskite layer from reaching the cathode.

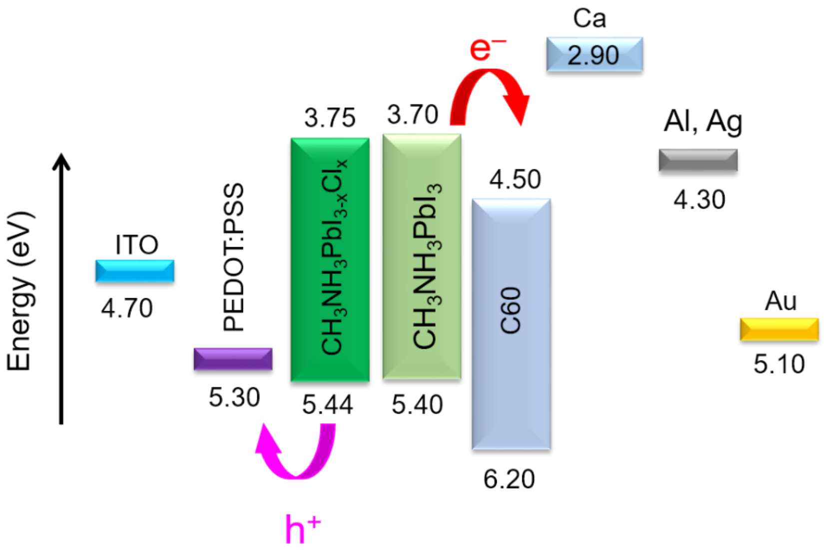

Figure 45. *Schematic energy level diagram of the materials used in this study, adapted from references.* [119-121]

The PV performance of the $CH_3NH_3PbI_3$ solar cell was tested under 1 sun AM1.5G illumination. Table 4 demonstrates the average PV performance of the $CH_3NH_3PbI_3$-devices. A PCE of 2.55% with a V_{OC} of 0.44 V, J_{SC} of 13.40 mA/cm^2, and a fill factor of 36.55 was achieved by the best device using $CH_3NH_3PbI_3$. Figure 46a shows the J-V characteristic of the best $CH_3NH_3PbI_3$-device.

The influence of chlorine incorporation on the performance of PSCs was investigated by employing the solution-processed $CH_3NH_3PbI_{3-x}Cl_x$ (dissolved in DMSO/GBL) as the light absorber layer in the PV device (Figure 15). Table 5 lists the average performance of the $CH_3NH_3PbI_{3-x}Cl_x$-devices. As can be seen, a high PCE of ~ 12 % was achieved with J_{SC} of 34 mA/cm^2, V_{OC} of 0.73 V, and FF of 47% for the best performance device. Figure 46b displays the J-V characteristic of the champion device under illumination. Since no mask was used for defining the active area of each device, the J_{SC} of these devices are overestimated.[122]

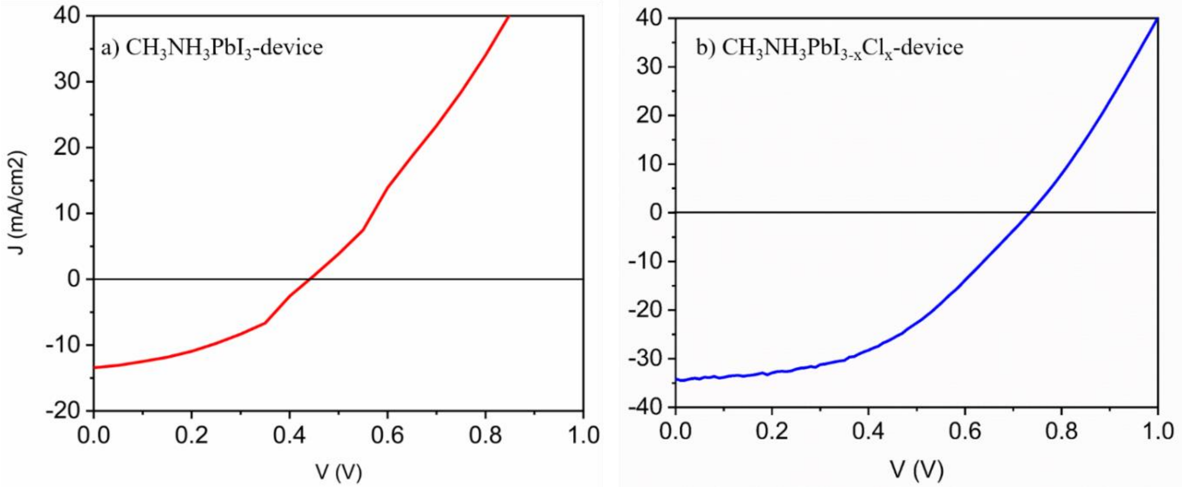

Figure 46. *Current density–voltage characteristics under simulated AM1.5 100 mW cm^{-2} illumination for a) $CH_3NH_3PbI_3$ and b) $CH_3NH_3PbI_{3-x}Cl_x$ solar cells.*

Table 4. *Photovoltaic performance parameters for $CH_3NH_3PbI_3$-solar cells.*

J_{SC} (mA/cm^2)	**V_{OC} (V)**	**FF (%)**	**PCE (%)**
12.40	0.35	32.60	1.45
13.40	0.44	36.55	2.55
13.58	0.36	36.55	1.83

Table 5. *Summary of photovoltaic performance of inverted $CH_3NH_3PbI_{3-x}Cl_x$ solar cell.*

J_{SC} (mA/cm^2)	**V_{OC} (V)**	**FF (%)**	**PCE (%)**
34	0.73	47	11.60
25.80	0.75	48.10	9.31
27.13	0.70	42.90	8.14

The slope of the measured JV curves near V_{OC} for $CH_3NH_3PbI_3$ and $CH_3NH_3PbI_{3-x}Cl_x$ solar cells displays that there is a high series resistance in the cells, which might originate from the high density of grain boundaries in the perovskite films.[123] Comparing JV characteristics of the $CH_3NH_3PbI_3$ and $CH_3NH_3PbI_{3-x}Cl_x$ solar cells an enhancement in the fill factor values of $CH_3NH_3PbI_{3-x}Cl_x$-solar cells is observed, which is related to the reduction of series resistance in this device. This can be attributed to the enhanced crystallinity and micrometer-sized grains resulting in a reduction in the density of defects in the system. Due to a suppression of the defect-assisted charge recombination centers, charge transportation in the perovskite layer can be effectively improved resulting in better performance devices.[109, 124] Further investigation needs to be performed to distinguish the causes of the high series resistance in these devices. Clearly, perovskite morphology and crystallinity have significant impacts on the performance of PSCs.

Figure 47 shows the normalized PV parameters over time for a $CH_3NH_3PbI_{3-x}Cl_x$-device. Evidently, PCE, V_{OC}, and J_{SC} of the device tremendously decrease over a 14-day period (storage in N_2), indicating a substantial degradation of the device performance. The high acidity of the PEDOT:PSS solution corrodes the ITO electrode and perovskite, which results in the reduction of V_{OC} and PCE of PSCs.[125] In addition, the color of the Ag electrode in this device turns from metallic gray to a vague dark gray over time, indicating electrode corrosion. A feasible reason for the observed color change might be the degradation of the Ag electrode over time due to the ion migration through the thin films of perovskite and C60/Ca. Utilizing more stable metal electrode such as gold (Au)) may enhance the stability of the perovskite devices.

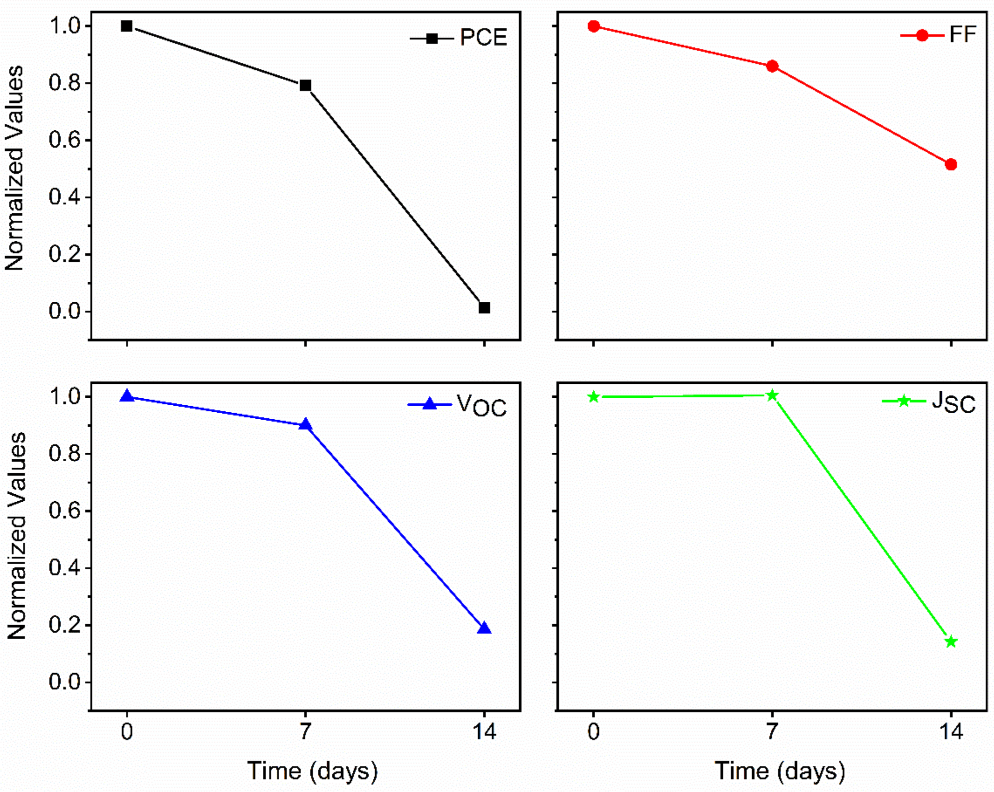

Figure 47. *Stability of the $CH_3NH_3PbI_{3-x}Cl_x$-device stored in the N_2-filled glovebox for two weeks.*

3.5 Conclusion

Solvent engineering results in the fabrication of compact and uniform $CH_3NH_3PbI_3$ films. It has been shown that the morphology of $CH_3NH_3PbI_3$ films improves by chlorine incorporation yielding an improved PV performance of the PSCs. XPS characterization of the annealed $CH_3NH_3PbI_3$ films deposited on PEDOT:PSS/ITO demonstrates traces of metallic lead, which was accompanied by a slight understoichiometry in iodine. Increasing annealing temperature and time yields an increase in the concentration of metallic lead consistent with the increase in the evaporated iodine from the annealed film. Degradation of the Al electrode in an inverted structure PSC was characterized using XPS. Apparently, chemical reactivity between the perovskite layer and the metal electrode causes metal degradation. This observation highlights the importance of utilizing either more stable metal electrodes such as silver or gold or a protective layer to protect the metal electrode from degradation. It was demonstrated that the inverted structure perovskite solar cells are unstable over time, which may originate from the degradation of the perovskite material or the electrodes in the PV devices.

Chapter 4.

Lead-Free Semiconductor Materials for Thin Film Solar Cells

4.1 Background and Motivation

Bismuth-based halide semiconductor materials with the chemical structure $A_3Bi_2I_9$ (A = K, Rb, Cs) contain a monovalent cation (K^+, Rb^+, or Cs^+), a trivalent bismuth cation (Bi^{3+}), and a monovalent iodine anion (I^-). The crystal structure of these substances consists of bismuth halide octahedra layers. The voids between the layers are filled by the metal cations (K^+, Rb^+, or Cs^+). Semiconducting bismuth halides, which are $A_3Bi_2I_9$ (A = Cs, Rb) and $Ag_xBi_yI_{x+3y}$ ($AgBi_2I_7$, $AgBiI_4$, and Ag_2BiI_5), are an interesting set of representative compounds, because the electronically-relevant framework of bismuth iodide octahedra can adopt different connectivity – i.e., from effectively zero-dimensional dimers of edge-sharing bismuth iodide octahedra in $Cs_3Bi_2I_9$, to two-dimensional (2D) sheets of corner-sharing bismuth iodide octahedra in $Rb_3Bi_2I_9$ and finally a three-dimensional (3D) network of edge-sharing alternating bismuth/silver iodide octahedra in silver bismuth iodide. "Both structural and electronic dimensionalities play essential roles in the optical and electronic properties of semiconductor materials.[21] Lower electronic dimensionality (generally arising from the lower dimensionality of the crystal structure) leads to a lower VBM and higher CBM and, therefore, a larger semiconductor band gap. Low electronic dimensionality may also promote larger and more anisotropic effective masses for the carriers, as well as deeper point defects, which may act as electron/hole traps and/or recombination centers." (taken from Ref. [66])

Despite the recent progress in PCEs of bismuth-based systems, they have shown efficiencies far below the achieved PCEs for lead-based PV devices.[69, 72, 126] One aspect that could strongly limit PV performance of bismuth halide semiconductors is the poor film morphology (i.e., high pinhole densities and small grains) of the active bismuth-iodide-based absorbers, particularly for films prepared by solution-based deposition methods. Therefore, it is crucial to develop robust methods for growing high-quality thin films with high crystallinity and minimal pinhole densities. One potential approach to achieve this is to use coevaporation, which has successfully led to growth of high-quality lead halide perovskite materials.[29, 44, 88, 127] In the present study, a facile and reproducible two-step fabrication approach was employed for obtaining smooth and pinhole-free $Cs_3Bi_2I_9$, $Rb_3Bi_2I_9$, Ag_2BiI_5, $AgBiI_4$ and $AgBi_2I_7$ films with grain sizes in the range of 100-200 nm for $Cs_3Bi_2I_9$ and Ag_2BiI_5 and > 2 µm for $Rb_3Bi_2I_9$, $AgBiI_4$, and $AgBi_2I_7$. The two-step deposition approach consists of coevaporation of the metal halide (MI, with M = Cs, Rb, Ag) and bismuth triiodide (BiI_3) followed by a post-deposition anneal under BiI_3 vapor or N_2. An analogous approach has been successfully demonstrated for the fabrication of high-quality films of $Cs_3Sb_2I_9$,[128] Cs_2SnI_6,[57] and most recently Cs_2TiBr_6.[129] By optimizing parameters such as film thickness, deposition rate ratio between the two precursors and annealing conditions, smooth and compact films are acquired.[66]

Among these compounds, the silver bismuth iodides have the most suitable band gap (1.7-1.9 eV) for single junction photovoltaic devices.[69, 71-72] Silver bismuth iodide with a general formula of $Ag_xBi_yI_z$, where z = x + 3y, can adopt either a $CdCl_2$ layered-form with $R\bar{3}m$ space group or a cubic spinel-defect structure with $Fd\bar{3}m$ space group. Owing to the crystal structure of this compound, a wide range of stoichiometries is allowed for this system. Formation of each of these structures in an Ag-Bi-I compound evidently depends on several parameters including composition, annealing conditions and preparation methods. Among the $Ag_xBi_yI_{x+3y}$ compounds, Sargent and co-workers reported on thin film fabrication of cubic $AgBi_2I_7$ and proposed a crystal structure similar to $ThZr_2H_7$, in which both $[AgI_6]$ octahedra and $[BiI_8]$ hexahedra coexist in the crystal structure.[69] However, Yan and co-workers argued that $AgBi_2I_7$ adopts an Ag-deficient $AgBiI_4$-type structure.[130] Further studies showed that Ag_3BiI_6 and $AgBiI_4$ are additional prospective ternary compounds in the AgI-BiI_3 phase diagram, in which Ag_3BiI_6 indexes to a rhombohedral unit cell (space group: $R\bar{3}m$) with $a = 4.3537(6)$ Å, $c = 20.810(4)$ Å and $Z = 1$, whereas $AgBiI_4$ crystalizes in the cubic space group $Fd\bar{3}m$ with $a = 12.223(1)$ Å and $Z = 8$.[70, 131] On the other hand, Rosseinsky et al. have reported both rhombohedral and cubic structures for $AgBiI_4$, depending on the synthesis approach employed for growing this nominal stoichiometry.[71] Although they have obtained a cubic structure (space group $Fd\bar{3}m$) with lattice parameters $a = 12.2104(3)$ Å and $a = 12.21446(4)$ Å, for $AgBiI_4$ synthesized by a solution-based process and in powder (bulk) form, respectively, single-crystal $AgBiI_4$ was indexed to a rhombohedral unit cell ($R\bar{3}m$) with $a = 4.3187(1)$ Å and $c = 20.6004(8)$ Å. Another reported composition for the Ag-Bi-I system, Ag_2BiI_5, has the same crystal structure as Ag_3BiI_6 and crystallizes in the space group $R\bar{3}m$ with $a = 4.350$ Å and $c = 20.820$ Å.[132] Based on the above studies, it is obvious that, not only the target composition of the compound, but also the synthesis pathway can have substantial influence on the formation of the final crystal systems. In most of these studies, solution-based approaches have been applied to grow thin films of silver bismuth iodide. Photovoltaic performance of solar cells with a mesoporous architecture and the solution-processed $AgBi_2I_7$,

Ag_2BiI_5, Ag_3BiI_6, and most recently $Ag_2Bi_3I_{11}$ (cubic structure) as absorber materials have been reported with efficiencies of 1.22,[69] 2.1[126] or 2.31,[133] 4.3,[72] and 0.78%,[134] respectively.[81]

To date, no report of the photovoltaic performance of vacuum-deposited bismuth iodide semiconductors in a planar device structure has appeared in the literature. This chapter deals with growth of bismuth iodide semiconductor thin films ($Cs_3Bi_2I_9$, $Rb_3Bi_2I_9$, and $Ag_xBi_yI_z$) followed by a comprehensive study on structural, optical, chemical and electrical properties of the grown films. Initial investigations on photovoltaic performance of vacuum-deposited $Rb_3Bi_2I_9$ and $AgBiI_4$ as light absorbers are shown in this chapter. [1]

4.2 Growth of Cesium Bismuth Iodide ($Cs_3Bi_2I_9$)

4.2.1 Crystal Structure of $Cs_3Bi_2I_9$

As a member of the $A_3Bi_2I_9$ family, $Cs_3Bi_2I_9$ possess a hexagonal crystal structure, which is formed by isolated pairs of face-sharing BiI_6 octahedra surrounded by cesium (Cs) cations (Figure 48). The isolated octahedra form a 0D dimer configuration in the crystal structure of $Cs_3Bi_2I_9$.

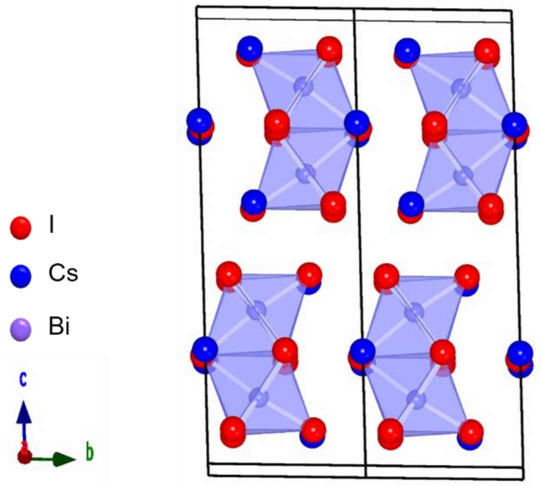

Figure 48. Scheme of 0D hexagonal $Cs_3Bi_2I_9$ ($P6_3/mmc$) crystal. The face-shared BiI_6 octahedra are surrounded by Cs cations.

4.2.2 Single Deposition Approach

To grow $Cs_3Bi_2I_9$ film, in the first approach, a thin film of CsI (300 nm) was deposited through evaporation followed by post-deposition annealing at 300 °C for 10 min under BiI_3 vapor. The XRD pattern for the post-annealed CsI film was collected to determine the associated crystal structure and

---

[1] The reported work in this chapter is adapted from the published articles in Chemistry of Materials 2018 [66] and Journal of Materials Chemistry A 2019.[81] Full-text was reprinted with permissions from (*Chem. Mater.*, 2018, **30**, 3538–3544)[66] Copyright (2018) American Chemical Society and(*J. Mater. Chem. A*, 2019,**7**, 2095-2105)[81] Royal Society of Chemistry.

to establish phase purity (Figure 49). Comparison of the pattern for the annealed film with the respective reference pattern confirms successful growth of a single-phase thin film of the $Cs_3Bi_2I_9$ compound, which indexes to a hexagonal unit cell with lattice parameters $a = b = 8.4053(1)$ Å and $c = 21.1926(5)$ Å, in the space group $P6_3/mmc$, no. 194. The Miller indices (*hkl*) of the strong diffraction peaks are labeled in Figure 49. As can be seen in Figure 49, the intense (*00l*) peaks show that the grown polycrystalline $Cs_3Bi_2I_9$ film is textured.

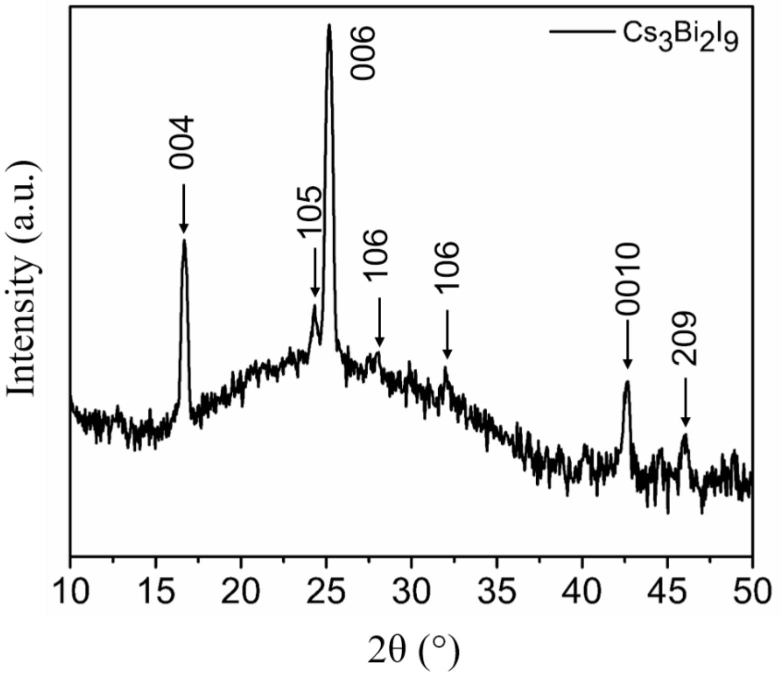

Figure 49. *Experimental XRD pattern of post-annealed CsI film in BiI_3 vapor at 300 °C for 10min. Selected strong diffraction peaks are labeled.*

Figure 50 displays top-down SEM micrographs for a post-deposition annealed thin film of CsI in BiI_3 vapor. After testing several annealing conditions, the CsI film was annealed at 300 °C for 10 min to obtain pinhole-free single-phase film of cesium bismuth iodide. The as-deposited film of CsI is colorless, however, it turns to orange color during the annealing process confirming formation of the Cs-Bi-I phase (inset of Figure 50). The post-deposition annealed film of Cs-Bi-I contains small grains with maximum width of ~ 180 nm (Figure 50).

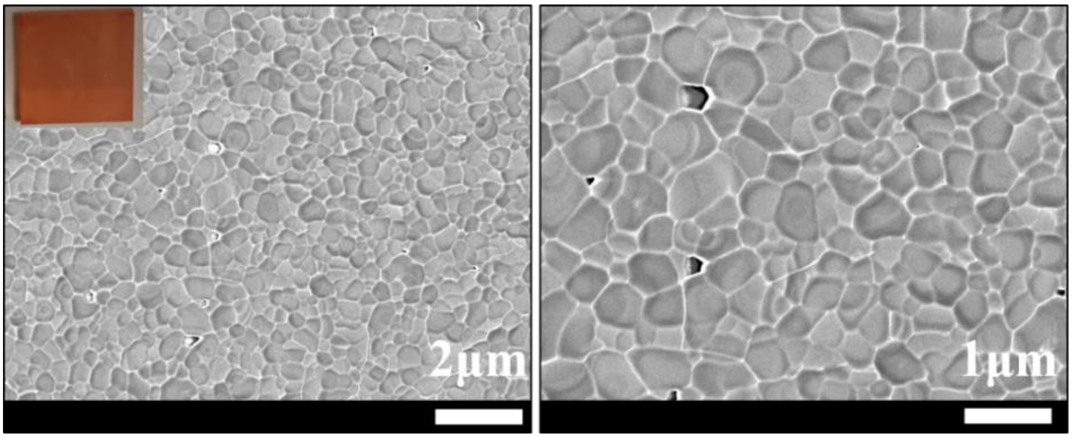

Figure 50. *Top-view SEM micrographs of post-deposition annealed thin film of CsI in BiI_3 vapor at 300 °C for 10 min. The inset image shows the annealed film which has orange color.*

4.2.3 Optical Properties of $Cs_3Bi_2I_9$ Film

The optical absorption spectrum of the $Cs_3Bi_2I_9$ film deposited using the single deposition approach was collected (Figure 51a). The linear extrapolation of the Tauc plots ($(\alpha h\nu)^n$ versus $h\nu = hc/\lambda$) provides the direct (n = 2) and indirect (n = ½) optical band gaps (Figure 51b), where α is the absorption coefficient, *h* is Planck's constant, c is the speed of light, λ is the wavelength and ν is the excitation frequency. Due to uncertainties in the directness or indirectness of the band gaps of $Cs_3Bi_2I_9$, both direct and indirect band gaps were derived. The linear fit of the Tauc plots yields a direct band gap of 2.19 eV and an indirect band gap of 2.3 eV, which are consistent with previously reported values for solution-processed films.[59-61]

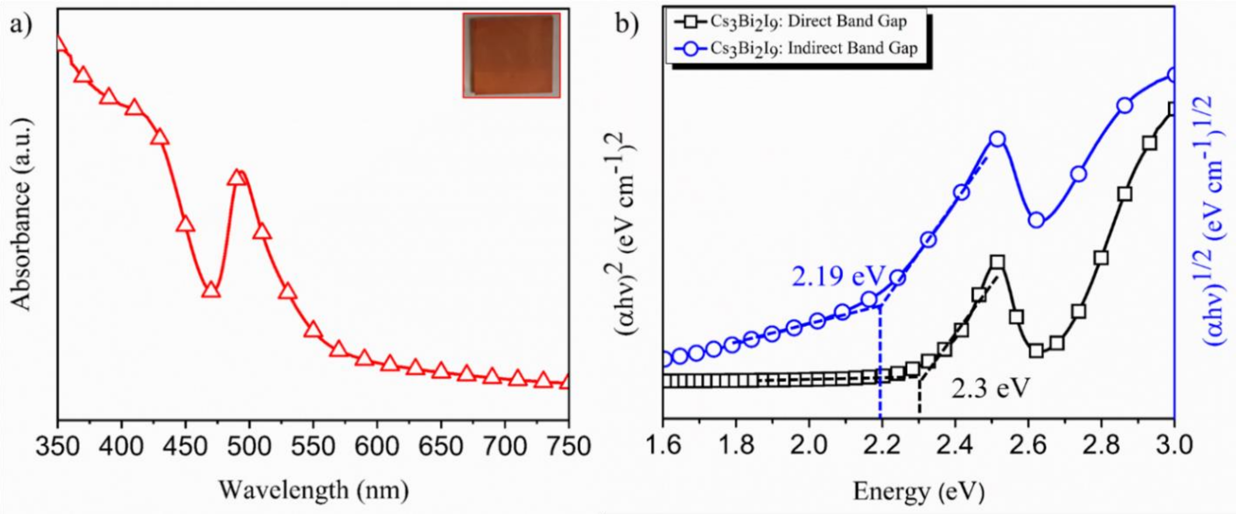

Figure 51. *a) Optical absorbance spectrum of the $Cs_3Bi_2I_9$ film and b) Tauc plots showing direct (black) and indirect (blue) band gaps for the $Cs_3Bi_2I_9$ film, deposited using the single deposition of CsI and post-annealing under BiI_3 vapor.*

4.2.4 Two-step Coevaporation Approach

In this approach, CsI and BiI_3 were coevaporated in the thermal evaporator. The deposition rate ratio (r) between CsI and BiI_3 was optimized by checking $r = 1.5$ and 1.2. Figure 52 shows the XRD patterns of the as-deposited thin films of CsI (Figure 52a) and Cs-Bi-I with $r = 1.5$ (Figure 52b). As it can be seen, there is a trace of CsI in the as-deposited Cs-Bi-I film confirming that the as-deposited film is rich in CsI. Post-annealing of the as-deposited film of $r = 1.5$ was performed in N_2 without providing an excess of BiI_3 vapor. For this purpose, several annealing conditions were tested consisting of annealing at 250 °C, 300 °C, and 350 °C for 10 min and XRD pattern for each of the film was collected (Figure 52). The dashed square in Figure 52 indicates the diffraction peaks associated to CsI. It is clear that increasing the annealing temperature from 250 °C to 350 °C results in intensification of CsI diffraction peaks verifying the evaporation of volatile BiI_3 from Cs-Bi-I films and leaving behind the CsI secondary phase. Therefore, it is vital to apply BiI_3 vapor during the post-deposition annealing process to grow a single-phase film of cesium bismuth iodide and avoid loss of BiI_3 from the thin film.

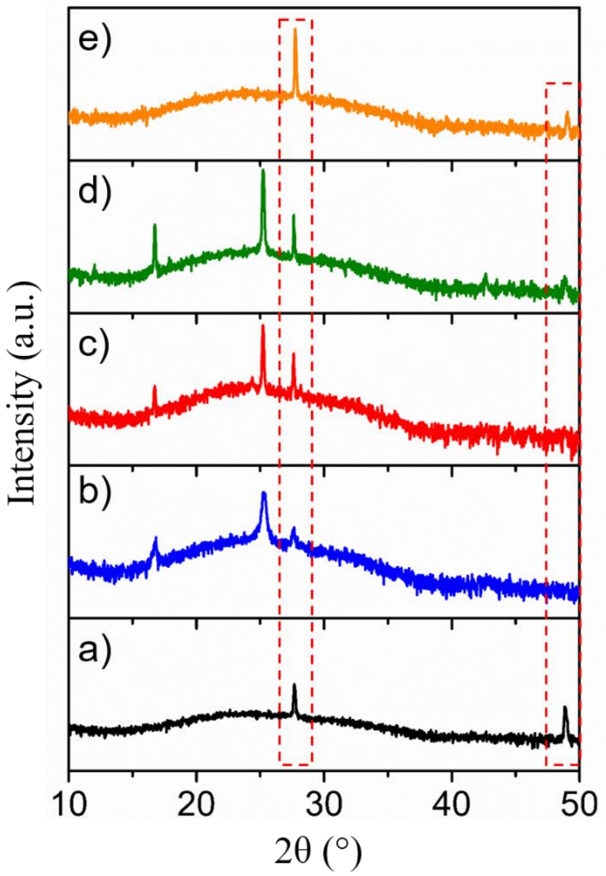

Figure 52. *XRD patterns for thin films of a) as-deposited CsI, b) as-deposited Cs-Bi-I (r = 1.5), annealed Cs-Bi-I film at c) 250 °C, d) 300 °C, e) 350 °C. Annealing was performed for 10 min under* N_2*. The marked dashed areas show the peaks corresponding to CsI.*

Morphology of the as-deposited and annealed (at 250 °C for 10 min) films was characterized using SEM (Figure 53). The as-deposited film has amorphous structure with some crystals formed on the surface which may originate from CsI. Upon annealing, grain growth occurs leading to grains as wide as 100 nm (Figure 53c and d).

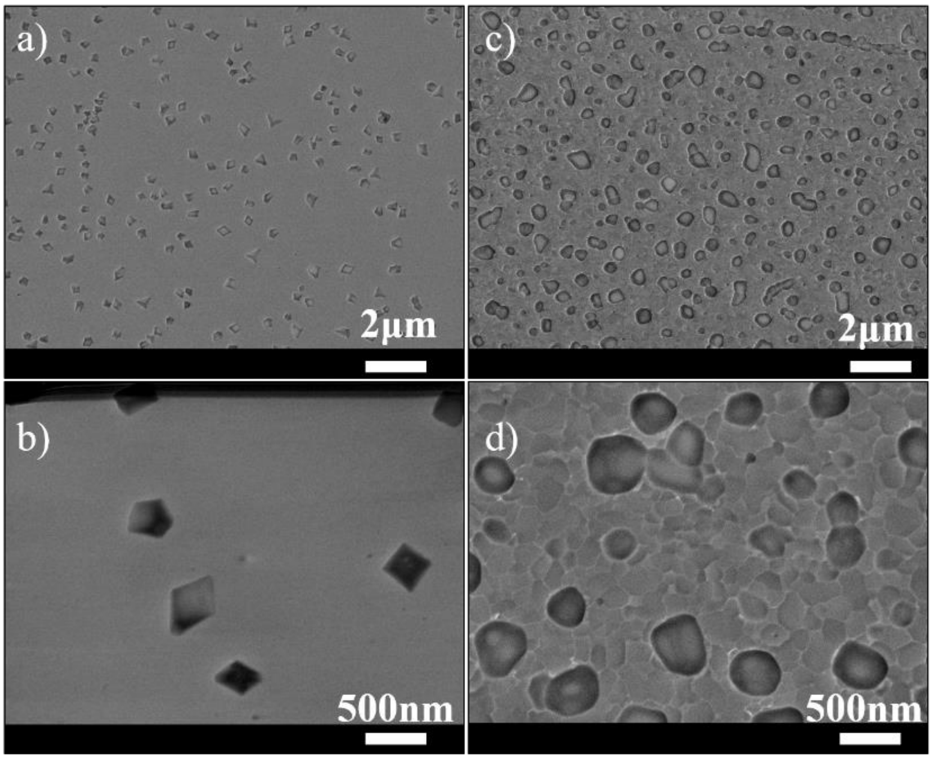

Figure 53. *SEM images of coevaporated Cs-Bi-I film with r = 1.5. a, b) as-deposited films and c,d) annealed films at 250 °C for 10 min.*

Since a trace of CsI was observed even for the as-deposited film, the amount of CsI was decreased in the as-deposited Cs-Bi-I film via decreasing the deposition rate ratio between the two precursors (CsI and BiI_3) during the coevaporation to $r = 1.2$. Post-deposition annealing temperatures ranging from 300-320 °C were optimized for achieving a pinhole-free polycrystalline $Cs_3Bi_2I_9$ thin film with high crystallinity. Figure 54 shows the XRD patterns of the as-deposited and post-deposition annealed (300 °C, 10 min under BiI_3 vapor) thin films of coevaporated Cs-Bi-I ($r = 1.2$). Comparison of the patterns for Cs-Bi-I films with the respective reference pattern from the database confirms successful growth of single-phase thin films of $Cs_3Bi_2I_9$. The as-deposited and annealed $Cs_3Bi_2I_9$ film indexes to a hexagonal unit cell (space group $P6_3/mmc$). The XRD pattern of the post-deposition annealed film has sharper peaks compared to the as-deposited one verifying a higher degree of crystallinity of the annealed film relative to the as-deposited film. The Pawley-refined unit cell parameters for the post-annealed Cs-Bi-I film is summarized in Table 6. The obtained unit cell parameters for the fabricated $Cs_3Bi_2I_9$ are in good agreement with previously reported values.[59, 135] The coevaporated post-annealed $Cs_3Bi_2I_9$ film is more polycrystalline than its counterpart grown by the single deposition approach. This may originate from an enhanced reaction between the precursors (CsI and BiI_3) due to the coevaporation of both precursors.

Table 6. *Crystallographic parameters of a post-annealed (under* BiI_3 *vapor) film of* $Cs_3Bi_2I_9$ *achieved by Pawley refinement.*

Compound	**Crystal System**	**Space group**	**Unit Cell Parameters**	**Fitting Parameters**
$Cs_3Bi_2I_9$	Hexagonal	*P6₃/mmc*	$a = b = 8.3855(3)$ Å $c = 21.146(1)$ Å	*goodness-of-fit = 1.31* *Rp = 8.9 %* *wRp = 11.33 %*

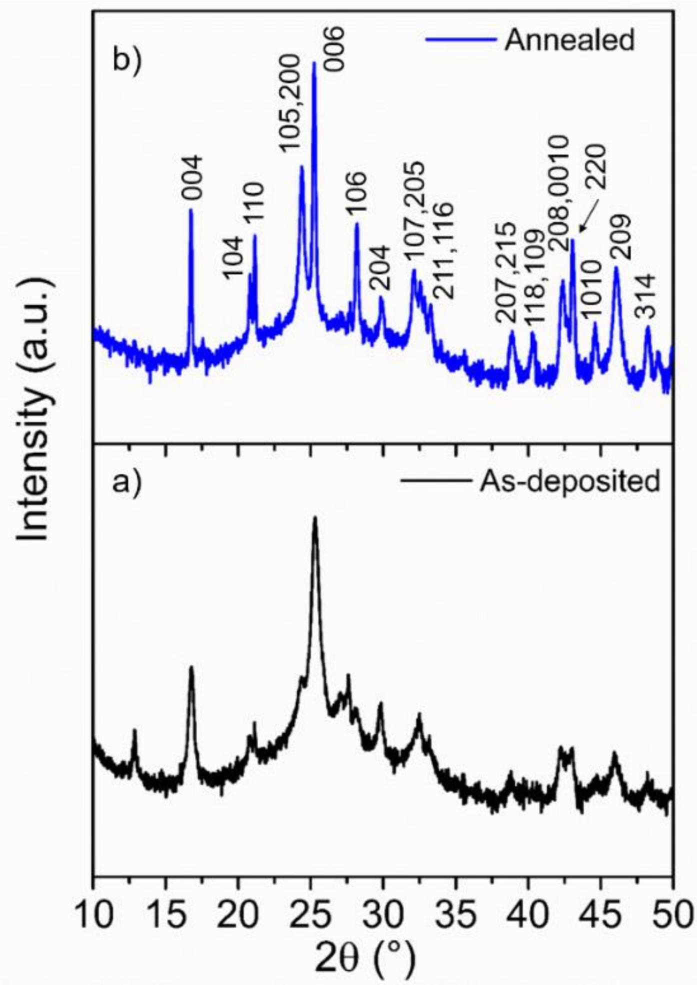

Figure 54. *Experimental XRD patterns for a) as-deposited and b) post-deposition annealed (300 °C, 10 min under* BiI_3 *vapor) films of coevaporated CsI/*BiI_3 *(r = 1.2). Selected strong diffraction peaks are labeled.*

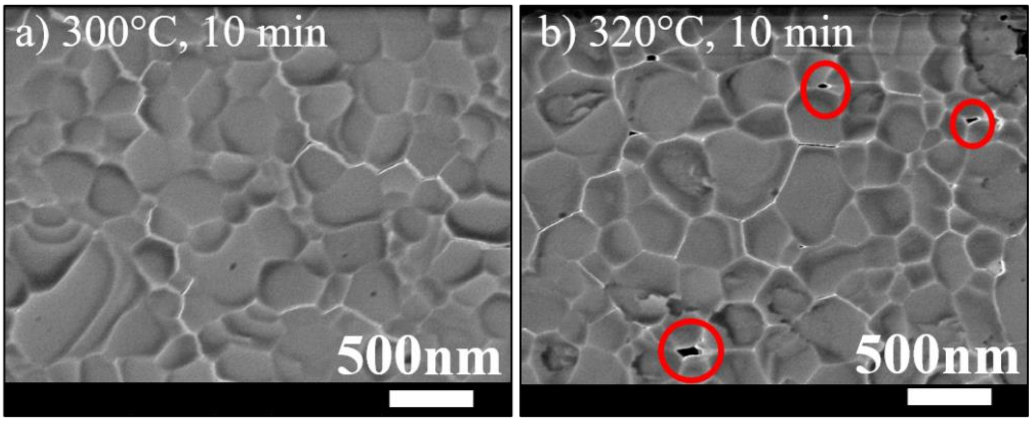

Figure 55. *Top-view SEM micrographs of annealed thin films of Cs-Bi-I (r = 1.2) at a) 300 °C and b) 320 °C for 10 min. The red circles mark the pinholes on the surface of the film.*

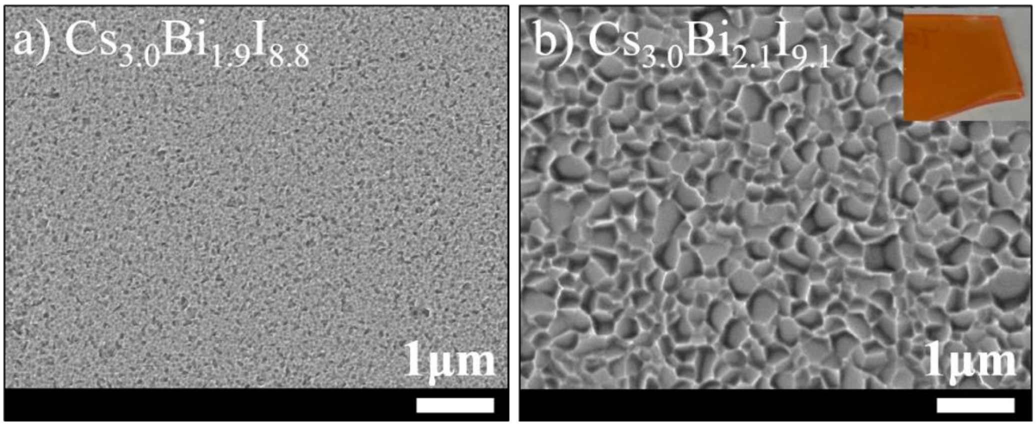

Figure 56. *SEM images of a) as-deposited and b) annealed (300 °C for 10 min under* BiI_3 *vapor) films of coevaporated Cs-Bi-I (r = 1.2). Average composition of each film was determined by SEM/EDX and is listed in each panel. The inset image depicts the fabricated orange Cs-Bi-I film on a glass substrate after the post-deposition annealing process.*

Figure 55a and b show SEM images for fabricated Cs-Bi-I films, which were annealed at 300 °C and 320 °C for 10 min under BiI_3 vapor. Apparently, annealing at 320 °C causes creation of pinholes on the surface of the $Cs_3Bi_2I_9$ film, which are marked with red circles in Figure 55b. Therefore, annealing at 300 °C for 10 min under BiI_3 vapor was selected as the optimized condition for growth of single-phase and pinhole-free $Cs_3Bi_2I_9$ films. Figure 56 displays SEM images of the as-deposited and annealed (300 °C, 10 min) thin films of Cs-Bi-I (r = 1.2). The average composition of each film was determined using SEM/EDX. The as-deposited film (Figure 56a) was found to have the average composition of $Cs_{3.0}Bi_{1.9}I_{8.8}$ and contains small grains (< 100 nm). Annealing of the film with an excess of BiI_3 resulted in a film with an average composition of $Cs_{3.0}Bi_{2.1}I_{9.1}$ (Figure 56b) with grains as wide as ~ 180 nm. Considering the error margins for compositional analysis via EDX, these results are consistent with successful formation of $Cs_3Bi_2I_9$. The measured composition for the annealed film is consistent with the composition of the as-deposited film revealing compositional stability of the annealed film under BiI_3 vapor.

4.2.5 Optical Properties of Coevaporated $Cs_3Bi_2I_9$

The optical properties of the film fabricated by the two-step coevaporation approach was characterized via collecting the absorption spectrum of the film using UV-Vis spectroscopy (Figure 57a) followed by plotting the Tauc plots for direct and indirect band gaps (Figure 57b). The absorption spectrum shows that the $Cs_3Bi_2I_9$ film absorbs visible light, with a band gap suitable for tandem solar cells. The estimated direct and indirect band gaps (E_g) for $Cs_3Bi_2I_9$ by this approach are 2.2 and 2.06 eV, respectively, which are in good agreement with previous reports for solution-processed films.[59-61]

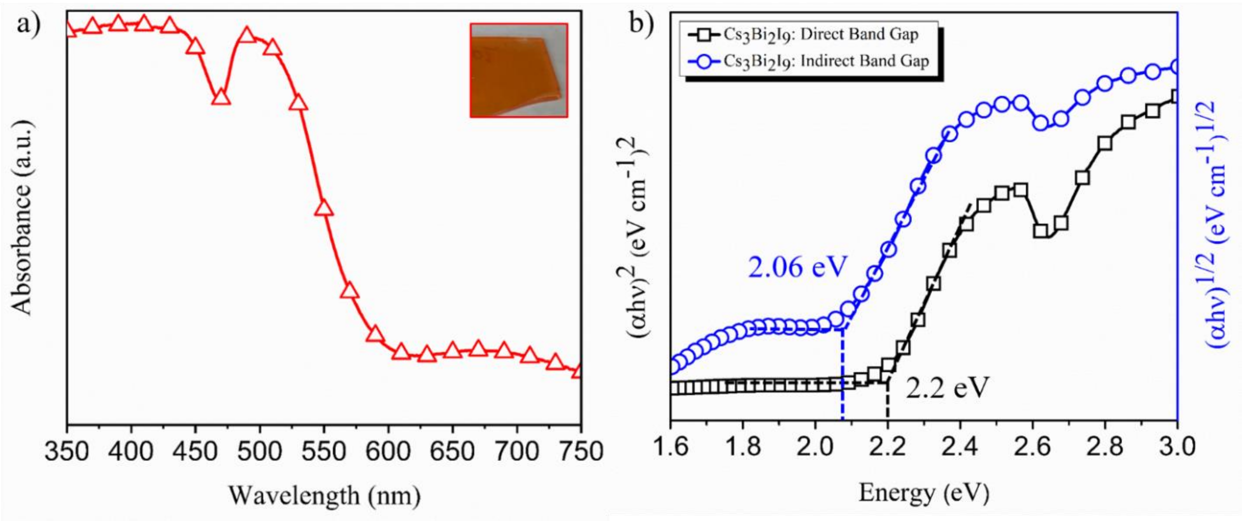

Figure 57. *a) Optical absorbance spectrum of the $Cs_3Bi_2I_9$ (r = 1.2) film using the two-step coevaporation/annealing approach and b) Tauc plots of the corresponding film showing direct (black) and indirect (blue) band gap values.*

4.2.6 Electronic Properties of Coevaporated $Cs_3Bi_2I_9$

In order to study the electronic properties of the coevaporated $Cs_3Bi_2I_9$ using the two-step coevaporation/annealing approach, PES measurements were performed. The surface composition of the annealed film of Cs-Bi-I was characterized by analyzing XPS core-level spectra (Figure 58). The results are compiled in Table 7. Apart from carbon (285 eV) and oxygen (530 eV), no traces of other contaminants were observed in both as-loaded and sputtered (5 s) samples (Figure 58). Table 7 shows that the surface composition of the as-loaded and sputtered Cs-Bi-I film is Bi and I-deficient compared to the bulk compositional analysis using SEM EDX, most likely due to the volatility of BiI_3 making it susceptible to be evaporated from the surface of the film during the post-deposition annealing process. Figure 59 shows the Al Kα close up scans of the Cs 3d, Bi 4f, and I 3d peaks. As can be seen, sputtering of $Cs_3Bi_2I_9$ results in a rigid shift of the XPS core level peaks by 0.5 eV to lower binding energy, indicating a shift of the Fermi level (0.5 eV) towards midgap, in addition to an increase in relative Cs content, a decrease in Bi content, and an approximately constant I content.

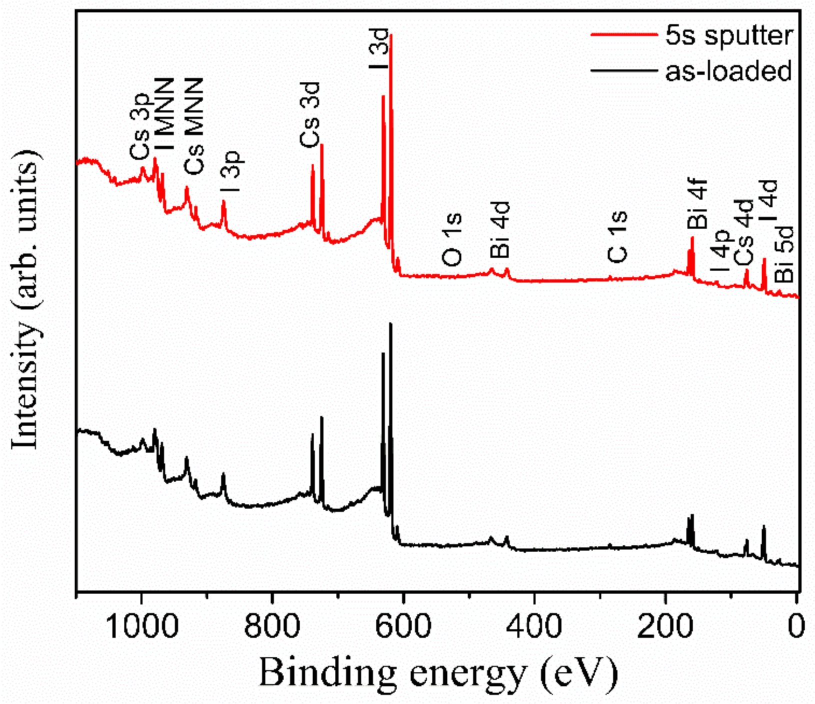

Figure 58. *XPS Al Kα survey scans of the as-loaded (black) and 5 s (red) sputtered film of $Cs_3Bi_2I_9$. Small trace of oxygen and carbon was observed.*

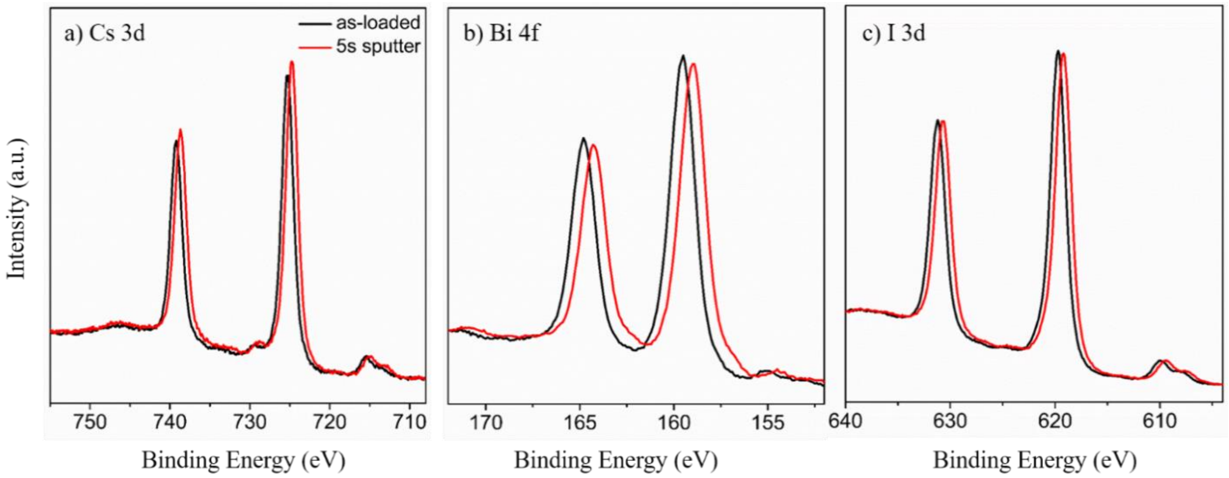

Figure 59. *Close-up Al Kα scans of a) Cs 3d, b) Bi 4f, and c) I 3d peaks for as-loaded (black) and 5 s sputtered (red) thin film of $Cs_3Bi_2I_9$, deposited using the two-step coevaporation (r = 1.2) approach.*

Table 7. *Atomic ratios (atom. %) derived from XPS data for the annealed coevaporated thin film of Cs-Bi-I (300 °C, 10 min). Annealing was performed under* BiI_3 *vapor.*

Compound	Sample	Cs (± 2%)	Bi (± 1%)	I (± 3%)	Composition
Cs-Bi-I	As-loaded	26	10	61	$Cs_3Bi_{1.1}I_7$
	5 s sputter	27	9	61	$Cs_3Bi_{1.0}I_{6.8}$

Further PES measurements were performed to characterize the positions of secondary electron onset, valence band maxima (VBM), conduction band minima (CBM), and ionization energy for the $Cs_3Bi_2I_9$ film. Figure 60a displays the UPS He I secondary electron onset and scan of valence band states of the as-loaded and 5 s sputtered films of $Cs_3Bi_2I_9$. In addition, UPS He I valence band edge and IPES spectra of the conduction band states are shown in Figure 60b. Sputtering of $Cs_3Bi_2I_9$ results in a rigid shift (0.5 eV) of the onset of UPS secondary electrons, IPES conduction band edge, and valence band edge peaks to lower binding energy consistent with the shift of the Fermi level towards midgap. The change to the UPS spectra with 5 s of sputtering involves a reduction in the density of states in the 5 to 10 eV binding energy region, consistent with a reduction in O 2p states. This reduction verifies the partial removal of oxygen impurities from the film surface.

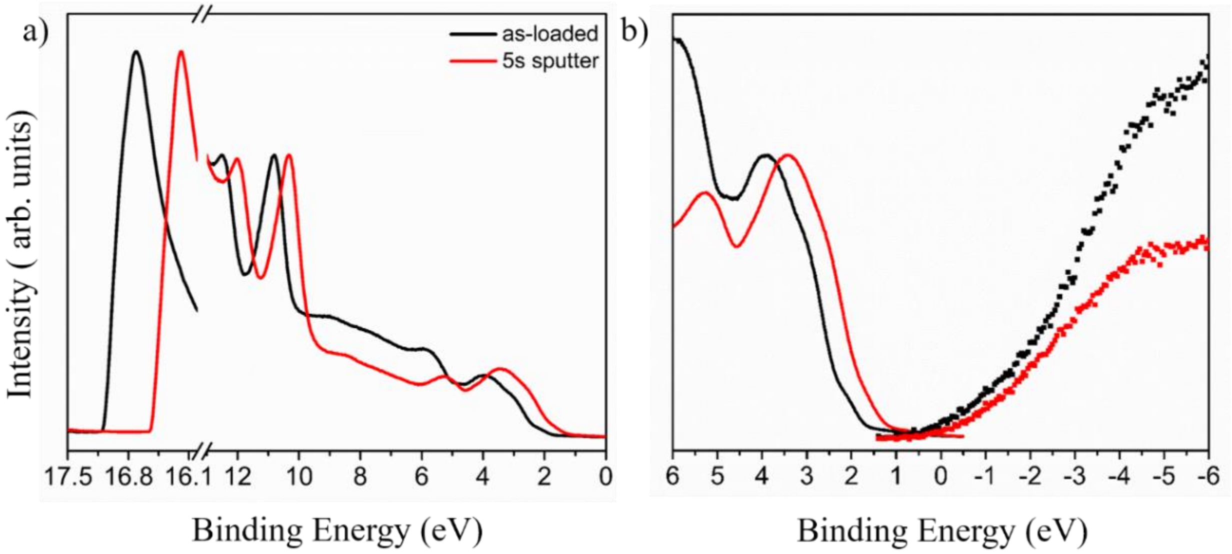

Figure 60. *a) Combined UPS He I onset of secondary electrons and scan of valence band states spectra. b) Combined UPS He I valence band edge and IPES spectra of conduction band states for as-loaded (black) and 5 s sputtered (red) post-deposition annealed coevaporated* $Cs_3Bi_2I_9$ *film.*

A close-up of UPS He I secondary electron onset, UPS He I valence band edge, and IPES conduction band edge is shown in Figure 61a and b for the as-loaded and sputtered films. The positions of the onsets of secondary electrons, valence band maxima (VBM), and conduction band minima (CBM) were determined via the intersection of tangent line fits to the features of interest and the background. Furthermore, ionization energies (IE = hν – (E_{onset} – E_{VBM})) were determined from UPS measurements of the film. Consequently, the band gap (E_g) of the fabricated $Cs_3Bi_2I_9$ film was derived as E_g = CBM – VBM. The slowly varying background in the IPES spectra makes the determination of the conduction band edge difficult and consequently results in a large uncertainty in the band gap calculation from UPS/IPES. However, within error the determined value (2 eV) is consistent with the calculated optical band gap (direct = 2.2 eV and indirect = 2.06 eV). A schematic illustration of the calculated band positions is shown in Figure 61c, confirming that $Cs_3Bi_2I_9$ behaves as a n-doped semiconductor. Table 8 summarizes the derived parameters from UPS and IPES measurements for the as-loaded and sputtered thin film of $Cs_3Bi_2I_9$. The calculated parameters regarding the electronic properties of vacuum-deposited $Cs_3Bi_2I_9$ film are consistent with previously reported values for solution-processed films.[59]

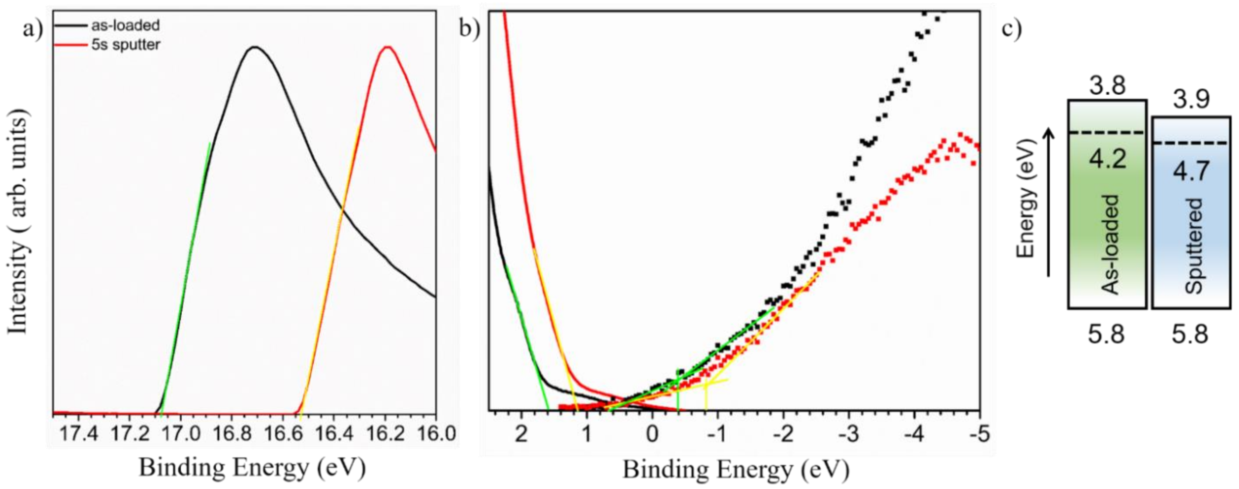

__Figure 61.__ Close-up of a) the UPS He I onset of secondary electrons and b) the UPS He I valence band edge and IPES conduction band edge. The tangent lines were draw to indicate the onset location. c) Band positions for the thin films of $Cs_3Bi_2I_9$ derived from UPS/IPES measurements.

__Table 8.__ Key parameters derived from UPS and IPES measurements on as-loaded and 5 s sputtered $Cs_3Bi_2I_9$ films. The energy values are referenced to the Fermi level.

Film	**E_{onset} (±0.02) (eV)**	**E_{VBM} (±0.1) (eV)**	**IE (±0.1) (eV)**	**E_{CBM} (±0.3) (eV)**	**E_g (± 0.3) (eV)**
As-loaded	17.07	1.6	5.8	-0.4	2.0
5 s sputter	16.54	1.1	5.8	-0.8	1.9

4.3 Growth of Rubidium Bismuth Iodide ($Rb_3Bi_2I_9$)

4.3.1 Crystal Structure of $Rb_3Bi_2I_9$

As another member of the $A_3Bi_2I_9$ family, $Rb_3Bi_2I_9$ possess a two dimensional layered structure. The crystal structure of the monoclinic 2D layered modification of $Rb_3Bi_2I_9$ consists of distorted corner-connected BiI_6 octahedra, in which only two-thirds of the octahedral Bi sites are occupied and one-third remain vacant $Rb(Bi_{2/3}\square_{1/3})I_3$ (Figure 62). This structure can be thought of as being derived from the hypothetical (not charge balanced) 3D perovskite $RbBiI_3$ by removing every third Bi layer along <111> to yield a layered perovskite structure. Each BiI_6 octahedra is coordinated by eight Rb atoms in the arrangement of a distorted cube; the unit cell of the perovskite type (AMX_3). The distorted BiI_6 octahedra of the two crystallographic Bi sites consists of three shorter (2.93 ± 1 Å) and three longer (3.20 to 3.25 Å) Bi−I distances, in which the shorter Bi-I bonds involve terminal I sites, while the longer Bi-I bonds exist for bridging I (connecting multiple Bi sites).[59] In addition, due to the relatively small ionic radius of Rb^+ (1.5 Å) compared to I^- (2.2 Å), the close packing of the ions is irregular, resulting in distorted and tilted BiI_6 octahedra. Therefore, the ideal bond angle of 180° between M-I-M atoms in cubic perovskite aristotype decreases to 147° to 153° in $Rb_3Bi_2I_9$.[59]

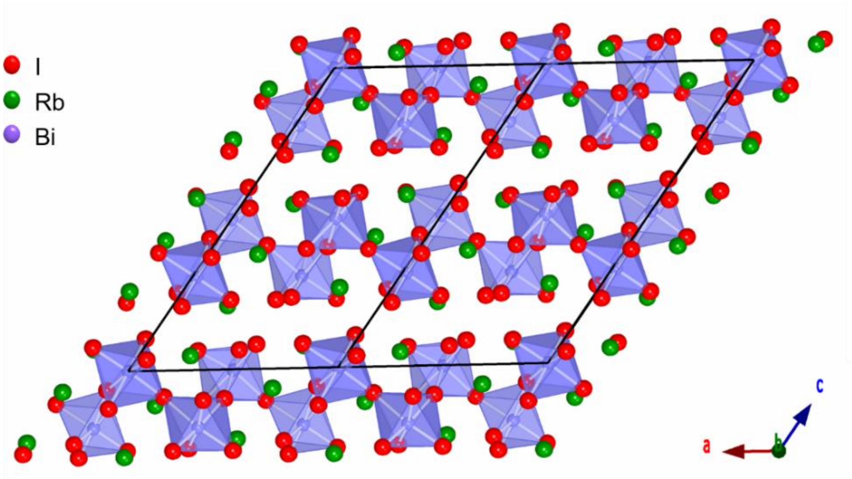

Figure 62. *Crystal structure of 2D layered-modification of $Rb_3Bi_2I_9$ ($P2_1/n$), which consists of Bi^{3+} cations and I^- anions forming layers of distorted octahedra. The voids between the layers are occupied by Rb^+ cations.*

4.3.2 Single Deposition Approach

The same methodology was applied to fabricate a rubidium bismuth iodide (Rb-Bi-I) film on a glass substrate (as described for fabrication of $Cs_3Bi_2I_9$). For this purpose, a thin film of RbI (300 nm) was evaporated by the thermal evaporator followed by post-deposition annealing under BiI_3 vapor at 250 °C for 10 min in a nitrogen-filled glovebox followed by quenching the film to room temperature. The XRD pattern of the post-deposition annealed film was collected to verify the phase purity of the film (Figure 63). Although $Rb_3Bi_2I_9$ was formed, there is a trace of BiI_3 impurity in the XRD pattern (at 17.34°). The XRD pattern of Rb-Bi-I film indexes to a monoclinic structure with lattice parameters a = 14.660(3) Å, b = 8.1888(4) Å, c = 20.8906(1) Å, and β = 91.345(1)°, in the space group $P2_1/n$. Several annealing temperatures ranging from 200-300 °C were tested to grow a single phase $Rb_3Bi_2I_9$ by this approach. However, most of them showed the impurity peak at 17.34°.

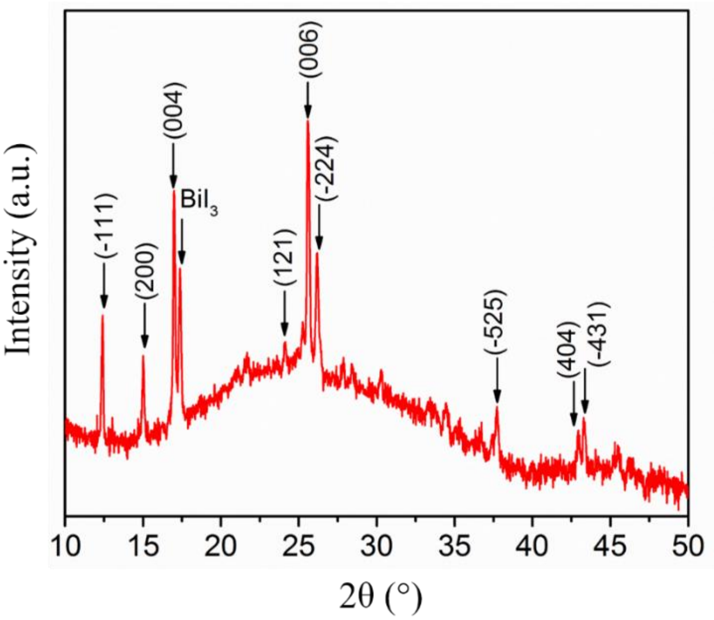

Figure 63. *XRD pattern of annealed thin film of Rb-Bi-I deposited via the single deposition approach. Annealing was performed at 250 °C for 10 min under BiI_3 vapor.*

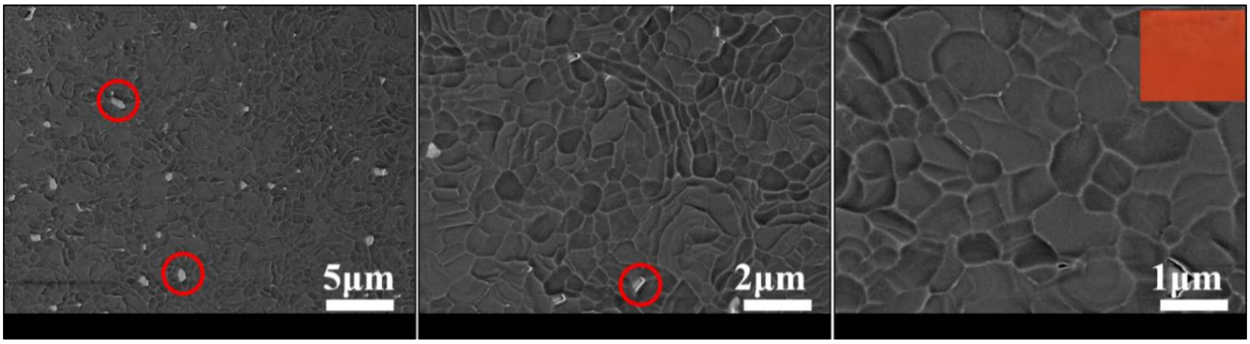

Figure 64. *Top-view SEM micrographs of post-deposition annealed thin film of RbI in BiI_3 vapor at 250 °C for 10 min. The layered modification of $Rb_3Bi_2I_9$ is red in color (the inset image showing the annealed film).*

The as-deposited RbI film is transparent, however annealing of the film under BiI_3 vapor results in formation of a red film (Figure 64, inset). Furthermore, SEM surface morphology characterization shows formation of grains as wide as 1 μm (Figure 64). However, the film is not compact and contains a significant number of pinholes marked with red circles in Figure 64. Since this film of Rb-Bi-I from this approach is not a smooth and single phase film, it is not the focus of this study and no further analysis was carried out on this film.

4.3.3 Two-step Coevaporation Approach

In this approach, thin films of Rb-Bi-I (thickness = 450 nm) were coevaporated in the thermal evaporator. The two Radak sources were filled with BiI_3 and RbI powders. To optimize the stoichiometry of the deposited film, various deposition rate ratios (r = RbI/BiI_3) for the two precursors – i.e. r = 0.7, 0.8, 1, and 1.2– were tested. Note that the specific rate ratios used do not, in general, translate to the same elemental ratios in the final films, due to different volatilities, evaporation and sticking properties for the different metal halides. Nevertheless, there is the expectation that changes in "r" will correlate with changes in the resulting film composition. The base pressure for the evaporation was below 2×10^{-6} Torr. During the deposition, no intentional substrate heating was applied. Post-deposition annealing of the films was performed inside the glovebox. For this purpose, an as-deposited film was placed under a quartz cover in preheated BiI_3 vapor and annealed at 225 °C for 10 min followed by quenching of the film to room temperature.

The compositional analysis of the fabricated films derived from SEM/EDX are tabulated in Table 9. Among the as-deposited films with different rate ratios, the as-deposited Rb-Bi-I film with r = 0.7 has an average composition of $Rb_3Bi_{2.26}I_9$, within the error of stoichiometry of $Rb_3Bi_2I_9$, and the yield decreases with increasing the deposition rate ratio (r) between RbI and BiI_3. The SEM/EDX results demonstrate that the deposited Rb-Bi-I film with r = 0.7 has the most appropriate composition (within the error of stoichiometry of $Rb_3Bi_2I_9$) compared to the other films. It is thus the focus of this study. Table 9 demonstrates that the composition of the post-deposition annealed Rb-Bi-I film deposited with r = 0.7 is Bi and I deficient compared to the as-deposited film indicating loss of BiI_3 from the film during annealing. Among the deposited Rb-Bi-I films with different rate ratios, the deposited Bi- and I-rich films (e.g. r = 0.7 and 0.8) are more prone to lose volatile BiI_3 during the annealing process (225 °C, 10 min) than the Rb- rich films (e.g., r = 1 and 1.2).

Morphological characterization of the fabricated $Rb_3Bi_2I_9$ film was performed using SEM (Figure 65). The as-deposited film of $Rb_3Bi_2I_9$ consists of very small grains (maximum width of 100 nm) (Figure 65 a-b). However, post-deposition annealing under excess of BiI_3 (225 °C, 10 min) causes grain growth and formation of wide grains (> 3 μm) with negligible pinhole densities on the surface of the film (Figure 65 c-d). Annealing of Rb-Bi-I film at temperatures higher than 180 °C under N_2 (without providing an excess of BiI_3) results in evaporation of volatile BiI_3, leaving behind the RbI secondary phase.

Table 9. *Elemental composition (atom. %) derived from SEM/EDX analysis of as-deposited and annealed thin films of rubidium bismuth iodide coevaporated with different rate ratios (r).*

r = RbI/BiI$_3$	Film	Rb	Bi	I	Composition
0.7	As-deposited	21.1	15.9	63.1	$Rb_3Bi_{2.26}I_9$
0.7	Annealed 225 °C, 10min	24.6	14.8	60.6	$Rb_3Bi_{1.8}I_{7.39}$
0.8	As-deposited	24.4	14.6	61	$Rb_3Bi_{1.79}I_{7.5}$
0.8	Annealed 225 °C, 10 min	25.1	14.6	60.2	$Rb_3Bi_{1.74}I_{7.19}$
1	As-deposited	28.2	13.6	58.3	$Rb_3Bi_{1.45}I_{6.2}$
1	Annealed-225 °C, 10min	25.8	14	60.2	$Rb_3Bi_{1.63}I_7$
1.2	As-deposited	28.4	13	58.5	$Rb_3Bi_{1.37}I_{6.18}$
1.2	Annealed-225 °C,10 min	27.4	14.6	58	$Rb_3Bi_{1.6}I_{6.35}$

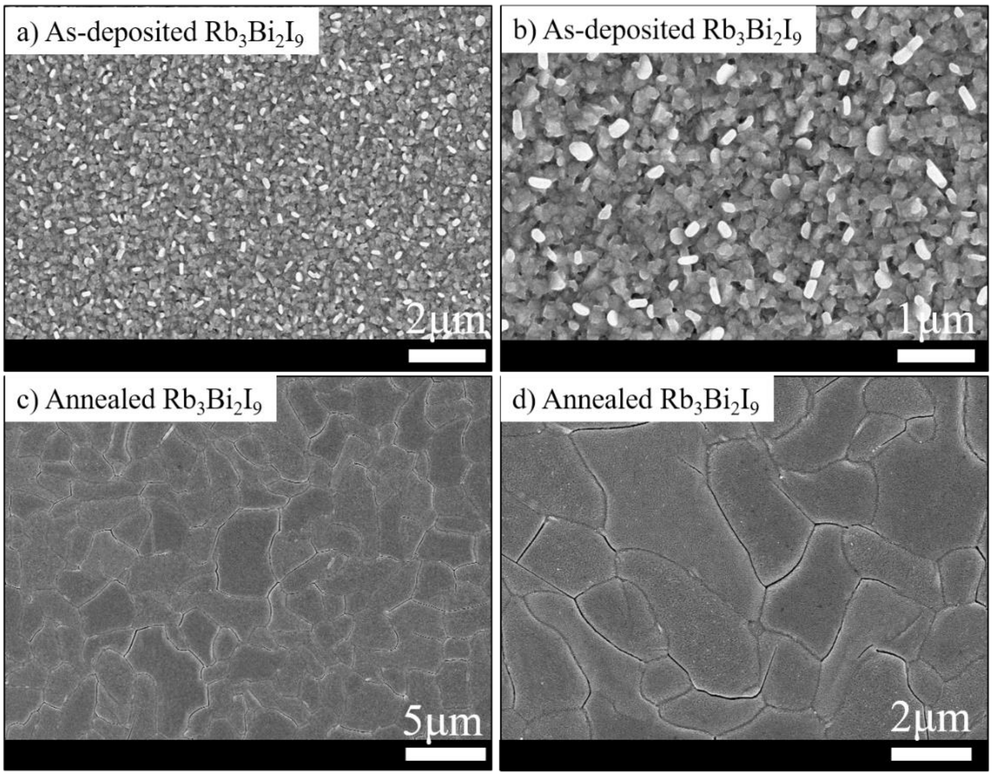

Figure 65. *SEM images of a-b) as-deposited and c-d) annealed thin films of* $Rb_3Bi_2I_9$ *grown with r = 0.7 under low and high magnifications. These films were deposited using the two-step coevaporation approach on glass substrates.*

XRD patterns of as-deposited and post-deposition annealed (225 °C, 10 min under BiI_3) films of coevaporated Rb-Bi-I (r = 0.7) were collected and shown in Figure 66. The XRD pattern of the as-deposited Rb-Bi-I film does not correspond to the final phase of crystalline $Rb_3Bi_2I_9$. However, post-deposition annealing of the coevaporated Rb-Bi-I film results in the formation of a polycrystalline single-phase $Rb_3Bi_2I_9$ film as shown in Figure 66. Fitting the experimental XRD pattern for the annealed film yields a monoclinic structure with lattice parameters a = 14.6451(1) Å, b = 8.1787(6) Å, c = 20.8940(2) Å, and β = 90.4283(1)°, in the space group $P2_1/n$. Figure 62 shows the crystal structure of the monoclinic 2D layered modification of $Rb_3Bi_2I_9$ consisting of corner-connected bismuth iodide octahedra. The Pawley-refined unit cell parameters (Table 10) for $Rb_3Bi_2I_9$ are in good agreement with previously reported values.[59, 136]

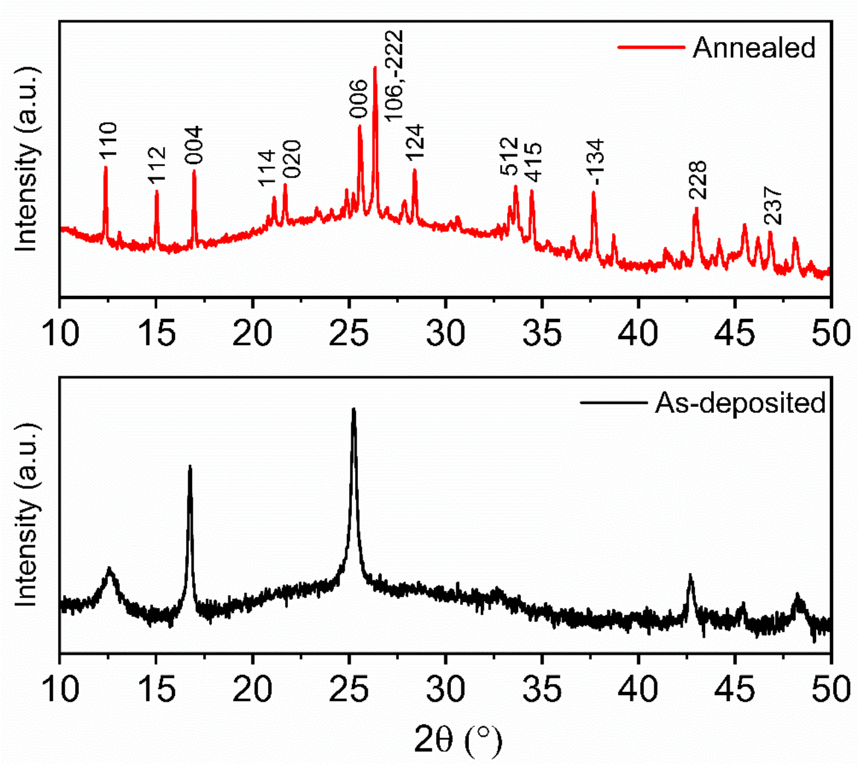

Figure 66. *XRD patterns of as-deposited (black) and annealed (red; 225 °C, 10 min under BiI_3 vapor) coevaporated Rb-Bi-I (r = 0.7) films. Selected strong diffraction peaks are labeled in the pattern of the annealed film.*

Table 10. *Crystallographic parameters of a post-annealed coevaporated $Rb_3Bi_2I_9$ film achieved by Pawley refinement.*

Compound	**Crystal System**	**Space group**	**Unit Cell Parameters**	**Fitting Parameters**
$\mathbf{Rb_3Bi_2I_9}$	Monoclinic	$P2_1/n$	a = 14.6451(1) Å; b = 8.1787(6) Å; c = 20.8940(2) Å β (°) = 90.4283(1)°	*goodness-of-fit = 1.52* *Rp = 3.26 %* *wRp = 4.57 %*

4.3.4 Optical Properties of $Rb_3Bi_2I_9$

The layered modification of $Rb_3Bi_2I_9$ is red (Figure 67a, inset) as opposed to the orange color of the dimer modification of $Cs_3Bi_2I_9$, implying a lower band gap of the layered structure $Rb_3Bi_2I_9$. An optical absorption measurement was performed for the post-deposition annealed $Rb_3Bi_2I_9$ film grown with $r = 0.7$ (Figure 67a). The calculated direct band gap from the Tauc plot of the absorbance data (Figure 67b, black) was found to be 2.08 eV. In comparison, the plot of $(\alpha h\nu)^{1/2}$ versus hν, assuming an indirect gap, yields a similar 2.02 eV band gap. The calculated band gaps for the $Rb_3Bi_2I_9$ film correspond well with the previously published values for solution-processed films.[59-60]

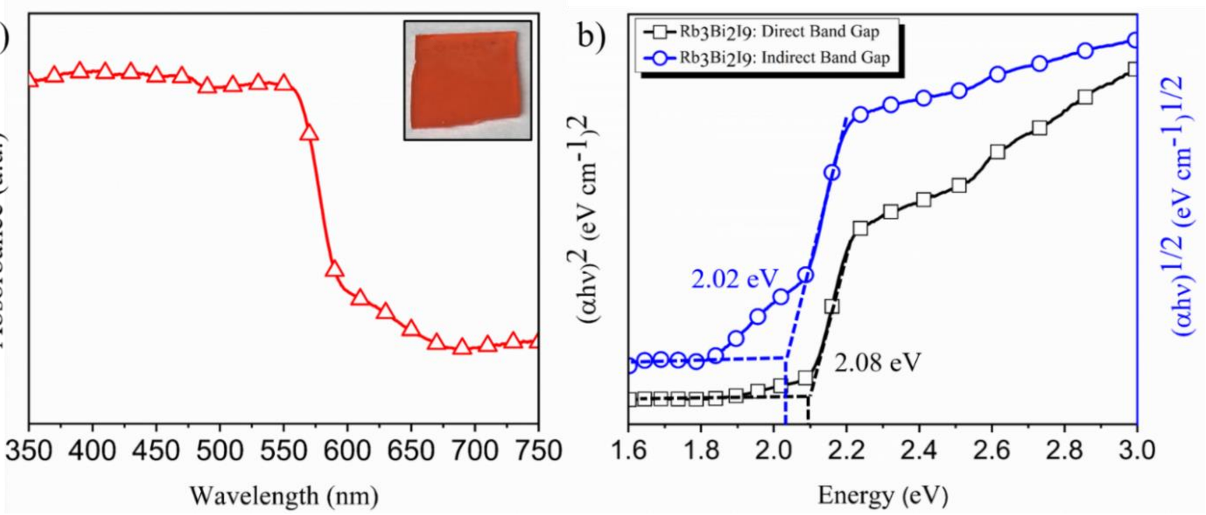

Figure 67. *a) Optical absorbance spectrum for the* $Rb_3Bi_2I_9$ *film grown with* $r = 0.7$ *(Inset image depicts the post-deposition annealed film). b) Tauc plots showing direct (black) and indirect (blue) band gaps for the film. Annealing was performed at 225 °C for 10 min under* BiI_3 *vapor.*

4.3.5 Electronic Properties of $Rb_3Bi_2I_9$

Surface composition of the annealed Rb-Bi-I film (225 °C, 10 min) coevaporated with $r = 0.7$ was characterized by analyzing XPS core-level spectra for as-loaded and after sputtering for 5 s, 10 s, and 70 s (Figure 68), with results compiled in Figure 69. Carbon (285 eV) and oxygen (530 eV) impurities are the only contaminations detected in the XPS spectra of as-loaded and sputtered films. Moreover, a trace of metallic Bi (Bi^0) appears in the Al Kα scan of the Bi 4f line for rubidium bismuth iodide films, in the form of two small shoulders at binding energies of ~162 eV and 157 eV for the as-loaded film, which become more distinguishable after sputtering (Figure 69b). No trace of metallic Bi was found for cesium bismuth iodide (Figure 59b).

Table 11 shows that the surface composition of Rb-Bi-I (as-loaded and sputtered films) is Bi and I-deficient compared to the bulk compositional analysis using SEM EDX, most likely due to the volatility of BiI_3 and the possibility of reducing Bi^{3+} to Bi^0, e.g., in an X-ray beam under ultra-high vacuum or during processing. Increasing sputtering time from 5 s to 10 s and 70 s results in a shift of the XPS features to lower binding energies (Figure 69), in addition to the removal of volatile BiI_3 from the film and the increase in the relative concentration of rubidium (Figure 69).

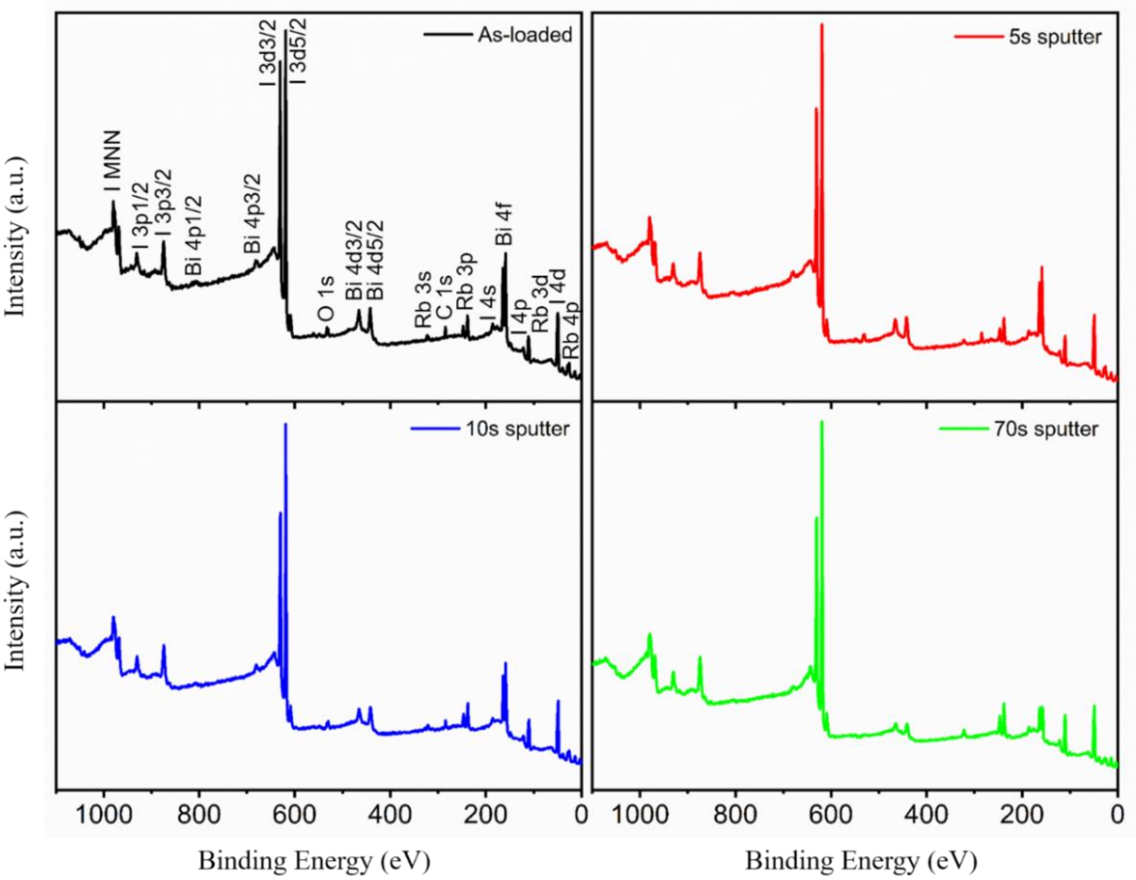

Figure 68. *XPS Al Kα survey scans of the as-loaded (black), 5 s (red), 10 s(blue), and 70 s(green) sputtered films of* $Rb_3Bi_2I_9$

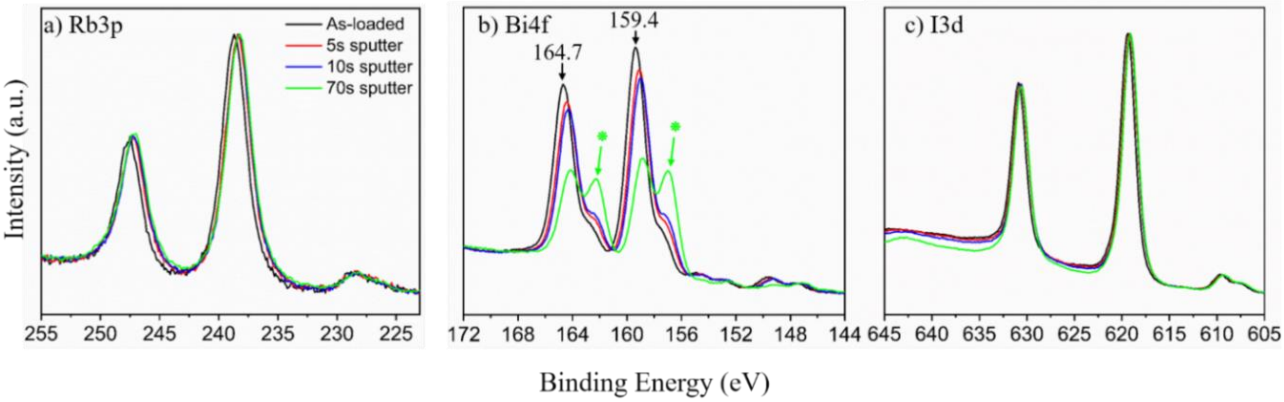

Figure 69. *Close-up Al Kα scans of a) Rb 3p, b) Bi 4f, and c) I 3d peaks for as-loaded, 5 s, 10 s, and 70 s sputtered thin film of Rb-Bi-I. Two small shoulders at ~162 eV and 157 eV in the scan of Bi 4f originate from metallic Bi (marked with "*" for the 70 s sputtered film).*

Table 11. *Atomic ratios (atom. %) derived from XPS data of as-loaded and sputtered thin films of Rb-Bi-I (225 °C, 10 min). Annealing was performed under BiI_3 vapor.*

Film	Rb	Bi (total)	Bi^0	Bi^{3+}	I	Composition
As-loaded	27.7	22.8	4.1	18.7	49.5	$Rb_{3.00}Bi_{2.47}I_{5.36}$
5 s sputter	31.8	20.4	4.3	16.1	47.8	$Rb_{3.00}Bi_{1.92}I_{4.50}$
10 s sputter	34.2	18.6	4.4	14.3	47.2	$Rb_{3.00}Bi_{1.63}I_{4.14}$
70 s sputter	41.6	11.6	5.5	6.1	46.8	$Rb_{3.00}Bi_{0.83}I_{3.37}$

Figure 70 demonstrates combined UPS He I secondary electron onset, scan of valence band spectra, and IPES spectra of the conduction band for the as-loaded and sputtered films of Rb-Bi-I fabricated with $r = 0.7$. The change to the UPS spectra with sputtering involves a reduction in the density of states in the 10−5 eV binding energy region, which is extremely intense for the 70 s sputtered film. This reduction is consistent with the removal of surface oxygen (O 2p states).

In addition, the valence band and conduction band edges get structured via increasing the sputtering time to 70 s (Figure 70b). A close up view of the UPS secondary electron onset and valence band edge regions depicts that sputtering results in a small shift of the onset values (Figure 71a and b). Furthermore, with increasing sputtering, the IPES data show an increasing intensity in the vicinity of the Fermi level, consistent with the formation of metallic surface domains.

Due to the detrimental impact of sputter cleaning, XPS, UPS, and IPES spectra of the as-loaded thin film of Rb-Bi-I are considered the more reliable data. The derived parameters from the PES study for the annealed Rb-Bi-I film (225 °C, 10 min) are tabulated in Table 12. The determined ionization energy (6.07 eV) and band gap (2.3 eV) values for the as-loaded film of Rb-Bi-I are consistent with previously reported values of 6 eV and 2.1 eV for solution-processed films,[59] respectively, within error originating from the IPES study. On the basis of the UPS/IPES result, the band positions of $Rb_3Bi_2I_9$ film (as-loaded) was calculated and is shown in the inset of Figure 71b.

A similar phenomenon occurred in a previously published XPS study by Mitzi et.al on the analogous Sb-based layered structure, $Cs_3Sb_2I_9$,[128] in which a trace of metallic antimony (Sb^0) was observed after 5 s sputtering of the annealed film of $Cs_3Sb_2I_9$, further highlighting another possible route of inducing Bi^0/Sb^0 on the surface of Bi- and Sb-based semiconductors. If present at the interface between the absorber and the other PV device layers, metallic Bi^0/Sb^0 could serve as a recombination site or facilitate Fermi level pinning, which might degrade device performance.[66]

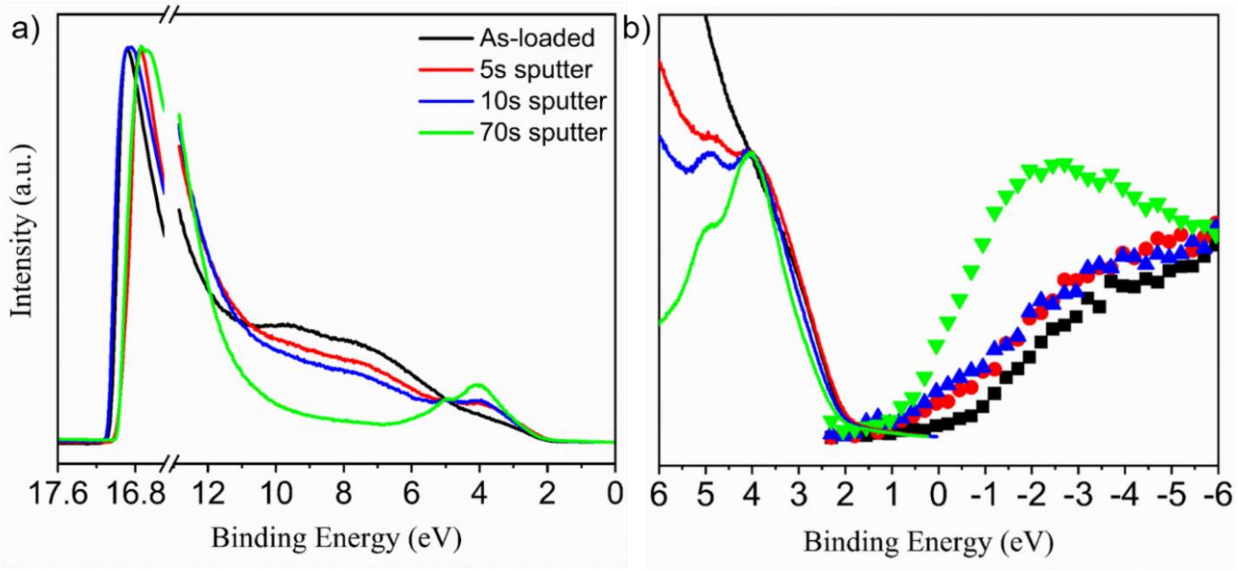

Figure 70. *a) Combined UPS He I secondary electron onset and scan of valence band states spectra and b) combined UPS He I valence band edge and IPES spectra of conduction band states for as-loaded (black),5 s (red), 10 s (blue), and 70 s sputtered post-deposition annealed Rb-Bi-I film fabricated with r = 0.7.*

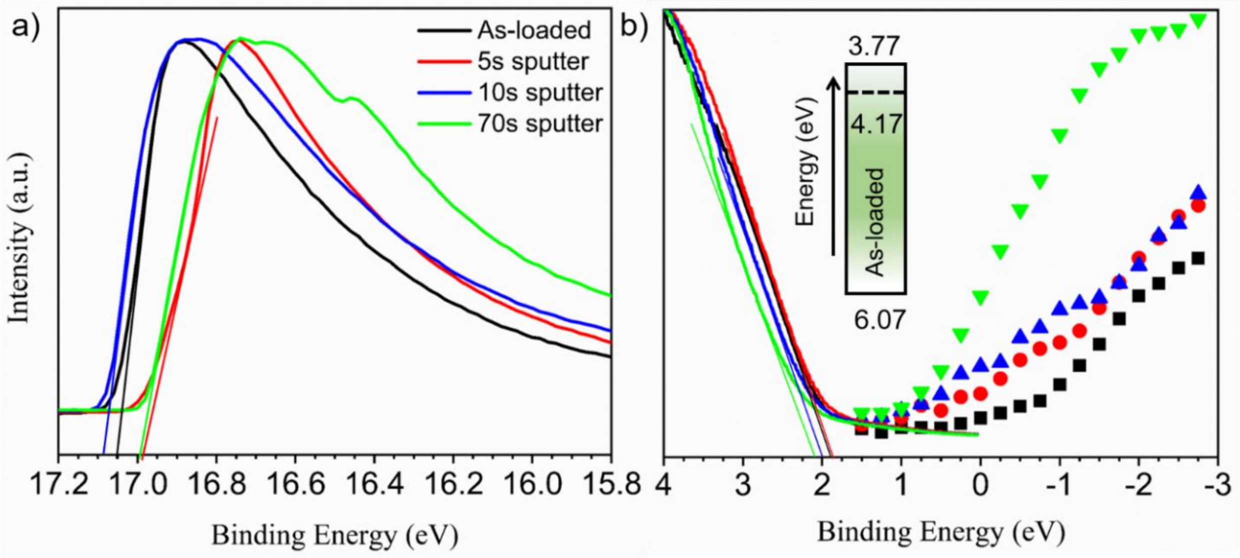

Figure 71. *Close-up of a) UPS He I secondary electron onset and b) combined UPS He I valence band edge and IPES conduction band edge for the grown thin film of Rb-Bi-I. Inset shows the band positions for the as-loaded thin film of Rb-Bi-I derived from UPS/IPES measurements.*

***Table 12**. Key parameters derived from UPS and IPES measurements on as-loaded and sputtered (5, 10, and 70 s) thin films of Rb-Bi-I.*

$Rb_3Bi_2I_9$ Film	**E_{onset}(±0.05)**	**E_{VBM}(±0.1)**	**IE(±0.07)**	**E_{CBM}(±0.25)**	**E_g (±0.25)**
	(eV)				
As-loaded	17.05	1.9	6.07	-0.4	2.3
5 s sputter	16.98	1.9	6.14	-0.3	2.2
10 s sputter	17.08	2.0	6.14	N/S	N/S
70 s sputter	16.98	2.1	6.34	N/S	N/S

4.3.6 Investigation of Possible Sources of Metallic Bismuth

4.3.6.1 XPS Analysis of Precursor Materials

In order to address the origin of the metallic Bi in the grown rubidium bismuth iodide film, in the first place, purity of the precursor materials (i.e. RbI and BiI_3) was checked using XPS. Thin films (300 nm) of RbI and BiI_3 were grown using the thermal evaporator followed by XPS analysis on the as-deposited films (Figure 72). The films were analyzed as-loaded. Apart from carbon and oxygen in the XPS spectra of RbI and BiI_3, a trace of silicon impurity was detected in the XPS spectrum of the RbI film, which originates from the glass residual underneath the ITO remaining on the surface after cutting/cleaning the substrate. No other contaminants were observed in the XPS spectra of these films confirming the purity of the precursors.

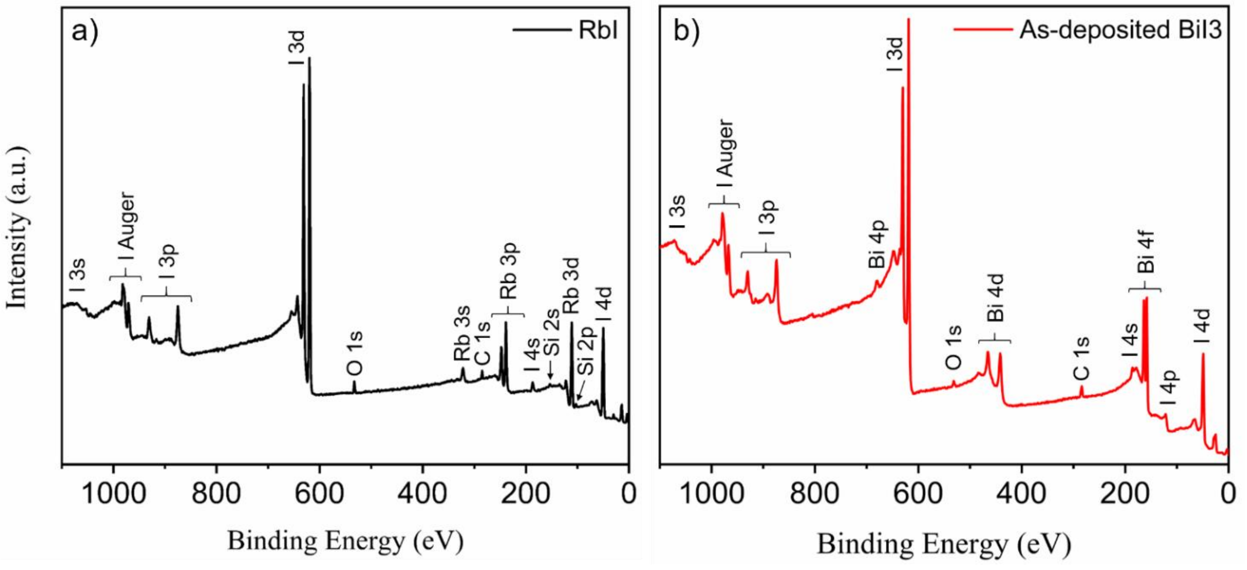

***Figure 72.** XPS Al Kα survey scans of the as-deposited films (300 nm) of a) RbI and b) BiI_3, deposited using the thermal evaporator. Films were analyzed as-loaded.*

XPS surface analysis was performed on the as-deposited and annealed thin films of BiI_3. The as-deposited BiI_3 film was annealed under N_2 at 180 °C for 10 min. Figure 73 depicts the Al Kα close up scans of the Bi 4f peaks for the as-deposited and annealed thin films of BiI_3. The as-deposited BiI_3 film does not exhibit any metallic Bi. However, a small amount of Bi^0 is detected for the annealed BiI_3 film marked by "*" in Figure 73 indicating that formation of Bi^0 is directly related to the annealing, which may cause evaporation of I_2 from the film.

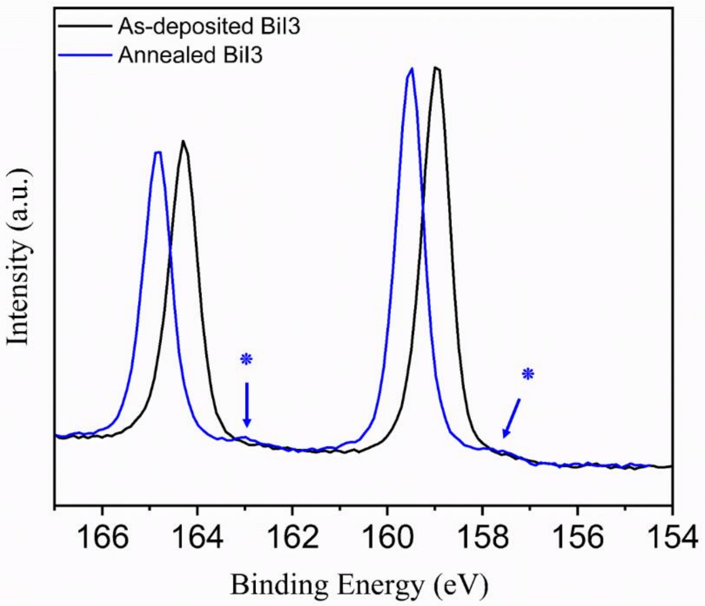

***Figure 73**. Close-up Al Kα scans of Bi 4f peaks for as-loaded thin films of a) as-deposited (black) and annealed (180°C in N_2) BiI_3. Small peaks due to metallic bismuth (Bi^0) impurity are marked with "*".*

4.3.6.2 Effect of Annealing Process

Furthermore, XPS Bi 4f spectra of as-deposited and post-deposition annealed films of rubidium bismuth iodide (annealed at 225 °C for 10 min under excess of BiI_3 vapor) were collected (Figure 74). The two small shoulders characteristic of Bi^0 (156.8° and 162°) are again realized only for the annealed film. Surface composition of the as-deposited and annealed films of Rb-Bi-I was derived by analyzing XPS core-level spectra listed in Table 13. Although metallic bismuth was not detectable in the XPS spectrum of the as-deposited film, 1.23 % of Bi^0 was found for the annealed film verifying formation of metallic bismuth via the annealing process.

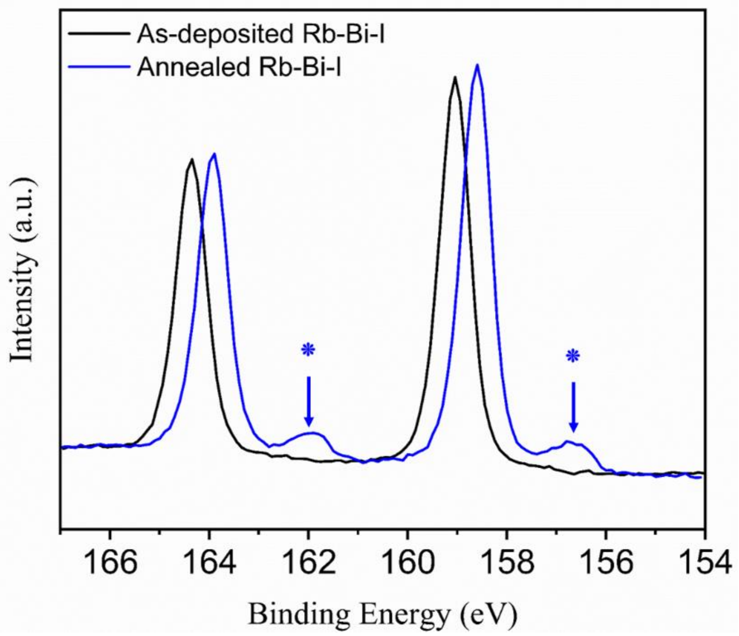

Figure 74. *Close-up Al Kα scans of Bi 4f peaks for as-deposited (black) and annealed (blue) Rb-Bi-I films (annealed with excess BiI_3 vapor). Small peaks due to the metallic bismuth (Bi^0) impurity are marked with "*".*

Table 13. *Atomic ratios (atom. %) derived from XPS data of the as-loaded thin films of as-deposited and annealed (225 °C, 10 min under BiI_3 vapor) Rb-Bi-I.*

Rb-Bi-I Film (r = 0.7)	**Rb**	**Bi (total)**	**Bi^0**	**Bi^{3+}**	**I**	**O**	**C**
As-deposited	13.80	11.64	-	11.64	39.17	10.60	24.78
Annealed	21. 02	11.59	1.23	10.36	40.32	6.77	20.31

4.3.6.3 Angle-resolved XPS Analysis of $Rb_3Bi_2I_9$ Film

ARXPS was used to further probe the surface composition of the annealed film of $Rb_3Bi_2I_9$ at different sampling depths. Core level XPS spectra were acquired at normal (90°) and grazing (35°) emission angles with respect to the sample surface followed by compositional analysis (Table 14). The amount of carbon and oxygen increases via tilting the sample verifying the reduction in the sampling depth. In addition, as the emission angle decreases from 90° to 35°, an increase in the intensity of the two shoulders at 162° and 157°, assigned to the metallic Bi is seen in the Bi 4f spectra (Figure 75) of these two films indicating the existence of more metallic Bi at the topmost surface of the sample than the layers underneath (Table 14).

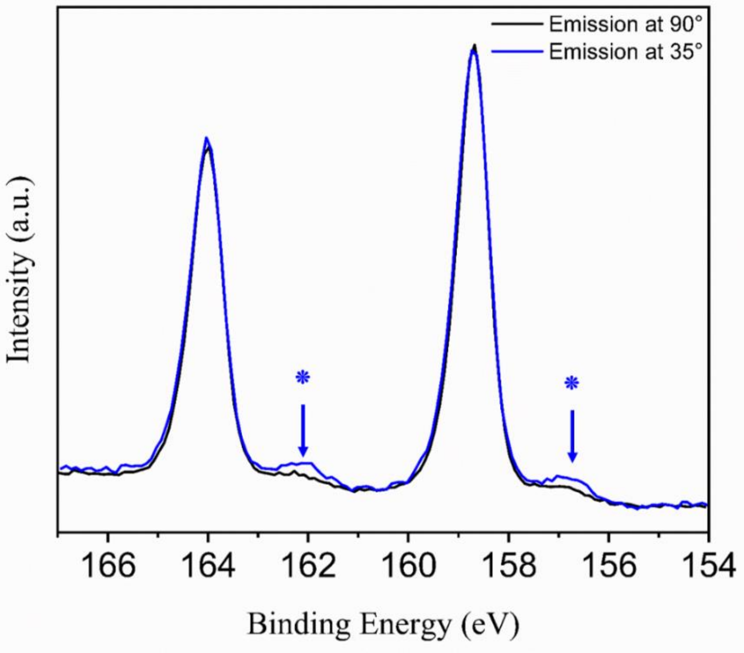

Figure 75. *Close-up Al Kα scans of Bi4f peaks for the as-loaded (black) and tilted (blue) annealed thin film of* $Rb_3Bi_2I_9$*. The assigned peaks to metallic bismuth (*Bi^0*) are labeled with "*".*

Table 14. *Atomic ratios (atom. %) derived from ARXPS of the annealed* $Rb_3Bi_2I_9$ *film (225 °C, 10 min).*

$Rb_3Bi_2I_9$ Film	**Rb**	**Bi (total)**	**Bi^0**	**Bi^{3+}**	**I**	**O**	**C**
As-loaded	20.1	11.98	0.77	11.21	42.36	7.01	18.55
Tilted	18.67	11.41	0.99	10.42	36.95	8.07	24.88

Based on the XPS characterization, it is obvious that the critical parameter affecting formation of metallic Bi is the annealing process. A trace of Bi^0 was observed in both annealed BiI_3 and $Rb_3Bi_2I_9$ films, while no trace of Bi^0 was detected for the as-deposited films. Furthermore, ARXPS has demonstrated that there is more Bi^0 at the topmost surface of the annealed $Rb_3Bi_2I_9$ film in comparison to the underneath layer. The formation of Bi^0 may be attributed to the layer structure of BiI_3 and $Rb_3Bi_2I_9$. However, further studies are needed to fully decipher the formation mechanism of the Bi^0 in these materials.

4.3.7 Device Performance

Next, photovoltaic performance of $Rb_3Bi_2I_9$ as the light absorber was studied in a planar configuration using the FTO/compact-TiO_2/$Rb_3Bi_2I_9$/P3HT/Au structure (Figure 76, inset), in which TiO_2 and P3HT serve as electron and hole transport layers, respectively. Figure 76 shows the J-V characteristics of the $Rb_3Bi_2I_9$-solar cell device measured under illumination in the forward and reverse scan directions. Here, forward and reverse scans refer to sweeping the bias from low to high values, and vice versa. Table 15 demonstrates the PV performance parameters achieved for the $Rb_3Bi_2I_9$-device. A slight hysteresis effect can be observed by comparing the forward and reverse scanning J-V curves in Figure 76, which may originate from low carrier injection in the absorber-TiO_2 interface. A J_{SC} of ~ 0.44 mA/cm^2, V_{OC} of ~ 0.37 V, FF of 30.8 %, and PCE of 0.05 % were obtained from the best solar cells confirming a low device performance, which may be attributed to the presence of Bi^0 on the $Rb_3Bi_2I_9$ film surface. Bi^0 centers could provide recombination sites at the interface between the absorber and the other PV device layers or facilitate Fermi level pinning, thereby degrading device performance. In addition, the 2D layer structure of $Rb_3Bi_2I_9$ has lower electrical conductivity with deeper point defects relative to the 3D structured organohalide lead system inducing lower carrier mobility and increased non-radiative recombination for this system. Further investigation is needed to examine the origin of the poor photovoltaic performance of $Rb_3Bi_2I_9$-solar cells.

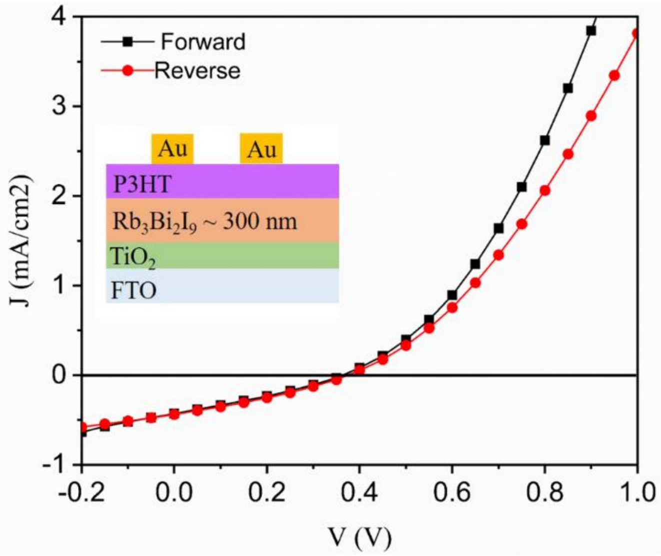

Figure 76. *J-V curves of $Rb_3Bi_2I_9$ solar cell. The inset shows the device structure employing a $Rb_3Bi_2I_9$ absorber layer and compact TiO_2/P3HT as electron/hole transport layers, respectively.*

Table 15. *Photovoltaice properties of FTO/TiO_2/$Rb_3Bi_2I_9$/P3HT/Au solar cell.*

Scan direction	**V_{OC} (V)**	**J_{SC} (mA/cm^2)**	**FF (%)**	**PCE (%)**
Forward	0.36	0.43	30.1	0.05
Reverse	0.37	0.44	30.8	0.05

4.4 Growth of Silver Bismuth Iodide

4.4.1 Crystal Structure of Silver Bismuth Iodide

Silver bismuth iodide with the general formula $Ag_xBi_yI_z$, where z = x + 3y, consists of the formally monovalent Ag^+ cation, trivalent Bi^{+3} cation and monovalent I^- anion, in which $[AgI_6]$ and $[BiI_6]$ octahedra share edges. The cationic sublattice of these compounds involves disorder due to the partial occupancy of a single position by silver, bismuth and vacancies, permitting the wide range of stoichiometries observed in literature. The edge-sharing octahedra arrange either in a rhombohedral $CdCl_2$ layer-type structure, in which every other ⟨111⟩ plane is occupied with Ag^+ or Bi^{+3}, or a closely-related 3D-network defect-spinel cubic structure with vacant tetrahedral sites (Figure 77). Formation of each of these structures in an Ag-Bi-I compound depends on several parameters including composition, annealing conditions and preparation methods. In the current study, effect of these various processing parameters on the final structure of Ag-Bi-I compound is examined using vacuum-deposited films.

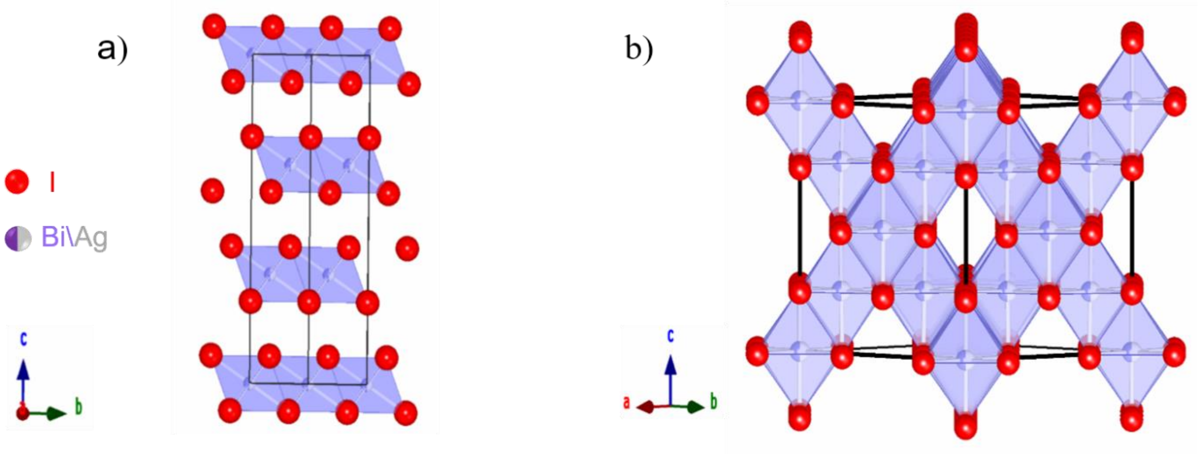

Figure 77. *Schematic illustrations of a) rhombohedral and b) cubic structures of silver bismuth iodide.*

4.4.2 Single Deposition Approach

In this approach, a thin film of AgI (300 nm) was deposited through evaporation using a Radak source followed by the post-deposition annealing under BiI_3 vapor in the glovebox. Several annealing temperatures and times ranging from 150-250 °C and 10-30 min were tested to achieve a smooth and pinhole-free film of Ag-Bi-I. The threshold temperature to evaporate BiI_3 is higher than 180 °C, therefore annealing of deposited AgI film at 150 °C did not yield formation of the Ag-Bi-I compound. In addition, increasing annealing temperatures above 200 °C has resulted in the formation of a yellowish film verifying removal of BiI_3 from the film and leaving behind the AgI on the film. As a result, the AgI film was annealed at 200 °C for 10 min under BiI_3 vapor followed by quenching of the film to room temperature. Phase purity and unit cell parameters of the annealed film were examined by collecting the XRD pattern of the film (Figure 78). The XRD pattern for the post-deposition annealed film matches to a rhombohedral unit cell ($R\bar{3}m$, no. 166) with lattice parameters $a = b = 4.3509(5)$ Å, $c = 20.8427(8)$ Å. Moreover, a trace of AgI was observed in the XRD pattern of the film verifying the existence of unreacted AgI with BiI_3 on the film.

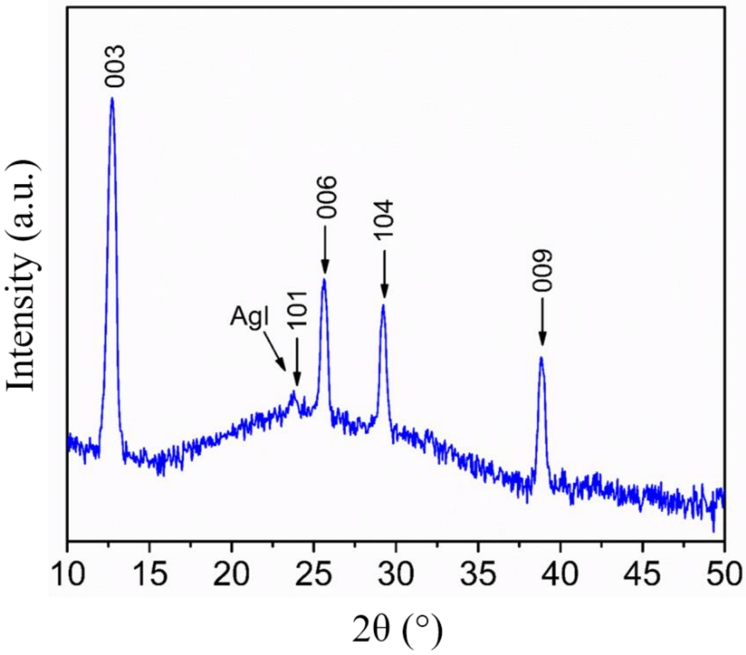

Figure 78*. Collected XRD pattern of the post-annealed AgI film in BiI_3 vapor at 200 °C for 10 min. Selected strong diffraction peaks are labeled.*

The digital photograph of the post-deposition annealed film (inset image in Figure 79) demonstrates a non-uniform morphology consisting of yellowish and brownish regions, which originate from AgI and Ag-Bi-I on the film, respectively. Furthermore, the microscopic film structure was investigated using secondary electron SEM imaging (Figure 79). As can be seen, there is a high density of pinholes on the surface of the film. Close up views of two regions marked with red circles in Figure 79 are shown in Figure 79I and II to compare the area with pinholes (yellowish-brownish region) with the area which is smooth (brownish region). The grain sizes in these two regions are in the range of 600-850 nm. An even longer annealing period (e.g. 20-30 min) does not cause formation of a uniform film of Ag-Bi-I using the single deposition approach.

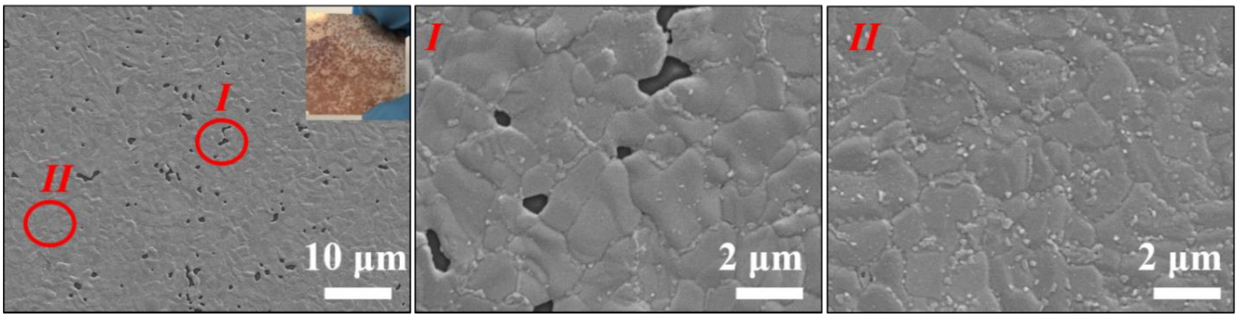

Figure 79. *Top-view SEM micrographs of post-deposition annealed thin film of AgI in* BiI_3 *vapor at 200 °C for 10 min. The inset image depicts the annealed film.*

4.4.3 Two-step Coevaporation Approach

Since a compact and homogeneous film of silver bismuth iodide has not formed using single deposition approach, the two-step coevaporation method was tested to grow single phase and pinhole-free silver bismuth iodide films. Thin films of silver bismuth iodide (thickness = 450 nm) were coevaporated in the thermal evaporator. The two Radak sources were filled with BiI_3 and AgI powders. To examine possible changes in the stoichiometry of the final films, various deposition rate ratios ($r = AgI/BiI_3$) for the two precursors – i.e. $r = 0.2$, 0.6, 0.8, and 1.2– were tested. There is the expectation that changes in “r” will correlate with changes in the resulting film composition.

Post-deposition annealing of the films was performed inside a nitrogen-filled glovebox. For this purpose, an as-deposited film was placed under a quartz cover in preheated BiI_3 vapor followed by quenching of the film to room temperature ($r = 0.6$, 0.8, 1.2). In addition, the as-deposited Bi-rich films (e.g. $r = 0.2$ and 0.6) were annealed at 180 °C for 20 min under N_2 without an excess of BiI_3 vapor. Annealing temperatures and times ranged over 150–200 °C and 10–30 min, respectively, for achieving single-phase and pinhole-free polycrystalline films. After testing various annealing conditions for the deposited films with different rate ratios, post-deposition annealing at 180 °C for 20 min under excess BiI_3 vapor was determined to be the optimal condition to achieve smooth and compact films with large grain sizes. Increasing the annealing temperature above 200 °C results in the evaporation of the volatile BiI_3 and remaining yellow AgI on the substrate. Phase purity and unit cell parameters of the grown films in the present study were examined by XRD and average compositions were characterized using SEM/EDX, as a function of component metal halide mixing ratio during co-evaporation.

4.4.4 Structural and Morphological Properties of Silver Bismuth Iodide

XRD patterns of the as-deposited and annealed thin films of Ag-Bi-I deposited with $r = 0.2$ were collected and shown in Figure 80a and b, respectively. The obtained XRD pattern for the as-deposited film of $r = 0.2$ matches a rhombohedral unit cell ($R\bar{3}m$, no. 166) with lattice parameters $a = b =$ 4.3502(3) Å, c = 20.693(2) Å (Figure 80a). Fitting the experimental XRD pattern for the annealed film of $r = 0.2$ (180 °C, 20 min under N_2) yields a double-phase rhombohedral unit cell ($R\bar{3}m$, no. 166) with $a = b$ = 4.3583(2) Å, c = 20.667(1) Å and a cubic phase ($Fd\bar{3}m$, no.227) with $a = b = c$ = 12.1944(4) Å (Figure 80b). BiI_3 impurity peaks are also observed for both as-deposited and annealed films, likely originating from the large amounts of BiI_3 applied during the coevaporation process.

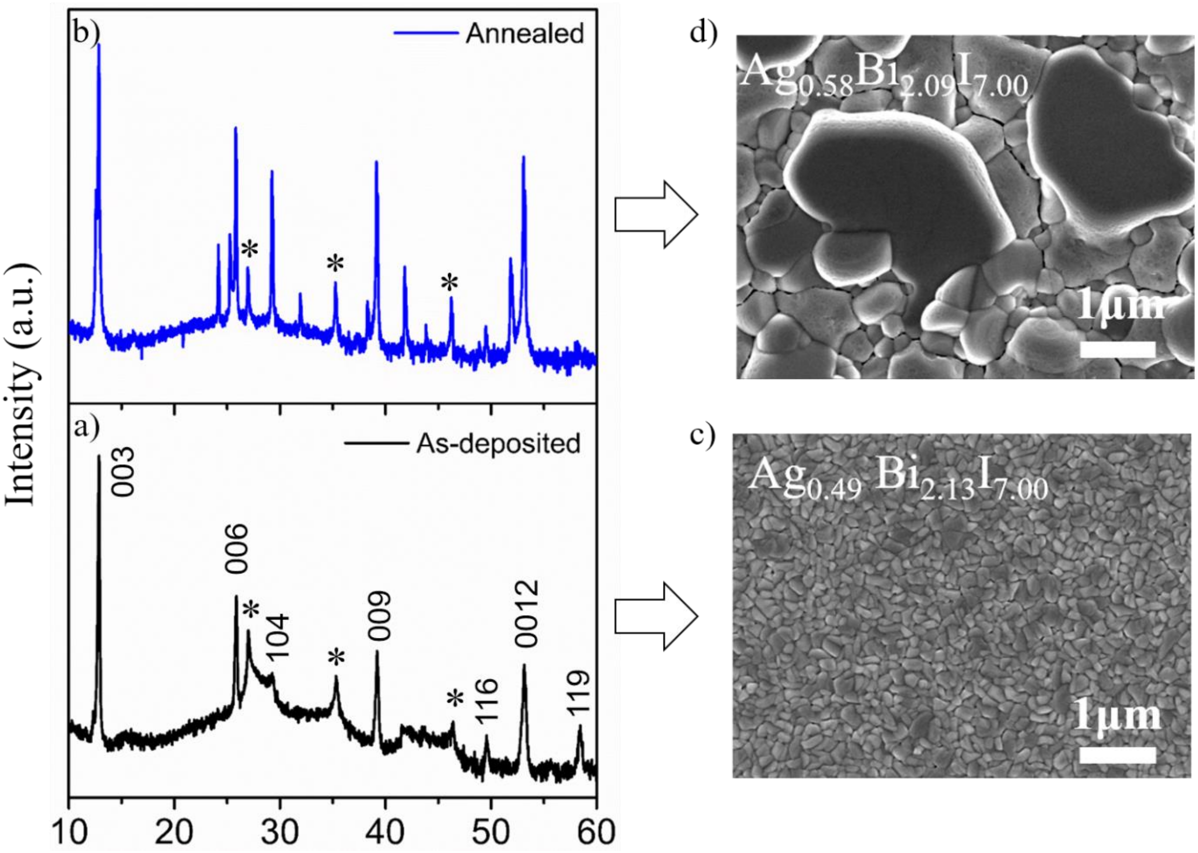

__Figure 80.__ Experimental XRD patterns for a) as-deposited (black) and b) annealed (blue) (180 °C for 20 min under N_2) thin films of Ag-Bi-I grown with $r = 0.2$. BiI_3 impurity peaks are marked with "". SEM images of c) the as-deposited and d) annealed thin films of Ag-Bi-I ($r = 0.2$) with the noted compositions.*

The microscopic film structures were investigated using secondary electron SEM imaging. Figure 80c and d show the surface morphology and associated composition of the as-deposited and post-annealed co-evaporated films with $r = 0.2$. Evidently, the as-deposited film consists of very small grains with average size of 100 nm. Upon annealing, significant grain growth occurs, leading to grains as wide as 3 μm with negligible pinhole densities. As can be seen in Figure 80d, two types of grains grow in the annealed film of $r = 0.2$, indicating (in accordance with the XRD results) the coexistence of cubic and rhombohedral phases in the film. SEM/EDX measurements verify high average Bi content, yielding $Ag_{0.49}Bi_{2.13}I_{7.00}$ and $Ag_{0.58}Bi_{2.09}I_{7.00}$ for the as-deposited and annealed films, respectively. Given the mixed phase nature of the $r = 0.2$ films, they are not further considered in this study.

Furthermore, the XRD pattern for the $r = 0.6$ as-deposited film indexes to a rhombohedral unit cell with lattice parameters $a = b = 4.3546(1)$ Å, $c = 20.7430(3)$ Å in the $R\bar{3}m$ space group (Figure 81a). A crystallographic phase transition from the rhombohedral to the cubic structure occurs upon post-deposition annealing of the as-deposited film. This phase transition occurs regardless of whether the film is annealed under BiI_3 vapor (Figure 81b) or only under N_2 (Figure 81c). The XRD pattern of the annealed film under N_2 yields a cubic structure ($Fd\bar{3}m$) with lattice parameters $a = b = c = 12.2079(2)$ Å, with lattice difference noted compared to films annealed under excess of BiI_3 vapor ($a = b = c = 12.2043(3)$ Å) and with previously published reports for the similar film compositions prepared via solution-processing.[70-71]

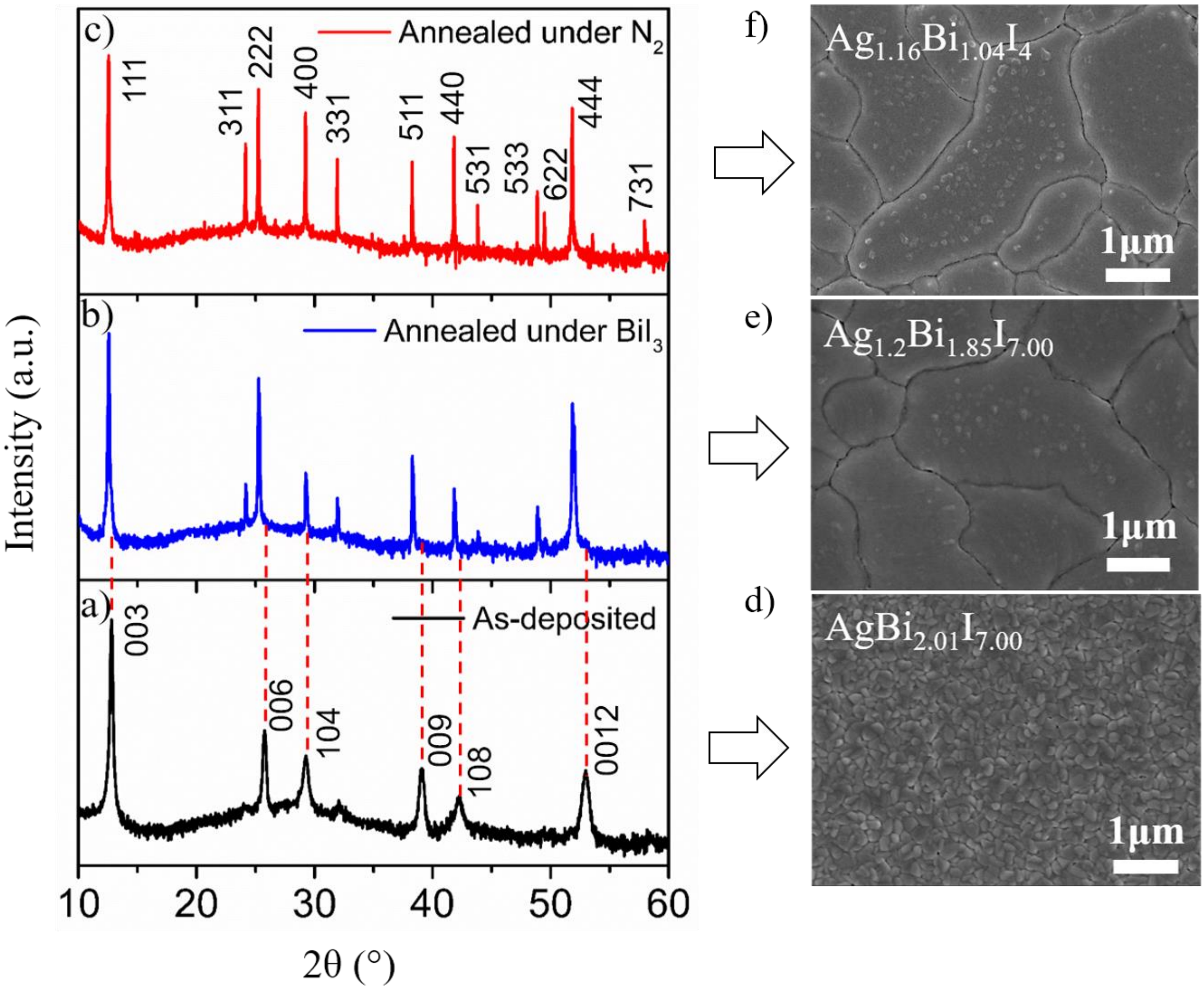

Figure 81. *Experimental XRD patterns for a) as-deposited (black), b) annealed under BiI_3 (blue), and c) annealed under N_2 (red) films of Ag-Bi-I grown with $r = 0.6$. Thin films were annealed at 180 °C for 20 min. SEM images of d) the as-deposited and annealed e) under BiI_3 or f) under N_2 films of Ag-Bi-I ($r = 0.6$).*

Similar to as-deposited Ag-Bi-I with r = 0.2, the as-deposited film of r = 0.6 consists of tiny grains (< 100 nm) (Figure 81d), while the post-deposition annealing of the as-deposited films leads to a significant grain growth and formation of grains as wide as > 3 μm (Figure 81e and f). The SEM/EDX compositional analysis for the r = 0.6 as-deposited, annealed under BiI_3 vapor, and annealed in N_2 films have average compositions of $AgBi_{2.01}I_{7.00}$, $Ag_{1.2}Bi_{1.85}I_{7.00}$, and $Ag_{1.16}Bi_{1.04}I_{4.00}$ (the first two within experimental uncertainty of $AgBi_2I_7$ and the last within experimental uncertainty of $AgBiI_4$), respectively. Considering the error margins for SEM/EDX analysis, these results indicate that annealing in the absence of excess BiI_3 vapor results in the removal of volatile BiI_3 from the film, while maintaining the cubic structure. The average composition of the annealed film under BiI_3 vapor slightly changes from $AgBi_{2.01}I_{7.00}$ to $Ag_{1.2}Bi_{1.85}I_{7.00}$ due to the loss of volatile BiI_3 during the post-annealing process, which may account for the phase transition from rhombohedral to cubic structure. Clearly, a change in the film composition (e.g. $AgBi_2I_7$ to $Ag_{1.2}Bi_{1.85}I_{7.00}$ or $AgBiI_4$) upon annealing represents a crucial factor affecting the crystal structure of silver bismuth iodide

As-deposited and post-deposition annealed (180 °C for 20 min under BiI_3 vapor) Ag-rich r = 0.8 films of silver bismuth iodide form in the rhombohedral crystal structure (Figure 82a and b), with the lattice parameters $a = b$ = 4.34789(4) Å, c = 20.8789(2) Å for the as-deposited film and $a = b$ = 4.3481(1) Å, c = 20.8308(8) Å for the annealed film under BiI_3 vapor. A small trace of AgI impurity was observed for the as-deposited film (Figure 82a), which disappeared after post-deposition annealing under BiI_3 vapor, verifying formation of final Ag-Bi-I phase via annealing. Note that the estimated lattice parameters for the r = 0.8 annealed film for vacuum-deposited films are consistent with the reported solution-processed Ag_2BiI_5.[126]

Clearly, further increase in the evaporation rate ratio to 0.8 results in formation of significantly smaller grains in the annealed film (Figure 82d) than the post-deposition annealed BiI_3-rich films deposited with r = 0.2 (Figure 80d) and r = 0.6 (Figure 81e). SEM/EDX measurements show that the as-deposited and annealed films of r = 0.8 have average compositions of $Ag_{1.62}Bi_{1.05}I_5$ (Figure 82c) and $Ag_{1.85}Bi_{1.03}I_5$ (Figure 82d), respectively, corresponding to (perhaps Ag-poor) Ag_2BiI_5.

Further increase in deposition rate ratio to r = 1.2 results in films with AgI impurity peaks in the XRD patterns for both as-deposited and annealed films marked with "+" in Figure 83a and b. The resulting cells have rhombohedral structure with $a = b$ = 4.3470(2) Å, c = 20.8617(9) for the as-deposited film and $a = b$ = 4.3510(2) Å, c = 20.859(1) Å for the annealed film at 180 °C for 20 min under BiI_3 vapor.

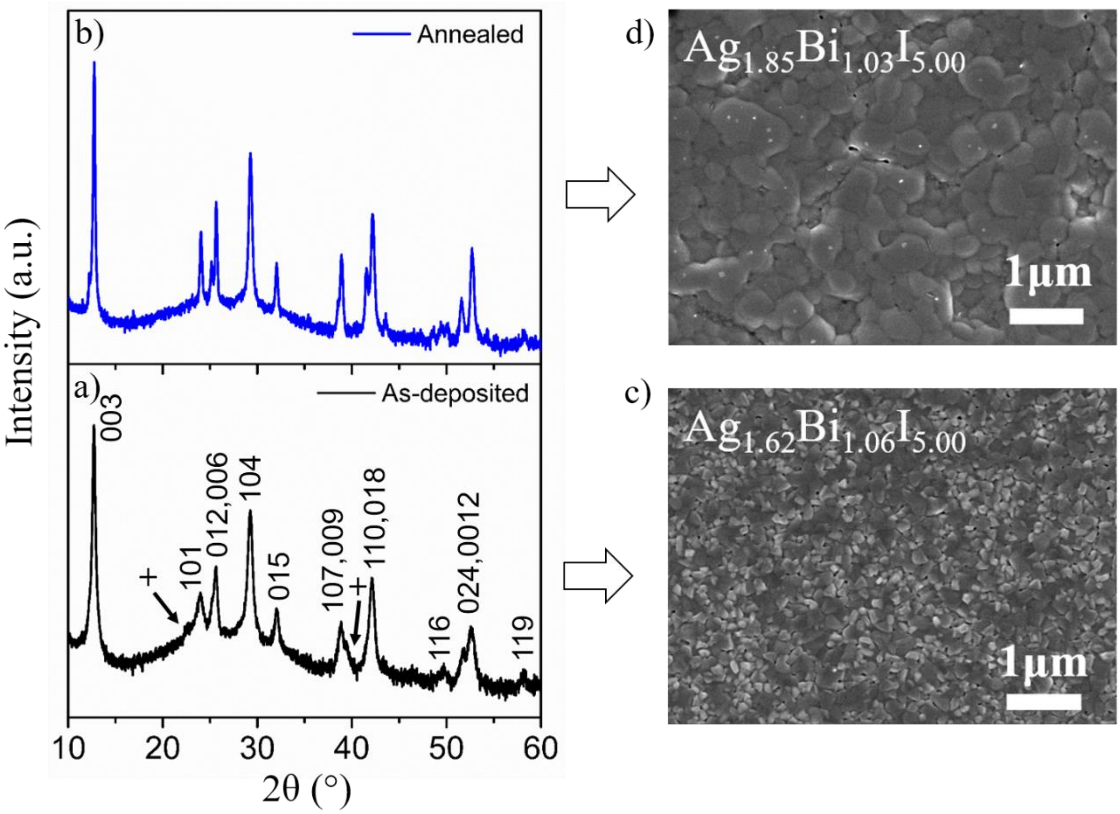

Figure 82. *Experimental XRD patterns for a) as-deposited (black) and b) annealed (blue) (at 180 °C for 20 min under* BiI_3*) thin films of grown Ag-Bi-I (r = 0.8) with associated SEM images shown in c) and d), respectively. The small peaks marked with "+" in the XRD pattern of the as-deposited film originate from AgI impurity.*

Figure 83c and d demonstrate the surface morphology and associated composition of as-deposited and post-deposition annealed films of Ag-Bi-I grown with $r = 1.2$ obtained using secondary electron SEM and SEM/EDX. It can be seen that these films consist of tiny grains (< 100 nm) with high pinhole densities marked by the white arrows in Figure 83c and d. SEM/EDX measurements show that the as-deposited and annealed films of $r = 1.2$ have average compositions of $Ag_{1.96}Bi_{0.95}I_5$ and $Ag_{1.91}Bi_{0.97}I_5$, respectively, consistent with the Ag_2BiI_5 composition.

From the obtained morphologies of these films, it is clear that Bi-rich films are susceptible to form large grains via annealing, regardless of whether the film is annealed under BiI_3 vapor ($r = 0.6$) or only under N_2 ($r = 0.2, 0.6$). SEM/EDX compositional analysis of the grown films in combination with SEM morphological characterization verify that sequential increase in the amount of AgI compared to BiI_3 during the co-evaporation process yields the formation of Ag-rich Ag_2BiI_5 compound promoting the growth of tiny grains via post-deposition annealing under BiI_3 vapor.

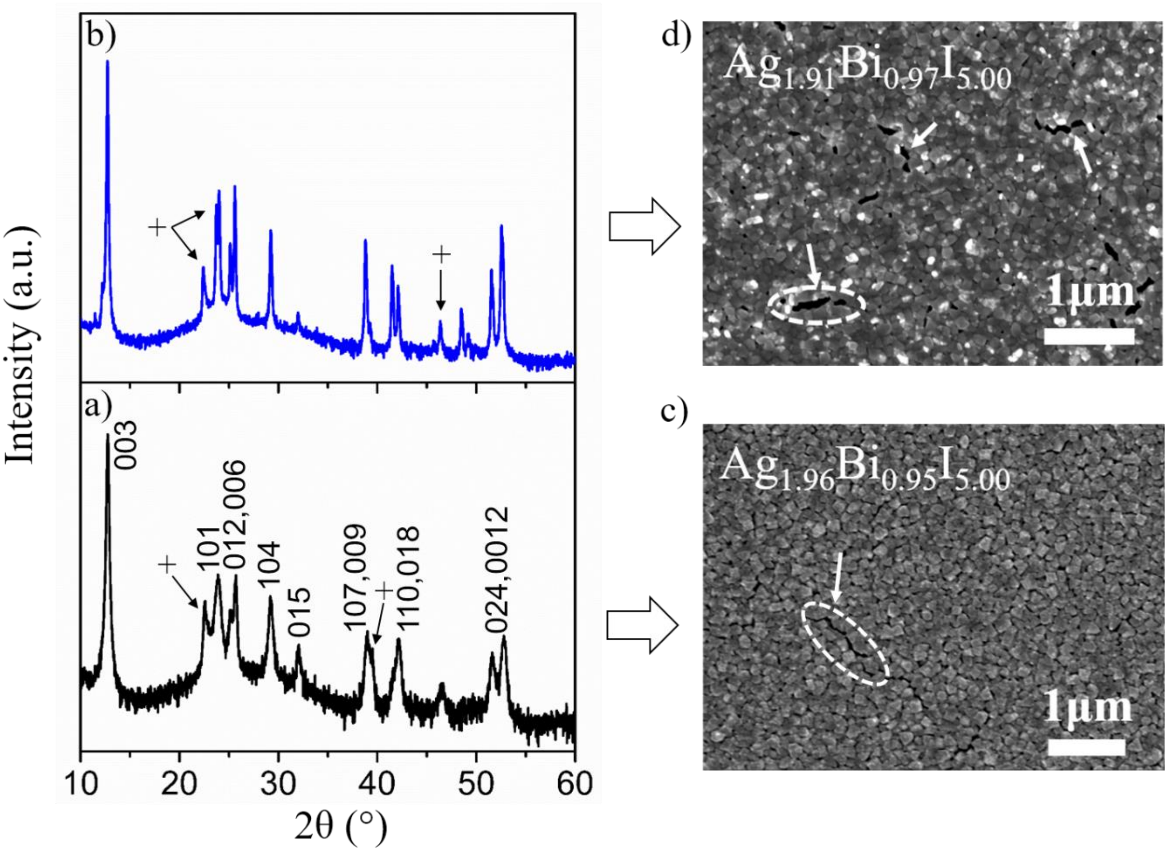

Figure 83. *XRD patterns of a) as-deposited and c) post-deposition annealed (180 °C for 20 min under* BiI_3*) thin films of Ag-Bi-I grown with r = 1.2. SEM images of the corresponding films with associated compositions are shown in c) and d), respectively. The labeled peaks with "+" originate from AgI impurity.*

The Pawley-refined unit cell parameters for the Ag-Bi-I films with different compositions are summarized in Table 16 along with the corresponding composition of each film obtained from SEM/EDX. Evidently, the gradual increase of the AgI content in the coevaporated Ag-Bi-I films (from $r = 0.2$ to $r = 1.2$) results in the enlargement of the c lattice constant of the corresponding cells, yielding unit cells with expanded volumes for both rhombohedral and cubic cells. This enlargement of the unit cells originates from the larger ionic radius of Ag^+ (115 pm) relative to that of Bi^{3+} (103 pm). Existence of vacancies in the crystal structure of Ag-Bi-I permits the wide range of stoichiometries and unit cell size-tunability within the Ag-Bi-I crystals.

Table 16. *Crystallographic parameters and corresponding compositions of as-deposited and post-deposition annealed films of Ag-Bi-I achieved by Pawley refinement and SEM/EDX, respectively.*

Ag-Bi-I Film	Composition (SEM/EDX)	Crystal System/space group	Unit Cell Parameters (Å)	Volume (Å^3)	Impurity	Fitting Parameters
0.2: As-deposited	$Ag_{0.49}$ $Bi_{2.13}I_{7.00}$	Rhombohedral/$R\bar{3}m$	$a = b =$ 4.3502(3); c = 20.693(2)	339.14	BiI_3	Rp = 6.84 % wRp = 8.54 % GOF = 1.03
0.2: Annealed under N_2	$Ag_{0.58}Bi_{2.09}I_{7.00}$	Rhombohedral / $R\bar{3}m$	$a = b =$ 4.3583(2); c = 20.667(1)	339.96	BiI_3	Rp = 7.82 % wRp =9.81 % GOF = 1.28
		Cubic/ $Fd\bar{3}m$	$a = b = c =$ 12.1944(4)	1813.35		
0.6: As-deposited	$AgBi_{2.00}I_{7.00}$	Rhombohedral/ $R\bar{3}m$	$a = b =$ 4.3546(1); c = 20.7430(3)	340.64		Rp = 6.84 % wRp = 8.94 % GOF = 1.35
0.6: Annealed under BiI_3	$Ag_{1.2}Bi_{1.85}I_{7.00}$	Cubic/ $Fd\bar{3}m$	$a = b = c =$ 12.2043(3)	1817.75		Rp = 7.97 % wRp =10.31 % GOF = 1.1
0.6: Annealed under N_2	$Ag_{1.16}Bi_{1.04}I_{4.00}$	Cubic/ $Fd\bar{3}m$	$a = b = c =$ 12.2079(2)	1819.39		Rp = 5.41 % wRp = 8.05 % GOF = 1.6
0.8: As-deposited	$Ag_{1.62}Bi_{1.06}I_{5.00}$	Rhombohedral/ $R\bar{3}m$	$a = b =$ 4.3479(1); c = 20.8789(2)	341.82	AgI	Rp = 4.25 % wRp = 5.43 % GOF= 1.1
0.8: Annealed under BiI_3	$Ag_{1.85}Bi_{1.03}I_{5.00}$	Rhombohedral/ $R\bar{3}m$	a =b = 4.3481(1); c = 20.8308(8)	341.06		Rp = 4.77 % wRp = 6.43 % GOF = 1.32
1.2: As-deposited	$Ag_{1.96}Bi_{0.95}I_{5.00}$	Rhombohedral/ $R\bar{3}m$	$a = b =$ 4.3470(2); c = 20.8617(9)	341.40	AgI	Rp = 5.32 % wRp = 6.95 % GOF = 1.45
1.2: Annealed under BiI_3	$Ag_{1.91}Bi_{0.97}I_{5.00}$	Rhombohedral/ $R\bar{3}m$	$a = b =$ 4.3510(2); c = 20.859(1)	341.98	AgI	Rp = 6.12 % wRp = 8.24 % GOF = 1.15

[§] *GoF: Goodness of Fit*

4.4.5 Mechanism of Crystallographic Phase Transition

TD-XRD measurements were carried out to gain insight into the observed rhombohedral to cubic phase transition mechanism. Figure 84 displays the contour plots of the collected XRD patterns from silver bismuth iodide films deposited with a) r = 0.6 and c) r = 0.8 in the 2θ range from 10°–28°, throughout the annealing and cooling processes under N_2 atmosphere. The temperature profile shown in Figure 84b has three stages: 1) heating from 25 °C to 180 °C with a 50 °C/min ramp rate; 2) hold at 180 °C for 1 hour; 3) cooling to 25 °C with a –10 °C/min ramp rate. In both Figure 84a and c, two regions identified by red and yellow dashed squares were zoomed in and shown in Figure 84d 1-2, and Figure 84e 3-4, respectively, to facilitate the observation of XRD characteristic peaks in these regions.

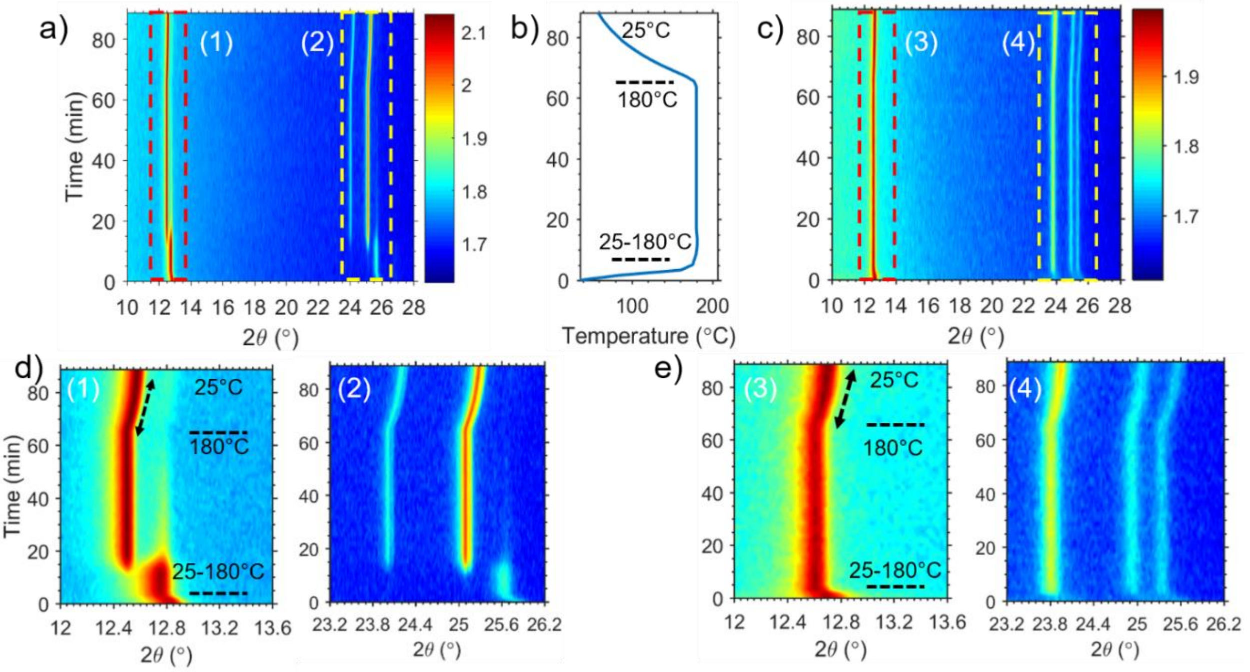

__Figure 84.__ Evolution of XRD patterns for Ag-Bi-I thin films deposited with a) 0.6 and c) 0.8 rate ratios, during the thermal annealing temperature vs. time profile shown in (b); in a nitrogen atmosphere, the temperature was raised from 25 to 180 °C using a 50 °C/min ramp rate, then held at 180 °C for 1 h, and finally cooled to 25 °C using a –10 °C/min ramp rate. d)1, 2 and e) 3,4 show the zoomed areas identified by red and yellow dashed squares in a) and c).

For the as-deposited film with r = 0.6, when the temperature was raised from 25 °C to 180 °C, the peaks at 12.84° and 25.82° assigned to the 003 and 006 reflections of rhombohedral silver bismuth iodide, shift to 12.76° and 25.66°, respectively, due to the thermal expansion of the unit cell (Figure 84d). During the dwell time at 180 °C, the diffraction peaks at 12.76°and 25.66° are substantially attenuated, and three other dominant peaks form at 12.5°, 24°, and 25.08° assigned to the 111, 311 and 222 reflections of a cubic silver bismuth iodide, indicating the phase transition from the rhombohedral to the cubic structure. The observed shift of the lattice constant from 180 °C to 25 °C originates from thermal contraction of the unit cell. The cubic phase remains stable, even upon cooling to room temperature (25 °C). Long-term N_2 stability of the cubic phase was monitored via collecting XRD patterns of the thin film for a period of 6 months. Figure 85 shows no significant difference in the XRD patterns collected in the 6-month period, indicating high stability of cubic silver bismuth iodide in a nitrogen environment at room temperature.[81]

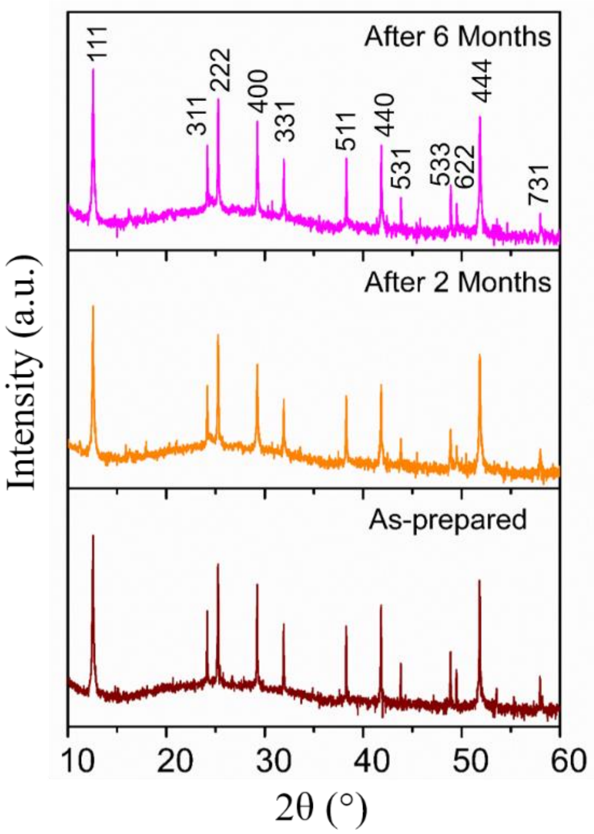

Figure 85. *Monitoring N_2 stability of the annealed Ag-Bi-I film (r = 0.6) without an excess of BiI_3 using XRD.*

For the as-deposited film with *r* = 0.8, at 25 °C four dominant diffraction peaks were observed at 12.68°, 23.97°, 25.06°, and 25.55°, characteristic of the rhombohedral crystal structure (Figure 84c). Appearance of two extra rhombohedral diffraction peaks for *r* = 0.8 compared to the as-deposited *r* = 0.6 indicates a higher favorability of randomly-oriented grains for the Ag-rich rhombohedral phase. No phase transition appears during annealing of the thin film, confirming the stability of the rhombohedral phase for deposited silver bismuth iodide films with *r* = 0.8 (AgI/BiI_3). The observed shifts via heating (25-180 °C) and cooling (180-25 °C) processes originate from thermal expansion and contraction of the unit cell, respectively. Owing to the overlap of the diffraction peaks detected from the as-deposited silver bismuth iodide film (*r* = 0.8) at 25 °C and the annealed film after the cooling process (from 180 to 25 °C) (Figure 86), it can be concluded that the size of the unit cell does not significantly change during annealing, confirming the stability of the stoichiometry of the treated film during TD XRD.[81]

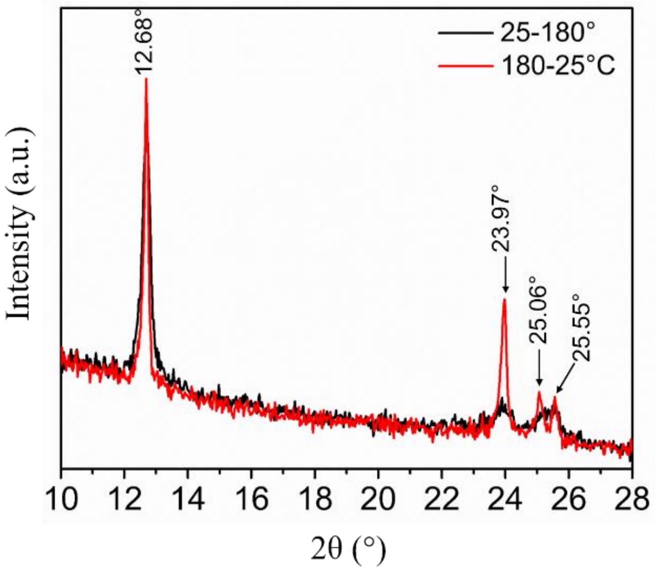

Figure 86. *Experimental XRD patterns of as-deposited thin film of Ag-Bi-I (black) with r = 0.8 at 25 °C and the annealed film during TD XRD (red) after cooling process reaching 25 °C. Diffraction peaks at 12.68°, 23.97°, 25.06°, and 25.55° are assigned to 003, 101, 012, and 006 of rhombohedral Ag-Bi-I.*

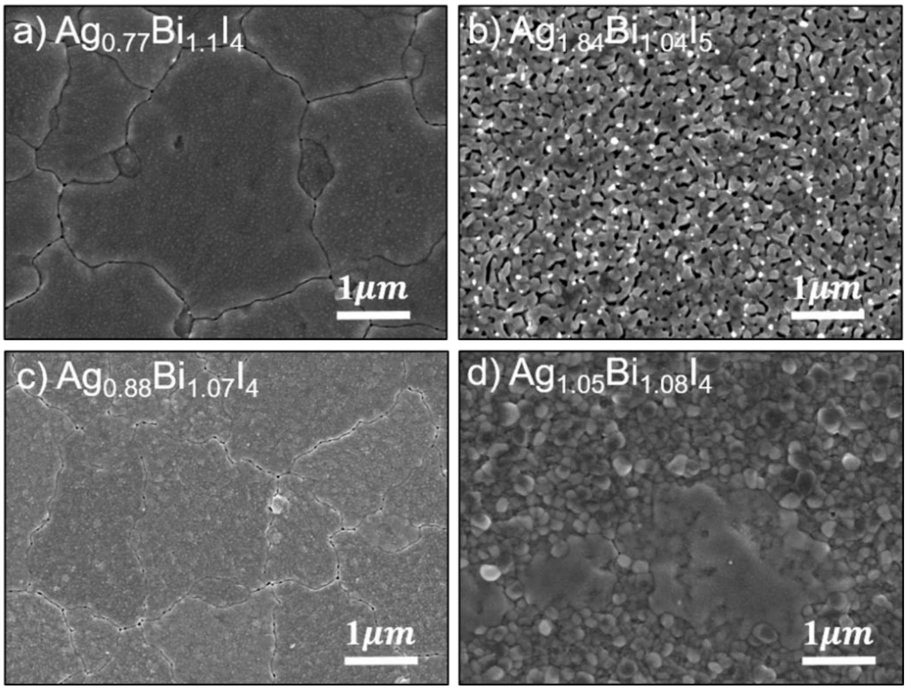

Figure 87. *SEM images of the annealed films during TD XRD with the associated compositions obtained from SEM/EDX; a) annealed film of r = 0.6 in* N_2 *(25°-180 °C, 180 °C for 1h and cooled to 25 °C); b) annealed film of r = 0.8 in* N_2 *(25°-180 °C, 180 °C for 1h and cooled to 25 °C); c) annealed film of r = 0.6 in air (25°-100 °C, 100-180 °C, 180 °C for 15min and cooled to 25 °C); d) annealed film of r = 0.6 in* N_2 *(25°-180 °C, 180 °C for 1h and cooled to 25 °C).*

Based on our previous results, the as-deposited Ag-Bi-I films with $r = 0.6$ (Figure 81d) and 0.8 (Figure 82c) consist of small grains (average size of < 100 nm). Figure 87a and b display the surface morphology of the treated films ($r = 0.6$ and 0.8) using TD XRD, respectively. Owing to the annealing process during TD XRD, the small grains in the as-deposited film of $r = 0.6$ significantly grow forming large grains with average size of 3 μm (Figure 87a). However, the Ag-rich film of $r = 0.8$ (Figure 87b) forms smaller grains in comparison with the treated film of $r = 0.6$ verifying the susceptibility of the Bi-rich film to form larger grains via annealing than the Ag-rich silver bismuth iodide film.

The as-deposited and annealed films of $r = 0.6$ exhibit average compositions (as determined by SEM/EDX) of $AgBi_{2.01}I_{7.00}$ and $Ag_{0.77}Bi_{1.10}I_{4.00}$, respectively, confirming removal of BiI_3 from the film during the annealing cycle. This observation is consistent with earlier-described results for the annealed film without excess of BiI_3. SEM/EDX compositional analysis of the Ag-rich film ($r = 0.8$) verifies that the obtained composition for the as-deposited film of $r = 0.8$ ($Ag_{1.62}Bi_{1.06}I_{5.00}$) remains largely unchanged (within the error of the EDX compositional analysis) for the annealed film ($Ag_{1.84}Bi_{1.05}I_{5.00}$) (Figure 87b), presumably because these films already are Bi-poor relative to the films deposited at $r = 0.6$ (which do exhibit a structural change with annealing).

4.4.6 Effect of Environment on the Phase Transition

A further TD-XRD study was carried out to determine the role of the annealing environment on the mechanism of the observed phase transition and the corresponding critical temperature at which the phase transition occurs. For this purpose, two as-deposited films of Ag-Bi-I with $r = 0.6$ were separately treated throughout the annealing and cooling processes under air and nitrogen (N_2 flow rate of 20 ml/min) atmospheres. Figure 88a and c display the contour plots of the collected XRD patterns from these films in the 2θ range from 10°–28°, under air (Figure 88a) and N_2 (Figure 88c) atmospheres. The temperature profile shown in Figure 88b has four stages: 1) heating from 25 °C to 100 °C with a 15 °C/min ramp rate; 2) further heating from 100 °C to 180 °C with a 4 °C/min ramp rate; 3) hold at 180 °C for 15 min; 4) cooling to 25 °C with a –10 °C/min ramp rate. Figure 88d 1–2 and Figure 88e 3–4 show the close-up of the two regions identified by red and yellow dashed squares in Figure 88a and Figure 88c, respectively.

For both of the films treated in air and N_2, the annealing (25–100–180 °C) and cooling (180–25 °C) processes cause the thermal expansion and contraction of the unit cells, respectively. Figure 88d 1-2 show that the as-deposited film of $r = 0.6$ at 25 °C contains two rhombohedral characteristic diffraction peaks at 12.84° and 25.82°. As in the previous study, the peaks belonging to the rhombohedral ($R\bar{3}m$) phase shift to lower angle during the heating phase as a result of thermal expansion. It is clear that no phase transition occurs at temperatures below 180 °C. During the dwell time at 180 °C, the two rhombohedral diffraction peaks (12.75° and 25.63°) are significantly attenuated, and three diffraction peaks from cubic silver bismuth iodide form at 12.5°, 24°, and 25.08° corresponding to the cubic 111, 311 and 222 reflections. Although a weak rhombohedral diffraction peak at 12.83° (at 25 °C) remains stable even upon cooling, the cubic phase is the dominant phase in the treated film in air.

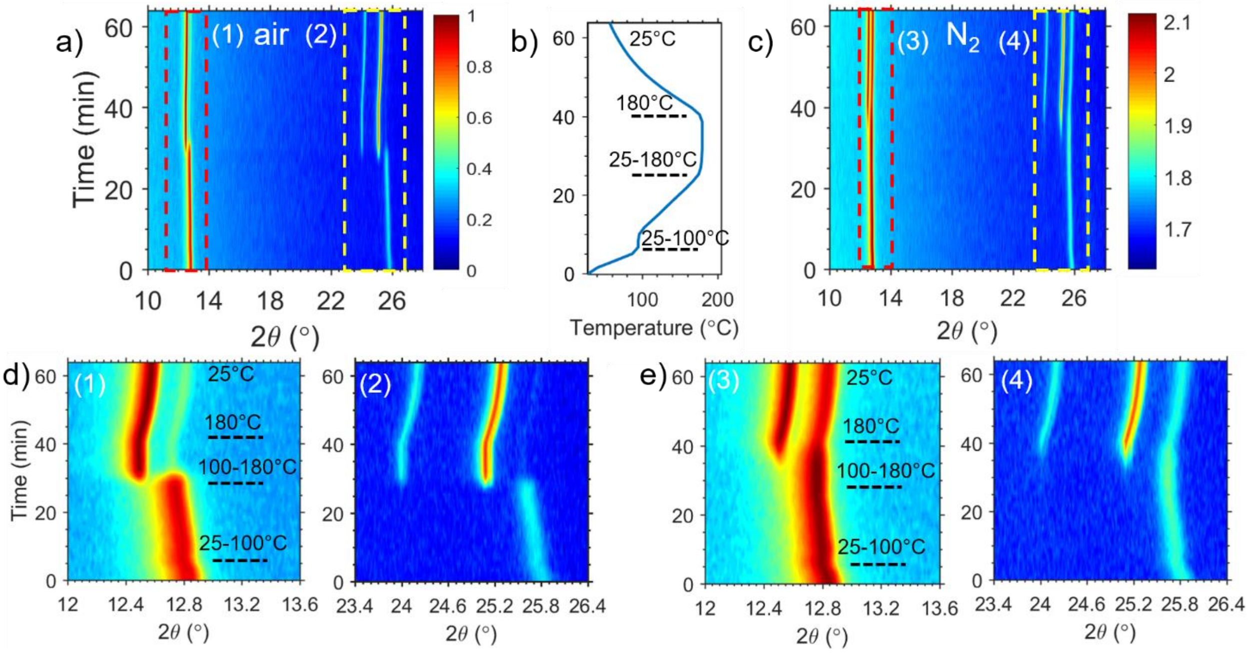

Figure 88. Evolution of XRD patterns for silver bismuth iodide thin films deposited with r = 0.6 in a) air and in c) N$_2$, during the thermal annealing temperature vs. time profile shown in (b);the temperature was raised from 25 to 100 °C using a 15 °C/min ramp rate followed by raising from 100 °C to 180 °C using a 4 °C/min ramp rate, then held at 180 °C for 15 min, and finally cooled down to 25 °C using a –10 °C/min ramp rate. d) 1, 2 and e) 3,4 show the zoomed areas identified by red and yellow dashed squares in a) and c).

Comparing TD-XRD results of the annealed film in air to analogous results in nitrogen (Figure 88e 3-4) reveals that the mechanism of the phase transition is slower for the annealed film in N$_2$ and, during the dwell time at 180 °C, the rhombohedral phase is still the dominant phase in the film. However, during the cooling process, the cubic diffraction peak (12.58°) intensifies consistent with further loss of BiI$_3$ from the film and transition from rhombohedral AgBi$_2$I$_7$ to cubic AgBiI$_4$. Figure 88e 3-4 shows that the final phase of the annealed film in N$_2$ is a mixture of cubic and rhombohedral silver bismuth iodide with a significant contribution from the rhombohedral phase (diffraction peaks at 12.84° and 25.84°). The slower phase transition for the annealed film in N$_2$ might arise from a decrease in the entropy of the system due to the nitrogen flow during the process, while no air flow was introduced to the system during the TD XRD in air.

The average compositions of Ag$_{0.88}$Bi$_{1.07}$I$_{4.00}$ and Ag$_{1.05}$Bi$_{1.08}$I$_{4.00}$ (within the error of stoichiometry of AgBiI$_4$) are realized for the annealed films in air and N$_2$ (Figure 87c and d) using

SEM/EDX, respectively. Since the as-deposited film of r = 0.6 has the average composition of $AgBi_{2.00}I_{7.00}$ (Figure 81d), the observed compositions for the annealed films confirm the loss of volatile BiI_3 during the annealing process.

All as-deposited films form within a rhombohedral structure type. Increasing Ag-content of the as-deposited films from $AgBi_2I_7$ to Ag_2BiI_5 causes formation of rhombohedral unit cells with bigger c lattice constant. From the TD-XRD results, the probability of the crystallographic phase transition to the cubic phase upon heating for silver bismuth iodide films is higher for bismuth-rich as-deposited film compositions. The phase transition occurs via a change in the composition from either $AgBi_2I_7$ to $AgBiI_4$, for anneals without BiI_3 vapor, or when the Bi-rich silver bismuth iodide film ($AgBi_2I_7$) slightly loses BiI_3 (i.e. $Ag_{1.2}Bi_{1.85}I_{7.00}$) via annealing under BiI_3 vapor. In addition, the annealing environment affects the rate of the phase transition, with the transition accelerating in air as compared to N_2. On the other hand, the rhombohedral phase is the more favorable phase for the Ag-rich film composition (i.e. near Ag_2BiI_5) at room and elevated temperatures (i.e. 180 °C). Composition is therefore clearly a critical parameter affecting the crystalline phase transition in silver bismuth iodide crystals. Since all compositions, regardless of Ag:Bi ratio form in the rhombohedral form, it appears that temperature and/or thermal annealing also play a role in the stabilization of the cubic phase. The structural phase transition might therefore additionally follow from an increase in the entropy of the system at elevated temperature. Further studies are needed to fully decipher the detailed nature of the crystallographic phase transitions.

4.4.7 Optical Properties of Silver Bismuth Iodide

In order to determine the optical band gap of the Ag-Bi-I annealed films with different compositions, optical absorption spectra were collected (Figure 89). To extract the band gaps, Tauc plots were constructed with the assumption of a direct band gap (Figure 90a), leading to the values 1.8 eV, 1.83 eV, and 1.9 eV for $AgBiI_4$, $AgBi_2I_7$, and Ag_2BiI_5, respectively, which correspond well with the previously published values for the solution-based films of $AgBiI_4$, $AgBi_2I_7$, and Ag_2BiI_5.[69, 71, 133-134] The increase in direct band gap energy from $AgBi_2I_7$ to Ag_2BiI_5 may perhaps be rationalized by an increased incorporation of the wide-band-gap AgI into the film. Furthermore, the indirect optical band gaps of $AgBiI_4$, $AgBi_2I_7$, and Ag_2BiI_5 are measured to be 1.72 eV, 1.72 eV, and 1.82 eV (Figure 90b).

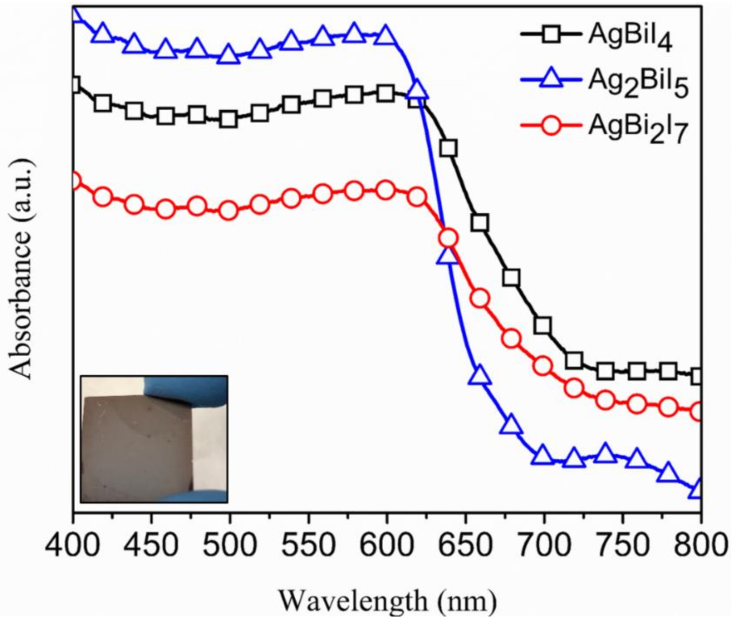

Figure 89. *Absorption spectra of* $AgBiI_4$, $AgBi_2I_7$ *and* Ag_2BiI_5 *films, deposited using the two-step coevaporation approach on glass substrates. The inset image shows the grown Ag-Bi-I film on a glass substrate.*

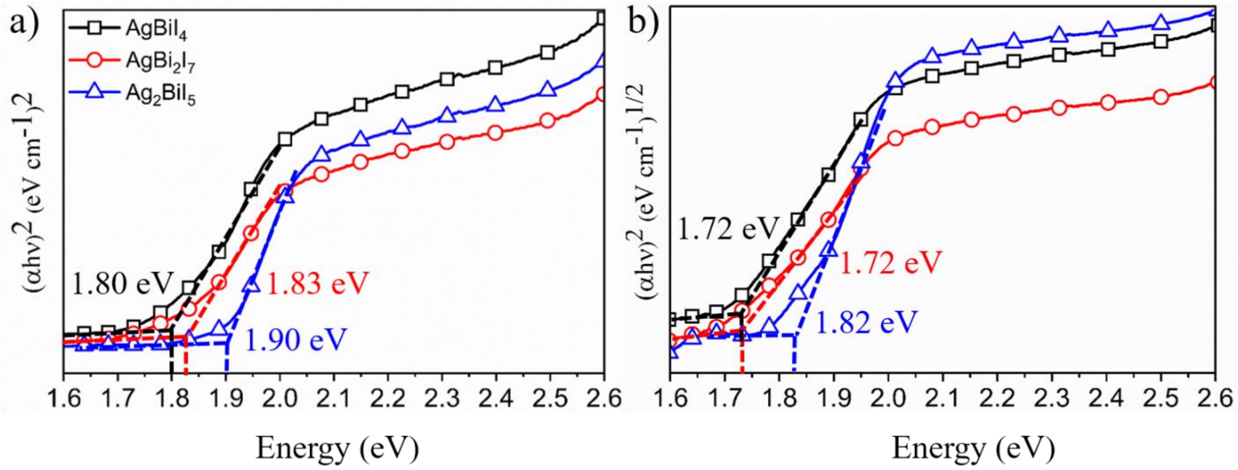

Figure 90*. Tauc plots of* $AgBiI_4$, $AgBi_2I_7$*, and* Ag_2BiI_5 *calculated from UV-Vis spectroscopy to determine a) direct and b) indirect band gaps of the grown films.*

4.4.8 Electronic Properties of Silver Bismuth Iodide

PES measurements were performed to investigate the electronic structure properties of the fabricated films of $AgBi_2I_7$, $AgBiI_4$, and Ag_2BiI_5 on ITO substrates. These measurements were conducted using as-loaded samples and after receiving sputtering treatments of different lengths (i.e., Ar ion source with an extractor voltage of 3 kV and a beam current of 5 µA, rastered over a 10 mm × 10 mm area). Surface sputtering was employed to test the effect of removing surface contaminants.

4.4.8.1 Electronic Properties of $AgBi_2I_7$

The post-annealed coevaporated film of Ag-Bi-I ($r = 0.6$; annealed at 180 °C for 20 min under BiI_3 vapor) with average composition of $AgBi_2I_7$ (determined using SEM/EDX) was prepared for PES measurements and analyzed as-loaded and after receiving 5 s and 10 s sputtering. Compositional characterization was accomplished for the as-loaded and sputtered films of silver bismuth iodide fabricated with $r = 0.6$ using XPS (Figure 91). Apart from presumably adventitious contributions of oxygen (530 eV) and carbon (285 eV), no other contaminants were detected for as-loaded and sputtered samples (Figure 91).

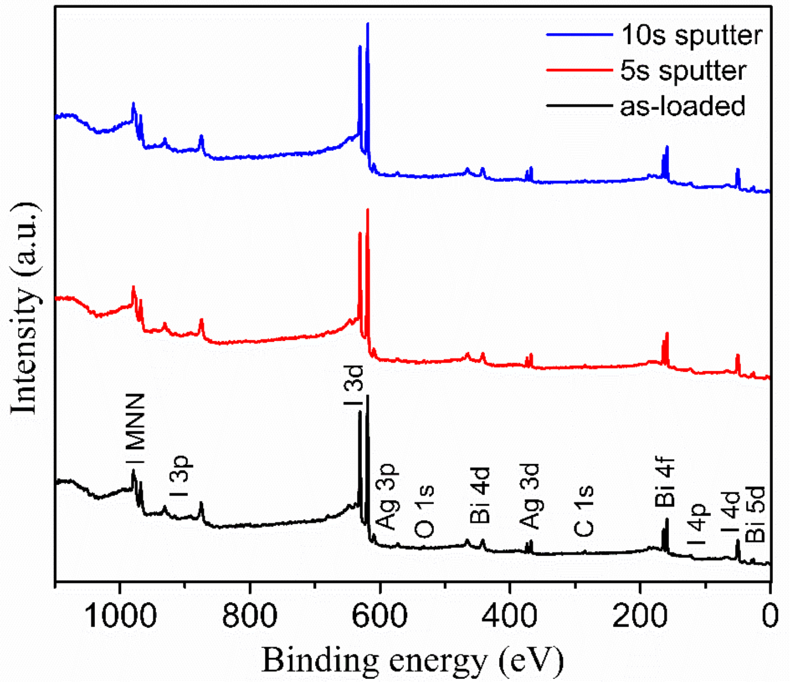

Figure 91. *XPS Al Kα survey scans of the as-loaded (black), 5 s (red), and 10 s (blue) sputtered film of* $AgBi_2I_7$*. Apart from oxygen and carbon impurities, there is no trace of other impurities.*

The XPS core peaks (Figure 92) show little change with sputtering, except for the Bi 4f spectra, which show a low binding energy shoulder emerging (Figure 92b) marked with "*". The lower binding energy is consistent with larger electron density on the Bi atoms. The observed trends in the XPS data for the fabricated films are consistent with the obtained compositions from EDX analysis (Table 17) confirming the consistency of the surface and bulk compositions. Surface sputtering for 10 s results in the evaporation of volatile BiI_3 from the film and the increase in the relative concentration of silver (Table 17).

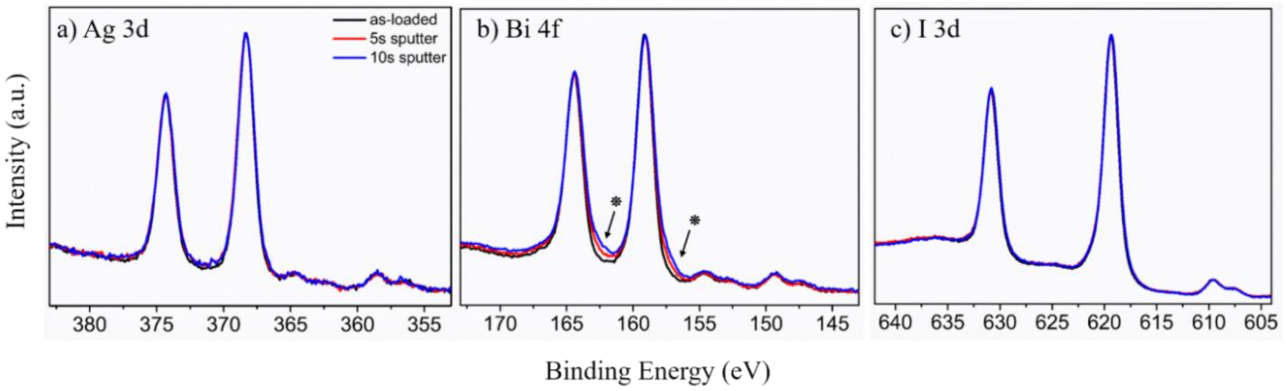

Figure 92. *Close-up Al Kα scans of a) Ag 3d, b) Bi 4f, and c) I 3d peaks for as-loaded (black), 5 s (red), and 10 s (blue) sputtered thin films of* $AgBi_2I_7$*. b) The emerging shoulders in the Bi 4f spectra due to sputtering are labeled with "*".*

Table 17. *Atomic ratios (%) derived from XPS for the annealed thin films of Ag-Bi-I (180 °C, 20 min under* BiI_3 *vapor) deposited with r = 0.6.*

Sample	Ag (± 2%)	Bi (± 1%)	I (±3%)	Composition
As-loaded	9	17	74	$AgBi_{1.88}I_{8.22}$
5 s sputter	9	17	74	$AgBi_{1.88}I_{8.22}$
10 s sputter	10	17	73	$AgBi_{1.7}I_{7.3}$

Figure 93a shows UPS spectra of the as-loaded, 5 s, and 10 s sputtered films of $AgBi_2I_7$. A reduction in the density of states in the 5 to 10 eV binding energy region with 5 s and 10 s sputtering verifies the reduction of O 2p states, which is consistent with removal of surface oxygen. The sputtering not only shifts the secondary electron onset to lower binding energy by ~ 0.3 eV (Figure 94a), consistent with removal of surface contaminants, but also a double onset feature emerges marked by "*" in Figure 94a, which indicates sputtering-induced surface inhomogeneity. The lower binding energy onset is indicative for the material of interest, with the small shoulder representing the damaged material.

In addition, UPS He I valence band edge and IPES spectra of conduction band states for these films are shown in Figure 93b. Intersection of tangent line fits to UPS He I valence band edge and IPES conduction band edge (Figure 94b) and the corresponding background indicate a shift of VBM and CBM to lower binding energies by ~ 100 meV via sputtering (Figure 94b). In addition, sputtering results in a shift of the Fermi level towards midgap. Figure 94c displays the determined band positions for the as-loaded and sputtered thin films of $AgBi_2I_7$ using UPS/IPES measurements. A summary of the measured key parameters from UPS and IPES is shown in Table 18. The PES study yields an ionization energy of 6.0 eV, with the VBM approximately 1.5 eV below the Fermi level, indicating an n-doped character for the as-loaded $AgBi_2I_7$ film. Furthermore, UPS analysis in combination with IPES yields a band gap of 1.7 eV for the $AgBi_2I_7$ film. Considering the error margins for IPES analysis, the calculated band gap of 1.7 eV is consistent with the measured optical band gap of 1.83 eV.

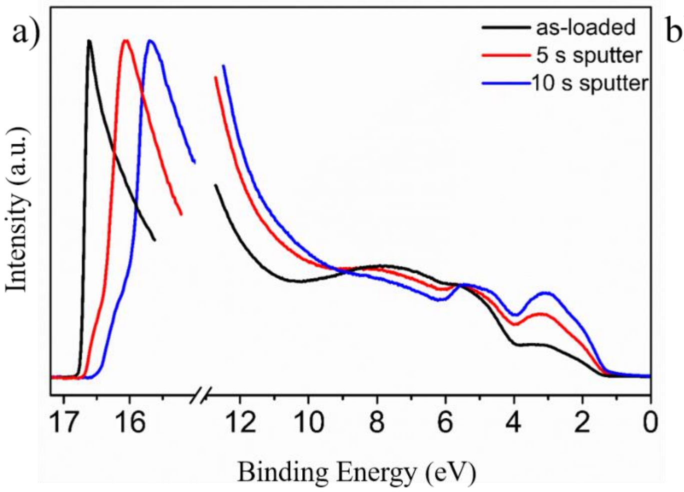

Figure 93. *a) Combined UPS He I secondary electron onset and scan of valence band states spectra and b) combined UPS He I valence band edge and IPES spectra of conduction band states for as-loaded (black),5 s (red), and 10 s (blue) sputtered post-deposition annealed Ag-Bi-I film fabricated with r = 0.6 ($AgBi_2I_7$).*

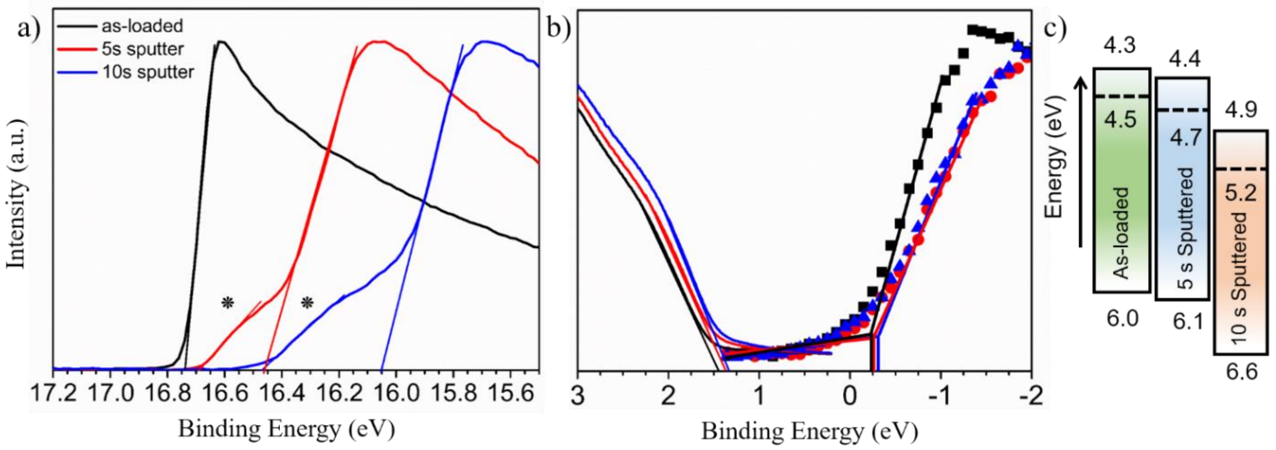

Figure 94. *Close-up of a) the UPS He I secondary electron onset and b) combined UPS He I valence band edge and IPES conduction band edge for the grown thin film of $AgBi_2I_7$. Two shoulders emerging via sputtering are labeled with "*" in the UPS He I onset of secondary electrons figure. c) Band positions for as-loaded and sputtered thin films of $AgBi_2I_7$ derived from UPS/IPES measurements.*

Table 18. *Key parameters derived from UPS and IPES measurements on as-loaded, 5 s, and 10 s sputtered $AgBi_2I_7$ films. The energy values are referenced to the Fermi level. Marked values with "*" were determined via the intersection of tangent line fits to the shoulder features (sputtered films) and the background.*

Sample	**Eonset(± 0.02)**	**EVBM(± 0.1)**	**IE(± 0.1)**	**ECBM (± 0.3)**	**Eg(± 0.3)**
	(eV)				
As-loaded	16.74	1.5	6.0	-0.2	1.7
5 s sputter	*16.69, 16.45	1.4	*5.9-6.1	-0.3	1.7
10 s sputter	*16.47, 16.05	1.4	*6.2-6.6	-0.3	1.7

4.4.8.2 Electronic Properties of $AgBiI_4$

PES measurements were performed on the as-loaded and sputtered (5 s and 10 s) post-annealed coevaporated film of Ag-Bi-I with $r = 0.6$. The as-deposited Ag-Bi-I was annealed at 180 °C for 20 min under N_2. SEM/EDX compositional analysis demonstrates that the as-deposited and annealed films have average compositions of $AgBi_{2.00}I_{7.00}$ and $Ag_{1.16}Bi_{1.04}I_{4.00}$, respectively, within experimental uncertainty of $AgBi_2I_7$ and the last within experimental uncertainty of $AgBiI_4$. Thereby, the post-deposition annealed film of Ag-Bi-I ($r = 0.6$) under N_2 was entitled as $AgBiI_4$. Similar to XPS analysis of $AgBi_2I_7$, there are only oxygen (530 eV) and carbon (285 eV) impurities on the surface of the as-loaded and sputtered film of $AgBiI_4$ (Figure 95).

Close-ups of the Ag 3d, Bi 4f, and I 3d regions are depicted in Figure 96 illustrating little change of Ag 3d and I 3d XPS core peaks with sputtering. The small features in the Ag 3d and I 3d spectra marked with “§” are the Kα3 satellites of the 3d3/2 peaks owing to a different excitation source (Mg vs. Al) used for core level spectra of $AgBiI_4$ ($\Delta E_{Mg\ K\alpha3\text{-}K\alpha1} = 8.5$ eV, $\Delta E_{Al\ K\alpha3\text{-}K\alpha1} = 9.7$ eV). Moreover, comparing the close-up of Bi 4f region of $AgBiI_4$ with $AgBi_2I_7$ reveals the appearance of two small shoulders at ~162 and 157 eV for the $AgBiI_4$ film (Figure 96b) originating from metallic Bi (Bi^0), which becomes more distinguishable after sputtering. Since no trace of metallic bismuth was realized for the annealed film under BiI_3 vapor ($AgBi_2I_7$), the Bi/I deficiency on the surface of the annealed Ag-Bi-I film under N_2 ($AgBiI_4$) might result in the formation of Bi^0 on the surface. Table 19 shows that the surface compositions of as-loaded and sputtered films of $AgBiI_4$ are Bi and I-deficient compared to the bulk compositional analysis using SEM EDX, most likely due to the removal of volatile BiI_3 from the surface of the film upon N_2 annealing of the deposited $r = 0.6$ Ag-Bi-I and the possibility of reducing Bi^{3+} to Bi^0, e.g., in an X-ray beam under ultrahigh vacuum conditions or during processing. Evidently, sputtering (5 and 10s) of the as-loaded Ag-Bi-I film causes the removal of volatile BiI_3 from the surface of the film, leaving behind Ag-rich silver bismuth iodide films.

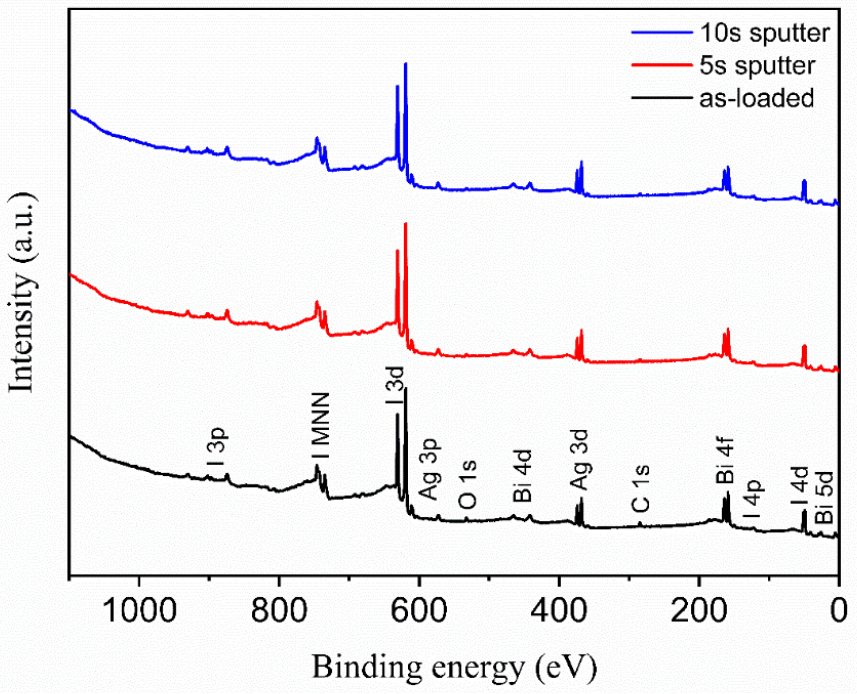

Figure 95. *XPS Mg Kα survey scans of the as-loaded (black), 5 s (red), and 10 s (blue) sputtered thin film of* $AgBiI_4$.

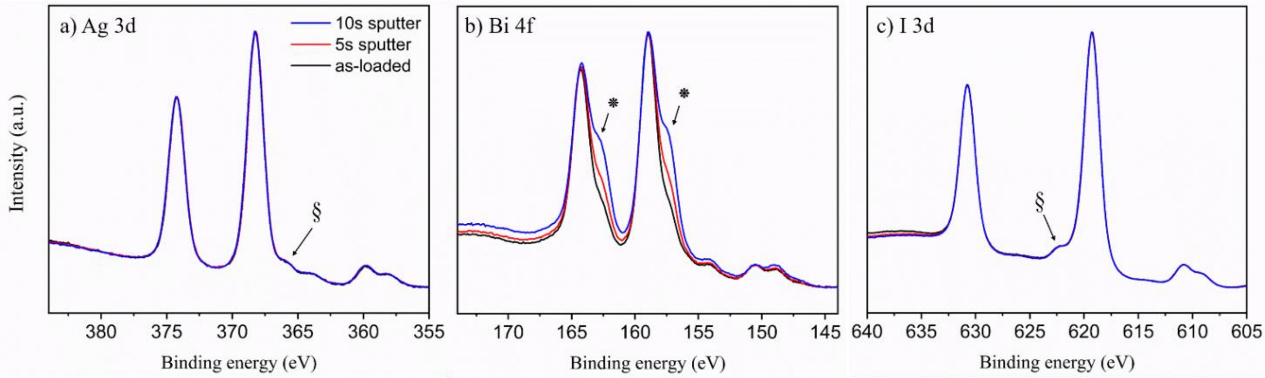

Figure 96. *Core level XPS (Al:*$AgBi_2I_7$*,* Ag_2BiI_5*; Mg:*$AgBiI_4$*) Kα spectra of a) Ag 3d, b) Bi 4f, and c) I 3d peaks for these films. Two small shoulders at ~162 eV and 157 eV in the Bi 4f spectrum for the* $AgBiI_4$ *film originate from metallic Bi (*Bi^0*). The small features marked with "§" are the Kα3 satellites of the 3d3/2 peaks, owing to a different excitation source (Mg vs. Al) used for core level spectra of* $AgBiI_4$ *(*$\Delta E_{Mg\ K\alpha3\text{-}K\alpha1} = 8.5$ *eV,* $\Delta E_{Al\ K\alpha3\text{-}K\alpha1} = 9.7$ *eV).*

Table 19. *Atomic ratios (%) derived from XPS for the as-loaded and sputtered annealed thin film of Ag-Bi-I (180 °C, 20 min) deposited with r = 0.6. Post-deposition annealing was performed under* N_2.

Sample	**Ag (± 2)**	**Bi (± 1)**	**I (± 3)**	**Composition**
As-loaded	21.0	22.0	57.0	$AgBiI_{2.70}$
5 s sputter	22.4	21.3	56.4	$AgBi_{0.95}I_{2.52}$
10 s sputter	24.0	21.0	55.0	$AgBi_{0.87}I_{2.30}$

Figure 97a and b show the UPS and IPES spectra of the as-loaded, 5 s, and 10 s sputtered film of $AgBiI_4$. Sputter-cleaning of the $AgBiI_4$ film for 5 s and 10 s results in a reduction of the density of states in the 5 to 10 eV binding energy region consistent with the removal of surface oxygen. A close-up of the UPS He I onsets of secondary electrons, and combined valence band and IPES conduction band edges of $AgBiI_4$ film is depicted in Figure 98a and b, respectively, along with tangent line fits to the features of interest.

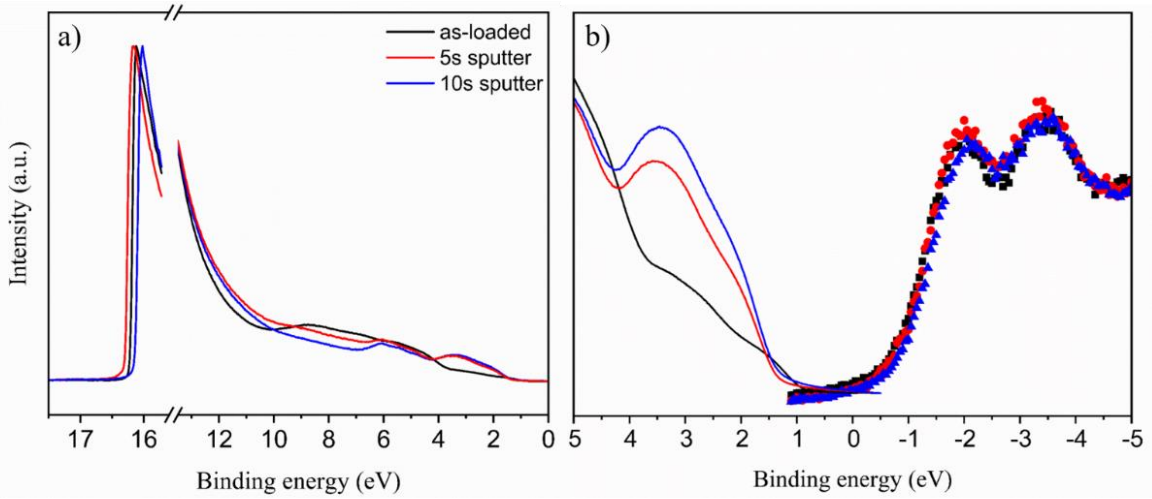

Figure 97. *a) Combined UPS He I secondary electron onset and scan of valence band states spectra and b) combined UPS He I valence band edge and IPES spectra of conduction band states for as-loaded (black), 5 s (red), and 10 s (blue) sputtered post-deposition annealed film of* $AgBiI_4$ *(r = 0.6).*

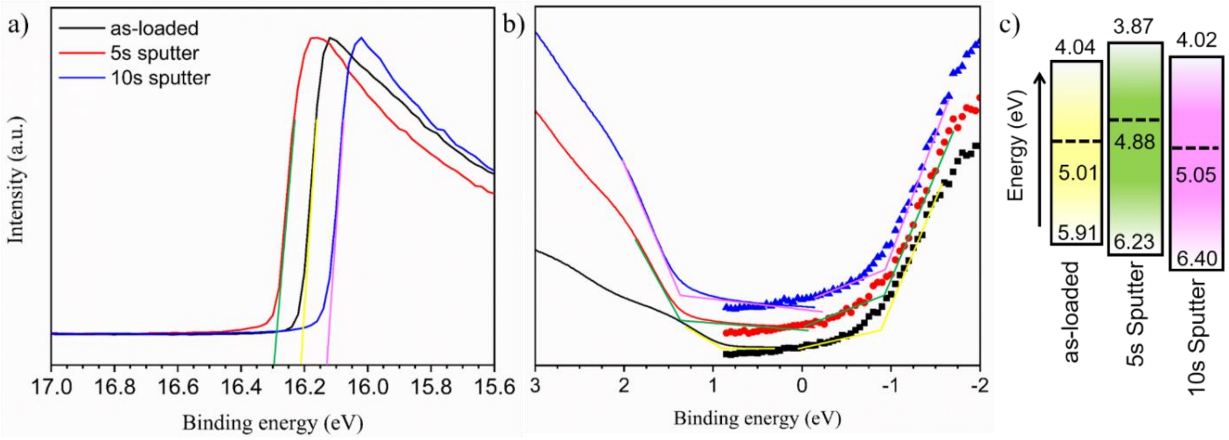

Figure 98. *Close-up of a) the UPS He I secondary electron onset, b) combined UPS He I valence band edge and IPES conduction band edge for the thin film of* $AgBiI_4$*, and c) band positions for as-loaded and sputtered films of* $AgBiI_4$ *derived from UPS/IPES measurements.*

The derived parameters from UPS and IPES are shown in Figure 98c and Table 20. Based on the UPS results, the ionization energies ($IE = h\nu - (E_{onset} - E_{VBM})$) are calculated to be 5.91 eV, 6.23 eV, and 6.40 eV for the as-loaded, 5 s, and 10 s sputtered film of $AgBiI_4$, respectively. The deep valence band position of $AgBiI_4$ highlights the necessity for employing hole transport materials with deep HOMO levels for prospective PV device design. From the UPS/IPES data, it is obvious that $AgBiI_4$ is an intrinsic semiconductor. Considering the error margins for the calculation of the conduction band edge using IPES, the calculated band gap from UPS/IPES for the as-loaded film (1.87 eV) is consistent with the optical band gap (1.80 eV).

Table 20. *Derived parameters from UPS and IPES data on the as-loaded, 5 s, and 10 s sputtered film of* $AgBiI_4$*. The energy values refer to the Fermi level.*

Sample	E_{VBM}**(± 0.05)**	E_{onset}**(± 0.1)**	**IE(± 0.1)**	E_{CBM} **(± 0.15)**	E_g**(± 0.15)**
	(eV)				
As-loaded	0.90	16.2	5.91	0.97	1.87
5 s sputter	1.35	16.3	6.23	1.01	2.36
10 s sputter	1.35	16.1	6.40	1.03	2.38

4.4.8.3 Electronic Properties of Ag_2BiI_5

Based on the PES results for $AgBiI_4$ and $AgBi_2I_7$, which suggest a detrimental impact of sputter cleaning, XPS, UPS, and IPES spectra of the as-loaded thin films of silver bismuth iodide are considered the more reliable data and are the focus of the current study. Thereby, the electronic properties of Ag_2BiI_5 were investigated by performing PES measurements only on the as-loaded film of Ag_2BiI_5. Figure 99 demonstrates that oxygen and carbon are the only contaminations detected on the surface of the as-loaded annealed film (180 °C, 20 min; under BiI_3 vapor) of Ag-Bi-I grown with $r = 0.8$. Analysis of XPS core-level spectra (Figure 100) results in the determination of the surface composition of the as-loaded film (Table 21), which is in good agreement with the estimated bulk composition using SEM/EDX ($Ag_{1.85}Bi_{1.03}I_5$).

Figure 101 demonstrates UPS He I secondary electron onset, scan of valence band state, and IPES spectra for an as-loaded thin film of Ag_2BiI_5 along with the calculated E_{onset} (16.71 eV), E_{VBM} (1.30 eV), and E_{CBM} (-0.4 eV) via the intersection of tangent line fits to the features of interest and the background. Furthermore, the ionization energy is calculated to be 5.80 eV for the deposited Ag_2BiI_5 film. A schematic illustration of the calculated band positions is shown in the inset of Figure 101, confirming that Ag_2BiI_5 behaves as an n-doped semiconductor.

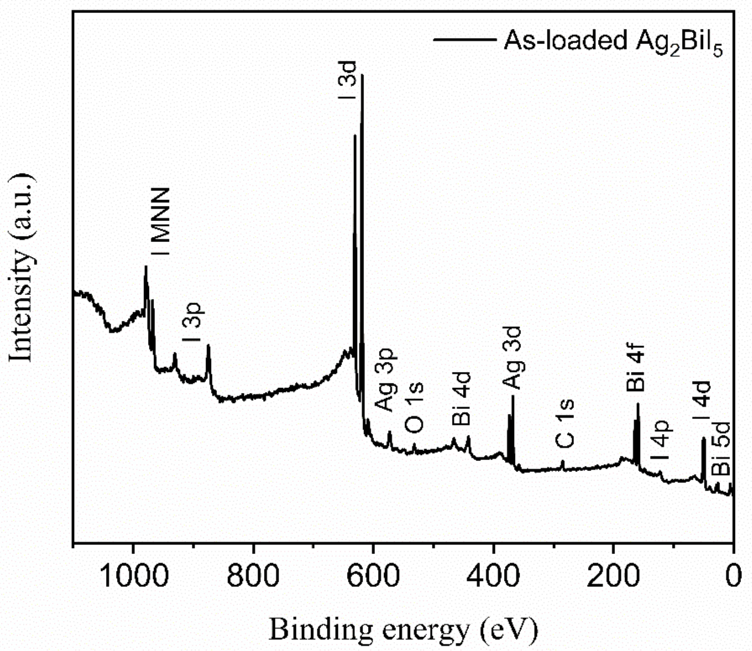

Figure 99. *XPS Al Kα survey scan of the as-loaded film of Ag-Bi-I deposited with r = 0.8 (Ag_2BiI_5). Annealing was performed at 180 °C for 20 min under BiI_3 vapor.*

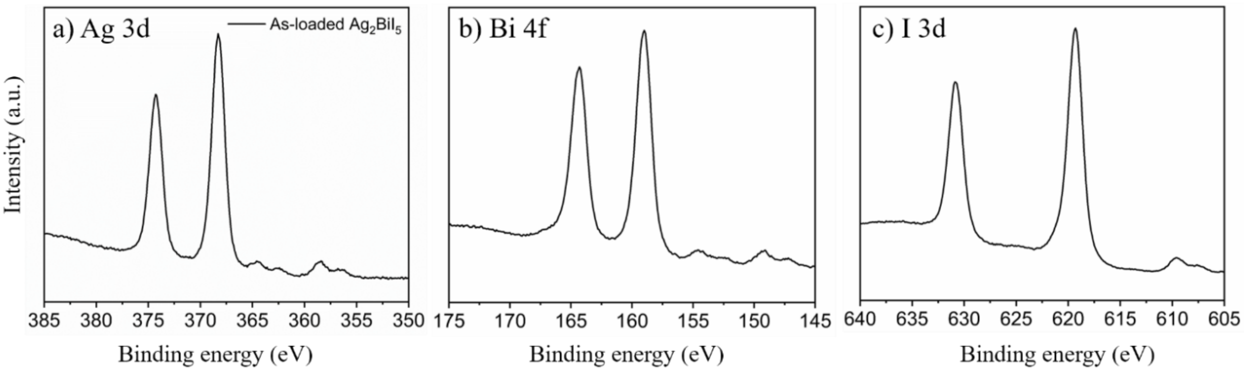

Figure 100. *Core level XPS Al Kα spectra of a) Ag 3d, b) Bi 4f, and c) I 3d peaks for the as-loaded thin film of Ag_2BiI_5.*

Table 21. *Atomic ratios (%) derived from XPS measurement for the as-loaded film of Ag-Bi-I deposited with r = 0.8 (Ag_2BiI_5). Annealing was performed at 180 °C for 20 min under BiI_3 vapor.*

Sample	**Ag (± 2)**	**Bi (± 1)**	**I (± 3)**	**Composition**
As-loaded	18.0	13.0	69.0	$Ag_{2.0}Bi_{1.1}I_{5.3}$

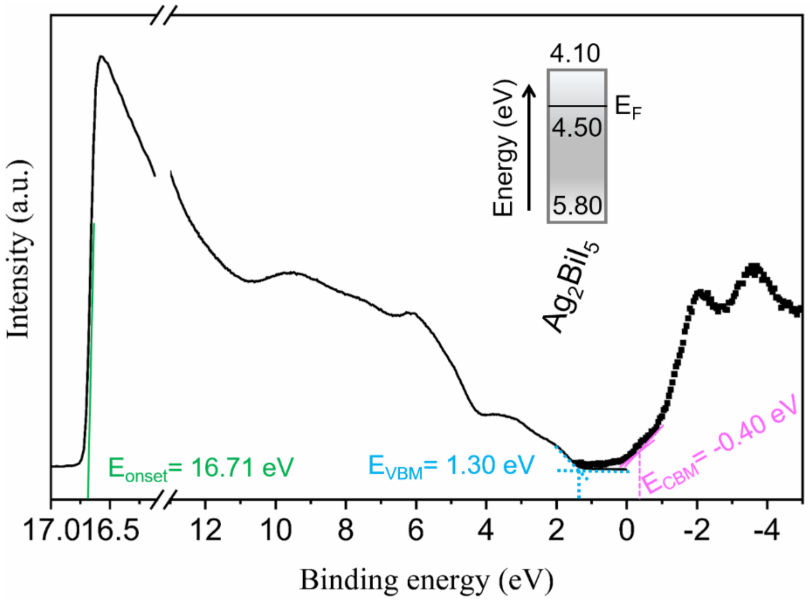

Figure 101. *Combined UPS He I secondary electron onset and scan of valence band state and IPES spectra for as-loaded post-deposition annealed Ag_2BiI_5 film. The inset gives the band positions for the thin film of Ag_2BiI_5.*

4.4.9 Device Performance

After characterizing coevaporated silver bismuth iodide film properties, initial photovoltaic devices were prepared using a glass/FTO/TiO_2/$AgBiI_4$/P3HT/Au structure (Figure 102a), in which the $AgBiI_4$ serves as the absorber. For this study, a nominally planar interface between the TiO_2 electron transport layer and $AgBiI_4$ is employed (in contrast to the more typical mesoporous interface, used to facilitate charge extraction).[69, 72, 126, 133-134] Based on the SEM cross-sectional image, the thickness of the $AgBiI_4$ layer is ~ 400 nm, while the thicknesses of the TiO_2/P3HT and the Au electrode are ~ 20 nm and 70 nm, respectively. The J-V curves were characterized by a large degree of hysteresis, with PCE measured with a reverse scan (0.89 %) falling higher than the PCE measured in the forward scan (0.13 %) (Figure 102b). Here, forward and reverse scans respectively refer to sweeping the bias from low to high values, and vice versa. Given the crucial role of interfaces in PV devices,[137-140] the observed hysteresis in this device architecture may originate from contact resistance or surface-trap defects at the absorber-TiO_2 interface, causing low carrier injection and interfacial recombination centers, respectively. Further investigation is needed to resolve the role and source of hysteresis, with respect to device performance.[81]

Table 22 lists the characteristics of the device for forward and reverse scan directions. The V_{OC} values are 0.73 V in the forward and 0.84 V in the reverse scan directions, which are among the highest reported V_{OC} values for the Ag-Bi-I systems.[69, 72, 126, 133-134] The EQE spectrum of the $AgBiI_4$ cell (Figure 103) shows a photocurrent edge below 700 nm (corresponding to ~ 1.77 eV) consistent with the calculated band gap from the Tauc plot (1.80 eV). The J_{SC} value (2.39 mA/cm^2) acquired from the integration of the EQE spectrum closely matches the value acquired from the reverse scan J-V curve in Figure 102b (2.37 mA/cm^2). The EQE maximum for this device is 20% at ~ 400 nm. The obtained low EQE, especially at higher wavelength, is ascribed to considerable charge recombination occurring in the device. A possible reason for the low device performance might be the presence of Bi^0 on the $AgBiI_4$ film surface, as detected during the XPS study. Bi^0 centers could provide recombination sites at the interface between the absorber and the other PV device layers or facilitate Fermi level pinning, thereby degrading device performance.[81]

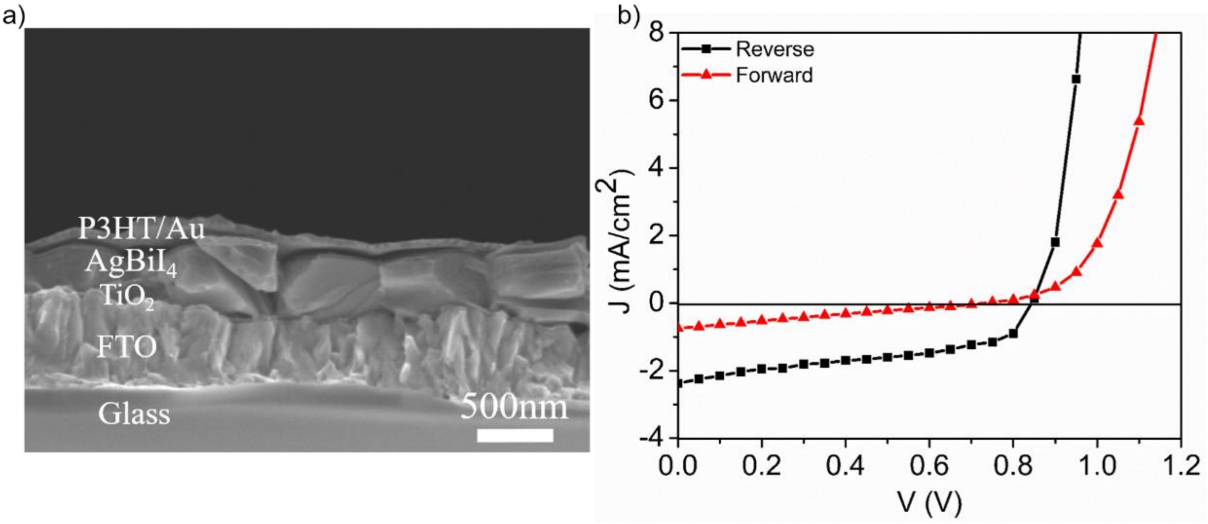

Figure 102. *a) SEM cross-sectional image of the solar cell device employing an $AgBiI_4$ absorber layer and compact TiO_2/P3HT as electron/hole transport layers, respectively; b) J-V curves of the $AgBiI_4$ solar cell.*

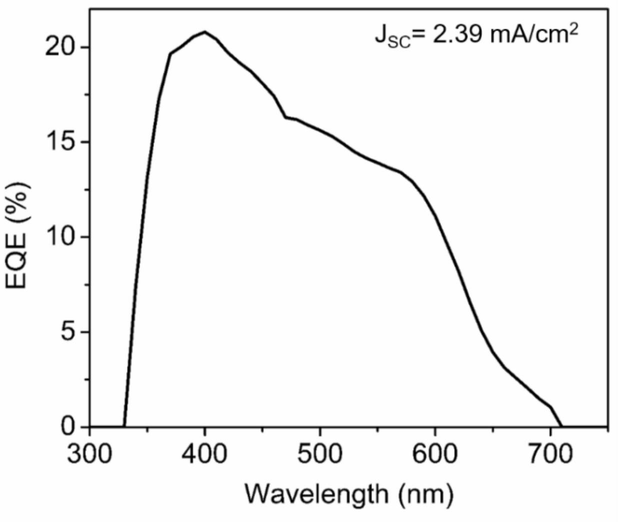

Figure 103. *EQE spectrum of FTO/TiO_2/$AgBiI_4$/P3HT/Au device. The short-circuit current density calculated from EQE is 2.39 mA/cm^2.*

Table 22. *Performance parameters of the FTO/TiO_2/$AgBiI_4$/P3HT/Au solar cell. The cell was measured for forward and reverse scans.*

Scan direction	V_{OC} (V)	J_{SC} (mA/cm^2)	FF (%)	PCE (%)
Forward	0.73	0.74	23.56	0.13
Reverse	0.84	2.37	44.46	0.89

4.5 Conclusion

In summary, both single deposition and coevaporation methodologies have been used to grow single-phase thin films of bismuth halide semiconductors. Although, the single deposition method results in the deposition of $Cs_3Bi_2I_9$, $Rb_3Bi_2I_9$, and silver bismuth iodide films, the obtained XRD patterns for these films are not single-phase and some impurity peaks were detected. In addition, the SEM study of the films deposited using the single deposition method demonstrates growth of non-uniform bismuth halide semiconducting films with high pinhole densities on glass substrates.

In contrast, the two-step approach including coevaporation of metal halides followed by post-annealing results in the fabrication of single-phase high-quality and pinhole-free multidimensional bismuth halide semiconductors. This approach has been introduced for growing high-quality thin films of $Cs_3Bi_2I_9$, $Rb_3Bi_2I_9$, $AgBi_2I_7$, $AgBiI_4$, and Ag_2BiI_5. Optimization of the coevaporation and post-deposition annealing processes using XRD and SEM/EDX led to the growth of single-phase hexagonal $Cs_3Bi_2I_9$ (0D), monoclinic $Rb_3Bi_2I_9$ (2D), cubic $AgBi_2I_7$ and $AgBiI_4$ (3D), as well as rhombohedral Ag_2BiI_5 (2D). All as-deposited Ag-Bi-I films form within a rhombohedral structure type. However, a crystallographic phase transition to the cubic phase occurs upon post-deposition annealing of Bi-rich as-deposited films. On the other hand, Ag-rich films (i.e. Ag_2BiI_5) tend to stay in the rhombohedral phase. TD-XRD in combination with SEM/EDX compositional analysis on fabricated Ag-Bi-I films reveal that, depending on the composition of the as-deposited films and annealing conditions, a phase transition from rhombohedral to spinel-defect cubic structure can occur.

Optical properties of the films have been characterized using UV-vis spectroscopy followed by constructing Tauc plots with the assumption of direct and indirect band gaps for the grown films. Among them, the silver bismuth iodides have the most suitable band gap (1.7-1.9 eV) for single junction photovoltaic devices.

XPS compositional characterization revealed that apart from oxygen and carbon, no trace of other contaminants exists on the surface of the films. XPS data also suggest the sensitivity of some of the film surfaces (most notably $Rb_3Bi_2I_9$ and $AgBiI_4$) to Bi^{3+} to Bi^0 reduction. The amount of metallic bismuth increases via applying sputter-cleaning of $Rb_3Bi_2I_9$ and $AgBiI_4$ film surfaces, pointing to the detrimental effects of sputtering on the films. The VBM positions relative to the vacuum level were determined by UPS, showing relatively deep VBM energy levels for the bismuth halide semiconducting films.

Initial studies on photovoltaic performance of $AgBiI_4$ and $Rb_3Bi_2I_9$ as light absorbers have been performed. Planar-junction PV devices are prepared based on the coevaporated $AgBiI_4$ or $Rb_3Bi_2I_9$ films, with TiO_2 and P3HT as electron and hole-transport layers, respectively. Poor photovoltaic performance is observed for the $Rb_3Bi_2I_9$-solar cell. Moreover, the best-performing device with coevaporated $AgBiI_4$ as absorber exhibited a PCE of as high as 0.9 % with open-circuit voltage (V_{OC}) > 0.8 V in the reverse scan direction.

Chapter 5.

Gas-Phase Functionalization and Characterization of Multiwalled Carbon Nanotubes

5.1 Background and Motivation

Multi-walled carbon nanotubes (MWCNTs) are composed of concentrically rolled graphene sheets and demonstrate remarkable optical, mechanical, and electrical properties,[141-142] which make them promising candidates for various applications. Owing to their high electrical conductivity in the range of 10^4 S/cm and high current densities at the level of 10^9 A/cm^2, they are superior candidates to be used in electronic devices.[143-145] The extraordinary electrical properties of CNT has encouraged researchers to apply them in electronic devices such as diodes,[146-147], light-emitting diodes (LED),[148-149] organic solar cells (OSCs),[150-152] and most recently in perovskite solar cells (PSCs).[76, 79, 153-154] Furthermore, an enhancment in stability and efficiency of PSCs is observed employing CNTs (see Section:1.3.4). The root-mean-square roughness (RMS) of the charge-transport layers in solar cells increases by incorporating CNTs, which might result in a larger contact area between these layers and the electrodes.[155] An increase in the roughness may cause superior charge collection and diminish series resistance.[156] Apparently, it is appealing to incorporate CNTs into the electron/hole conductive layers of solar cells.

The high aspect ratio of carbon nanotubes (CNTs) and the existence of strong π-π interaction between the tubes (0.5–2 eV/nm) in vacuum give them a hydrophobic nature,[157-158] which hinders their solubility in aqueous and related solvents. As a result, they have the tendency to aggregate in these media. The modification of the CNT surface can not only alter the hydrophobic nature of the tubes but can also be purposefully beneficial for changing the electronic properties of the tubes. Doping of the graphitic structure of CNTs can lead to n-doping or p-doping by altering the work function of the tubes.[151] Among different materials used for the modification of the tubes, oxygen and nitrogen atoms are the most commonly used heteroatoms which have been incorporated into the graphitic structure of CNTs.[159-162] Substantial efforts have been carried out to functionalize graphene and CNTs with oxygen species including liquid-phase acid treatment of CNTs,[163-164] plasma purification and oxidation,[165-166] and gas phase oxidation.[159, 167]

Liquid-phase acid treatment is one of the main methodologies to functionalize CNTs with different oxygen species. Although this method results in the efficient functionalization of the tubes, the crystalline structure of CNTs is enormously deteriorated because of the direct contact between CNTs and strong acids. Compared to the liquid-phase acid treatment, gas-phase oxidation of the tubes is a promising method, which can create low damage to the surface of CNTs.[82] In addition, the CNT modified by oxygen groups can provide a proper platform for further nitrogen modification to the tubes via the post-treatment procedure of the oxygen modified CNTs (OCNTs).

One of the essential issues that has to be addressed prior to applying CNTs to electronic devices is the interface between the tubes and a metal or semiconductor material. Relative values of the work functions of the interface materials can determine the interaction between them at the interface. Although substantial studies have been done to assess the work function of oxygen/nitrogen-modified tubes prepared via liquid phase treatment,[168-171] reliable work functions of gas-phase oxygen/nitrogen modified tubes has not been addressed yet. Another fundamental investigation is to systematically specify the nature of the functional groups introduced via these reactions.

This chapter is dedicated to the study of gas-phase oxygen and nitrogen functionalization of multiwalled carbon nanotubes (MWCNT). Alteration in the graphitic structure of the tubes due to the functionalization was quantified by high resolution transmission electron microscopy (HRTEM). In order to obtain information regarding the surface functional groups, temperature-programmed desorption (TPD), Fourier transform infrared spectroscopy (FTIR), TEM/EDX, and XPS were employed. The work function of each of the tubes was characterized using Kelvin probe force microscopy (KPFM). Furthermore, the dispersibility of pristine and functionalized tubes in organic solvents was examined.[1]

---

[1] The reported work in this chapter is reprinted from the published article in Scientific Reports 2016.[82] Full-text permission was obtained from the respective journal licensed under Creative Commons Attribution 4.0 International license.

5.2 Chemical and Structural Characterization

Depending on the experimental parameters (e.g. temperature, treatment time) applied for the gas-phase functionalization of CNTs, several oxygen and/or nitrogen functional groups can be formed on the CNT surface (Figure 104).

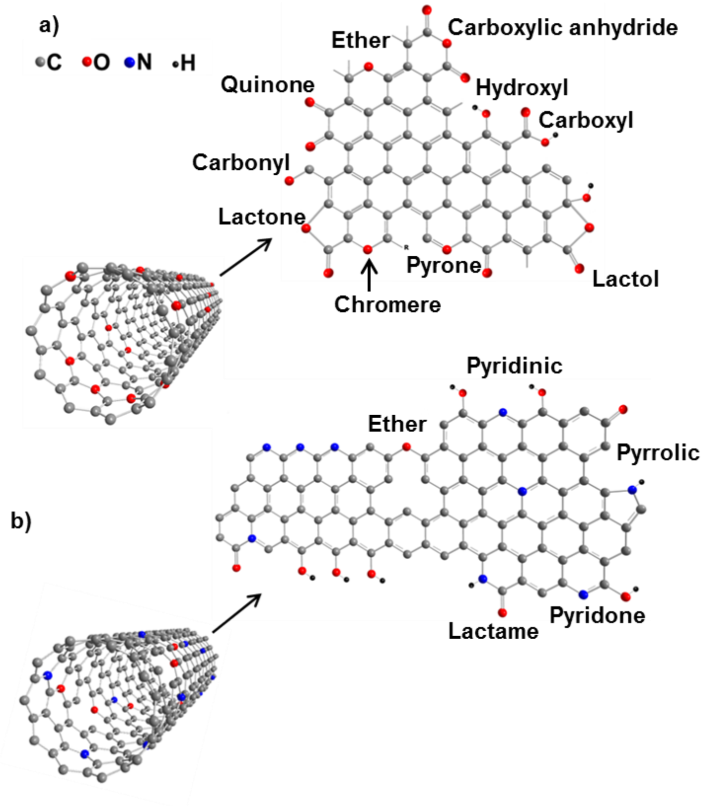

Figure 104. *Schematic representation of a) oxygen doped MWCNT and b) nitrogen doped MWCNT. Several types of oxygen and nitron chemical groups can be added to the surface of the tubes.*

High resolution transmission electron microscopy (HRTEM) images of the tubes were collected using an aberration-corrected high resolution TEM at an accelerating voltage of 80 keV (FEI Titan TEM). Figure 105 depicts HRTEM images of the pristine MWCNT (a), purified MWCNT (b), OMWCNT-48 (c), OMWCNT-72 (d), NMWCNT-48 (e), and NMWCNT-72 (f). Clearly, most of the pristine and purified tubes are free of metal contaminations (> 95 % carbon purity) and there is a limited number of defects on the tube sidewalls. In addition, amorphous carbon is wrapped around pristine and purified tubes. The purification process was not deleterious for the pristine tubes. However, functionalization of the tubes by oxygen and nitrogen resulted in the creation of a bumpy morphology in all of the functionalized tubes which may be attributed to the introduction of new defects on the CNT sidewalls. The red arrows in Figure 105 highlight the locations of amorphous carbon and sidewall damages in the pristine and functionalized tubes, respectively. In addition, the amount of amorphous carbon was enormously decreased on the functionalized tube sidewalls, as compared with pristine MWCNT. It can be concluded that oxygen and nitrogen functionalization of MWCNT leads to the removal of amorphous carbon from the tube sidewall and introduces some defects along the CNT surface.

These defect sites could enhance the susceptibility of the tubes to interact with other functional groups. The chemical composition of the functionalized tubes was determined applying EDX inside the TEM column (Figure 106) to provide insight into the concentration of trace metal impurities. Owing to the vapor phase oxygen modification of the tubes, traces of oxygen can be seen in all the EDX spectra. The spectra indicate the presence of significant amounts of copper (Cu) which is related to the TEM grid. However no peak appeared regarding the metal contaminations verifying high purity of the tubes.

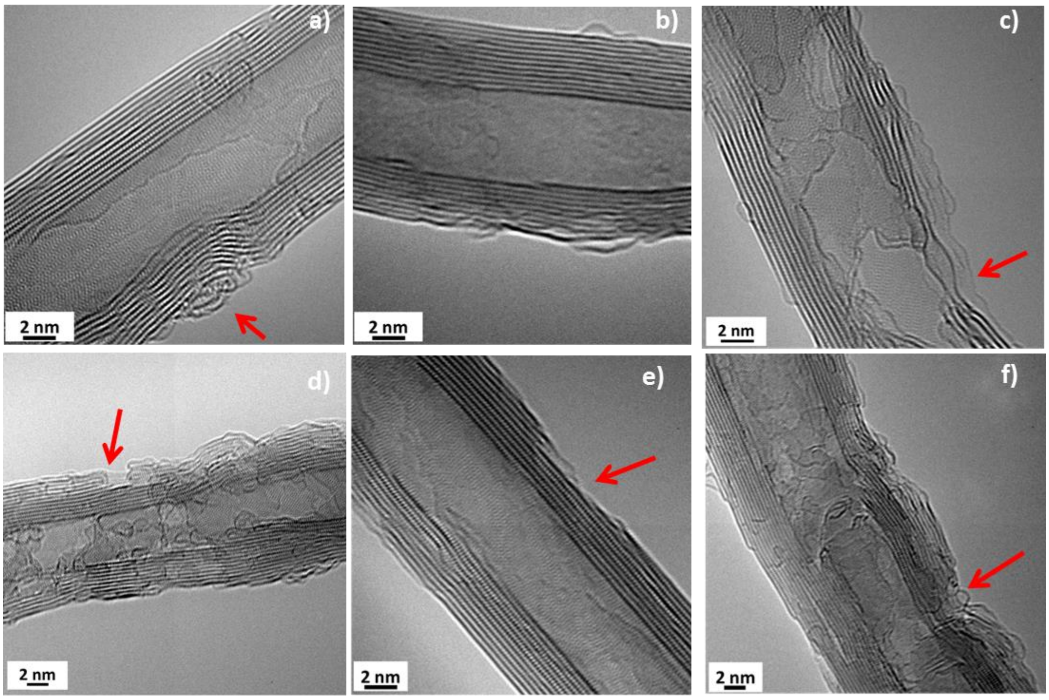

Figure 105. *HRTEM images of a) pristine MWCNTs, b) PMWCNTs, c) OMWCNT-48, d) OMWCNT-72, e) NMWCNT-48 and f) NMWCNT-72. The red arrows indicate the presence of amorphous carbon on pristine MWCNT (a) and the created defects on the functionalized tubes.*

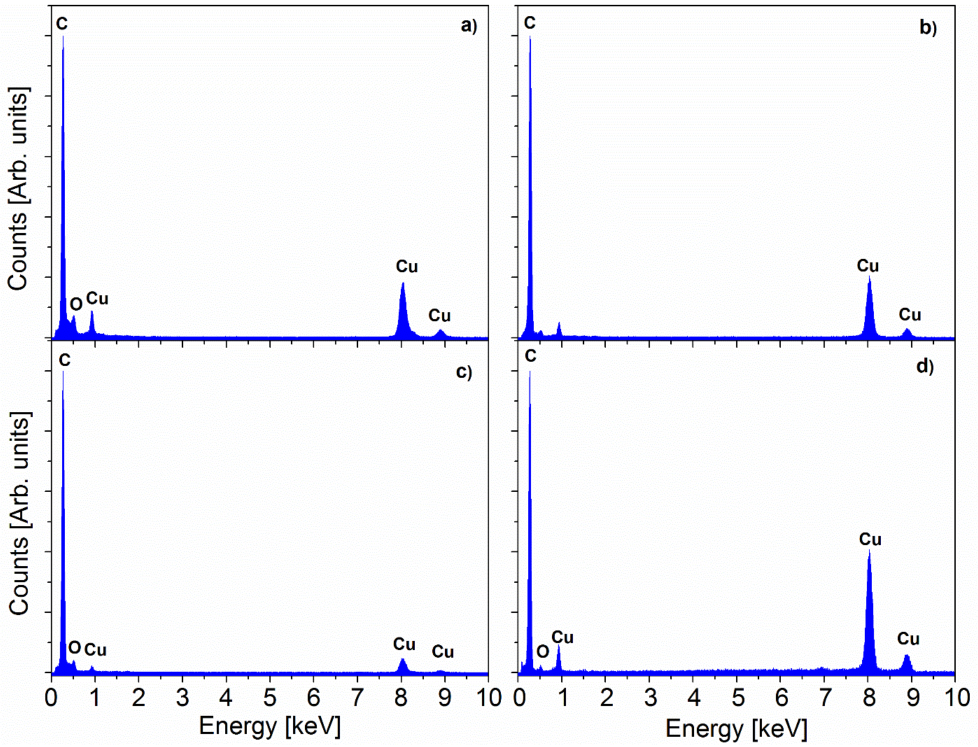

Figure 106. *EDX spectra comparing the response of a) OMWCNT-48, b) OMWCNT-72, c) NMWCNT-48, and d) NMWCNT-72. The strong Cu peaks originate from the TEM Cu grid.*

In order to examine the type, amount, and thermal stability of surface oxygen groups which were produced during gas phase oxidation of purified MWCNTs (OMWCNTs-48 h and OMWCNTs-72 h), TPD experiments were carried out. Figure 107 shows CO_2 and CO desorption profiles obtained upon heating OMWCNTs from room temperature to 1000 °C at a heating rate of 2 °C min^{-1}. The notable desorption of CO and CO_2 from the oxygen functionalized tubes shows that a considerable amount of surface oxygen groups was created by HNO_3 vapor treatment. The amount of released CO_2 and CO from OMWCNTs was determined by quantitative analysis of TPD results (Table 23). These results indicate that the amount of released CO_2 did not increase by extending the oxygen modification time from 48 h to 72 h, whereas the amount of CO rose remarkably from 1.3 mmol g^{-1} to 1.61 mmol g^{-1}. This can be attributed to the type of functionalized groups on the OMWCNT surfaces. A small surface area of the tubes limits the incorporation of large functional groups consisting of carboxylic groups and carboxylic anhydrides onto the tube surface which are the origin of desorbed CO_2.[172] On the other hand, the increase in the amount of desorbed CO confirms the existence of more small functional groups on the tubes, since CO mainly originates from the decomposition of hydroxyl, carbonyl, and ether groups.[173] Therefore, it appears that by increasing the treatment time in HNO_3 vapor, more phenol and ether groups are created on the sidewalls of the tube than carboxylic acid groups.

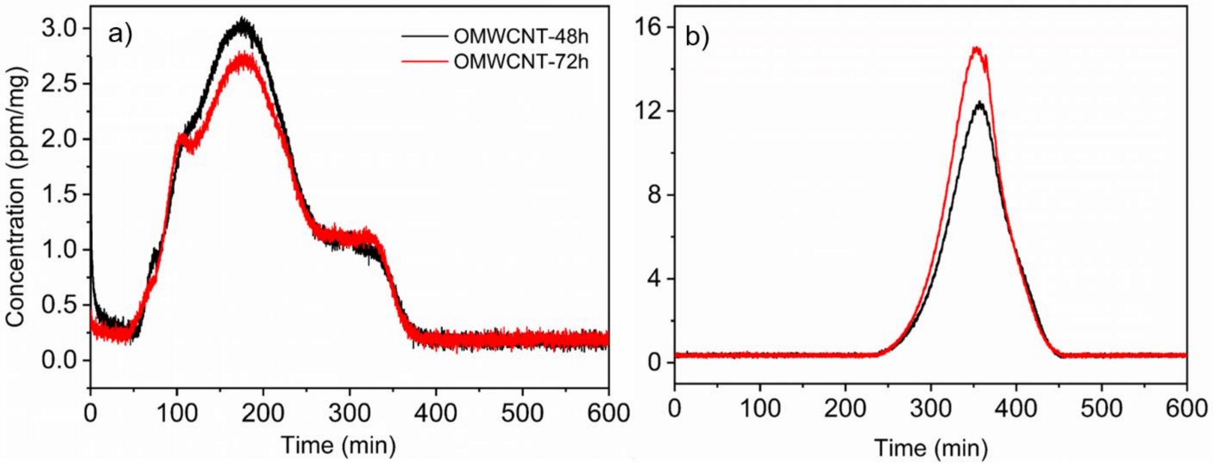

Figure 107. *a) CO_2 and b) CO profiles of oxygen vapor treated MWCNTs for 48 hours (red) and 72 hours (black) performed in helium at a heating rate of 2 °C min^{-1}.*

Table 23. *Determined amount of desorbed CO_2 and CO from TPD.*

CNTs	CO2 (mmolg-1)	CO (mmolg-1)
OMWCNT-48	0.65	1.3
OMWCNT-72	0.643	1.61

Fourier transform infrared spectroscopy (FTIR; Bruker VERTEX 70 spectrometer) was performed to specify the functional groups on the CNT surface (Figure 108). In this case, IR spectra were measured in transmittance mode by grinding a very low concentration of CNTs into potassium bromide. In these spectra, the dominant transmittance at 3430 cm^{-1} was assigned to the O-H stretching vibration which could be due to absorbed water from the environment, O-H or carboxylic groups on CNT surfaces. In the spectrum of the as-received MWCNT (Figure 108f), the small peaks around 2920 cm^{-1} and 2850 cm^{-1} are consistent with asymmetric and symmetric CH_2 stretching vibration bands, respectively.[174] These functional groups could be formed at defect sites of the MWCNT surface. In the spectra of OMWCNTs (Figure 108c and d) and NMWCNTs (Figure 108a and b), these peaks are diminished, which can be correlated to the removal of chemisorbed hydrogen from the MWCNT surface during tube functionalization and generation of some other functional groups on the defect sites. The bands in the 1750-1550 cm^{-1} range can be assigned to C=O or C=C groups. Therefore, the bands around 1635 cm^{-1} and 1550 cm^{-1} in these spectra are correlated to the carboxylic groups and aromatic and unsaturated structure of >C=C< bonds. The characteristic band of C-O appears near 1430 cm^{-1} in these spectra. As it is depicted, the intensity of this peak intensifies with oxidation of the MWCNTs implying modification of the oxygen groups on the CNT surface, whereas the intensity of this feature decreases by nitrogen doping of OMWCNTs emphasizing the decomposition of surface oxygen groups from the surface of the tubes. No distinct peak was observed related to the nitrogen groups on the CNT surface, which is in good agreement with the TEM/EDX result. This phenomenon may be due to the existence of only a small amount of nitrogen in the functionalized tubes.

Elemental analysis (elemental analyzer EuroVector EA 3000) was performed to investigate the average amount of modified oxygen and nitrogen groups to the CNTs surface (Table 24). The elemental percentages represent the means from two independent measurements. Carbon was obviously the most abundant element observed in all CNTs. The highest level of carbon was detected in as-received MWCNT (98.75 wt.%) then in purified tubes (98.2 wt.%). A little decrease in the carbon content in the purified tubes can be attributed to the removal of amorphous carbon from the surface of the tubes. It can be seen from Table 24 that the content of carbon was reduced by oxygen and nitrogen doping of the tubes. Low traces (< 0.2 wt.%) of detected hydrogen in all the samples suggest low levels of adsorbed hydrogen gas and hydrogen-terminated carbon atoms.

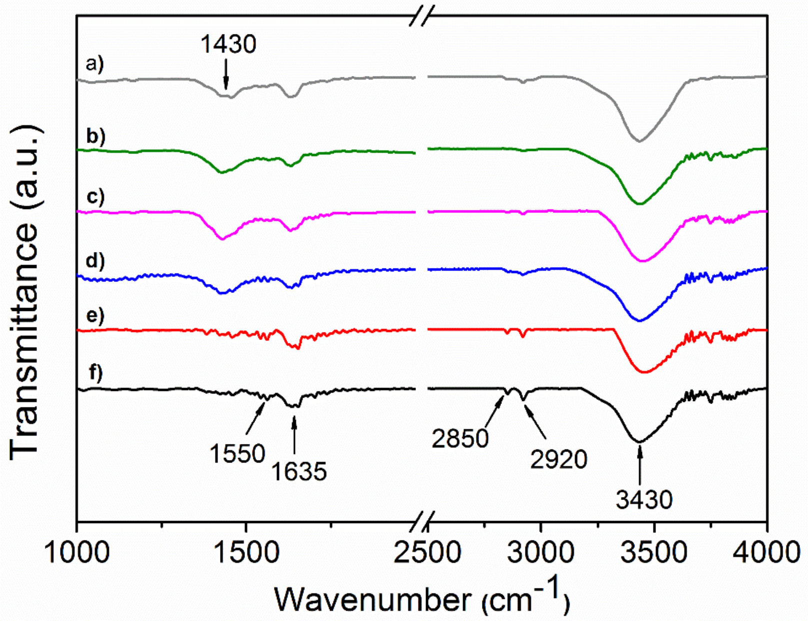

Figure 108. *FTIR spectra of a) NMWCNT-72, b) NMWCNT-48, c) OMWCNT-72, d) OMWCNT-48, e) PMWCNTs, and f) as-received MWCNTs.*

Table 24. *Elemental composition (wt.%) of pristin, purified, and functionalized multiwalled carbon nanotubes.*

Tube	**Elemental analysis (wt.%)§**			
	C	**N**	**H**	**O**
MWCNT	98.75	n.d.*	< 0.1	< 1
PMWCNT	98.2	n.d.	0.14	0.8
OMWCNT-48	91.9	n.d.	< 0.1	5.55
OMWCNT-72	91.8	n.d.	< 0.1	6
NMWCNT-48	95.3	0.89	0.13	2.58
NMWCNT-72	95.55	1	0.11	3.05

§ The rest elements in the tubes could be metal impurity
* n.d.: not detected element

The highest content of oxygen was detected in the tubes treated by vapor HNO_3 providing oxygen modified tubes (OMWCNTs). The observed reduction in the oxygen content of nitrogen functionalized tubes can be ascribed to the decomposition of oxygen groups from OMWCNTs and doping of the tubes by nitrogen groups. Moreover, traces of nitrogen were observed in the samples treated for 6 h under flowing NH_3. As the nitrogen content enhanced from 0.89 wt.% to 1 wt.% by increasing the treatment time of OMWCNT from 48 h to 72 h, it can be concluded that the content of nitrogen on NMWCNT prepared by post-treatment of OMWCNT depends on the treatment time of MWCNT in HNO_3 vapor.

XPS was employed as an inherently surface sensitive technique to quantify the atomic concentrations of the modified species to the tubes. The C 1s, O 1s and N 1s regions of the nanotubes were studied. No trace of metal impurities was detected in the XPS spectra of both pristine and treated tubes which is consistent with the HRTEM observation. The region spectra were normalized to the intensity of the C 1s peak of graphitic carbon at 284.5 eV and in each region, the same range of intensities was considered for the investigated spectra. XP C 1s spectra of the pristine, purified, oxygen and nitrogen modified tubes were measured and shown in Figure 109, where the spectra were normalized to the intensity of the C 1s peaks at 284.4 eV. The C 1s region can be deconvoluted mainly into five Gaussian peaks centered at 284.4 ± 0.2, 286.1 ± 0.2, 287.5 ± 0.2, 288.9 ± 0.2, and 291 ± 0.2 eV. These peaks can be assigned to carbon in graphite (C=C, sp^2), singly bonded carbon to oxygen in phenols and ethers (*i.e.*, C-O), carbon atoms doubly bound to oxygen in ketones and quinones (i.e., >C=O), carbon bound to two oxygens in carboxyls, carboxylic anhydrides, and esters (*i.e.*, -COO-), and the characteristic shakeup line of carbon in the aromatic compounds (π-π^* transition), respectively. The relative concentration of the corresponding functional groups was derived and summarized in Table 25.

The amount of graphitic carbon decreases slightly upon modification of the tubes. It can be seen that the functional groups with C-O bonds (phenols, ethers, etc.) are the dominant species on the pristine and the functionalized tubes. In addition, the amount of the functional group with C=O bonds was increased via purification, HNO_3, and NH_3 treatments. It is also obvious that a higher number of -COO- groups can be added to the tube via 48 h treatment of the purified tubes in HNO_3, whereas it decreases by increasing the treatment time from 48 h to 72 h. From these results, it can be concluded that the surface area of MWCNT is susceptible to accept smaller size chemical groups consisting of phenols, ethers, ketones, and quinones rather than large chemical groups e.g. carboxyls and carboxylic anhydrides, or esters.

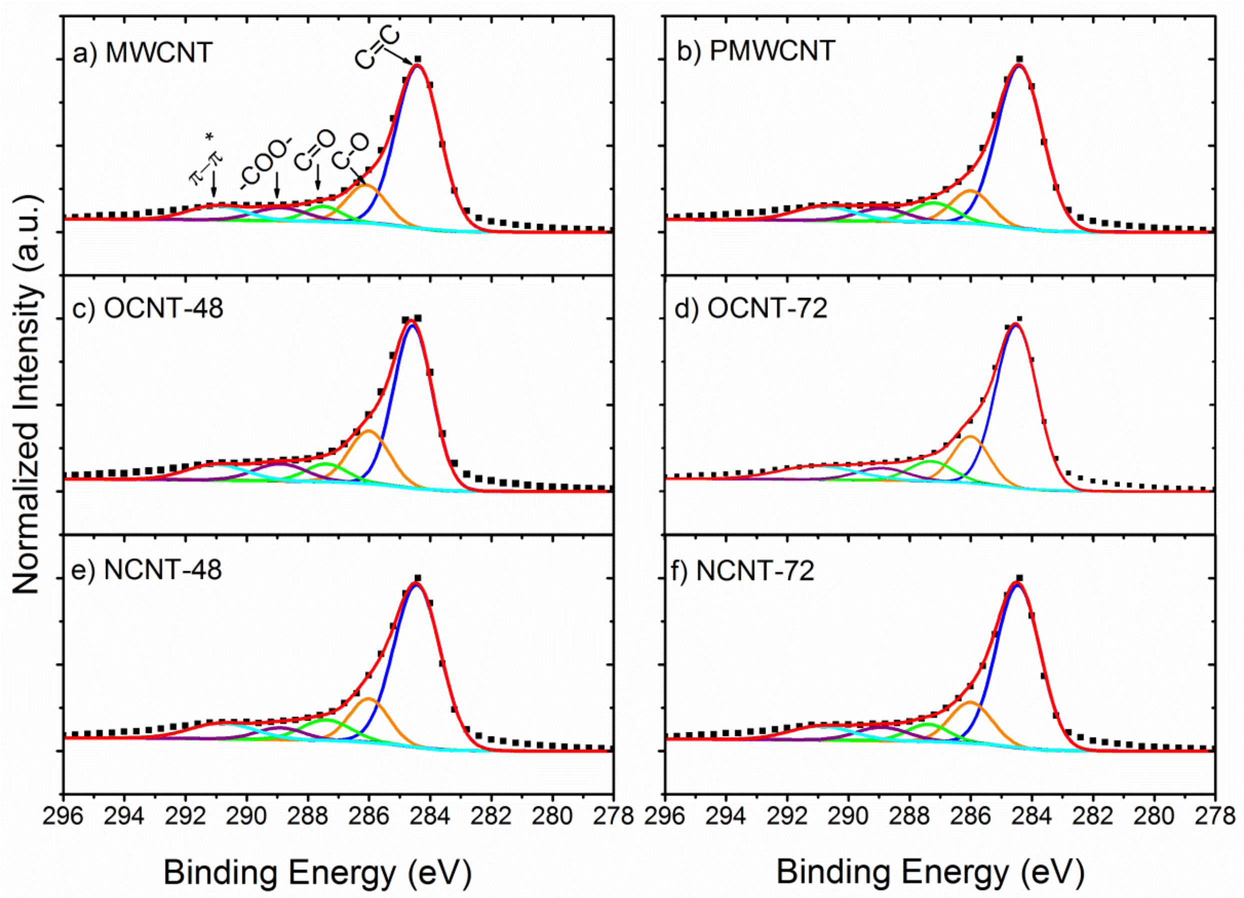

Figure 109. *XP C 1s deconvoluted spectra of as received MWCNT, PMWCNT, and the modified tubes.*

The deconvolution of the O 1s spectra of these tubes results in two main contributions at 531.6 ± 0.2 and 533.4 ± 0.2 eV (Figure 110) assigned to oxygen-carbon double bonds (C=O) and oxygen-carbon single bonds (C-O), respectively. Figure 110a and b show that the O 1s peak intensities in MWCNT and PMWCNT are negligible which is attributed to the existence of little amount of oxygen on the tube surface. The intensity of these two peaks increases remarkably via HNO_3 treatment of the tubes providing oxygen species on the surface of the tubes (Figure 110c and d). As Table 25 shows, the amount of modified oxygen to the tubes increased via prolongation of the HNO_3 treatment from 48 h to 72 h. In this case more C-O bounds are added to the surface of the tubes. Further NH_3 treatment of the tubes results in the reduction of the oxygen content of the tubes which may be attributed to the decomposition of the oxygen groups from the surface of the tubes and further substitution with nitrogen groups.

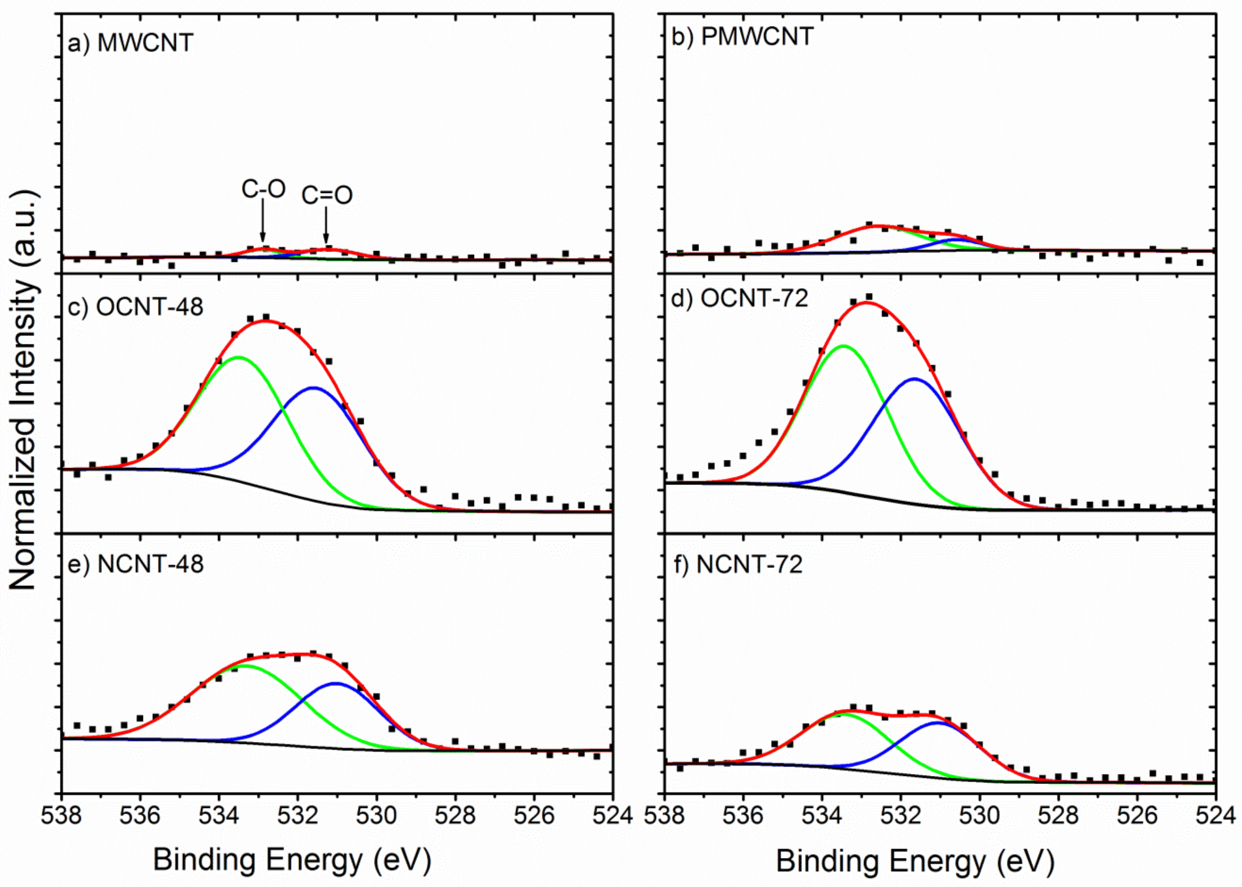

Figure 110. *Deconvoluted XP spectra of O 1s region. The spectra were normalized in intensity to the corresponding C 1s peaks and the same intensity range was considered for all the tubes.*

The deconvoluted XP N 1s spectra of the NCNT-48 and NCNT-72 are shown in Figure 111. The N 1s region can be deconvoluted mainly into three peaks including pyridinic (398.5 ± 0.2), pyrrolic (399.7 ± 0.2 eV), and quaternary (401 ± 0.2) groups. It has to be pointed out that the amount of modified nitrogen on the surface of the tubes is rather low. The N 1s spectra were normalized to the intensity of the corresponding C 1s peaks. Obviously, the amount of nitrogen species did not vary significantly in the post treated OCNT-48 and OCNT-72. Quantitative analysis of the N 1s spectra resulted in the derivation of the relative concentration of the modified nitrogen groups which are summarized in Table 25. A slight increase in the concentration of pyridinic and pyrrolic nitrogen groups was observed via extending the HNO_3 treatment time of the tubes. This might be attributed to the existence of a higher number of oxygen species on the surface of the tubes assisting further nitrogen modification of the tubes.

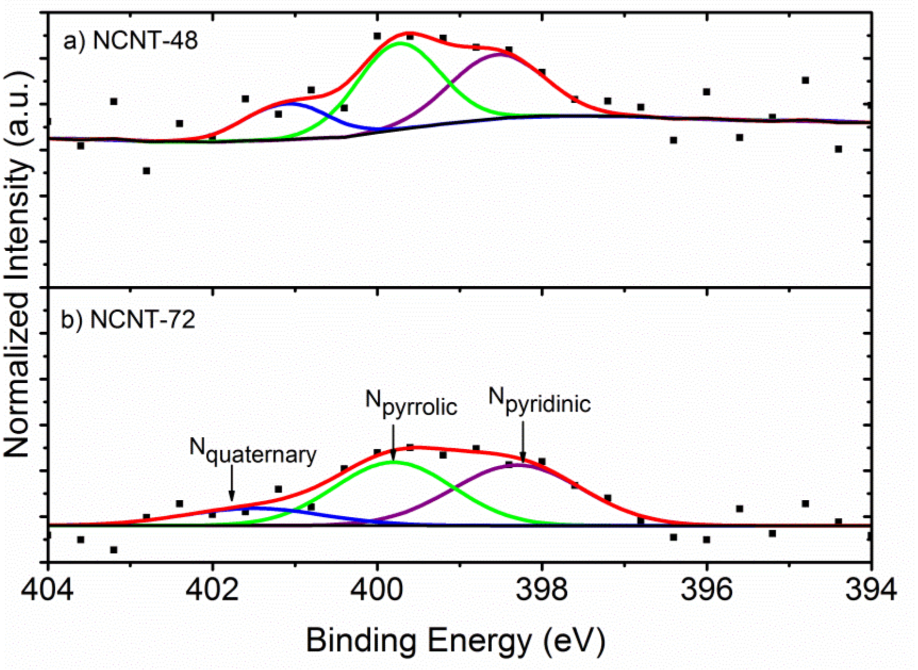

Figure 111. *XP N1s spectra of NCNTs obtained by post-treatment of OCNTs under NH_3 at 400 °C for 6 h. The spectra were normalized in intensity to the corresponding C 1s peaks.*

Table 25. *Relative content of functional groups (wt.%) present in XP C 1s spectra of MWCNT, PMWCNT and the functionalized ones.*

Sample	**Peak I (C=C)**	**Peak II (C-O)**	**Peak III (C=O)**	**Peak IV (COO-)**	**Peak V (π-π^*)**
MWCNT	67.2	13.8	5.1	6.3	7.5
PMWCNT	67.3	11.5	7.7	5.8	7.7
OCNT-48	57.6	19.2	6.7	8.1	8.4
OCNT-72	61.3	15.3	8	5.7	9.6
NCNT-48	64	14.2	8.5	4.6	8.5
NCNT-72	64.4	15.1	6.4	6.2	7.8

A quantitative analysis of the C 1s, O 1s, and N 1s spectra resulted in the estimation of the surface atomic concentrations of C, O, and N (Table 26 and Figure 112). The most abundant element in all of the tubes is carbon. Similar carbon content in the purified tubes (99.3 wt.%) as that of as received tubes (99.7wt.%) confirms that purification of the tubes did not provide any damage to the tubes. A little decrease in the carbon content in the purified tubes can be attributed to the removal of amorphous carbon from the surface of the tubes. Table 26 indicates that oxygen and nitrogen modification of the tubes caused the reduction in the content of carbon, which is in good agreement with the HRTEM study. No trace of nitrogen was observed in the pristine, purified, and oxygen-modified nanotubes and little amount of nitrogen exists on the surface of the NCNT-48 and NCNT-72 verifying the low yield of nitrogen modification to the surface of the tubes via this method.

Table 26. *Surface atomic concentrations of different tubes obtained by deconvolution of the XPS spectra.*

Sample	**C %**	**O%**			**N %**			
	Ctotal	**Ototal**	**C-O**	**C=O**	**Ntotal**	**Npyridinic**	**Npyrrolic**	**Nquaternary**
MWCNT	99.7	0.2	0.07	0.13	-	-	-	-
PMWCNT	99.3	0.6	0.5	0.1	-	-	-	-
OCNT-48	95	4.9	2.5	2.4	-	-	-	-
OCNT-72	94.7	5.2	2.8	2.4	-	-	-	
NCNT-48	96.4	3	1.8	1.2	0.5	0.21	0.25	0.1
NCNT-72	97.1	2.1	1.1	1	0.6	0.3	0.28	0.09

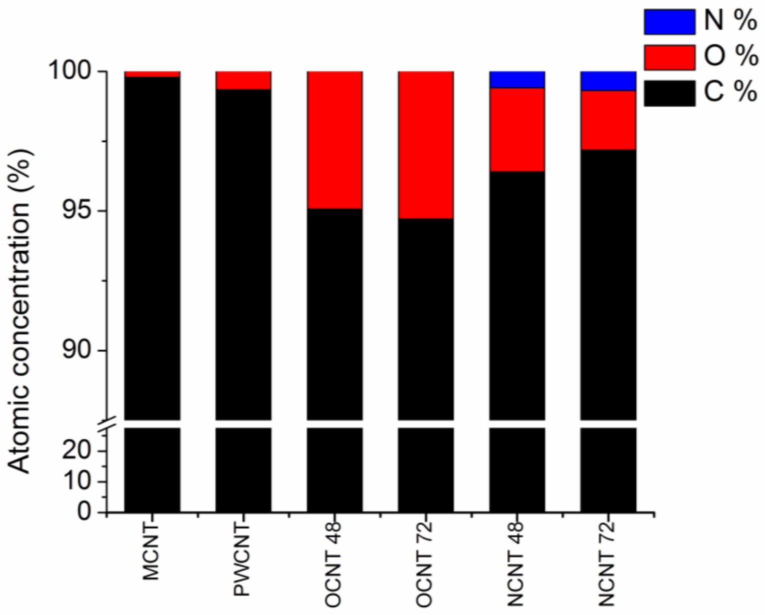

***Figure 112**. XPS compositional analysis of pristine, purified and functionalized tubes*

Figure 113 represents the Raman spectra (Renishaw, inVia Raman microscope) of as-received MWCNTs, PMWCNT, and the functionalized tubes. The two main characteristic bands presented in all the spectra at 1335 cm^{-1} and 1576 cm^{-1} can be assigned to the D-band and the G-band, respectively. The existence of amorphous carbon and any defects on the tubes result in the D-band as a double-resonance Raman mode. Moreover, the G-band is related to the crystallinity of the tubes. The Raman spectrum of MWCNT (Figure 114) shows multiple splitting of the G-band mode. A weak peak at 1506 cm^{-1} and a strong peak at 1576 cm^{-1} with two shoulders at 1557 cm^{-1} and 1607 cm^{-1} can be seen in the spectrum f. Interlayer interactions are likely inducing such graphite-like behavior in the tubes.[175]

The intensity ratio of the D-band to the G-band in this figure provides information regarding the produced structural disorder in the tubes due to various surface treatments. The higher I_D/I_G of the functionalized tubes as compared to that of pristine tubes suggests a higher number of defects, which has modified the tubes and altered the sp^2 hybridization of the carbon atoms in the graphene layer to sp^3 hybridization.

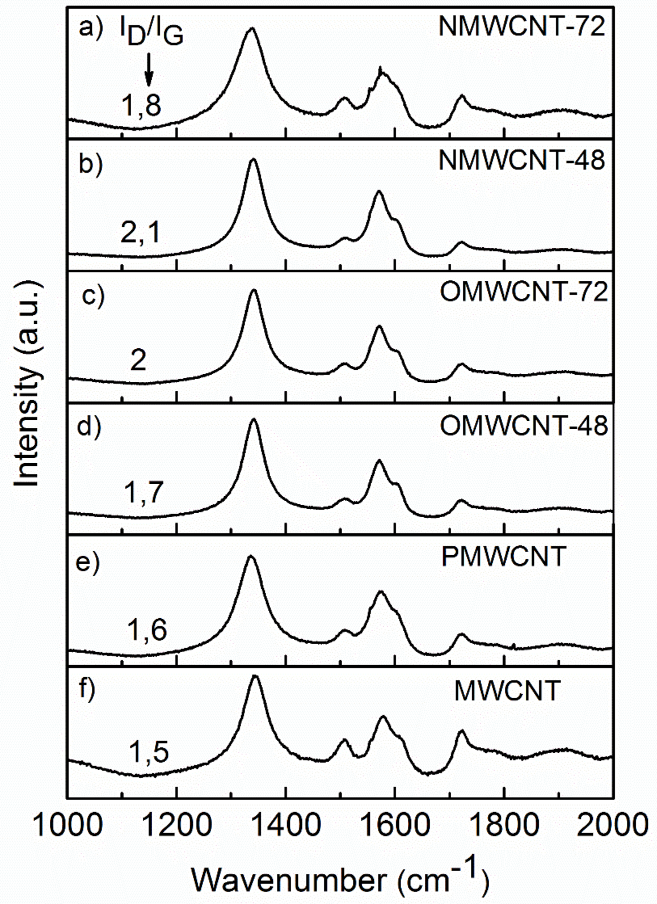

Figure 113. *Raman spectra of a) NMWCNT-72, b) NMWCNT-48, c) OMWCNT-72, d) OMWCNT-48, e) PMWCNT, and f) MWCNT. The D-band and G-band were observed at 1335 cm*$^{-1}$ *and 1576 cm*$^{-1}$*, respectively.*

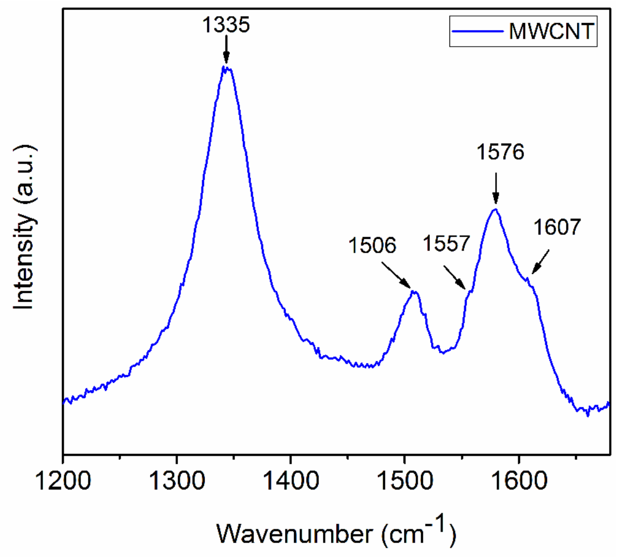

Figure 114. *Close up of Raman spectrum of pristine MWCNT.*

5.3 Thermal Stability Analysis

Thermal stability of CNTs tremendously depends on the degree of structural order.[174] Defect sites on the tubes are the sources of faster corrosion of the tubes. Thermogravimetric analysis (TGA) is an appropriate methodology to characterize the structural order of CNTs via investigating their thermal stability. TGA experiments were fulfilled using a NETZSCH STA 409 PC Luxx® to represent the thermal stability and purity of the different tubes by characterizing the weight loss of tubes during heating. In each experiment, carbon nanotubes (5 mg) were heated from 30 °C to 1000 °C at a heating rate of 5 K/min under O_2 flow. Figure 115 shows the thermogravimetric analysis of the as-received, purified, and functionalized tubes presenting the thermal stability of each tube during heating. Since the oxidation of carbon happens at temperatures higher than 200 °C, the graphs were normalized to this temperature. At lower temperatures, the absorbed water and organic impurities are removed from the tube walls.[176] The TGA curve of the as- received MWCNT (Figure 115I) shows that the oxidation of the pristine tubes begins at 493.3 °C and reaches a maximum weight loss rate at 533.2 °C. However, the initiation and oxidation temperatures of the functionalized tubes are lower than those of pristine tubes. As can be seen in Figure 115II and Table 27, after the pristine MWCNTs were purified, the initiation and oxidation temperatures increase compared to pristine tubes. It is ascribed to the removal of catalyst particles and amorphous carbon from the tube wall. However, the initiation and oxidation temperatures of the functionalized MWCNTs decrease noticeably. This behavior can be interpreted by referring back to the TEM figures. Premier stability of pristine MWCNTs and PMWCNTs than modified tubes toward high temperature oxidation is due to the existence of fewer defects in the tubes. Functionalization of CNT via vapor phase HNO_3 and NH_3 treatments alters the hexatomic structure of the tubes via modification of the chemical structure of the tubes. The added defects to the CNT surface decrease the oxidation stability of the tubes. Furthermore, it is feasible to estimate the residual mass for each sample from the weight loss curves after complete combustion of the tubes at 800 °C (Table 27). The calculated residual mass is attributed to the amount of metal oxides remnants of each tube. Since some carbon is removed during purification and modification of the tubes, a higher residual mass is observed owing to the higher catalyst residual.

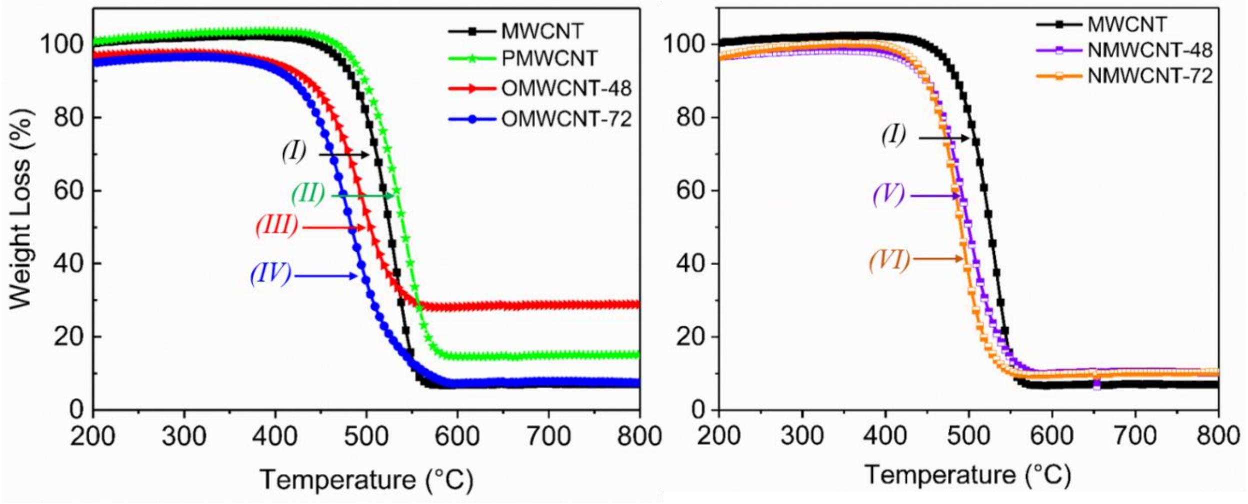

Figure 115. *TGA curves of (I) pristine MWCNT, (II) PMWCNT, (III) OMWCNT-48, (IV) OMWCNT-72, (V) NMWCNT-48, and (VI) NMWCNT-72.*

Table 27. *The TGA parameters obtained for the pristine, purified, and functionalized CNTs.*

Sample	Initiation T (°C)	Oxidation T (°C)	Residual mass percent (%)
MWCNT	493.3	533.2	6.71
PMWCNT	500.6	542.95	14.57
OMWCNT-48	448.0	494.11	28.11
OMWCNT-72	435.4	479.37	7.37
NMWCNT-48	457.8	498.74	10.03
NMWCNT-72	456.0	488.84	9.06

5.4 Surface Potential Characterization

For contact potential difference (CPD) measurements, the samples were transferred to a silicon substrate using a drop-casting method. As the tubes partially cover the silicon substrate, the measured CPD value on the silicon substrate can be used as reference value. Thereby, the work function of each of the different types of tubes can be determined without any ambiguity.

1,2-dichlorobenzene has been used as an appropriate solvent for dispersion of these tubes. Figure 116 depicts the SEM images of the dispersed (1,2-dichlorobenzene as dispersant) and drop-cast tubes on Si substrates. The topographical data were measured in tapping mode during the first pass for every scan line (Figure 117a-e). In the second pass, the tip lifted off the surface collects the CPD map of the samples, while following the height profile of the first pass (Figure 117f-j). The line profiles of the samples were collected along the white dashed lines of the tubes shown in Figure 117 k-o.

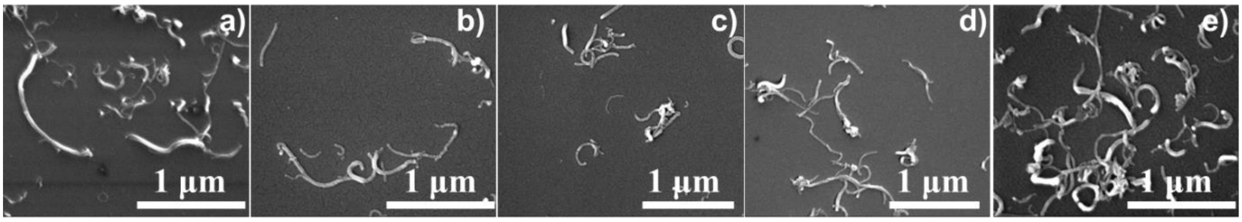

Figure 116. *SEM images of dispersed MWCNT (a), OCNT-48(b), OCNT-72 (c), NCNT-48 (d), and NCNT-72 (e) in 1,2-dichlorobenzene.*

The height of these nanotubes was typically 20-40 nm. The dark contrast observed in the CPD image of the OCNT-72 indicates a higher sample work function compared with the other samples. Therefore, the φ of the OCNT-48 is higher than that of the silicon substrate by ≈ 50 mV (Figure 117 m). Considering that φ_{si} is reported as 4.9 eV in literature, [177-178] the measured value of the work function of the oxygen-modified nanotube is consistent with the previously reported values for the acid-treated tubes in the liquid phase.[150, 168] In contrast to the OCNT-72, the CPD maps of pristine, OCNT-48, and nitrogen-modified tubes display a slight difference between the work function of silicon and these tubes (Figure 117k,l,n,o). The bright contrast in the CPD images of these tubes corresponds to a lower work function than observed with φ_{si} by 40, 38, 35, and 30 mV, respectively. The probable reason for this little alteration in the work function of these nanotubes might be due to the low degree of modification of the tubes using the gas-phase methodology.

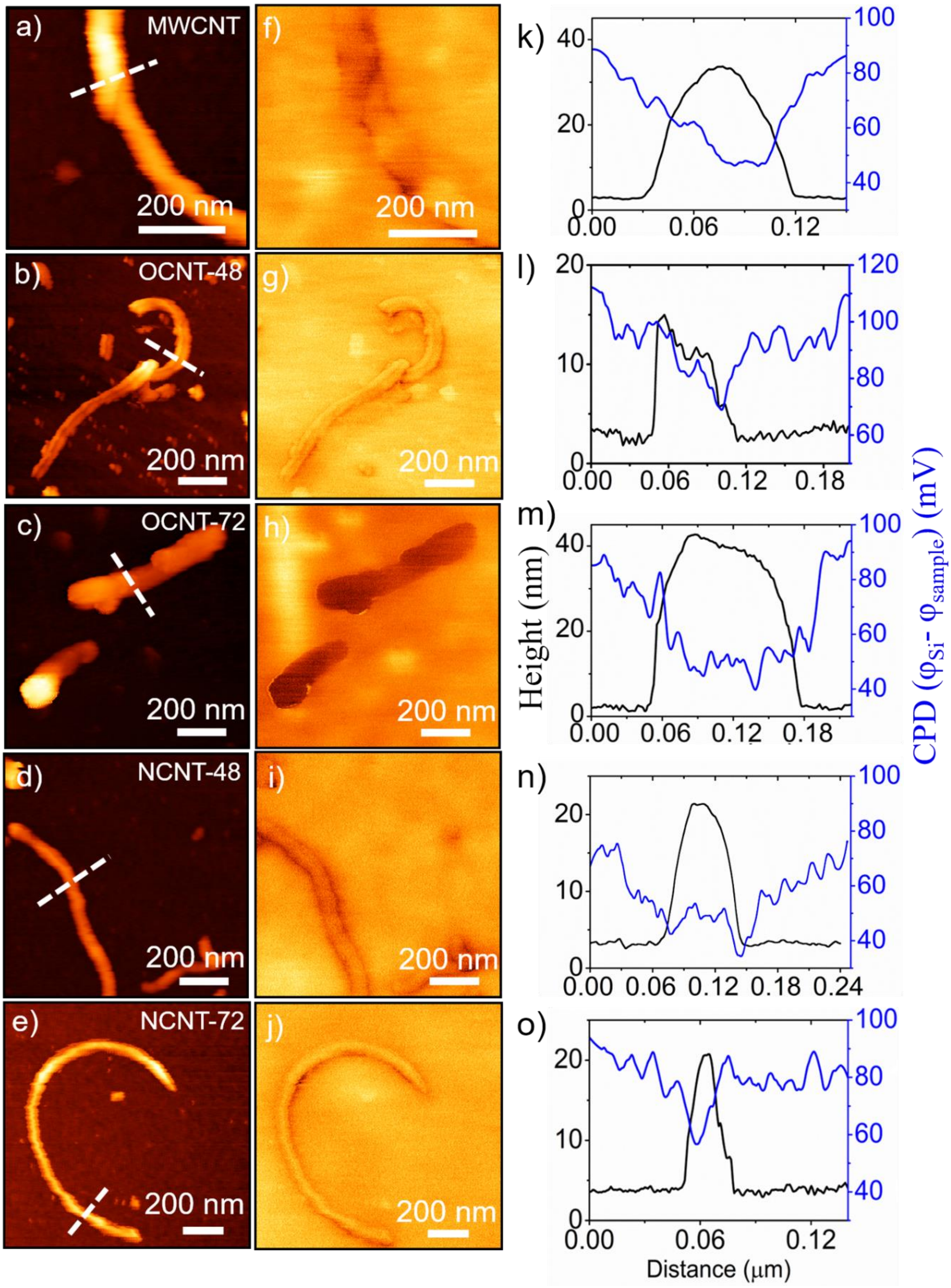

Figure 117. *The topography (a-e) and CPD images (f-j) of the tubes. The height and CPD profiles along the white dashed (k-o) as the black and blue lines, respectively.*

The KPFM study confirms that oxygen-modification of the tubes increased the value of the work function of the tubes emphasizing the p-doping of the tubes. Since the valence band maxima (VBM) position of most of the hole transport materials used in organic and perovskite solar cells is located around 5 eV,[119, 179] the obtained work function of the oxygen-modified tubes is consistent with the VBM of these hole transport materials confirming gas-phase oxygen-modified tubes are promising candidates to be applied to the hole transport layer (p-doped material) of solar cells. Further studies are needed to be accomplished to investigate the effect of pristine and oxygen-modified MWCNTs on the performance of perovskite solar cells.

5.5 Dispersibility of CNTs in Organic Solvents

The hydrophobic nature of the CNTs and the strong van-der-Waals interaction between the tubes hinder their solubility in most solvents. Utilizing CNTs in thin film solar cells raises concerns with regard to appropriate individualization of the tubes in order to provide convenient transport pathways for charges to the electrodes. Agglomeration of the tubes can be detrimental for the performance of the devices.[180] Optimized spatial distribution and improved solubility of CNTs on solvents are, therefore, the major requirements to acquire desirable properties of CNTs.

Among several organic solvents utilized for dispersion of the tubes, 1,2-dichlorobenzene was selected as a proper solvent for the dispersion of pristine MWCNT, PMWCNT and functionalized tubes and determination of the extinction coefficient of each of the tubes. For this purpose, UV-Vis spectra were collected for each of the diluted samples (Figure 118) and absorbance at 500 nm, A_{500}, was measured and then divided to the optical length, l, to give A_{500}/l. These data are plotted versus the initial concentration of CNTs (Figure 119). Based on the Beer-Lambert law, the slopes of these graphs provide extinction coefficients for each type of tube. The inset table in Figure 119 depicts the variation of the extinction coefficients due to functionalization. MWCNTs and purified ones show the lowest extinction coefficients attributed to their low solubility in the organic solvent. Moreover, enhancement in the extinction coefficients of the oxidized tubes (34.3 ml mg^{-1} cm^{-1}) confirms that oxygen functionalization of MWCNT improved the solubility of the tubes in the organic solvent. From these values, it is evident that the OMWCNT has the highest degree of dispersibility in the organic solvent compared to the other tubes. However, no considerable improvement is observed for the extinction coefficient of NMWCNTs (27.5 ml mg^{-1} cm^{-1}). It can be concluded that the type of functional group can determine the solubility of the tubes in the organic solvents. As a consequence, it can be inferred that the CNT structure, solubility, amount of defects, and type of functional groups influence the extinction coefficient, which is in agreement with previous research for SWCNTs.[181]

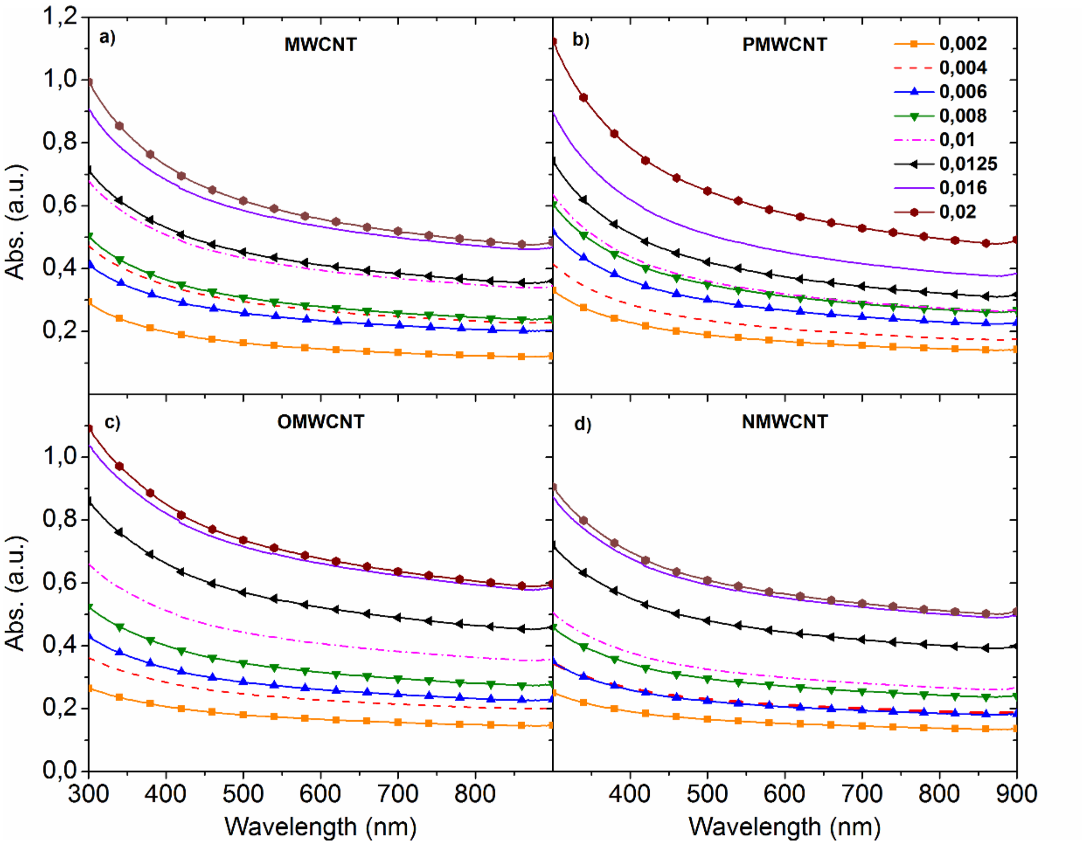

Figure 118. *UV-Vis spectra of dispersed a) pristine MWCNTs, b) PMWCNT, c) OMWCNT-48, and d) NMWCNT-48 in 1,2-dichlorobenzene.*

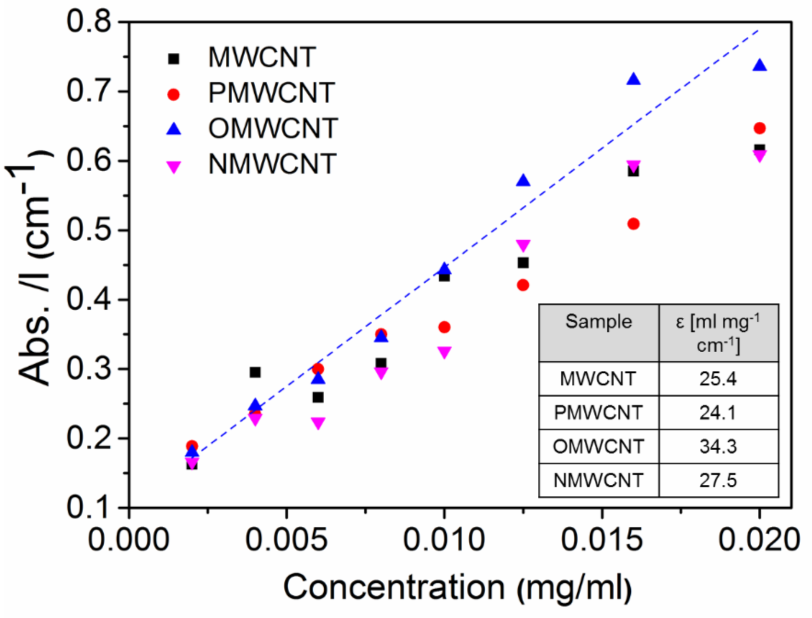

Sample	ε [ml mg^{-1} cm^{-1}]
MWCNT	25.4
PMWCNT	24.1
OMWCNT	34.3
NMWCNT	27.5

Figure 119. *Absorbance per optical length measured at λ = 500 nm, A_{500}/l, before centrifugation as a function of nanotube concentration. The dashed line depicts the fitted line to the scattered values of OMWCNT. The inset table shows the calculated extinction coefficient for the tubes.*

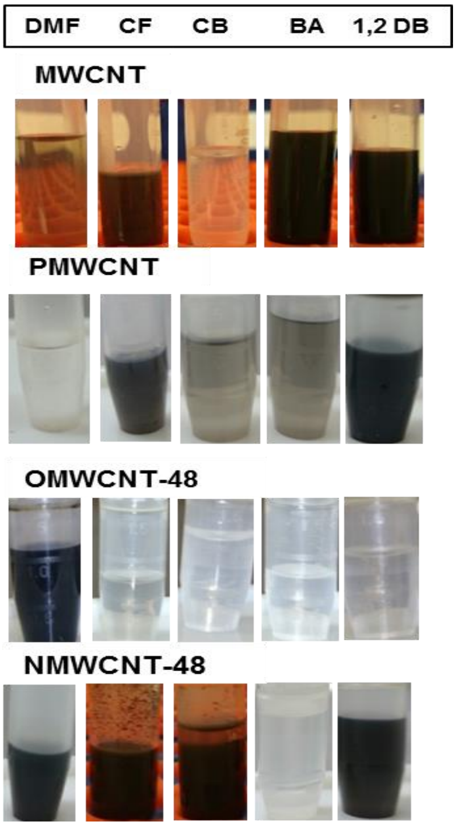

Figure 120. *Digital photo images of a) MWCNT, b) PMWCNT, c) OMWCNT-48, and d) NMWCNT-48 in organic solvents (DMF, CF, CB, BA and 1,2-DB).*

Table 28. *Capability of different organic solvents for dispersion of pristine, purified, and functionalized CNTs.*

Tube	1,2-DB	BA	CF	CB	DMF
MWCNT	Yes	Yes	Yes	No	Yes
PMWCNT	Yes	Yes	Yes	Yes	No
OMWCNT-48	Yes	No	Yes	No	Yes
NMWCNT-48	Yes	Yes	No	No	Yes

Figure 120 shows the digital photographs of supernatants of sonicated 1 mg ml^{-1} CNTs in different organic solvents followed by 1 h centrifugation at 10 k rpm. The supernatants of the tubes were collected after centrifugation. A summary of the dispersion ability of these solvents is depicted in Table 28. As this figure shows, a huge amount of MWCNTs are transferred to the organic phase when benzyl alcohol, 1,2-dichlorobenzene, chloroform, and dimethylformamide were utilized. NMWCNT-48 was sonicated in the same organic solvents. However, in the chloroform and chlorobenzene-NMWCNT solutions, phase separation between organic solvent and tubes is observed ascribed to the incompatibility of the tubes with these organic solvents. Therefore, no further centrifugation was performed for these two solutions. Among these solutions, the samples with bright colors confirm no compatibility of the tubes with the solvents. In order to visualize the quality of dispersion, SEM was performed. Figure 121 shows SEM images of pristine MWCNTs and purified MWCNTs dispersed in various organic solvents. As evidenced by SEM (Figure 121a-d), pristine MWCNTs could be dispersed properly in 1,2-dichlorobenzene and chloroform. However, they aggregate in benzyl alcohol and dimethylformamide.

The same experimental procedures were used for dispersion of purified MWCNTs in organic solvents. SEM images of these samples (Figure 121e-h) display how PMWCNTs dispersed in different organic solvents. From these images, it can be deduced that all of these solvents have appropriate ability to individualize PMWCNTs. OMWCNT-48 was utilized to investigate the compatibility of oxygen functionalized tubes with an organic phase. Among these supernatants DMF-OMWCNT depicts dark black color (Figure 120) emphasizing the existence of a large amount of tubes in the solution. In addition, SEM images (Figure 122) depict that the tubes modified by oxygen and nitrogen were properly dispersed in 1,2-dichlorobenzene and dimethylformamide. Moreover, chloroform and benzyl alcohol could appropriately disperse oxygen and nitrogen functionalized tubes, respectively.

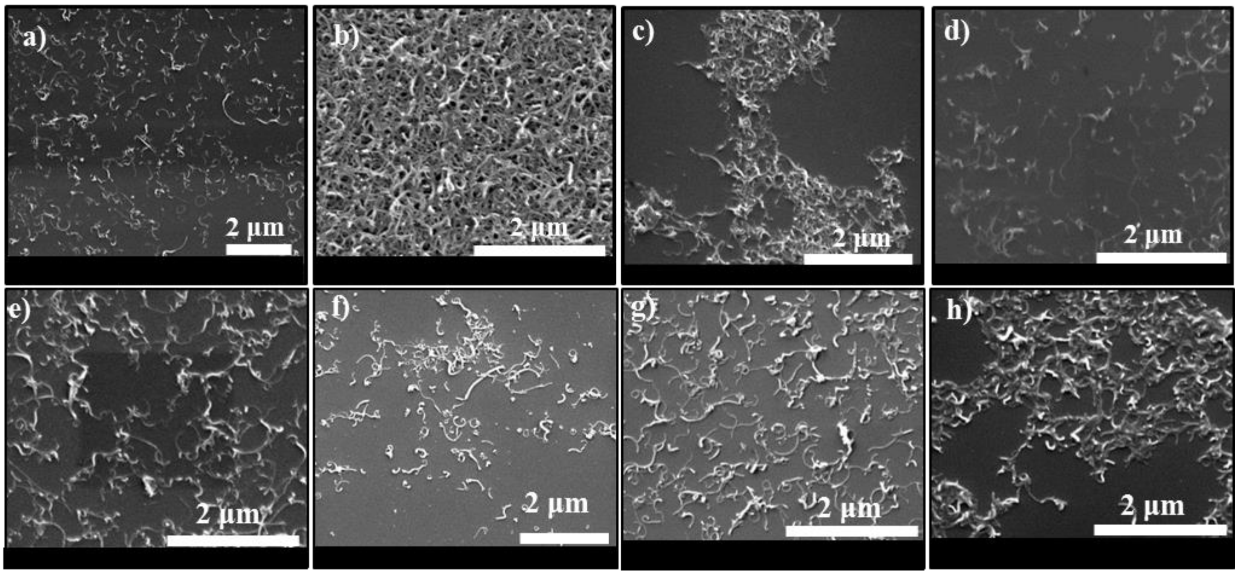

Figure 121. *SEM images of dispersed MWCNTs in a) 1,2-dichlorobenzene, b) benzyl alcohol, c) dimethylformamide and d) chloroform. SEM images of dispersed PMWCNT in e) 1,2-dichlorobenzene, f) benzyl alcohol, g) chlorobenzene and h) chloroform deposited on Si wafer.*

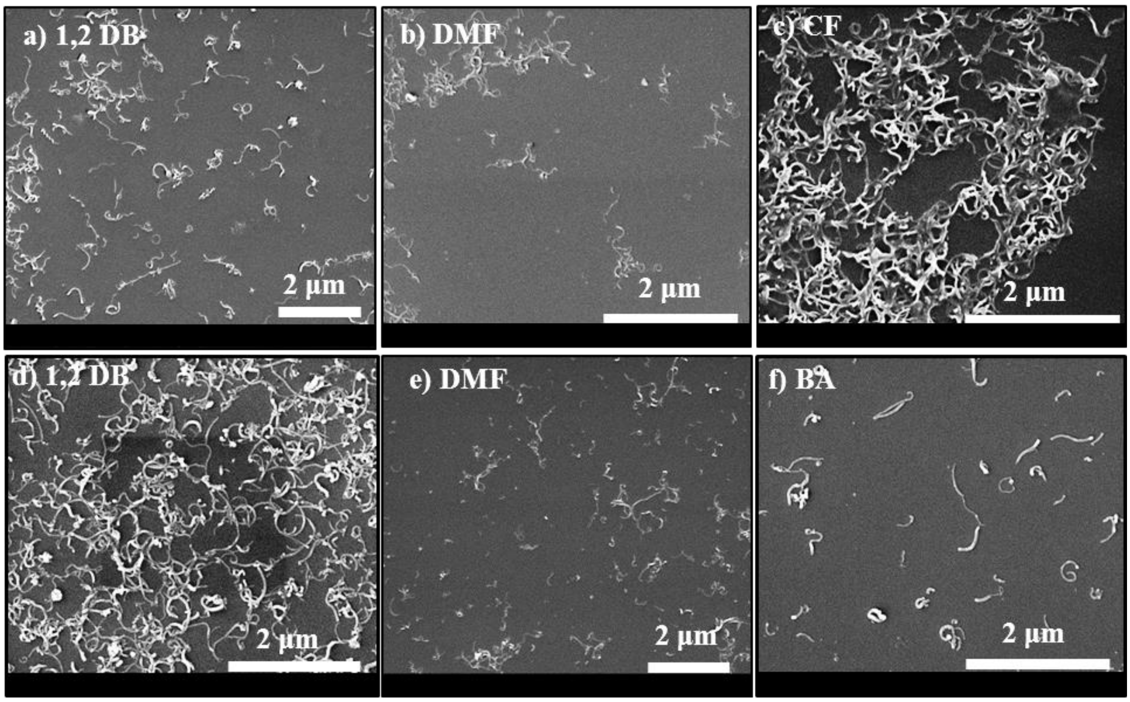

Figure 122. *SEM images of dispersed oxidized MWCNTs in a) 1,2-dichlorobenzene, b) dimethylformamide and c) chloroform. Second row: SEM images of dispersed nitrogen doped MWCNT in d) 1,2-dichlorobenzene, e) dimethylformamide and f) benzyl alcohol deposited on Si wafer.*

5.6 Conclusions

In this chapter, gas-phase oxygen and nitrogen modification of MWCNTs, and chemical, thermal, and electrical properties of the pristine and functionalized tubes were presented. TEM and Raman studies demonstrated that functionalization of the tubes generated more defects on the tube sidewall. Elemental analysis revealed that the increase in the treatment time of MWCNT in HNO_3 vapor resulted in the increase of oxygen content as well as enhancement in the nitrogen content. The type and amount of these functional oxygen and nitrogen groups were characterized using XPS measurements. Evidently, the limited surface area of the nanotubes makes them capable of accepting smaller oxygen species at the surface of the tubes than large oxygen groups. Creation of these defects on the tubes diminished the thermal stability of the functionalized tubes, as disclosed by TGA. Work function of the tubes were measured by KPFM indicating an increase in the work function of the oxygen modified tube in comparison with the pristine tubes.

Oxygen modification of MWCNT ameliorated the extinction coefficients of the tubes as compared to that of pristine, purified, and nitrogen-modified ones. This study revealed the dispersibility of pristine and functionalized CNTs in various organic solvents, which gives an insight for the incorporation of these tubes into charge conductive layers of thin film solar cells.

Chapter 6.
Conclusions and Future Work

6.1 Conclusions

The main aim of this research work concerns the study of several parameters affecting fabrication of high-quality solution-processed perovskite films and subsequently their PV performance in addition to proposing lead-free semiconducting and carbon-based materials to overcome the toxicity and stability issues associated with lead-based perovskite materials. This work is expected to facilitate realization of high-performance Pb-free halide semiconductor systems, through the prospect of a robust approach for producing high-quality films of controlled thickness and morphology. Moreover, it provides technical knowledge and know-how for utilization of oxygen and nitrogen modified carbon nanotubes in any electronic application.

Organic-inorganic Perovskite Solar Cells

A single-step solution-processed approach was developed to deposit uniform and compact pristine and chlorine incorporated $CH_3NH_3PbI_3$ films. Structural and morphological characterization were carried out to investigate the influence of antisolvent treatment, solvent evaporation rate, chlorine incorporation, and casting solvent on $CH_3NH_3PbI_3$ films. A $CH_3NH_3PbI_3$ film with high surface coverage is achievable with solvent engineering using DMSO additive to CH_3NH_3I-PbI_2-GBL solution and applying antisolvent (toluene) during spin coating. The single-step solution processed $CH_3NH_3PbI_3$ using DMF, DMF/GBL, and DMSO/GBL results in the formation of needle like perovskite films. Annealing conditions and spin coating parameters affecting solvent evaporation rate significantly modify the crystallization of $CH_3NH_3PbI_3$ film, most notably the average grain size and roughness of the film. Chlorine incorporation into $CH_3NH_3PbI_3$ film yields improvement of perovskite morphology as well as PV performance in the inverted device architecture. The results obtained in this study highlight the importance of solvent engineering to fabricate compact and pinhole-free films of $CH_3NH_3PbI_3$.

XPS analysis demonstrates formation of metallic lead (Pb^0) on the surface of annealed $CH_3NH_3PbI_3$ film. Increasing annealing time and temperature results in an increase in the amount of

Pb^0 suggesting the sensitivity of perovskite film to the annealing process. Degradation behavior of pinhole-free inverted-structure PSCs based on ITO/PEDOT:PSS/$CH_3NH_3PbI_3$/C60/Ca/Al was investigated by XPS. In the absence of moisture, illumination, and heat, iodine migration from the perovskite layer through ETL (C60/Ca) was detected resulting in the formation of stable AlI_3 compound on the surface of the cathode. The use of the more stable silver (Ag) cathode preserves the device from prompt degradation. XPS study reveals the importance of using a protective layer between the perovskite/ETL and metal cathode to suppress the degradation of the perovskite and the metal cathode.

Multidimensional Bismuth Halide Semiconductors

Non-toxic bismuth based semiconducting materials have been introduced as alternative compounds to lead-based perovskite materials for optoelectronic applications. A versatile two-step approach consisting of coevaporation of metal halides followed by annealing under various atmospheres has been applied for growing smooth and compact films of $Cs_3Bi_2I_9$, $Rb_3Bi_2I_9$, $AgBi_2I_7$, $AgBiI_4$, and Ag_2BiI_5. Optimization of the coevaporation and post-deposition annealing processes led to the growth of single-phase hexagonal $Cs_3Bi_2I_9$ (0D dimer), monoclinic $Rb_3Bi_2I_9$ (2D layer), cubic $AgBi_2I_7$ and $AgBiI_4$ (3D), and rhombohedral Ag_2BiI_5 structures.

Increasing the Ag-content of the as-deposited films from $AgBi_2I_7$ to Ag_2BiI_5 causes formation of rhombohedral unit cells with bigger c lattice constant along with promoting the growth of smaller grains. Although several stoichiometries of as-deposited silver bismuth iodide films form within a rhombohedral structure type, depending on the composition of the as-deposited film a crystallographic phase transition from the rhombohedral to cubic structures can occur via a post-deposition annealing process. TD-XRD in combination with SEM/EDX compositional analysis reveal that the probability of the crystallographic phase transition to the cubic phase upon heating for silver bismuth iodide films is higher for bismuth-rich as-deposited film compositions.

The optical band gaps were determined by UV-vis spectroscopy suggesting direct band gaps of ~ 2 eV for $Cs_3Bi_2I_9$ and $Rb_3Bi_2I_9$ and ~ 1.8 eV for silver bismuth iodide compounds. XPS surface compositional analysis suggests the sensitivity of annealed BiI_3, $Rb_3Bi_2I_9$, and $AgBiI_4$ film surfaces (not the as-deposited films) to Bi^{3+} to Bi^0 reduction. Angle resolved XPS analysis reveals higher concentration of Bi^0 at the topmost surface of $Rb_3Bi_2I_9$ than in the layers underneath.

Electronic structure properties of these compounds were studied using the UPS and IPES techniques. The VBM positions relative to the vacuum level were determined by UPS, showing relatively deep VBM energy levels (~ 6 eV) compared to the widely used lead-based halide perovskites. Except $AgBiI_4$ which shows intrinsic semiconducting behavior, other compounds namely $Cs_3Bi_2I_9$, $Rb_3Bi_2I_9$, $AgBi_2I_7$, and Ag_2BiI_5 are n-type semiconductors. Photovoltaic performance of $AgBiI_4$ as light absorber has been studied in a planar heterojunction solar cell. A large degree of hysteresis and V_{OC} of as high as 0.84 V and PCE of ~ 0.9 % in the reverse scan were achieved.

Gas-phase Functionalized Multiwalled Carbon Nanotubes

Vapor-phase oxygen and nitrogen modifications of MWCNTs were performed. Structural characterization of the tubes reveals formation of defects on the surface of the tubes in the functionalization process. Extending the treatment time of the purified tubes in HNO_3 yields an increase in the content of the modified oxygen groups. The amount of nitrogen groups that can be inserted into the surface of the nanotubes after a post-treatment with NH_3 correlates well with the oxygen content in the OCNTs. Elemental analysis was performed to analyze the type and amount of the functional groups on the tube surface. XPS in combination with TPD studies reveal that nitrogen modification of the tubes occurs via decomposition of surface oxygen groups and further substitution with nitrogen species. MWCNTs tend to accept smaller oxygen functional groups such as hydroxyl, carbonyl, and ether on the surface than the larger oxygen species (e.g. carboxylic groups and carboxylic anhydrides). Thermal stability of the pristine and functionalized tubes has been checked by TGA demonstrating lower stability of the functionalized tubes relative to the pristine MWCNTs. Oxygen functionalization of MWCNTs enhances the dispersibility of the tubes in organic solvents. Modification of the CNTs by more electronegative oxygen atoms increased the work function of the tubes making them a proper material for the hole transport layer of solar cells. This study can help to utilize oxygen and nitrogen functionalized tubes in thin film solar cells.

6.2 Future Work

A comprehensive study has been carried out on the functionalization and characterization of CNTs. A worthwhile extension of this work would be to measure work functions of the tubes using UPS to provide a reliable comparison with the results from KPFM. In addition, utilization of these tubes in perovskite solar cells as either a hydrophobic protective layer or as a highly conductive material for the transport layers can be examined to explore the possibility of stability and performance enhancement of the cells. Within the scope of perovskite fabrication, further studies are needed to explore the origin of the detected Pb^0 on the surface of the $CH_3NH_3PbI_3$ film. More thorough optimization of the annealing process may prevent formation of metallic lead on the surface.

An improvement in the device PCE for bismuth-based solar cells is a clear objective. This goal may be achieved by further improvement of several inherent properties of these materials such as mobility of charge carriers, defect density, transport and trapping. It may also be worth investigating the origin of the observed metallic bismuth on the surface of the annealed BiI_3, $Rb_3Bi_2I_9$, and $AgBiI_4$ films to avoid creation of recombination centers, which deteriorate the performance of these materials in optoelectronic applications. Another possibility which may enhance the efficiency of Bi-based solar cells is to use hole transport materials with deep VBM to provide better band alignment with the deep VBM of bismuth based semiconductors.

A detailed investigation of the mechanism of the observed crystallographic phase transition in silver bismuth iodide could also prove to be interesting for the utilization of this material for single junction solar cells. In addition, a study of possible differences in the electrical properties of cubic and rhombohedral silver bismuth iodide can give us an insight for the appropriate utilization of this material.

Finally, the optical properties of $Cs_3Bi_2I_9$ and $Rb_3Bi_2I_9$ have been studied revealing wide band gaps of ~ 2 eV for these compounds. Such relatively low toxic and stable materials might be promising candidates for making a top cell in a tandem configuration with silicon or CIGS solar cells. The combination of a top cell with 2.1 eV band gap with a bottom cell of 1.1-1.3 eV band gap is expected to achieve over 25% PCE under 1 sun illumination.[182]

List of Figures

List of Tables

References

1. Stocker, T., Climate change 2013: the physical science basis: Working Group I contribution to the Fifth assessment report of the Intergovernmental Panel on Climate Change. *Cambridge University Press*: **2014**.

2. Masanet, E. R.; Poponi, D.; Bryant, T.; Burnard, K.; Cazzola, P.; Dulac, J.; Pales, A. F.; Husar, J.; Janoska, P.; Munuera, L., Energy technology perspectives 2016-towards sustainable urban energy systems. *International Energy Agency*: **2016**.

3. Europe, S. P. *"Global Market Outlook For Solar Power"*; 2017-2022.

4. Research Cell Efficiency Records; National Center for Photovoltaics at the National Renewable Energy Laboratory: Golden, CO. https://www.nrel.gov/pv/ (accessed July 10, **2018**)

5. Nelson, J., The physics of solar cells. *World Scientific Publishing Company*: **2003**.

6. Shockley, W.; Queisser, H. J., Detailed balance limit of efficiency of p-n junction solar cells. *Journal of applied physics* **1961**, 32, 510-519.

7. Etgar, L.; Gao, P.; Xue, Z.; Peng, Q.; Chandiran, A. K.; Liu, B.; Nazeeruddin, M. K.; Grätzel, M., Mesoscopic $CH_3NH_3PbI_3/TiO_2$ heterojunction solar cells. *Journal of the American Chemical Society* **2012**, 134, 17396-17399.

8. Kojima, A.; Teshima, K.; Miyasaka, T.; Shirai, Y., Novel photoelectrochemical cell with mesoscopic electrodes sensitized by lead-halide compounds *(2)*, Meeting Abstracts, *The Electrochemical Society* **2006**, 397-397.

9. Kojima, A.; Teshima, K.; Shirai, Y.; Miyasaka, T., Organometal halide perovskites as visible-light sensitizers for photovoltaic cells. *Journal of the American Chemical Society* **2009**, 131, 6050-6051.

10. Stranks, S. D.; Eperon, G. E.; Grancini, G.; Menelaou, C.; Alcocer, M. J. P.; Leijtens, T.; Herz, L. M.; Petrozza, A.; Snaith, H. J., Electron-hole diffusion lengths exceeding 1 micrometer in an organometal trihalide perovskite absorber. *Science* **2013**, 342, 341-344.

11. De Wolf, S.; Holovsky, J.; Moon, S.-J.; Löper, P.; Niesen, B.; Ledinsky, M.; Haug, F.-J.; Yum, J.-H.; Ballif, C., Organometallic halide perovskites: sharp optical absorption edge and its relation to photovoltaic performance. *The Journal of Physical Chemistry Letters* **2014**, 5, 1035-1039.

12. Ehtesham, A.; Wong, W.; Wong, H. Y.; Zaman, M., Recent advances in fabrication techniques of perovskite solar cells: A Review. *American Journal of Applied Sciences* **2016**, 13, 1290-1314.

13. Jeon, N. J.; Noh, J. H.; Yang, W. S.; Kim, Y. C.; Ryu, S.; Seo, J.; Seok, S. I., Compositional engineering of perovskite materials for high-performance solar cells. *Nature* **2015**, 517, 476-480.

14. McMeekin, D. P.; Sadoughi, G.; Rehman, W.; Eperon, G. E.; Saliba, M.; Hörantner, M. T.; Haghighirad, A.; Sakai, N.; Korte, L.; Rech, B.; Johnston, M. B.; Herz L. M.; Snaith, H.J., A mixed-cation lead mixed-halide perovskite absorber for tandem solar cells. *Science* **2016**, 351, 151-155.

15. Green, M. A.; Ho-Baillie, A.; Snaith, H. J., The emergence of perovskite solar cells. *Nature Photonics* **2014**, 8, 506-514.

16. Li, C.; Lu, X.; Ding, W.; Feng, L.; Gao, Y.; Guo, Z., Formability of ABX_3 (X= F, Cl, Br, I) halide perovskites. *Acta Crystallographica Section B* **2008**, 64, 702-707.

17. Im, J.-H.; Chung, J.; Kim, S.-J.; Park, N.-G., Synthesis, structure, and photovoltaic property of a nanocrystalline 2H perovskite-type novel sensitizer $(CH_3CH_2NH_3)PbI_3$. *Nanoscale Research Letters* **2012**, 7, 353.

18. Koh, T. M.; Fu, K.; Fang, Y.; Chen, S.; Sum, T. C.; Mathews, N.; Mhaisalkar, S. G.; Boix, P. P.; Baikie, T., Formamidinium-containing metal-halide: an alternative material for near-IR absorption perovskite solar cells. *The Journal of Physical Chemistry C* **2014**, 118, 16458-16462.

19. Zhao, Y.; Zhu, K., Organic–inorganic hybrid lead halide perovskites for optoelectronic and electronic applications. *Chemical Society Reviews* **2016**, 45, 655-689.

20. Cao, D. H.; Stoumpos, C. C.; Farha, O. K.; Hupp, J. T.; Kanatzidis, M. G., 2D homologous perovskites as light-absorbing materials for solar cell applications. *Journal of the American Chemical Society* **2015**, 137, 7843-7850.

21. Xiao, Z.; Meng, W.; Wang, J.; Mitzi, D. B.; Yan, Y., Searching for promising new perovskite-based photovoltaic absorbers: the importance of electronic dimensionality. *Materials Horizons* **2017**, 4, 206-216.

22. Umari, P.; Mosconi, E.; De Angelis, F., Relativistic GW calculations on $CH_3NH_3PbI_3$ and $CH_3NH_3SnI_3$ perovskites for solar cell applications. *Scientific Reports* **2014**, 4, 4467.

23. Noel, N. K.; Stranks, S. D.; Abate, A.; Wehrenfennig, C.; Guarnera, S.; Haghighirad, A.-A.; Sadhanala, A.; Eperon, G. E.; Pathak, S. K.; Johnston, M. B.; Petrozza, A.; Herz, L. M.; Snaith, H. M., Lead-free organic–inorganic tin halide perovskites for photovoltaic applications. *Energy & Environmental Science* **2014**, 7, 3061-3068.

24. Stoumpos, C. C.; Malliakas, C. D.; Kanatzidis, M. G., Semiconducting tin and lead iodide perovskites with organic cations: phase transitions, high mobilities, and near-infrared photoluminescent properties. *Inorganic Chemistry* **2013**, 52, 9019-9038.

25. Yang, W. S.; Noh, J. H.; Jeon, N. J.; Kim, Y. C.; Ryu, S.; Seo, J.; Seok, S. I., High-performance photovoltaic perovskite layers fabricated through intramolecular exchange. *Science* **2015**, 348, 1234-1237.

26. Hao, F.; Stoumpos, C. C.; Cao, D. H.; Chang, R. P. H.; Kanatzidis, M. G., Lead-free solid-state organic–inorganic halide perovskite solar cells. *Nature Photonics* **2014**, 8, 489-494.

27. Lin, Q.; Armin, A.; Burn, P. L.; Meredith, P., Organohalide perovskites for solar energy conversion. *Accounts of Chemical Research* **2016**, 49, 545-553.

28. Chen, Q.; De Marco, N.; Yang, Y. M.; Song, T.-B.; Chen, C.-C.; Zhao, H.; Hong, Z.; Zhou, H.; Yang, Y., Under the spotlight: The organic–inorganic hybrid halide perovskite for optoelectronic applications. *Nano Today* **2015**, 10, 355-396.

29. Lin, Q.; Armin, A.; Nagiri, R. C. R.; Burn, P. L.; Meredith, P., Electro-optics of perovskite solar cells. *Nature Photonics* **2015**, 9, 106-112.

30. Miyata, A.; Mitioglu, A.; Plochocka, P.; Portugall, O.; Wang, J. T.-W.; Stranks, S. D.; Snaith, H. J.; Nicholas, R. J., Direct measurement of the exciton binding energy and effective masses for charge carriers in organic-inorganic tri-halide perovskites. *Nature Physics* **2015**, 11, 582-587.

31. Wehrenfennig, C.; Eperon, G. E.; Johnston, M. B.; Snaith, H. J.; Herz, L. M., High charge carrier mobilities and lifetimes in organolead trihalide perovskites. *Advanced Materials* **2014**, 26, 1584-1589.

32. Ponseca Jr, C. S.; Savenije, T. J.; Abdellah, M.; Zheng, K.; Yartsev, A.; Pascher, T.; Harlang, T.; Chabera, P.; Pullerits, T.; Stepanov, A.; Wolf, J.-P.; Sundström, V., Organometal halide perovskite solar cell materials rationalized: ultrafast charge generation, high and microsecond-long balanced mobilities, and slow recombination. *Journal of the American Chemical Society* **2014**, 136, 5189-5192.

33. Zhu, X.-Y.; Podzorov, V., Charge carriers in hybrid organic–inorganic lead halide perovskites might be protected as large polarons. *The Journal of Physical Chemistry Letters* **2015**, 6, 4758-4761.

34. Xing, G.; Mathews, N.; Sun, S.; Lim, S. S.; Lam, Y. M.; Grätzel, M.; Mhaisalkar, S.; Sum, T. C., Long-range balanced electron-and hole-transport lengths in organic-inorganic $CH_3NH_3PbI_3$. *Science* **2013**, 342, 344-347.

35. Lee, M. M.; Teuscher, J.; Miyasaka, T.; Murakami, T. N.; Snaith, H. J., Efficient hybrid solar cells based on meso-superstructured organometal halide perovskites. *Science* **2012**, 338, 643-647.

36. Song, Z.; Watthage, S. C.; Phillips, A. B.; Tompkins, B. L.; Ellingson, R. J.; Heben, M. J., Impact of processing temperature and composition on the formation of methylammonium lead iodide perovskites. *Chemistry of Materials* **2015**, 27, 4612-4619.

37. Wang, Q.; Shao, Y.; Dong, Q.; Xiao, Z.; Yuan, Y.; Huang, J., Large fill-factor bilayer iodine perovskite solar cells fabricated by a low-temperature solution-process. *Energy & Environmental Science* **2014**, 7, 2359-2365.

38. Burschka, J.; Pellet, N.; Moon, S.-J.; Humphry-Baker, R.; Gao, P.; Nazeeruddin, M. K.; Grätzel, M., Sequential deposition as a route to high-performance perovskite-sensitized solar cells. *Nature* **2013**, 499, 316–319.

39. Hu, L.; Peng, J.; Wang, W.; Xia, Z.; Yuan, J.; Lu, J.; Huang, X.; Ma, W.; Song, H.; Chen, W.; Cheng, Y.-B.; Tang, J., Sequential deposition of $CH_3NH_3PbI_3$ on planar NiO film for efficient planar perovskite solar cells. *Acs Photonics* **2014,** 1, 547-553.

40. Brittman, S.; Adhyaksa, G. W. P.; Garnett, E. C., The expanding world of hybrid perovskites: materials properties and emerging applications. *MRS Communications* **2015**, 5, 7-26.

41. Nicolosi, V.; Chhowalla, M.; Kanatzidis, M. G.; Strano, M. S.; Coleman, J. N., Liquid exfoliation of layered materials. *Science* **2013**, 340, 1226419.

42. Chen, Q.; Zhou, H.; Hong, Z.; Luo, S.; Duan, H.-S.; Wang, H.-H.; Liu, Y.; Li, G.; Yang, Y., Planar heterojunction perovskite solar cells via vapor-assisted solution process. *Journal of the American Chemical Society* **2014**, 136, 622-625.

43. Hao, F.; Stoumpos, C. C.; Liu, Z.; Chang, R. P. H.; Kanatzidis, M. G., Controllable perovskite crystallization at a gas–solid interface for hole conductor-free solar cells with steady power conversion efficiency over 10%. *Journal of the American Chemical Society* **2014**, 136, 16411-16419.

44. Liu, M.; Johnston, M. B.; Snaith, H. J., Efficient planar heterojunction perovskite solar cells by vapour deposition. *Nature* **2013**, 501, 395-398.

45. Hariz, A. J., Perspectives on organolead halide perovskite photovoltaics. *Journal of Photonics for Energy* **2016,** 6, 032001.

46. Tavakoli, M. M.; Gu, L.; Gao, Y.; Reckmeier, C.; He, J.; Rogach, A. L.; Yao, Y.; Fan, Z., Fabrication of efficient planar perovskite solar cells using a one-step chemical vapor deposition method. *Scientific Reports* **2015**, 5, 14083.

47. Song, Z.; Watthage, S. C.; Phillips, A. B.; Heben, M. J., Pathways toward high-performance perovskite solar cells: review of recent advances in organo-metal halide perovskites for photovoltaic applications. *Journal of Photonics for Energy* **2016**, 6, 022001.

48. Aristidou, N.; Sanchez-Molina, I.; Chotchuangchutchaval, T.; Brown, M.; Martinez, L.; Rath, T.; Haque, S. A., The role of oxygen in the degradation of methylammonium lead trihalide perovskite photoactive layers. *Angewandte Chemie International Edition* **2015**, 54, 8208-8212.

49. Babayigit, A.; Ethirajan, A.; Muller, M.; Conings, B., Toxicity of organometal halide perovskite solar cells. *Nature Materials* **2016**, 15, 247-251.

50. Bag, M.; Renna, L. A.; Adhikari, R. Y.; Karak, S.; Liu, F.; Lahti, P. M.; Russell, T. P.; Tuominen, M. T.; Venkataraman, D., Kinetics of ion transport in perovskite active layers and its implications for active layer stability. *Journal of the American Chemical Society* **2015**, 137, 13130-13137.

51. Habisreutinger, S. N.; Leijtens, T.; Eperon, G. E.; Stranks, S. D.; Nicholas, R. J.; Snaith, H. J., Carbon nanotube/polymer composites as a highly stable hole collection layer in perovskite solar cells. *Nano Letters* **2014**, 14, 5561-5568.

52. Eperon, G. E.; Stranks, S. D.; Menelaou, C.; Johnston, M. B.; Herz, L. M.; Snaith, H. J., Formamidinium lead trihalide: a broadly tunable perovskite for efficient planar heterojunction solar cells. *Energy & Environmental Science* **2014**, 7, 982-988.

53. Beal, R. E.; Slotcavage, D. J.; Leijtens, T.; Bowring, A. R.; Belisle, R. A.; Nguyen, W. H.; Burkhard, G. F.; Hoke, E. T.; McGehee, M. D., Cesium lead halide perovskites with improved stability for tandem solar cells. *The Journal of Physical Chemistry Letters* **2016**, 7, 746-751.

54. Li, Z.; Yang, M.; Park, J.-S.; Wei, S.-H.; Berry, J. J.; Zhu, K., Stabilizing perovskite structures by tuning tolerance factor: formation of formamidinium and cesium lead iodide solid-state alloys. *Chemistry of Materials* **2016**, 28, 284-292.

55. Saliba, M.; Matsui, T.; Domanski, K.; Seo, J.-Y.; Ummadisingu, A.; Zakeeruddin, S. M.; Correa-Baena, J.-P.; Tress, W. R.; Abate, A.; Hagfeldt, A.; Grätzel, M., Incorporation of rubidium cations into perovskite solar cells improves photovoltaic performance. *Science* **2016**, 354, 206-209.

56. Clark, S. J.; Donaldson, J. D.; Harvey, J. A., Evidence for the direct population of solid-state bands by non-bonding electron pairs in compounds of the type $CsM^{II}X_3$ (M^{II}= Ge, Sn, Pb; X= Cl, Br, I). *Journal of Materials Chemistry* **1995**, 5, 1813-1818.

57. Saparov, B.; Sun, J.-P.; Meng, W.; Xiao, Z.; Duan, H.-S.; Gunawan, O.; Shin, D.; Hill, I. G.; Yan, Y.; Mitzi, D. B., Thin-film deposition and characterization of a Sn-deficient perovskite derivative Cs_2SnI_6. *Chemistry of Materials* **2016**, 28, 2315-2322.

58. Stoumpos, C. C.; Frazer, L.; Clark, D. J.; Kim, Y. S.; Rhim, S. H.; Freeman, A. J.; Ketterson, J. B.; Jang, J. I.; Kanatzidis, M. G., Hybrid germanium iodide perovskite semiconductors: active lone pairs, structural distortions, direct and indirect energy gaps, and strong nonlinear optical properties. *Journal of the American Chemical Society* **2015,** 137, 6804-6819.

59. Lehner, A. J.; Fabini, D. H.; Evans, H. A.; Hébert, C.-A.; Smock, S. R.; Hu, J.; Wang, H.; Zwanziger, J. W.; Chabinyc, M. L.; Seshadri, R., Crystal and electronic structures of complex bismuth iodides $A_3Bi_2I_9$ (A= K, Rb, Cs) related to perovskite: aiding the rational design of photovoltaics. *Chemistry of Materials* **2015**, 27, 7137-7148.

60. McCall, K. M.; Stoumpos, C. C.; Kostina, S. S.; Kanatzidis, M. G.; Wessels, B. W., Strong electron–phonon coupling and self-trapped excitons in the defect halide perovskites $A_3M_2I_9$ (A= Cs, Rb; M= Bi, Sb). *Chemistry of Materials* **2017**, 29, 4129-4145.

61. Park, B. -W.; Philippe, B.; Zhang, X.; Rensmo, H.; Boschloo, G.; Johansson, E. M. J., Bismuth based hybrid perovskites $A_3Bi_2I_9$ (A: methylammonium or cesium) for solar cell application. *Advanced Materials* **2015**, 27, 6806-6813.

62. Pazoki, M.; Johansson, M. B.; Zhu, H.; Broqvist, P.; Edvinsson, T.; Boschloo, G.; Johansson, E. M. J., Bismuth iodide perovskite materials for solar cell applications: electronic structure, optical transitions, and directional charge transport. *The Journal of Physical Chemistry C* **2016**, 120, 29039-29046.

63. Ran, C.; Wu, Z.; Xi, J.; Yuan, F.; Dong, H.; Lei, T.; He, X.; Hou, X., Construction of compact methylammonium bismuth iodide film promoting lead-free inverted planar heterojunction organohalide solar cells with open-circuit voltage over 0.8 V. *The Journal of Physical Chemistry Letters* **2017**, 8, 394-400.

64. Singh, T.; Kulkarni, A.; Ikegami, M.; Miyasaka, T., Effect of electron transporting layer on bismuth-based lead-free perovskite $(CH_3NH_3)_3Bi_2I_9$ for photovoltaic applications. *ACS Applied Materials & Interfaces* **2016**, 8, 14542-14547.

65. Sun, S.; Tominaka, S.; Lee, J.-H.; Xie, F.; Bristowe, P. D.; Cheetham, A. K., Synthesis, crystal structure, and properties of a perovskite-related bismuth phase,$(NH_4)_3Bi_2I_9$. *APL Materials* **2016**, 4, 031101.

66. Khazaee, M.; Sardashti, K.; Sun, J.-P.; Zhou, H.; Clegg, C.; Hill, I. G.; Jones, J. L.; Lupascu, D. C.; Mitzi, D. B., A versatile thin-film deposition method for multidimensional semiconducting bismuth halides. *Chemistry of Materials* **2018**, 30, 3538–3544.

67. Du, K.-Z.; Meng, W.; Wang, X.; Yan, Y.; Mitzi, D. B., Bandgap engineering of lead-free double perovskite $Cs_2AgBiBr_6$ through trivalent metal alloying. *Angewandte Chemie International Edition* **2017**, 56, 8158-8162.

68. McClure, E. T.; Ball, M. R.; Windl, W.; Woodward, P. M., Cs_2AgBiX_6 (X= Br, Cl): new visible light absorbing, lead-free halide perovskite semiconductors. *Chemistry of Materials* **2016**, 28, 1348-1354.

69. Kim, Y.; Yang, Z.; Jain, A.; Voznyy, O.; Kim, G. -H.; Liu, M.; Quan, L. N.; García de Arquer, F. P.; Comin, R.; Fan, J. Z.; Sargent, E. H., Pure cubic-phase hybrid iodobismuthates $AgBi_2I_7$ for thin-film photovoltaics. *Angewandte Chemie International Edition* **2016**, 55, 9586-9590.

70. Oldag, T.; Aussieker, T.; Keller, H. L.; Preitschaft, C.; Pfitzner, A., Solvothermale synthese und bestimmung der kristallstrukturen von $AgBiI_4$ und Ag_3BiI_6. *Zeitschrift für anorganische und allgemeine Chemie* **2005**, 631, 677-682.

71. Sansom, H. C.; Whitehead, G. F.; Dyer, M. S.; Zanella, M.; Manning, T. D.; Pitcher, M. J.; Whittles, T. J.; Dhanak, V. R.; Alaria, J.; Claridge, J. B., $AgBiI_4$ as a lead-free solar absorber with potential application in photovoltaics. *Chemistry of Materials* **2017**, 29, 1538-1549.

72. Turkevych, I.; Kazaoui, S.; Ito, E.; Urano, T.; Yamada, K.; Tomiyasu, H.; Yamagishi, H.; Kondo, M.; Aramaki, S., Photovoltaic rudorffites: structure and optoelectronic properties. *ChemSusChem* **2017**, 10, 3754-3759.

73. Song, Z.; Watthage, S. C.; Phillips, A. B.; Liyanage, G. K.; Khanal, R. R.; Tompkins, B. L.; Ellingson, R. J.; Heben, M. J., Investigation of degradation mechanisms of perovskite-based photovoltaic devices using laser beam induced current mapping, *Thin Films for Solar and Energy Technology VII* **2015**, 9561, 956107.

74. Li, X.; Tschumi, M.; Han, H.; Babkair, S. S.; Alzubaydi, R. A.; Ansari, A. A.; Habib, S. S.; Nazeeruddin, M. K.; Zakeeruddin, S. M.; Grätzel, M., Outdoor performance and stability under elevated temperatures and long-term light soaking of triple-layer mesoporous perovskite photovoltaics. *Energy Technology* **2015**, 3, 551-555.

75. Mei, A.; Li, X.; Liu, L.; Ku, Z.; Liu, T.; Rong, Y.; Xu, M.; Hu, M.; Chen, J.; Yang, Y., A hole-conductor-free, fully printable mesoscopic perovskite solar cell with high stability. *Science* **2014**, *345*, 295-298.

76. Habisreutinger, S. N.; Leijtens, T.; Eperon, G. E.; Stranks, S. D.; Nicholas, R. J.; Snaith, H. J., Enhanced hole extraction in perovskite solar cells through carbon nanotubes. *The Journal of Physical Chemistry Letters* **2014**, 5, 4207-4212.

77. Aitola, K.; Sveinbjörnsson, K.; Correa-Baena, J.-P.; Kaskela, A.; Abate, A.; Tian, Y.; Johansson, E. M. J.; Grätzel, M.; Kauppinen, E. I.; Hagfeldt, A.; Boschloo, G., Carbon nanotube-based hybrid hole-transporting material and selective contact for high efficiency perovskite solar cells. *Energy & Environmental Science* **2016**, 9, 461-466.

78. Aitola, K.; Domanski, K.; Correa-Baena, J. P.; Sveinbjörnsson, K.; Saliba, M.; Abate, A.; Grätzel, M.; Kauppinen, E.; Johansson, E. M.; Tress, W., High temperature-stable perovskite solar cell based on low-cost carbon nanotube hole contact. *Advanced Materials* **2017**, 29, 1606398.

79. Lee, J.; Menamparambath, M. M.; Hwang, J. -Y.; Baik, S., Hierarchically structured hole transport layers of spiro-OMeTAD and multiwalled carbon nanotubes for perovskite solar cells. *ChemSusChem* **2015**, 8, 2358-2362.

80. Tonui, P.; Oseni, S. O.; Sharma, G.; Yan, Q.; Mola, G. T., Perovskites photovoltaic solar cells: An overview of current status. *Renewable and Sustainable Energy Reviews* **2018**, 91, 1025-1044.

81. Khazaee, M.; Sardashti, K.; Chung, C.-C.; Sun, J.-P.; Zhou, H.; Bergmann, E.; Dunlap-Shohl, W. A.; Han, Q.; Hill, I. G.; Jones, J. L.; Lupascu, D. C.; Mitzi, D. B., Dual-source evaporation of silver bismuth iodide films for planar junction solar cells. *Journal of Materials Chemistry A* **2019**, 7, 2095-2105.

82. Khazaee, M.; Xia, W.; Lackner, G.; Mendes, R. G.; Rümmeli, M.; Muhler, M.; Lupascu, D. C., Dispersibility of vapor phase oxygen and nitrogen functionalized multi-walled carbon nanotubes in various organic solvents. *Scientific Reports* **2016**, 6, 26208.

83. Heo, J. H.; Han, H. J.; Kim, D.; Ahn, T. K.; Im, S. H., Hysteresis-less inverted $CH_3NH_3PbI_3$ planar perovskite hybrid solar cells with 18.1% power conversion efficiency. *Energy & Environmental Science* **2015**, 8, 1602-1608.

84. Jeon, N. J.; Noh, J. H.; Kim, Y. C.; Yang, W. S.; Ryu, S.; Seok, S. I., Solvent engineering for high-performance inorganic–organic hybrid perovskite solar cells. *Nature Materials* **2014**, 13, 897-903.

85. Williams, A. E.; Holliman, P. J.; Carnie, M. J.; Davies, M. L.; Worsley, D. A.; Watson, T. M., Perovskite processing for photovoltaics: a spectro-thermal evaluation. *Journal of Materials Chemistry A* **2014**, 2, 19338-19346.

86. Cheon, J. Y.; Kim, J. H.; Kim, J. H.; Goddeti, K. C.; Park, J. Y.; Joo, S. H., Intrinsic relationship between enhanced oxygen reduction reaction activity and nanoscale work function of doped carbons. *Journal of the American Chemical Society* **2014**, 136, 8875-8878.

87. Liu, D.; Kelly, T. L., Perovskite solar cells with a planar heterojunction structure prepared using room-temperature solution processing techniques. *Nature Photonics* **2014**, 8, 133-138.

88. Malinkiewicz, O.; Yella, A.; Lee, Y. H.; Espallargas, G. M.; Graetzel, M.; Nazeeruddin, M. K.; Bolink, H. J., Perovskite solar cells employing organic charge-transport layers. *Nature Photonics* **2014**, 8, 128-132.

89. Docampo, P.; Ball, J. M.; Darwich, M.; Eperon, G. E.; Snaith, H. J., Efficient organometal trihalide perovskite planar-heterojunction solar cells on flexible polymer substrates. *Nature Communications* **2013**, 4, 2761.

90. You, J.; Hong, Z.; Yang, Y.; Chen, Q.; Cai, M.; Song, T.-B.; Chen, C.-C.; Lu, S.; Liu, Y.; Zhou, H.; Yang, Y., Low-temperature solution-processed perovskite solar cells with high efficiency and flexibility. *ACS Nano* **2014**, 8, 1674-1680.

91. Seo, J.; Park, S.; Kim, Y. C.; Jeon, N. J.; Noh, J. H.; Yoon, S. C.; Seok, S. I., Benefits of very thin PCBM and LiF layers for solution-processed p–i–n perovskite solar cells. *Energy & Environmental Science* **2014**, 7, 2642-2646.

92. Jeng, J. -Y.; Chiang, Y. -F.; Lee, M. -H.; Peng, S. -R.; Guo, T. -F.; Chen, P.; Wen, T. -C., $CH_3NH_3PbI_3$ perovskite/fullerene planar-heterojunction hybrid solar cells. *Advanced Materials* **2013**, 25, 3727-3732.

93. Dualeh, A.; Tétreault, N.; Moehl, T.; Gao, P.; Nazeeruddin, M. K.; Grätzel, M., Effect of annealing temperature on film morphology of organic–inorganic hybrid pervoskite solid-state solar cells. *Advanced Functional Materials* **2014**, 24, 3250-3258.

94. Eperon, G. E.; Burlakov, V. M.; Docampo, P.; Goriely, A.; Snaith, H. J., Morphological control for high performance, solution-processed planar heterojunction perovskite solar cells. *Advanced Functional Materials* **2014**, 24, 151-157.

95. Hörantner, M. T.; Nayak, P. K.; Mukhopadhyay, S.; Wojciechowski, K.; Beck, C.; McMeekin, D.; Kamino, B.; Eperon, G. E.; Snaith, H. J., Shunt-blocking layers for semitransparent perovskite solar cells. *Advanced Materials Interfaces* **2016**, 3, 1500837.

96. Zhang, F.; Song, J.; Hu, R.; Xiang, Y.; He, J.; Hao, Y.; Lian, J.; Zhang, B.; Zeng, P.; Qu, J., Interfacial passivation of the p-doped hole-transporting layer using general insulating polymers for high-performance inverted perovskite solar cells. *Small* **2018**, 14, 1704007.

97. Green, M. A.; Hishikawa, Y.; Warta, W.; Dunlop, E. D.; Levi, D. H.; Hohl-Ebinger, J.; Ho-Baillie, A. W. H., Solar cell efficiency tables (version 50). *Progress in Photovoltaics* **2017**, 25, 668-676.

98. Zheng, X.; Chen, B.; Dai, J.; Fang, Y.; Bai, Y.; Lin, Y.; Wei, H.; Zeng, X. C.; Huang, J., Defect passivation in hybrid perovskite solar cells using quaternary ammonium halide anions and cations. *Nature Energy* **2017**, 2, 17102.

99. Yang, W. S.; Park, B.-W.; Jung, E. H.; Jeon, N. J.; Kim, Y. C.; Lee, D. U.; Shin, S. S.; Seo, J.; Kim, E. K.; Noh, J. H.; Seok, S. I., Iodide management in formamidinium-lead-halide–based perovskite layers for efficient solar cells. *Science* **2017**, 356, 1376-1379.

100. Salim, T.; Sun, S.; Abe, Y.; Krishna, A.; Grimsdale, A. C.; Lam, Y. M., Perovskite-based solar cells: impact of morphology and device architecture on device performance. *Journal of Materials Chemistry A* **2015**, 3, 8943-8969.

101. Bi, C.; Wang, Q.; Shao, Y.; Yuan, Y.; Xiao, Z.; Huang, J., Non-wetting surface-driven high-aspect-ratio crystalline grain growth for efficient hybrid perovskite solar cells. *Nature Communications* **2015**, 6, 7747.

102. Lee, K.-M.; Lin, C.-J.; Liou, B.-Y.; Yu, S.-M.; Hsu, C.-C.; Suryanarayanan, V.; Wu, M.-C., Selection of anti-solvent and optimization of dropping volume for the preparation of large area sub-module perovskite solar cells. *Solar Energy Materials and Solar Cells* **2017**, 172, 368-375.

103. Paek, S.; Schouwink, P.; Athanasopoulou, E. N.; Cho, K. T.; Grancini, G.; Lee, Y.; Zhang, Y.; Stellacci, F.; Nazeeruddin, M. K.; Gao, P., From Nano-to Micrometer Scale: The role of antisolvent treatment on high performance perovskite solar cells. *Chemistry of Materials* **2017**, 29, 3490-3498.

104. Bai, S.; Wu, Z.; Wu, X.; Jin, Y.; Zhao, N.; Chen, Z.; Mei, Q.; Wang, X.; Ye, Z.; Song, T.; Liu, R.; Lee, S.-T.; Sun, B., High-performance planar heterojunction perovskite solar cells: Preserving long charge carrier diffusion lengths and interfacial engineering. *Nano Research* **2014**, 7, 1749-1758.

105. Yin, X.; Que, M.; Xing, Y.; Liu, X.; Que, W.; Niu, C., Solution-induced morphology change of organic-inorganic hybrid perovskite films for high efficiency inverted planar heterojunction solar cells. *Electrochimica Acta* **2016**, 191, 750-757.

106. Kang, R.; Kim, J.-E.; Yeo, J.-S.; Lee, S.; Jeon, Y.-J.; Kim, D.-Y., Optimized organometal halide perovskite planar hybrid solar cells via control of solvent evaporation rate. *The Journal of Physical Chemistry C* **2014**, 118, 26513-26520.

107. Stranks, S. D.; Snaith, H. J., Metal-halide perovskites for photovoltaic and light-emitting devices. *Nature Nanotechnology* **2015**, 10, 391-402.

108. Tidhar, Y.; Edri, E.; Weissman, H.; Zohar, D.; Hodes, G.; Cahen, D.; Rybtchinski, B.; Kirmayer, S., Crystallization of methyl ammonium lead halide perovskites: implications for photovoltaic applications. *Journal of the American Chemical Society* **2014**, 136, 13249-13256.

109. Qing, J.; Chandran, H.-T.; Cheng, Y.-H.; Liu, X.-K.; Li, H.-W.; Tsang, S.-W.; Lo, M.-F.; Lee, C.-S., Chlorine incorporation for enhanced performance of planar perovskite solar cell based on lead acetate precursor. *ACS Applied Materials & Interfaces* **2015**, 7, 23110-23116.

110. Sadoughi, G.; Starr, D. E.; Handick, E.; Stranks, S. D.; Gorgoi, M.; Wilks, R. G.; Bär, M.; Snaith, H. J., Observation and mediation of the presence of metallic lead in organic–inorganic perovskite films. *ACS Applied Materials & Interfaces* **2015**, 7, 13440-13444.

111. Ahmad, Z.; Najeeb, M. A.; Shakoor, R.; Alashraf, A.; Al-Muhtaseb, S. A.; Soliman, A.; Nazeeruddin, M. K., Instability in $CH_3NH_3PbI_3$ perovskite solar cells due to elemental migration and chemical composition changes. *Scientific Reports* **2017**, 7, 15406.

112. Guerrero, A.; You, J.; Aranda, C.; Kang, Y. S.; Garcia-Belmonte, G.; Zhou, H.; Bisquert, J.; Yang, Y., Interfacial degradation of planar lead halide perovskite solar cells. *Acs Nano* **2016**, 10, 218-224.

113. Besleaga, C.; Abramiuc, L. E.; Stancu, V.; Tomulescu, A. G.; Sima, M.; Trinca, L.; Plugaru, N.; Pintilie, L.; Nemnes, G. A.; Iliescu, M.; Svavarsson, H. G.; Manolescu, A.; Pintilie, I., Iodine migration and degradation of perovskite solar cells enhanced by metallic electrodes. *The Journal of Physical Chemistry Letters* **2016**, 7, 5168-5175.

114. Eames, C.; Frost, J. M.; Barnes, P. R. F.; O'regan, B. C.; Walsh, A.; Islam, M. S., Ionic transport in hybrid lead iodide perovskite solar cells. *Nature Communications* **2015**, 6, 7497.

115. Forgács, D.; Sessolo, M.; Bolink, H. J., Lead acetate precursor based pin perovskite solar cells with enhanced reproducibility and low hysteresis. *Journal of Materials Chemistry A* **2015**, 3, 14121-14125.

116. Feng, W.; Rangan, S.; Cao, Y.; Galoppini, E.; Bartynski, R. A.; Garfunkel, E., Energy level alignment of polythiophene/ZnO hybrid solar cells. *Journal of Materials Chemistry A* **2014**, 2, 7034-7044.

117. Scharber, M. C.; Mühlbacher, D.; Koppe, M.; Denk, P.; Waldauf, C.; Heeger, A. J.; Brabec, C. J., Design rules for donors in bulk-heterojunction solar cells—Towards 10% energy-conversion efficiency. *Advanced Materials* **2006**, 18, 789-794.

118. Schulz, P.; Edri, E.; Kirmayer, S.; Hodes, G.; Cahen, D.; Kahn, A., Interface energetics in organo-metal halide perovskite-based photovoltaic cells. *Energy & Environmental Science* **2014**, 7, 1377-1381.

119. Bakr, Z. H.; Wali, Q.; Fakharuddin, A.; Schmidt-Mende, L.; Brown, T. M.; Jose, R., Advances in hole transport materials engineering for stable and efficient perovskite solar cells. *Nano Energy* **2017**, 34, 271-305.

120. Zhou, Z.; Pang, S.; Liu, Z.; Xu, H.; Cui, G., Interface engineering for high-performance perovskite hybrid solar cells. *Journal of Materials Chemistry A* **2015**, 3, 19205-19217.

121. Wang, W.; Yuan, J.; Shi, G.; Zhu, X.; Shi, S.; Liu, Z.; Han, L.; Wang, H.-Q.; Ma, W., Inverted planar heterojunction perovskite solar cells employing polymer as the electron conductor. *ACS Applied Materials & Interfaces* **2015**, 7, 3994-3999.

122. Xu, X.; Shi, J.; Wu, H.; Yang, Y.; Xiao, J.; Luo, Y.; Li, D.; Meng, Q., The influence of different mask aperture on the open-circuit voltage measurement of perovskite solar cells. *Journal of Renewable and Sustainable Energy* **2015**, *7*, 043104.

123. Im, J.-H.; Jang, I.-H.; Pellet, N.; Grätzel, M.; Park, N.-G., Growth of $CH_3NH_3PbI_3$ cuboids with controlled size for high-efficiency perovskite solar cells. *Nature Nanotechnology* **2014**, *9*, 927-932.

124. Chen, Q.; Zhou, H.; Fang, Y.; Stieg, A. Z.; Song, T.-B.; Wang, H.-H.; Xu, X.; Liu, Y.; Lu, S.; You, J.; Sun, P.; McKay, J.; Goorsky, M. S.; Yang, Y., The optoelectronic role of chlorine in $CH_3NH_3PbI_3(Cl)$-based perovskite solar cells. *Nature Communications* **2015**, 6, 7269.

125. Yu, J. C.; Hong, J. A.; Jung, E. D.; Kim, D. B.; Baek, S.-M.; Lee, S.; Cho, S.; Park, S. S.; Choi, K. J.; Song, M. H., Highly efficient and stable inverted perovskite solar cell employing PEDOT: GO composite layer as a hole transport layer. *Scientific Reports* **2018**, 8, 1070.

126. Zhu, H.; Pan, M.; Johansson, M. B.; Johansson, E. M. J., High photon-to-current conversion in solar cells based on light-absorbing silver bismuth iodide. *ChemSusChem* **2017**, 10, 2592-2596.

127. Chen, Y.; Chen, T.; Dai, L., Layer-by-layer growth of $CH_3NH_3PbI_{3-x}Cl_x$ for highly efficient planar heterojunction perovskite solar cells. *Advanced Materials* **2015**, 27, 1053-1059.

128. Saparov, B.; Hong, F.; Sun, J.-P.; Duan, H.-S.; Meng, W.; Cameron, S.; Hill, I. G.; Yan, Y.; Mitzi, D. B., Thin-film preparation and characterization of $Cs_3Sb_2I_9$: A lead-free layered perovskite semiconductor. *Chemistry of Materials* **2015**, 27, 5622-5632.

129. Chen, M.; Ju, M.-G.; Carl, A. D.; Zong, Y.; Grimm, R. L.; Gu, J.; Zeng, X. C.; Zhou, Y.; Padture, N. P., Cesium titanium (IV) bromide thin films based stable lead-free perovskite solar cells. *Joule* **2018**, 2, 558-570.

130. Xiao, Z.; Meng, W.; Mitzi, D. B.; Yan, Y., Crystal structure of $AgBi_2I_7$ thin films. *The Journal of Physical Chemistry Letters* **2016**, 7, 3903-3907.

131. Dzeranova, K.; Kaloev, N.; Bulakhova, G., System BiI_3-AgI. *Zhurnal Neorganicheskoj Khimii* **1985**, 30, 2983-2985.

132. Mashadieva, L. F.; Aliev, Z. S.; Shevelkov, A. V.; Babanly, M. B., Experimental investigation of the Ag–Bi–I ternary system and thermodynamic properties of the ternary phases. *Journal of Alloys and Compounds* **2013**, 551, 512-520.

133. Jung, K. W.; Sohn, M. R.; Lee, H. M.; Yang, I. S.; Do Sung, S.; Kim, J.; Diau, E. W.-G.; Lee, W. I., Silver bismuth iodides in various compositions as potential Pb-free light absorbers for hybrid solar cells. *Sustainable Energy & Fuels* **2018**, 2, 294-302.

134. Shao, Z.; Le Mercier, T.; Madec, M.; Pauporté, T., Exploring $AgBi_xI_{3x+1}$ semiconductor thin films for lead-free perovskite solar cells. *Materials & Design* **2018**, 141, 81-87.

135. Lindqvist, O.; Johansson, G.; Sandberg, F.; Norin, T., Crystal structure of caesium bismuth iodide, $Cs_3Bi_2I_9$. *Acta Chemica Scandinavica* **1968**, 22, 2943-2952.

136. Sidey, V. I.; Voroshilov, Y. V.; Kun, S. V.; Peresh, E. Y., Crystal growth and X-ray structure determination of $Rb_3Bi_2I_9$. *Journal of Alloys and Compounds* **2000**, 296, 53-58.

137. Weber, S. A. L.; Hermes, I. M.; Turren-Cruz, S. -H.; Gort, C.; Bergmann, V. W.; Gilson, L.; Hagfeldt, A.; Graetzel, M.; Tress, W.; Berger, R., How the formation of interfacial charge causes hysteresis in perovskite solar cells. *Energy & Environmental Science* **2018**, 11, 2404-2413.

138. Snaith, H. J.; Abate, A.; Ball, J. M.; Eperon, G. E.; Leijtens, T.; Noel, N. K.; Stranks, S. D.; Wang, J. T.-W.; Wojciechowski, K.; Zhang, W., Anomalous hysteresis in perovskite solar cells. *The Journal of Physical Chemistry Letters* **2014**, 5, 1511-1515.

139. Shi, J.; Xu, X.; Li, D.; Meng, Q., Interfaces in perovskite solar cells. *Small* **2015**, 11, 2472-2486.

140. Fakharuddin, A.; Schmidt-Mende, L.; Garcia-Belmonte, G.; Jose, R.; Mora-Sero, I., Interfaces in perovskite solar cells. *Advanced Energy Materials* **2017**, 7, 1700623.

141. Tasis, D.; Tagmatarchis, N.; Bianco, A.; Prato, M., Chemistry of carbon nanotubes. *Chemical Reviews* **2006**, 106, 1105-1136.

142. Niyogi, S.; Hamon, M.; Hu, H.; Zhao, B.; Bhowmik, P.; Sen, R.; Itkis, M.; Haddon, R., Chemistry of single-walled carbon nanotubes. *Accounts of Chemical Research* **2002**, 35, 1105-1113.

143. Dai, H.; Wong, E. W.; Lieber, C. M., Probing electrical transport in nanomaterials: conductivity of individual carbon nanotubes. *Science* **1996**, 272, 523-526.

144. Miao, M., Electrical conductivity of pure carbon nanotube yarns. *Carbon* **2011**, 49, 3755-3761.

145. Yao, Z.; Kane, C. L.; Dekker, C., High-field electrical transport in single-wall carbon nanotubes. *Physical Review Letters* **2000**, 84, 2941.

146. Lee, J. U.; Gipp, P. P.; Heller, C. M., Carbon nanotube p-n junction diodes. *Applied Physics Letters* **2004**, 85, 145-147.

147. Wang, S.; Zhang, Z.; Ding, L.; Liang, X.; Shen, J.; Xu, H.; Chen, Q.; Cui, R.; Li, Y.; Peng, L. -M., A doping-free carbon nanotube CMOS inverter-based bipolar diode and ambipolar transistor. *Advanced Materials* **2008**, 20, 3258-3262.

148. Li, J.; Hu, L.; Wang, L.; Zhou, Y.; Grüner, G.; Marks, T. J., Organic light-emitting diodes having carbon nanotube anodes. *Nano Letters* **2006**, 6, 2472-2477.

149. Wang, S.; Zeng, Q.; Yang, L.; Zhang, Z.; Wang, Z.; Pei, T.; Ding, L.; Liang, X.; Gao, M.; Li, Y.; Peng, L.-M., High-performance carbon nanotube light-emitting diodes with asymmetric contacts. *Nano Letters* **2011**, 11, 23-29.

150. Hatton, R. A.; Blanchard, N. P.; Tan, L. W.; Latini, G.; Cacialli, F.; Silva, S. R. P., Oxidised carbon nanotubes as solution processable, high work function hole-extraction layers for organic solar cells. *Organic Electronics* **2009**, 10, 388-395.

151. Lee, J. M.; Park, J. S.; Lee, S. H.; Kim, H.; Yoo, S.; Kim, S. O., Selective electron-or hole-transport enhancement in bulk-heterojunction organic solar cells with N-or B-doped carbon nanotubes. *Advanced Materials* **2011**, 23, 629-633.

152. Pradhan, B.; Batabyal, S. K.; Pal, A. J., Functionalized carbon nanotubes in donor/acceptor-type photovoltaic devices. *Applied Physics Letters* **2006**, 88, 093106.

153. Li, Z.; Kulkarni, S. A.; Boix, P. P.; Shi, E.; Cao, A.; Fu, K.; Batabyal, S. K.; Zhang, J.; Xiong, Q.; Wong, L. H.; Mathews, N.; Mhaisalkar, S. G., Laminated carbon nanotube networks for metal electrode-free efficient perovskite solar cells. *ACS Nano* **2014**, 8, 6797-6804.

154. Wang, J.; Li, J.; Xu, X.; Xu, G.; Shen, H., Enhanced photovoltaic performance with carbon nanotubes incorporating into hole transport materials for perovskite solar cells. *Journal of Electronic Materials* **2016**, 45, 5127-5132.

155. Lu, L.; Xu, T.; Chen, W.; Lee, J. M.; Luo, Z.; Jung, I. H.; Park, H. I.; Kim, S. O.; Yu, L., The role of N-doped multiwall carbon nanotubes in achieving highly efficient polymer bulk heterojunction solar cells. *Nano Letters* **2013**, 13, 2365-2369.

156. Li, C.; Chen, Y.; Wang, Y.; Iqbal, Z.; Chhowalla, M.; Mitra, S., A fullerene–single wall carbon nanotube complex for polymer bulk heterojunction photovoltaic cells. *Journal of Materials Chemistry* **2007**, 17, 2406-2411.

157. Dyke, C. A.; Tour, J. M., Covalent functionalization of single-walled carbon nanotubes for materials applications. *The Journal of Physical Chemistry A* **2004**, 108, 11151-11159.

158. Lu, W.; Chou, T.-W., Analysis of the entanglements in carbon nanotube fibers using a self-folded nanotube model. *Journal of the Mechanics and Physics of Solids* **2011**, 59, 511-524.

159. Chen, P.; Chew, L. M.; Kostka, A.; Xie, K.; Muhler, M.; Xia, W., Purified oxygen-and nitrogen-modified multi-walled carbon nanotubes as metal-free catalysts for selective olefin hydrogenation. *Journal of Energy Chemistry* **2013**, 22, 312-320.

160. Kim, S. W.; Kim, T.; Kim, Y. S.; Choi, H. S.; Lim, H. J.; Yang, S. J.; Park, C. R., Surface modifications for the effective dispersion of carbon nanotubes in solvents and polymers. *Carbon* **2012**, 50, 3-33.

161. Wepasnick, K. A.; Smith, B. A.; Schrote, K. E.; Wilson, H. K.; Diegelmann, S. R.; Fairbrother, D. H., Surface and structural characterization of multi-walled carbon nanotubes following different oxidative treatments. *Carbon* **2011**, 49, 24-36.

162. Zhao, A.; Masa, J.; Schuhmann, W.; Xia, W., Activation and stabilization of nitrogen-doped carbon nanotubes as electrocatalysts in the oxygen reduction reaction at strongly alkaline conditions. *The Journal of Physical Chemistry C* **2013**, 117, 24283-24291.

163. Datsyuk, V.; Kalyva, M.; Papagelis, K.; Parthenios, J.; Tasis, D.; Siokou, A.; Kallitsis, I.; Galiotis, C., Chemical oxidation of multiwalled carbon nanotubes. *Carbon* **2008**, 46, 833-840.

164. Osorio, A. G.; Silveira, I. C. L.; Bueno, V. L.; Bergmann, C. P., $H_2SO_4/HNO_3/HCl$–functionalization and its effect on dispersion of carbon nanotubes in aqueous media. *Applied Surface Science* **2008**, 255, 2485-2489.

165. Lee, S.; Peng, J.-W.; Liu, C.-H., Probing plasma-induced defect formation and oxidation in carbon nanotubes by Raman dispersion spectroscopy. *Carbon* **2009**, 47, 3488-3497.

166. Xu, T.; Yang, J.; Liu, J.; Fu, Q., Surface modification of multi-walled carbon nanotubes by O_2 plasma. *Applied Surface Science* **2007**, 253, 8945-8951.

167. Li, C.; Zhao, A.; Xia, W.; Liang, C.; Muhler, M., Quantitative studies on the oxygen and nitrogen functionalization of carbon nanotubes performed in the gas phase. *The Journal of Physical Chemistry C* **2012**, 116, 20930-20936.

168. Ago, H.; Kugler, T.; Cacialli, F.; Salaneck, W. R.; Shaffer, M. S.; Windle, A. H.; Friend, R. H., Work functions and surface functional groups of multiwall carbon nanotubes. *The Journal of Physical Chemistry B* **1999**, 103, 8116-8121.

169. Suzuki, S.; Bower, C.; Watanabe, Y.; Zhou, O., Work functions and valence band states of pristine and Cs-intercalated single-walled carbon nanotube bundles. *Applied Physics Letters* **2000**, 76, 4007-4009.

170. Urbina, A.; Park, J. S.; Lee, J. M.; Kim, S. O.; Kim, J.-S., Work function engineering of ZnO electrodes by using p-type and n-type doped carbon nanotubes. *Nanotechnology* **2013**, 24, 484013.

171. Zhao, J.; Han, J.; Lu, J. P., Work functions of pristine and alkali-metal intercalated carbon nanotubes and bundles. *Physical Review B* **2002**, 65, 193401.

172. Kundu, S.; Xia, W.; Busser, W.; Becker, M.; Schmidt, D. A.; Havenith, M.; Muhler, M., The formation of nitrogen-containing functional groups on carbon nanotube surfaces: a quantitative XPS and TPD study. *Physical Chemistry Chemical Physics* **2010**, 12, 4351-4359.

173. Jin, C.; Xia, W.; Chen, P.; Muhler, M., On the role of the residual iron growth catalyst in the gasification of multi-walled carbon nanotubes with carbon dioxide. *Catalysis Today* **2012**, 186, 128-133.

174. Scheibe, B.; Borowiak-Palen, E.; Kalenczuk, R. J., Oxidation and reduction of multiwalled carbon nanotubes – preparation and characterization. *Materials Characterization* **2010**, 61, 185-191.

175. Lehman, J. H.; Terrones, M.; Mansfield, E.; Hurst, K. E.; Meunier, V., Evaluating the characteristics of multiwall carbon nanotubes. *Carbon* **2011**, 49, 2581-2602.

176. Osswald, S.; Havel, M.; Gogotsi, Y., Monitoring oxidation of multiwalled carbon nanotubes by Raman spectroscopy. *Journal of Raman Spectroscopy* **2007**, 38, 728-736.

177. Allen, F. G.; Gobeli, G. W., Work function, photoelectric threshold, and surface states of atomically clean silicon. *Physical Review* **1962**, 127, 150.

178. Dillon Jr, J. A.; Farnsworth, H. E., Work function and sorption properties of silicon crystals. *Journal of Applied Physics* **1958**, 29, 1195-1202.

179. Calió, L.; Kazim, S.; Grätzel, M.; Ahmad, S., Hole-transport materials for perovskite solar cells. *Angewandte Chemie International Edition* **2016**, 55, 14522-14545.

180. Choi, H. J.; Shin, J. E.; Lee, G.-W.; Park, N.-G.; Kim, K.; Hong, S. C., Effect of surface modification of multi-walled carbon nanotubes on the fabrication and performance of carbon nanotube based counter electrodes for dye-sensitized solar cells. *Current Applied Physics* **2010**, 10, S165-S167.

181. Ansón-Casaos, A.; González-Domínguez, J. M.; Lafragüeta, I.; Carrodeguas, J. A.; Martínez, M. T., Optical absorption response of chemically modified single-walled carbon nanotubes upon ultracentrifugation in various dispersants. *Carbon* **2014**, 66, 105-118.

182. Jacobsson, T. J.; Correa-Baena, J.-P.; Pazoki, M.; Saliba, M.; Schenk, K.; Grätzel, M.; Hagfeldt, A., Exploration of the compositional space for mixed lead halogen perovskites for high efficiency solar cells. *Energy & Environmental Science* **2016**, 9, 1706-1724.